JOINT EUROPEAN TORUS

JET–P(90)62

Many JET Authors

JET Papers Presented to 13th IAEA Conference on Plasma Physics and Controlled Nuclear Fusion Research

JET Papers Presented to 13th IAEA Conference on Plasma Physics and Controlled Nuclear Fusion Research

Many JET Authors

JET-Joint Undertaking, Culham Science Centre, OX14 3DB, Abingdon, UK

** See Appendix 1*

Preprint of Paper to be submitted for publication in
Nuclear Fusion Supplement

JET Papers presented to
13th IAEA Conference on Plasma Physics and
Controlled Nuclear Fusion Research

IAEA-CN-53/A-1-2

Recent JET Results and Future Prospects

by

The JET Team*

(presented by PH Rebut)

JET Joint Undertaking, Abingdon,
Oxon. OX14 3EA, UK

* See Appendix I

Recent JET Results and Future Prospects

Abstract

The latest results of JET plasmas in transient and steady states are presented. Substantial improvements in plasma purity and corresponding reductions in plasma dilution have resulted from the use of beryllium as the first wall material facing the hot plasma. As a consequence, plasmas with a fusion triple product ($n_D(0)\tau_E T_i(0)$) in the range 8-9x10^{20}m^{-3}skeV have been achieved (within a factor of 8 of that required in a fusion reactor), albeit under transient conditions. The general JET performance has also improved, allowing the parameters of a reactor plasma to be individually achieved in JET. In view of their importance for reactors, the JET results are presented with particular emphasis on their significance for the formulation of a plasma model for the Next Step. However, impurity influxes limit the attainment of better parameters and prevent the realisation of steady state conditions at high heating powers. To address this problem of impurity control, and those of plasma fuelling and helium ash exhaust, a New Phase is planned for JET with an axi-symmetric pumped divertor configuration that will allow operating conditions close to those of a reactor. The divertor configuration should demonstrate a concept of impurity control and determine the size and geometry needed to fulfil this concept in a reactor. It should identify appropriate materials for plasma facing components and define the operational domain for the Next Step.

1. INTRODUCTION

The objective of JET is to obtain and study plasmas in conditions and dimensions approaching those needed in a thermonuclear reactor [1,2]. The present paper concentrates on progress towards this objective during the last two years of JET operation, since the 1988 IAEA Conference [3]. The transient and steady state behaviour of JET plasmas are presented in view of their importance for reactor plasmas. JET operation and the consequences of using a beryllium "first wall" are discussed and the best fusion performance and general plasma behaviour in JET are reported. The underlying results are presented with particular emphasis on their significance for the formulation of a plasma model for a Next Step tokamak. In view of the importance of dilution and exhaust for ignition [4] and the need for adequate impurity control and understanding of the scrape-off layer plasma, a New Phase is planned for JET with a divertor configuration and this is also discussed.

2. JET OPERATION

Since 1988, further additions and technical enhancements to JET have been made:

- reinforcement of the vacuum vessel to withstand radial and vertical instabilities and permit operation at full power up to 7MA in the material limiter configuration and up to 6MA in the X-point configuration (inconel rings fitted above and below the mid-plane at the in-board walls to stiffen and strengthen the vessel);
- belt limiter tiles, ion cyclotron resonance heating (ICRH) antennae screens and lower X-point dump plates were changed to beryllium and beryllium evaporation has also been used;
- one neutral beam injection (NBI) box was modified to operate at 140kV to provide better penetration at higher density. The other NBI box remained at 80kV. This gave a total power of 18MW (instead of 21MW with both boxes at 80kV);

- each ICRH generator power unit was upgraded to 2MW, offering the potential of 32MW total power source and ~24MW coupled to the plasma through eight antennae;
- a prototype lower hybrid current drive (LHCD) system has been installed, offering the potential of 4MW at 3.7GHz;

In addition, a faulty toroidal field coil has been removed and replaced successfully with a spare coil.

JET is now about midway through its experimental programme. The technical design specification of JET has been achieved in all parameters and exceeded in several cases (see Table I). The plasma current of 7MA in the limiter configuration [5] and the current duration of up to 30s at 3MA are world records and are over twice the values achieved in any other fusion experiment. 5.1MA and 4.5MA are also world records in the single-null and double-null divertor configurations, respectively [6]. NBI heating has been brought up to full power (~21MW) and ICRH power has been increased to ~22MW in the plasma. In combination, these systems have delivered 35MW to the plasma.

3. THE USE OF BERYLLIUM IN JET

Over the last two years impurities and density control have been the main obstacles to the improvement of JET performance. Carbon first-wall components had been developed so that they were mechanically able to withstand the power loads encountered. However, the interaction of the plasma with these components, even under quiescent conditions, caused unacceptable dilution of the plasma fuel. In addition, imperfections in the positioning of the components led to localised heating at high power, and the following problems occurred:

- the production of impurities increased with the input power to the plasma;
- at high power, the heat load on the tiles caused a plasma evolution which exhibited a catastrophic behaviour - the so-called "carbon catastrophe". Increased plasma dilution, increased power radiated, reduced neutral beam penetration and a threefold fall of fusion yield resulted from the carbon influx;
- for lower input power with long duration, problems were also encountered. Without fuelling, deuterium was pumped by the carbon and replaced by impurities, resulting in severe dilution of the plasma;
- the maximum density achieved without the occurrence of plasma disruptions appeared to be limited by edge radiation.

The situation has been redressed by the progressive introduction of beryllium "first-wall" components since 1989 [7]. First, beryllium was evaporated as a thin layer on the carbon walls and limiters; then, as the material for the limiter tiles; and finally, as the material for the lower X-point target tiles and the open screens of the ICRH antennae.

With a carbon first-wall, the main impurities were carbon (2-10%) and oxygen (1-2%). With beryllium evaporated inside the vessel, oxygen was reduced by factors >20, and carbon by >2. Although beryllium increased, carbon remained the dominant impurity for this phase. With beryllium limiters, the carbon concentration was reduced by a further factor of 10, but beryllium levels increased by ~10, and became the dominant impurity. Due to the virtual elimination of oxygen and replacement of carbon by beryllium, impurity influxes were reduced significantly, in line with model calculations [8] which take account of impurity self-sputtering. In addition, nickel was eliminated from the plasma when the nickel screens for the ICRH antennae were replaced by beryllium.

During 1989, plasma dilution and the effective plasma charge, Z_{eff}, were reduced significantly in ohmic plasmas and with strong additional heating. Fig. 1(a) shows the dilution factor, n_D/n_e, as a function of input power per particle,

$P_t/\langle n_e \rangle$. The corresponding values of Z_{eff} are shown in Fig. 1(b). With moderate power, it was not possible to maintain n_D/n_e much above 0.6 with carbon, but values greater than 0.8 were routinely achieved with beryllium. Furthermore, high power operation was possible only with beryllium.

Impurity radiation was also reduced and operation with beryllium gettering allowed improved density control (due to high wall pumping of both deuterium and helium). On the longer timescale (minutes to hours), very little deuterium was retained compared with a carbon first-wall; >80% of the neutral gas admitted to JET is recovered, compared with ~50% with a carbon first-wall. This has important advantages for the tritium phase of JET operation.

4. JET PERFORMANCE

4.1. Fusion performance

With carbon X-point target plates, the length of the H-mode has been extended (up to 5.3s) either by sweeping the X-point (both in the radial and vertical directions) to reduce the X-point tile temperature, or by using strong gas puffing in the divertor region. This, together with the better plasma purity achieved with a beryllium first-wall, resulted in increased ion temperatures ($T_i(0)$ in the range 20-30keV) and improved plasma performance, with the fusion triple product ($n_D(0)\tau_E T_i(0)$) increasing significantly. Such improved fusion performance could otherwise have been achieved only with a substantial increase in energy confinement.

In a particular case, the central ion temperature reached 22keV, the energy confinement time, τ_E, was 1.1s, with a record fusion triple product ($n_D(0)\tau_E T_i(0)$) of 8–9x10^{20}m^{-3}skeV. The neutron yield for this discharge was also amongst the highest achieved on JET at 3.5x10^{16}ns^{-1}, with Q_{DD}= 2.4x10^{-3}. A full D-T simulation of the pulse showed that 12MW of fusion power would have been obtained transiently with 16MW of NBI power, giving an equivalent fusion amplification factor Q_{DT} ~ 0.8, reaching near breakeven conditions and within a factor of 8 of that required by a reactor. Similar results were also obtained at medium temperatures, with $T_e \sim T_i \sim 10$keV.

The overall fusion triple product as a function of central ion temperature is shown in Fig. 2 for a number of tokamaks.

4.2. General behaviour

Reduced impurity levels allowed prolonged operation at higher densities and improved the general JET performance, as follows:

- the pumping of deuterium with a beryllium first-wall was more efficient than with a carbon first-wall and provided improved density control. This permitted low density and high temperature (up to 30keV) operation for times >1s;
- the density limit increased [9], and a peak density of 4x10^{20}m^{-3} was achieved with pellet fuelling. The density is limited principally by fuelling and not by disruptions, as was found with carbon limiters;
- sawtooth free periods exceeding 5s were achieved, but the stabilisation mechanism is still not yet clear [10]. The central electron temperature appears to saturate at about 12keV, even though the central heating power to the electrons can be higher than that to the ions;
- H-modes were established with ICRH alone and for periods >1s. With beryllium antennae screens, H-modes were established with either monopole or dipole phasing [11]. The confinement characteristics of ICRH H-modes were similar to those with NBI alone;
- β-values up to the Troyon limit were obtained in double-null X-point plasmas [9].

Thus, the parameters of a reactor plasma have been achieved individually in JET.

However, the best fusion performance was obtained in a **transient** state and could not be sustained in steady state. Ultimately, the influx of impurities caused a degradation in plasma parameters. Furthermore, a severe carbon influx ("carbon catastrophe") was still a problem for inner wall and X-point operation, and is a serious limitation in H-mode studies.

5. UNDERLYING RESULTS AND THEIR SIGNIFICANCE

The underlying JET results are presented with particular emphasis on their significance for the formulation of a plasma model for the Next Step.

5.1. Density limit

With a carbon first-wall, the plasma density was limited, in general, when the radiated power reached 100% of the input power. This led to the growth of MHD instabilities and ended in a major disruption. The density limit was dependent on plasma purity and power to the plasma.

With a beryllium first-wall, the maximum operating density increased significantly by a factor of 1.6-2. A record central density of $4x10^{20}m^{-3}$ was achieved by strongly peaking the density profile using a sequence of 4mm solid deuterium pellets injected at intervals throughout the current rise phase of an X-point discharge. Furthermore, the nature of the density limit changed and the frequency of disruptions at the density limit were much reduced. Disruptions did not usually occur, and the limit was associated rather with the formation of a poloidally asymmetric, but toroidally symmetric radiating structure (a "MARFE"), which limits the plasma density to within the stable operating domain. These results constitute a substantial enhancement of JET's operating capability.

Heating and fuelling were varied systematically, using both gas and pellet fuelling. With deep pellet fuelling and either NBI or ICRH, peaked profiles were obtained (Fig. 3). Just before a density limit MARFE occurred, pellet fuelled discharges reached the same edge density as gas fuelled discharges, but the central densities were considerably higher. The central density depends, therefore, on the fuelling method used. The profiles are similar near the edge, but are remarkably flat with gas fuelling.

These observations suggest that the edge density may be correlated with the density limit and is found to increase approximately as the square root of power (Fig. 4). This endorses the view that the density limit is determined by a power balance at the plasma edge and the cause of disruptions is related to radiation near the q=2 surface. Thus, under beryllium conditions, when the radiation is low, or confined to the outermost edge, there are no density limit disruptions.

5.2. Density profiles and transport

Of significance also are the density profiles obtained with edge fuelling, which tend to be flatter with the lower Z_{eff} achieved with beryllium, in contrast to those obtained with carbon, which tended to be more peaked, even with edge fuelling. The occurrence of flat density profiles suggest that there is no need for an anomalous inward particle pinch, except perhaps on impurities. This observation poses important questions related to particle transport, and in particular, the transport and exhaust of helium ash products.

The relaxation of the peaked density profiles achieved with pellet injection allows an estimate of particle transport. For a 4mm pellet injected into 3MA/3.1T plasma, the decay of the central electron density is shown in Fig. 5. Following injection, the decay constants are 1.8s for the ohmically heated discharge and 1s when ~8MW ICRH is applied. The global energy confinement

times are in a similar ratio. It is therefore reasonable to assume that particle and energy transport are linked. Furthermore, modelling studies of similar discharges suggest that the diffusion coefficient is lower in the central plasma than further out and that there is no need for a large anomalous inward particle pinch in the central plasma [12].

Impurity transport studies have been possible from the measurement of emissivity profiles by the soft X-ray cameras following the injection of laser-ablated, high-Z impurities. The evolution of the nickel density profile has been determined (Fig. 6(a)) and so the particle fluxes can be plotted as a function of the density gradient at different radii. Fig. 6(b) shows that fluxes and gradients are linearly related through a diffusion coefficient which increases with radius. There is no evidence of a significant pinch term for the impurities.

This measurement also provides evidence of better confinement in H-modes. The temporal evolution of NiXXVI emission is shown in Fig. 7 for the L- and H-phases of two similar discharges with ~9MW of additional heating. In contrast to the decaying signal of the L-phase, the signal rises rapidly to a steady value which persists to the end of the H-phase. This shows that impurities have considerably longer confinement times in the H-phase and endorses the view that an edge transport barrier exists, which could be destroyed (for example, by ELMs) on transition from the H- to the L-phase.

5.3. Temperature

High ion temperatures have been obtained at the low densities possible with a beryllium first-wall and with the better penetration afforded by NBI at 140kV. Record ion temperatures were achieved of up to 18keV in limiter plasmas and up to 30keV in X-point plasmas (with powers up to 17MW). In this mode, the ion temperature profile is sharply peaked and the electron temperature is significantly lower than the ion temperature, by a factor of 2-3. The central ion temperature (as shown in Fig. 8) increases approximately linearly with power per particle up to the highest temperatures, indicating that ion thermal losses are anomalous, but ion confinement degrades little with input power. On the other hand, the central electron temperature saturates at ~12keV, even though with ICRH the central heating power to the electrons can be higher than that to the ions. Electron thermal transport is also anomalous and electron confinement degrades strongly with increased heating power. This suggests that electrons are primarily responsible for confinement degradation.

At higher densities with combined NBI and ICRH, central ion and electron temperatures were both above 11keV in a 3MA plasma for power input of 33MW (21 MW NBI and 12MW ICRH).

Extensive studies have also been performed in the 'monster-sawtooth' regime [10] in which sawteeth oscillations have been suppressed for up to 5s by central ICRH. Peaked temperature profiles (with both central ion and electron temperatures above 10keV) were maintained for several seconds. In an equivalent D-T mixture, this would result in a significant enhancement in the time-averaged neutron rate compared with a sawtoothing discharge. This does not mean, however, that ion losses are necessarily small.

5.4. Electron heat pulse propagation

The propagation of temperature perturbations (determined from the electron cyclotron polychromator) and density perturbations (determined from the multichannel reflectometer) following the collapse of a sawtooth provide good measurements of energy and particle transport. The decay of the temperature perturbation at different radii in a 3MA/3.1T ohmically heated discharge is shown in Fig. 9(a). This decay can be modelled with an heat pulse diffusivity, χ_{HP}~3.2m^{2}s^{-1}, which should be compared with χ_e~1m^{2}s^{-1}, obtained from power balance considerations. The results in an L-mode plasma, heated with 9.5MW of ICRH, are shown in Fig.9(b) and indicate that, although χ_e~2m^{2}s^{-1}, the same χ_{HP}~3.2m^{2}s^{-1} can be used in the simulation to fit the data. It is also

found that, within experimental uncertainties, the same χ_{HP} can be used also for H-regime plasmas and does not depend on heating power.

The propagation characteristics of the density perturbation indicate that the density pulse is slower than the temperature pulse and that the density pulse is comprised of both an outward and inward propagating perturbation (the latter resulting from the earlier interaction of the temperature pulse with the limiters) [12].

Furthermore, simultaneous measurements of the temperature and density perturbations indicate that the particle pulse diffusion coefficient, $D_{DP} \sim D_e \ll \chi_{HP}$.

5.5. Global energy confinement

With a carbon first-wall, the energy confinement time improves with increasing current and degrades with increasing heating power, independent of the heating method. With a beryllium first-wall, energy confinement times and their dependences are effectively unchanged: energy confinement does not appear to be affected by the impurity mix (carbon or beryllium in deuterium plasmas).

In the X-point configuration, high power H-modes (up to 25MW) have been studied. In comparison with limiter plasmas, confinement is a factor ~2 better, but the dependences with current and heating power are similar (Fig. 10).

With a carbon first-wall, H-modes with ICRH alone were not obtained. Beryllium evaporation on the nickel antennae screens led to lower impurity production and H-modes were successfully obtained with ICRH alone. With beryllium antennae screens, the threshold for the H-mode was reduced somewhat for dipole phasing, and ICRH H-modes were also obtained with monopole phasing. However, this required feedback control of the plasma position to allow for the movement of the plasma boundary during the L-H transition. In all cases, H-mode confinement with ICRH alone was similar to that with NBI, that is independent of the heating method.

A particular discharge (Fig. 11) exhibited an H-mode and pellet enhanced performance [11]. A 4mm pellet was injected into a 3MA/2.8T double null X-point plasma, heated with 9MW of ICRH and 2.5MW of NBI (which served primarily as a diagnostic for the measurement of the ion temperature). The stored plasma energy increased to 8MJ (still increasing at a rate ~4MW when the period of pellet enhanced confinement ceased). The energy confinement time reached ~1.0s and with central electron density $\sim 8 \times 10^{19} m^{-3}$, $Z_{eff} \sim 1$ and central electron and ion temperatures ~10keV, the fusion triple product was $\sim 8 \times 10^{20} m^{-3} skeV$. The neutron yield was $10^{16} s^{-1}$. This phase terminated as the central density decayed, although the stored energy remained high (again favouring the existence of an edge confinement barrier) until the end of the H-mode. Subsequently, plasma temperatures recovered, with the bulk deuterium ions being effectively heated in this ICRH scheme which used a high concentration of hydrogen minority ions.

5.6. Beta limits

Experiments have explored the plasma pressure (indicated by the β-value) that can be sustained in JET and investigated the plasma behaviour near the expected β-limit in a double-null H-mode configuration, at high density and temperature and low magnetic field ($B_t = 1T$). β_t values up to ~ 5.5% were obtained, close to the Troyon limit $\beta_t(\%) = 2.8 I_p(MA)/B_t(T)a(m)$, where I_p is the plasma current and a is the plasma minor radius [9]. Significantly, the JET limit does not appear to be disruptive at present power levels. Rather, a range of MHD instabilities occur, limiting the maximum β-value without causing a disruption. The behaviour near both the density and β-limits may be interpreted in terms of resonant instabilities which have the magnetic topology of an island.

5.7. Alpha-particle simulations

The behaviour of alpha-particles has been simulated in JET by studying energetic particles such as 1MeV tritons, and ^{3}He and H minority ions accelerated to a few MeV by ICRH [11]. The energetic population has up to 50% of the stored energy of the plasma and possesses all the characteristics of alpha-particles in an ignited plasma, except that in the JET experiments, the ratio of the perpendicular to parallel pressure was above three, while in a reactor plasma the distribution will be approximately isotropic. The mean energy of the minority species was about 1MeV, and the relative concentration of the ^{3}He ions to the electron density was 1-2%, which is comparable to the relative concentration of alpha-particles in a reactor (7%). Under conditions with little MHD activity, no evidence of non-classical loss or deleterious behaviour of minority ions was observed, even though the ratio of the fast ion slowing down time to the energy confinement time in JET is greater than that expected in a reactor.

Fusion reactivity measurements were undertaken on the D-^{3}He reaction when minority ^{3}He ions were accelerated to energies in the MeV range using ICRH. During a 5s monster sawtooth produced by 10MW of ICRH, a reaction rate of $4\times10^{16}s^{-1}$ was achieved, which corresponded to 100kW of fusion power and Q≈1% was reached. This was carried out with a beryllium first-wall and benefitted from an improved fuel concentration n_D/n_e of up to 0.7. Comparison of the measurements with theoretical predictions suggest nearly classical trapping and thermalisation of the energetic particles.

6. PLASMA MODELLING

6.1. Formulation of a plasma model

Any model used to predict the performance of a Next Step tokamak must be consistent with the foregoing data. In particular, it must explain:

- the resilience of the electron temperature to heating;
- the heat and density pulse propagation studies;
- no intrinsic degradation of ion confinement with ion heating;
- the density decay after pellet injection; and
- the similar behaviour of particle and heat transport.

It is possible to formulate a transport model, based on one phenomenon and consistent with JET data and with physics constraints. Specifically, above a critical threshold, $(\nabla T_e)_c$, in the electron temperature gradient, the transport is anomalous and greater than the underlying neoclassical transport. The electrons are primarily responsible for the anomalous transport, but ion heat and particle transport are also anomalous. The general expressions for the conductive heat fluxes and the anomalous transport coefficients are:

$$Q_e \equiv -n_e\chi_e\nabla T_e = -n_e\chi_{an,e}\,(\nabla T_e - (\nabla T_e)_c)$$

$$Q_i \equiv -n_i\chi_i\nabla T_i \quad \text{and} \quad \chi_i = 2\chi_e \frac{Z_i}{\sqrt{1+Z_{eff}}}\sqrt{\frac{T_e}{T_i}}$$

$$D_i \approx (0.3\text{÷}0.5)\,\chi_i$$

The critical electron temperature gradient model of Rebut et al [13] specifies possible dependences for χ and D and this is explored further in [12].

6.2. To model a Next Step tokamak

The fuelling, impurity control and exhaust capability of a Next Step tokamak will be dependent on whether deuterium and impurities (including helium) accumulate in the plasma centre. The production and transport of helium ash towards the plasma edge (where it must be exhausted) will depend on the

relative importance of energy and particle confinement, the effect of sawteeth, the effect of the edge transport barrier in the H-mode and the behaviour of the scrape-off layer plasma.

Although the transport model of Section 6.1 applies in both L- and H-regimes, and ensures that particle and energy transport will follow each other in the transition from the L- to H-regime (since χ and D are linked in the model), it is necessary to include several additional elements in order to complete the model for a Next Step tokamak. For example, the spontaneous improvement in edge confinement has yet to be modelled. The reduction in MHD activity observed experimentally suggests the presence of some other instability at the edge of L-mode plasmas, where the effect of atomic physics on MHD might be important. This is apparently easier to suppress in an X-point configuration with high edge magnetic or rotational shear. Furthermore, an understanding of the scrape-off-layer (SOL) plasma is also needed.

7. IMPURITY CONTROL AND THE NEW PHASE PLANNED FOR JET

Achieving control of the impurity influx into the plasma is a pre-requisite to the construction of a tokamak reactor. In the case of high Z impurities, radiation losses may prevent reaching ignition. The presence of low Z impurities, in addition to helium produced by nuclear reactions, dilutes the concentration of reacting ions and therefore reduces the alpha-particle power. Under present conditions, the lifetime of the plasma facing components would be severely limited. Understanding the SOL plasma is needed because of the importance of dilution and exhaust for ignition.

So far, JET has concentrated on **passive** methods of impurity control. Studies of **active** methods of impurity control are a natural development of the JET programme and accordingly, a New Phase for JET is planned to start in 1992 [4], with first results becoming available in 1993 and continuing to the end of 1996.

The aim of the New Phase is to demonstrate, prior to the introduction of tritium, effective methods of impurity control in operating conditions close to those of the Next Step, with a stationary plasma of 'thermonuclear grade' in an axisymmetric pumped divertor configuration. Successful impurity control would lead also to an increase in alpha-particle power by more than a factor of two.

Specifically, the New Phase should demonstrate:

- control of impurities generated at the divertor target plates;
- decrease of the heat load on the target plates;
- control of plasma density;
- the exhaust capability;
- a realistic model of particle transport.

7.1. Key concepts of the JET pumped divertor

Since sputtering of the target plates cannot be suppressed, the impurities produced must be retained close to the target plates for effective impurity control. This can be achieved by friction with a strong plasma flow, directed along the divertor channel plasma (DCP) towards the target plates. If large enough, the frictional force between the plasma and the impurities should prevent impurity migration towards the X-point. The plasma flow will be generated by a combination of gas puffing, the injection of low speed pellets and the recycling and recirculation of some of the flow at the target plates towards the X-point. The connection length along the magnetic field line between the X-point and the target plates should be sufficiently long to achieve effective screening of impurities.

Rapid sweeping of the target plates to limit the localised heat load, to limit erosion and to affect redeposition is an important feature. Methods of ensuring

that a substantial fraction of input power can be radiated in a controlled way in the DCP remain key elements.

7.2. Modelling the edge plasma

The plasma behaviour in the SOL and the DCP can be qualitatively understood. Impurity retention in the divertor is determined from the steady state momentum equation for impurity ions, which for the simplest, realistic case gives the impurity density, n_z, decaying exponentially with distance from the target on a scale length, λ_z, given by:

$$\lambda_z^{-1} = \lambda_F^{-1} - \lambda_e^{-1}, \qquad \text{with} \quad \lambda_F^{-1} = \frac{m_z v_z}{T \tau_z} \quad \text{and} \quad \lambda_e^{-1} = \alpha_z \frac{1}{T} \frac{dT}{dx}$$

The temperature gradient scale length is given by the heat transport equation with electron heat conductivity parallel to the magnetic field ($\kappa=\kappa_0 T^{5/2}$) being dominant and dependent primarily on the input power. To ensure impurity control, the frictional force must exceed the sum of the pressure and thermal forces, that is:

$$\lambda_F^{-1} > \lambda_e^{-1}.$$

To increase the hydrogen-impurity friction and radiated power in front of the target plates, a low temperature, high density plasma is needed. This will also limit erosion and therefore increase the lifetime of the target plates.

To solve the full set of classical fluid equations for the conservation of particles, momentum and energy in the SOL and DCP, a numerical 1-$^1/_2$ D transport model has been developed [14]. Monte Carlo methods are used for neutral deuterium and impurities in the flux surface geometry of the pumped divertor. Erosion at the target plates is determined by a model of sputtering tested against JET experimental data [8]. The calculations show that impurities can be retained near the target plates for plasma flows, typically ~$10^{23}s^{-1}$ near the X-point. The steady state distributions of Z_{eff} (with beryllium impurities), for conditions in the SOL and DCP, with and without flow, are shown in Fig. 12(a). These results are obtained for an electron density ~$10^{20}m^{-3}$ at the target plates. At target densities approaching $10^{21}m^{-3}$, the reduction of erosion and the plasma flow associated with high recycling at the target plates ensures impurity control. Furthermore, the calculations show that the ion temperature in the SOL can be substantially larger than the electron temperature (Fig. 12(b)). In present JET discharges, probe measurements indicate, that at low density, the electron temperature at the target plates is lower than the ion temperature, determined from broadening of the H_α emission and power balance considerations [7].

7.3. The pumped divertor configuration

The aims of the New Phase can be realised with the internal multi-coil configuration shown in Fig. 13. The design allows a large plasma volume at 6MA and the operational flexibility to modify the magnetic configuration in the vicinity of the X-point independent of the plasma current and separately on the high and low field sides. In contrast to the normal configuration for a divertor, all divertor coils carry current flowing in the same direction as the plasma current.

Water-cooled, hypervapotron elements, made of copper and covered by beryllium, will be used for the high heat flux components of the target plates, and these are expected to accommodate power fluxes up to 15MWm^{-2} at the copper-beryllium interface. A pumping chamber is introduced in the vicinity of the target plates to provide control of the main plasma density. Pumping is achieved by a cryo-pump to avoid excessive hydrogen retention and to be compatible with the tritium phase.

With this configuration, single null X-point operation should be possible for performance and impurity control studies. Plasmas should be obtained at 6MA for 10s, a volume ~93m^{-3} and a connection length from the X-point to the target plates of 3m, and at 5MA for 10s, a volume ~80m^{-3} and a connection length ~10m should be achieved. In addition, it should be possible to run 3MA double null X-point plasmas for up to 20s at 3.4T and for up to 1 minute at 2.1T.

7.4. JET programme in the New Phase

A schedule for the JET programme incorporating the New Phase is shown in Table II. The earliest date to have a pumped divertor in JET is 1992. Further optimisation would likely be necessary about 18 months later, in the light of new experimental results.

By the end of 1994, all information on particle transport, exhaust and fuelling, first wall requirements and enhanced confinement regimes needed to construct a Next Step tokamak, should be available. Final tests with tritium, including alpha-particle heating studies could be performed in the two years following, leading to completion of the JET programme by the end of 1996. During the tritium phase of operation, and even later, tests on prototype elements for a Next Step tokamak could be undertaken on the JET site, using the test facilities, tritium plant and power supplies.

8. CONCLUSIONS

In summary, the paper sets out the main JET results and future prospects. JET has successfully achieved and contained plasmas of thermonuclear grade. **Individually**, parameters required for a fusion reactor have been obtained, and **simultaneously**, the fusion product ($n_D(0)\tau_E T_i(0)$) has reached 8-9x$10^{20}m^{-3}$skeV, for both medium (~10keV) and high (>20keV) central temperatures, and is within a factor of 8 of that required in a fusion reactor; neutron yield has increased to ~3.5x$10^{16}ns^{-1}$, corresponding to an equivalent Q_{DT}~0.8. However, these values were in a **transient** state and could not be sustained in steady state.

A clearer picture of energy and particle transport also starts to emerge. The resilience of the electron temperature suggests that the electrons are primarily responsible for confinement degradation. The occurrence of flat density profiles suggests that there is no need for an inward pinch term, except perhaps for impurities. Particle and energy transport exhibit similar behaviour. The critical electron temperature gradient model is one such model consistent with these observations.

In a reactor, the density limit should not be a problem; high densities and flat profiles are likely; an advanced divertor concept for impurity control is required. These conditions of high plasma density at the separatrix are unfavourable for the methods of non-inductive current drive envisaged at present.

A New Phase is planned for JET with an axi-symmetric pumped divertor configuration to operate with a stationary plasma (10s-1minute) of thermonuclear grade. In this New Phase, JET should be able to:

- demonstrate a concept of impurity control;
- determine the geometry needed to fulfil this concept in a reactor;
- identify appropriate materials for plasma facing components;
- define the operational domain for the Next Step.

To ensure the success of a Next Step ignition device, it is imperative that all aspects of plasma behaviour, impurity control and plasma exhaust be included in the model used to define the size of the device and its toroidal field, plasma current and operating conditions.

9. REFERENCES

[1] The JET Project - Design Proposal: EUR-JET-R5.

[2] Rebut, P-H., et al, Fusion Technology, **11**, (1987), 13-281.

[3] The JET Team, Proc. of 12th Int. Conf. on Plasma Phys. and Contr. Nucl. Fus. Res., (Nice, France, 1988), Nuclear Fusion Supplement, **1**, 41.

[4] Rebut, P-H., Lallia, P.P., and Keen, B.E., Proc. of the 13th Symposium on Fusion Engineering, (Knoxville, USA, 1989), **1**, 227.

[5] Lomas, P.J. and The JET Team, Proc. of 13th Int. Conf. on Plasma Phys. and Contr. Nucl. Fus. Res., (Washington, USA, 1990), Paper IAEA-CN-53/A-6-2.

[6] Tanga, A. and The JET Team, Proc. of 13th Int. Conf. on Plasma Phys. and Contr. Nucl. Fus. Res., (Washington, USA, 1990), Paper IAEA-CN-53/A-4-1.

[7] Thomas, P.R. and The JET Team, Proc. of 13th Int. Conf. on Plasma Phys. and Contr. Nucl. Fus. Res., (Washington, USA, 1990), Paper IAEA-CN-53/A-5-3.

[8] Summers, D.D.R., et al, J. Nuclear Mater., to be published (1990).

[9] Smeulders, P. and The JET Team, Proc. of 13th Int. Conf. on Plasma Phys. and Contr. Nucl. Fus. Res., (Washington, USA, 1990), Paper IAEA-CN-53/A-3-4.

[10] Campbell, D.J. and The JET Team, Proc. of 13th Int. Conf. on Plasma Phys. and Contr. Nucl. Fus. Res., (Washington, USA, 1990), Paper IAEA-CN-53/A-6-3.

[11] Start, D.F.H. and The JET Team, Proc. of 13th Int. Conf. on Plasma Phys. and Contr. Nucl. Fus. Res., (Washington, USA, 1990), Paper IAEA-CN-53/E-2-1.

[12] Taroni, A., et al, Proc. of 13th Int. Conf. on Plasma Phys. and Contr. Nucl. Fus. Res., (Washington, USA, 1990), Paper IAEA-CN-53/A-2-1.

[13] Rebut, P-H., Lallia, P.P., and Watkins, M.L., Proc. of 12th Int. Conf. on Plasma Phys. and Contr. Nucl. Fus. Res., (Nice, France, 1988) Nuclear Fusion Supplement, **2**, 191.

[14] Keilhacker, M., et al, Proc. of 13th Int. Conf. on Plasma Phys. and Contr. Nucl. Fus. Res., (Washington, USA, 1990), Paper IAEA-CN-53/A-5-1.

Table I

JET Parameters

Parameters	Design Values	Achieved values
Plasma Major Radius (R_O)	2.96m	2.5-3.4m
Plasma Minor Radius horizontal (a)	1.25m	0.8-1.2m
Plasma Minor Radius vertical (b)	2.1m	0.8-2.1m
Toroidal Field at R_O	3.45T	3.45T
Plasma Current:		
Limiter mode	4.8MA	7.1MA
Single null X-point	not foreseen	5.1MA
Double null X-point	not foreseen	4.5MA
Neutral Beam (NB) Power		
(80kV, D)	20MW	21MW
(140kV, D)	15MW	8MW (one box converted, so far)
Ion Cyclotron Resonance Heating (ICRH) Power to Plasma	15MW	22MW

Table II : JET Development Programme

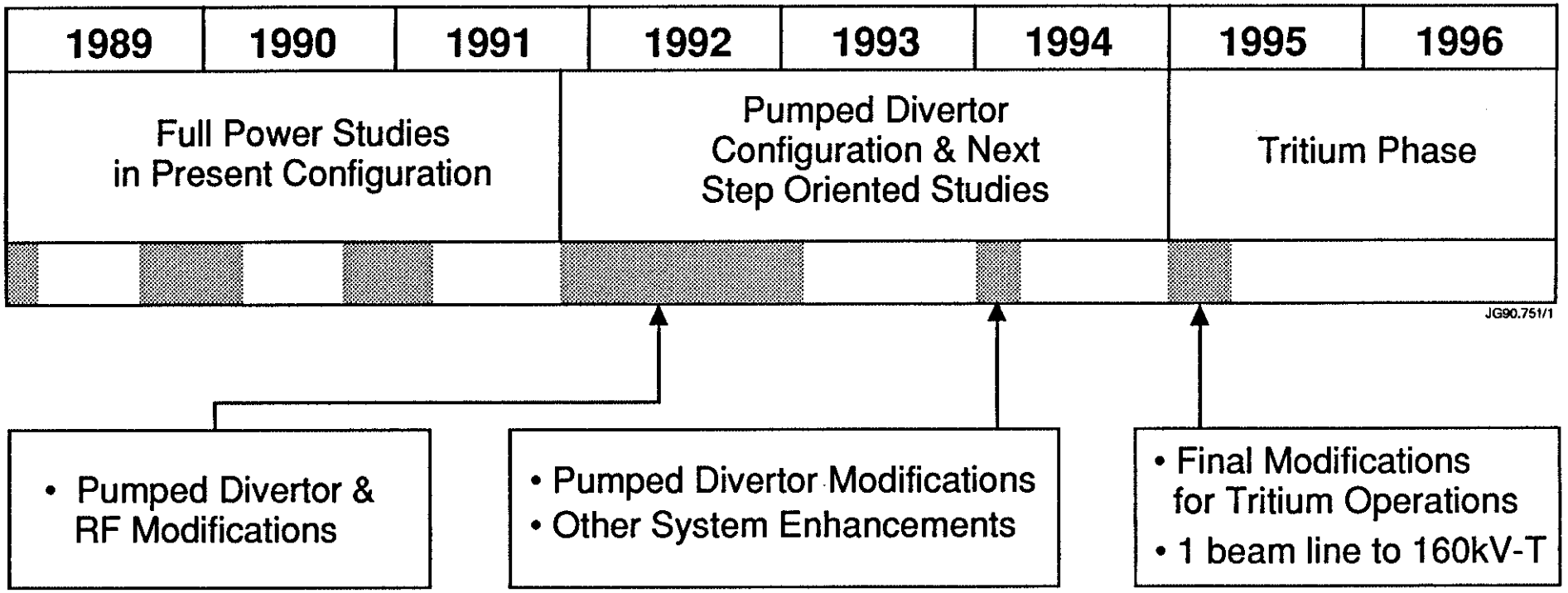

Appendix I

THE JET TEAM

JET Joint Undertaking, Abingdon, Oxon, OX14 3EA, U.K.

J.M. Adams[1], H. Altmann, A. Andersen[14], S. Attenberger[23], W. Bailey, P. Ballantyne, B. Balet, R. Barnsley[2], M. Baronian, D.V. Bartlett, L.R. Baylor[23], A.C. Bell, H. Bergsaker[11], P. Bertoldi, E. Bertolini, V. Bhatnagar, A.J. Bickley, H. Bindslev[14], T. Bonicelli, S.J. Booth, G. Bosia, M. Botman, D. Boucher, H. Brelen, H. Brinkschulte, T. Brown, M. Brusati, T. Budd, M. Bures, T. Businaro, P. Butcher, H. Buttgereit, C. Caldwell-Nichols, D.J. Campbell, P. Card, G. Celentano, C.D. Challis, D. Chiron, J. Christiansen, C. Christodoulopoulos, P. Chuilon, R. Claesen, S. Clement[21], E. Clipsham, J.P. Coad, M. Comiskey, S. Conroy[12], M. Cooke, S. Cooper, J.G. Cordey, W. Core, G. Corrigan, S. Corti, A.E. Costley, G. Cottrell, J-P. Coulon[16], M. Cox[7], P. Cripwell, H. de Blank[15], G. Decker[17], H. de Esch, L. de Kock, E. Deksnis, G.B. Denne-Hinnov, G. Deschamps, G. Devillers, K.J. Dietz, S.L. Dmitrenko, J. Dobbing, N. Dolgetta, S.E. Dorling, P.G. Doyle, D.F. Düchs, H. Duquenoy, A. Edwards, J. Ehrenberg, A. Ekedahl, T. Elevant[11], S.K. Erents[7], L.G. Eriksson, H. Fajemirokun[12], H. Falter, D. Flory, M. Forrest[7], J. Freiling[15], C. Froger, P. Froissard, K. Fullard, M. Gadeberg, A. Galetsas, D. Gambier, M. Garribba, P. Gaze, X. Ge[25], R. Giannella, A. Gibson, R.D. Gill, A. Gondhalekar, C. Gormezano, N.A. Gottardi, C. Gowers, B.J. Green, K. Guenther[26], R. Haange, G Haas, G. Hammett[6], C.J. Hancock, P.J. Harbour, N.C. Hawkes[7], P. Haynes[7], J.L. Hemmerich, R. Hemsworth, F.B. Herzog, R.F. Herzog, J. Hoekzema, G Hogeweij[15], J. How, M. Huart, T.P. Hughes[4], M. Hugon, M. Huguet, A. Hwang[7], B. Ingram, M. Irving, J. Jacquinot, H. Jaeckel, J.F. Jaeger, G. Janeschitz[13], O.N. Jarvis, F. Jensen, E.M. Jones, L.P.D.F. Jones, T.T.C. Jones, J. Junique, A. Kaye, B.E. Keen, M. Keilhacker, G.J. Kelly, W. Kerner, R. Konig, A. Konstantellos, M. Kovanen[20], P. Kupschus, R. Lässer, J.R. Last, B. Laundy, L. Lauro-Taroni, K. Lawson[7], M. Lennholm, A. Loarte, R. Lobel, P. Lomas, M. Loughlin, C. Lowry, B. Macklin, G. Maddison[7], G. Magyar, W. Mandl[13], V. Marchese, F. Marcus, J. Mart, E. Martin, R. Martin-Solis[8], P. Massmann, G. McCracken[7], P. Meriguet, S.F. Mills, P. Millward, S.L. Milora[23], E. Minardi[22], P.L. Mondino, F. Montvai[3], P. Morgan, H. Morsi, G. Murphy, M. Mynarends, O. Naito[11], C. Nardone, F. Nave[21], G. Newbert, M. Newman, P. Nielsen, P. Noll, W. Obert, D. O'Brien, J. O'Rourke, R. Ostrom, M. Pain, F. Paoletti, S. Papastergiou, D. Pasini, A. Peacock, N. Peacock[7], D. Pearson[12], C. Perry, V. Phillips[28], M. Pick, R. Pitts[7], J. Plancoulaine, J-P. Poffé, F. Porcelli, L. Porte[19], R. Prentice, G. Radford[9], T. Raimondi, P-H. Rebut, R. Reichle[13], G. Rey[16], F. Rimini, D. Robinson[7], A. Rolfe, R.T. Ross, L. Rossi, P. Rutter, H.C. Sack, G. Sadler, G. Saibene, G. Sanazzaro, A. Santagiustina, R. Sartori, C. Sborchia, P.H. Schild, M. Schmid, G. Schmidt[6], B. Schunke, S.M. Scott, A. Sibley, R. Simonini, A. Sips[15], P. Smeulders, S. Sommers, R. Stankiewicz[27], M. Stamp, P. Stangeby[18], D.F. Start, C.A. Steed, D. Stork, P.E. Stott, T.E. Stringer, P. Stubberfield, D. Summers, H. Summers[19], L. Svensson, J.A. Tagle[21], H. Tamnen, A. Tanga, A. Taroni, A. Tesini, P.R. Thomas, E. Thompson, K. Thomsen, J.M. Todd, P. Trevalion, B. Tubbing, F. Tibone, E. Usselmann, H. van der Beken, G. Vlases, M. von Hellermann, T. Wade, C. Walker, R. Walton[6], D. Ward, M.L. Watkins, M.J. Watson, H. Weisen[10], J. Wesson, J. Wilks, U. Willen[5], D. Wilson, T. Winkel, S. Wolfe, B. Wolle[24], D. Wong, C. Woodward, M. Wykes, I.D. Young, L. Zannelli, Z. Zheng[25], Y. Zhu[26], W. Zwingmann.

PERMANENT ADDRESSES

1. UKAEA, Harwell, Didcot, Oxon, UK.
2. University of Leicester, Leicester, UK.
3. Central Research Institute for Physics, Academy of Sciences, Budapest, Hungary.
4. University of Essex, Colchester, UK.
5. Chalmers University of Technology, Göteborg, Sweden.
6. Princeton Plasma Physics Laboratory, New Jersey, USA.
7. UKAEA Culham Laboratory, Abingdon, Oxon, UK.
8. Universidad Complutense de Madrid, Spain.
9. Institute of Mathematics, University of Oxford, UK.
10. CRPP/EPFL, 21 Avenue des Bains, CH-1007 Lausanne, Switzerland.
11. Swedish Energy Research Commission, S-10072 Stockholm, Sweden.
12. Imperial College of Science and Technology, University of London, UK.
13. Max Planck Institut für Plasmaphysik, D-8046 Garching bei München, FRG.
14. Risø National Laboratory, Denmark.
15. FOM Instituut voor Plasmafysica, 3430 Be Nieuwegein, The Netherlands.
16. Commissiariat à L'Énergie Atomique, Cadarache, F-13108 St. Paul Lez Durance, France.
17. University of Dusseldorf, FRG.
18. Institute for Aerospace Studies, University of Toronto, Downsview, Ontario, Canada.
19. University of Strathclyde, 107 Rottenrow, Glasgow, G40NG, UK.
20. Nuclear Engineering Laboratory, Lapeenranta University, Finland.
21. CIEMAT, Madrid, Spain.
22. ENEA-CNR, Milano, Italy.
23. Oak Ridge National Laboratory, Oak Ridge, Tenn., USA.
24. University of Heidelberg, Heidelberg, FRG.
25. Institute for Mechanics, Academia Sinica, Beizjing, P.R. China.
26. Akademie der Wissenschaften der DDR, Berlin, DDR.
27. RCC Cyfronet, Otwock Swierk, Poland.

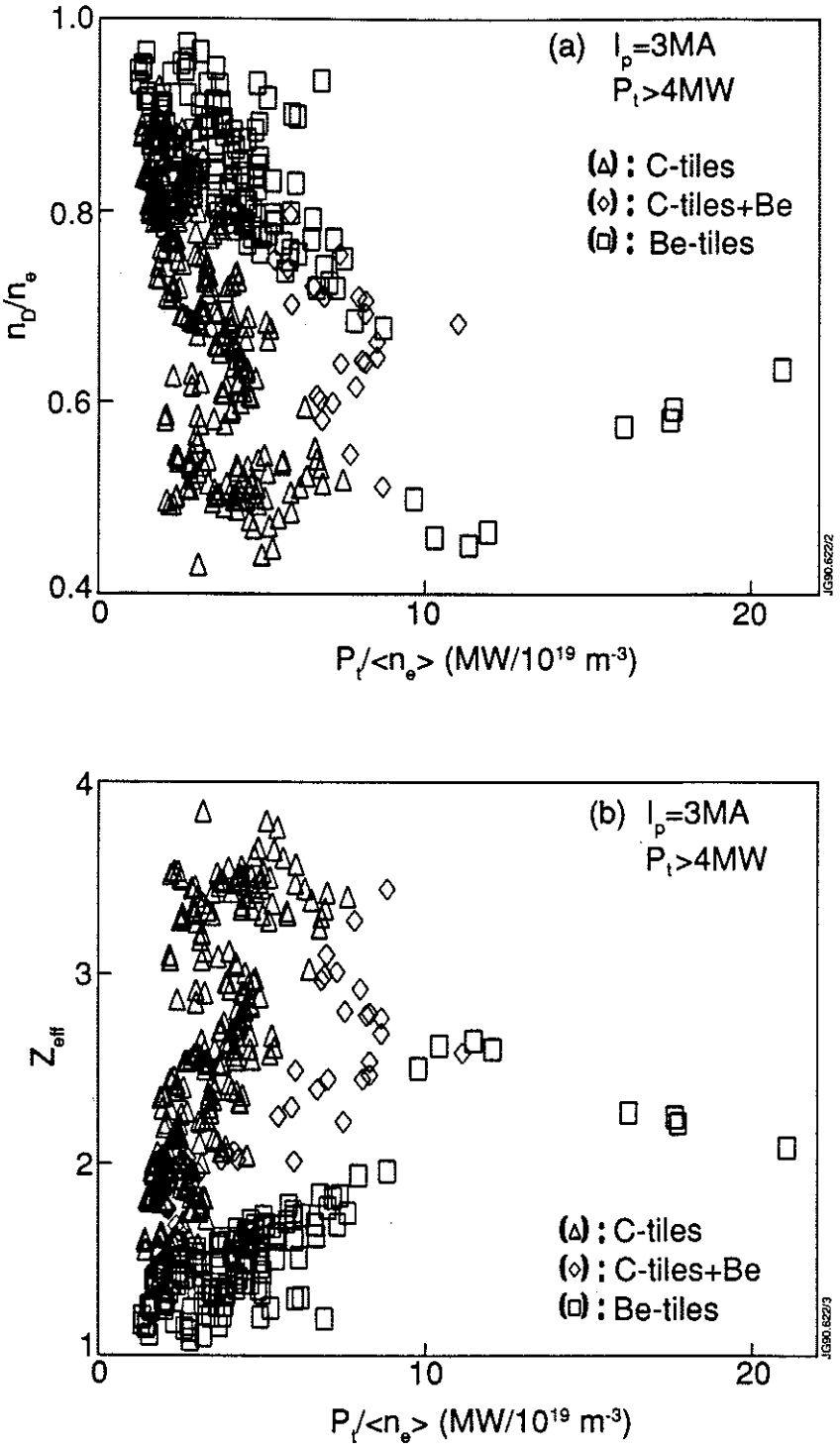

Fig. 1 (a) Dilution factor, n_D/n_e, and (b) the effective charge, Z_{eff}, as functions of power per particle ($P_t/<n_e>$) for carbon limiter tiles, beryllium gettering and beryllium limiter tiles.

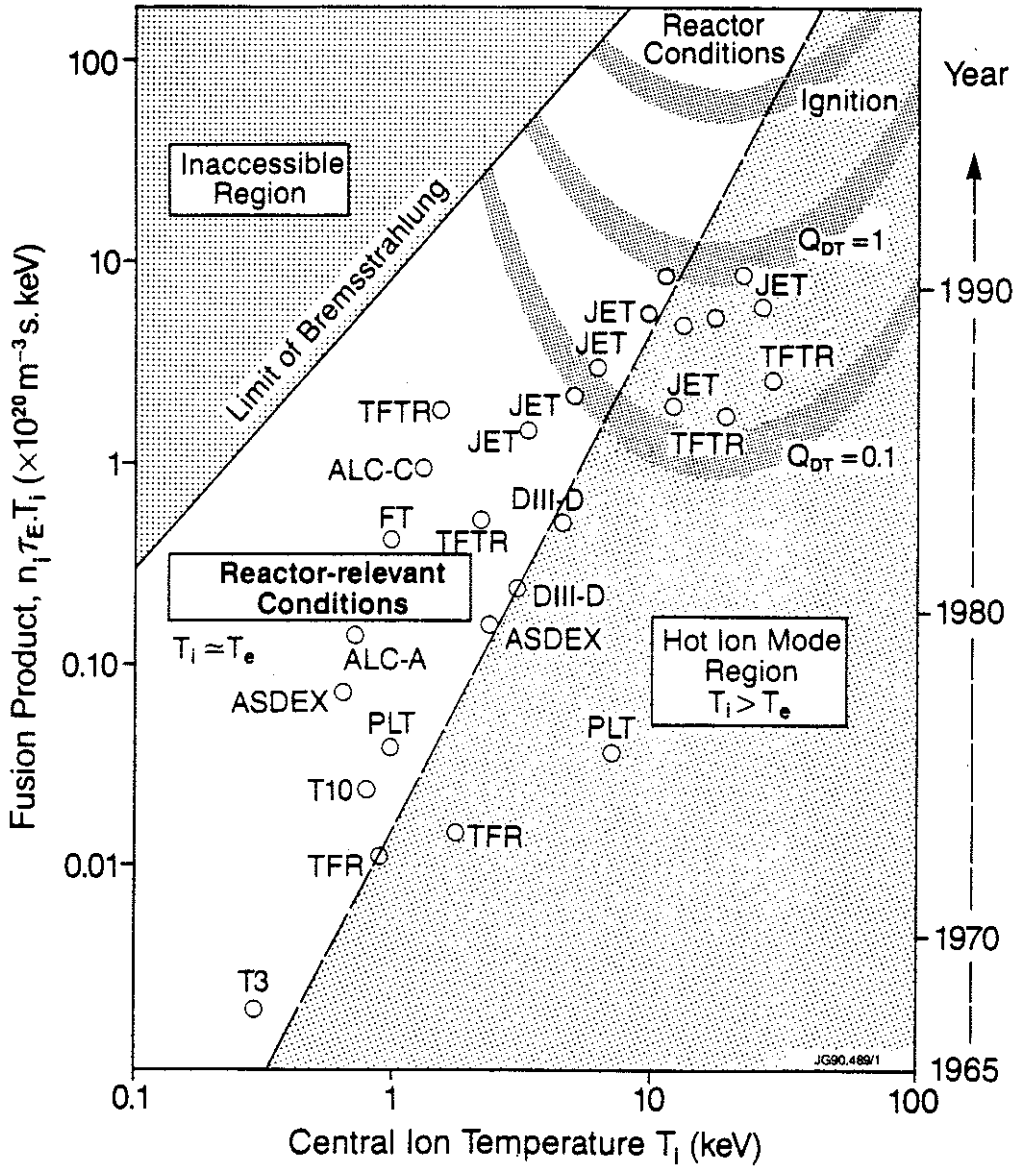

Fig. 2 Overall performance of the fusion product ($n_D(0)\tau_E T_i(0)$) as a function of central ion temperature ($T_i(0)$), for a number of tokamak devices.

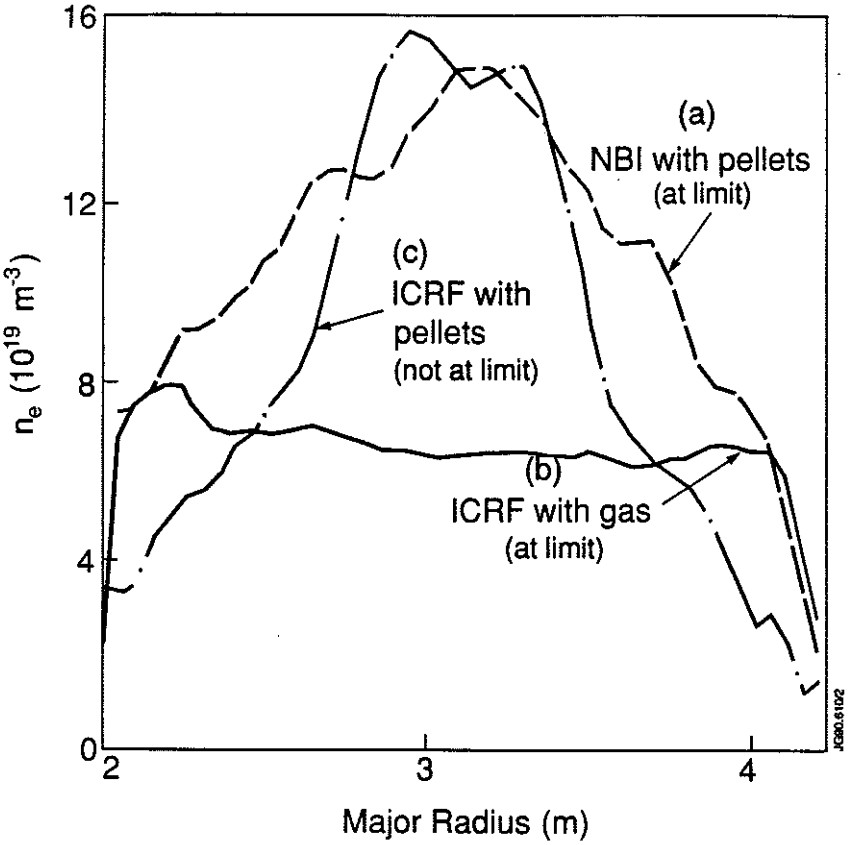

Fig. 3 Electron density profiles for different fuelling and heating methods.

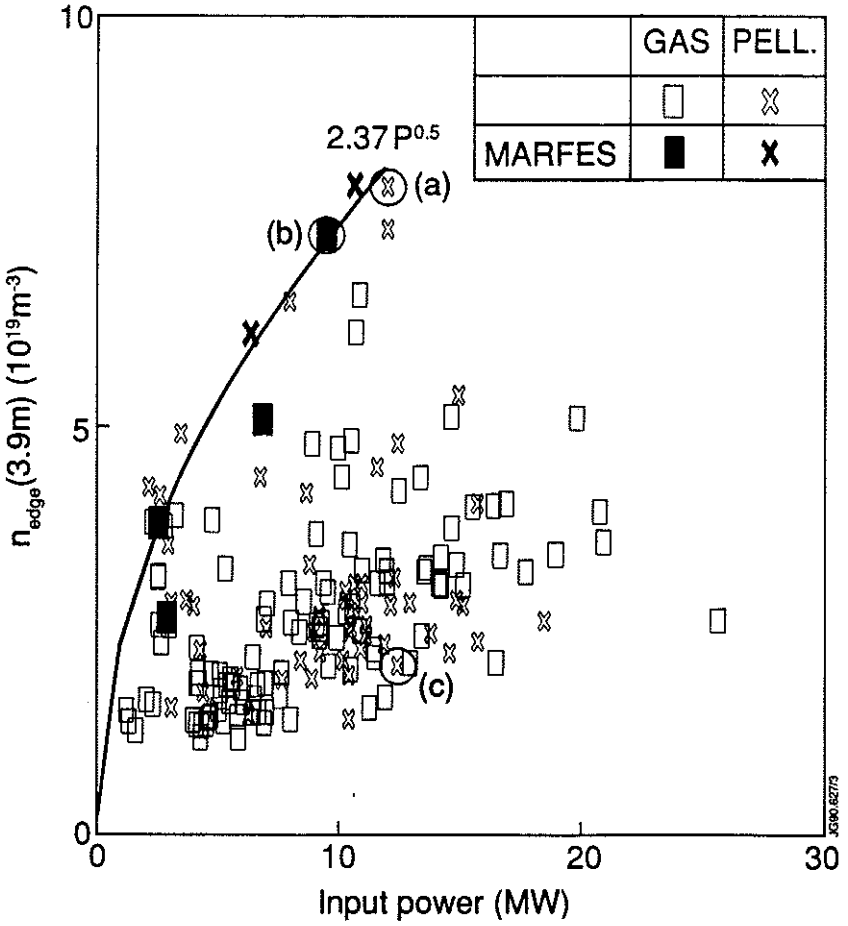

Fig. 4 The edge electron density (n_{edge}) versus input power (P) showing that the density limit occurs at the boundary of the operational domain close to the curve n_{edge} (x10^{19}m^{-3}) = 2.37 P$^{1/2}$(MW). The profiles shown in Fig. 3 correspond to the three data points circled.

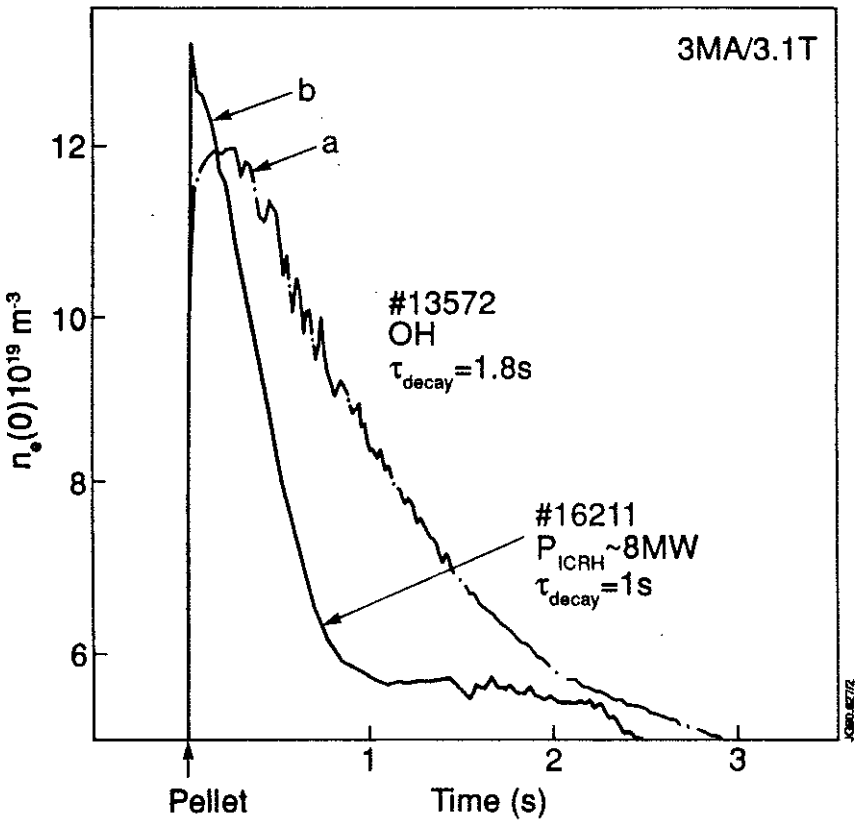

Fig. 5 Decay of central density following pellet injection into discharges with (a) ohmic heating only and (b) ~8MW ICRH.

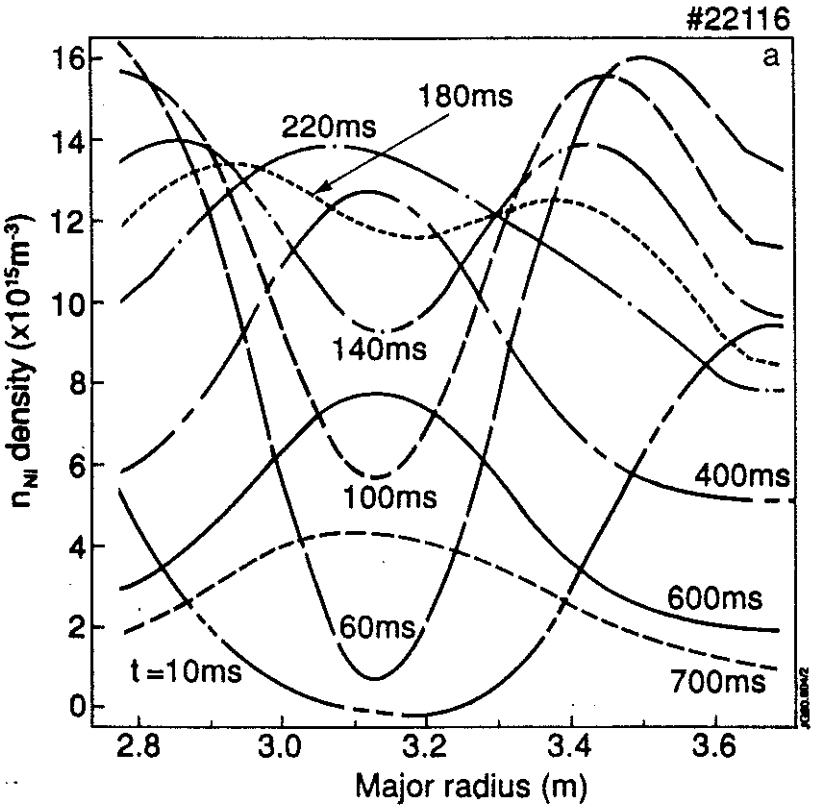

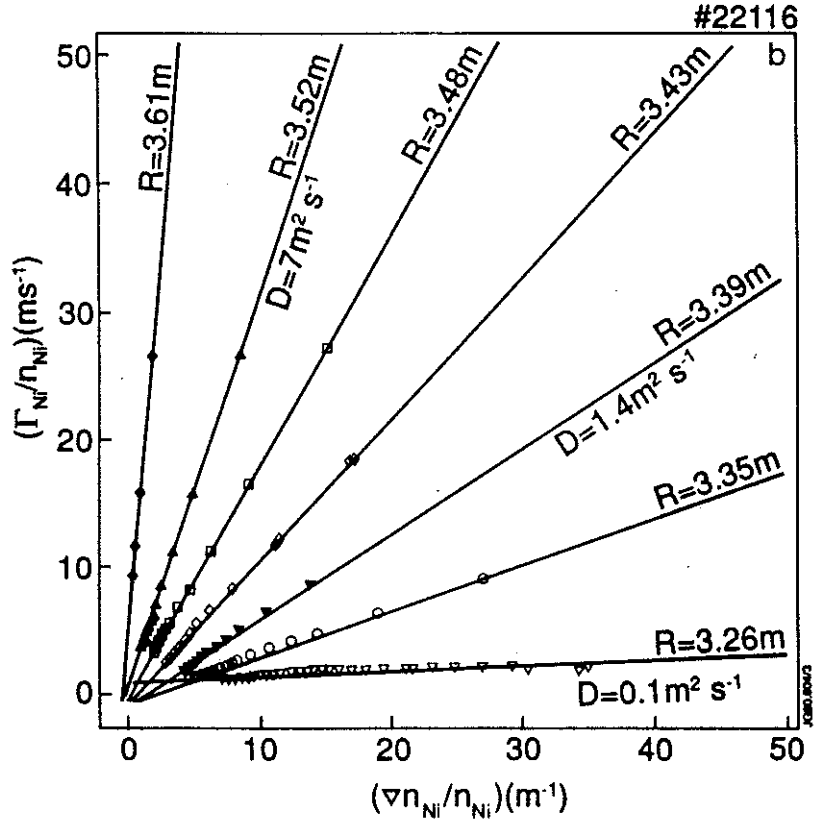

Fig. 6 (a) Nickel density profiles from X-ray tomography at times following laser ablation and (b) normalised particle fluxes versus normalised density gradients for nickel impurities at different plasma radii.

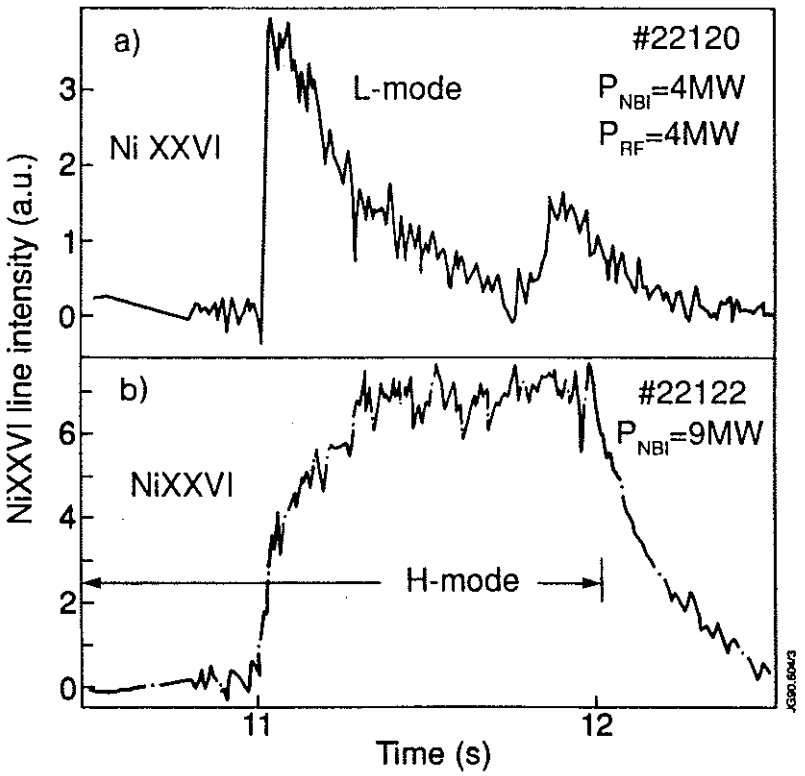

Fig. 7 (a) Temporal evolution of NiXXVI emission in (a) the L-phase and (b) the H-phase of two similar discharges with ~9MW of additional heating.

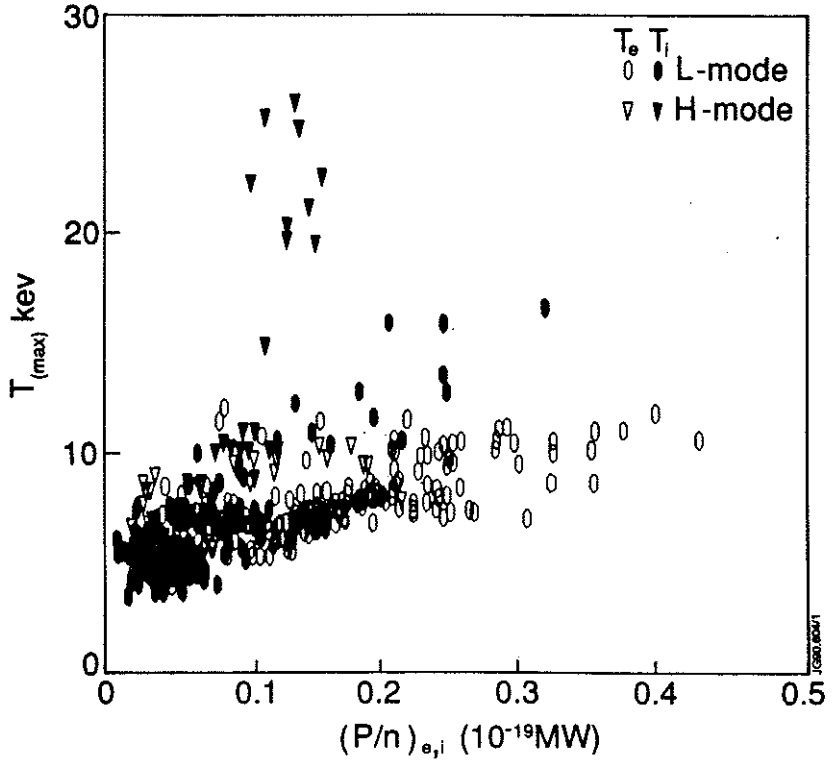

Fig. 8 Central ion (T_i) and electron (T_e) temperatures as functions of power per particle $(P/n)_{e,i}$ to either species.

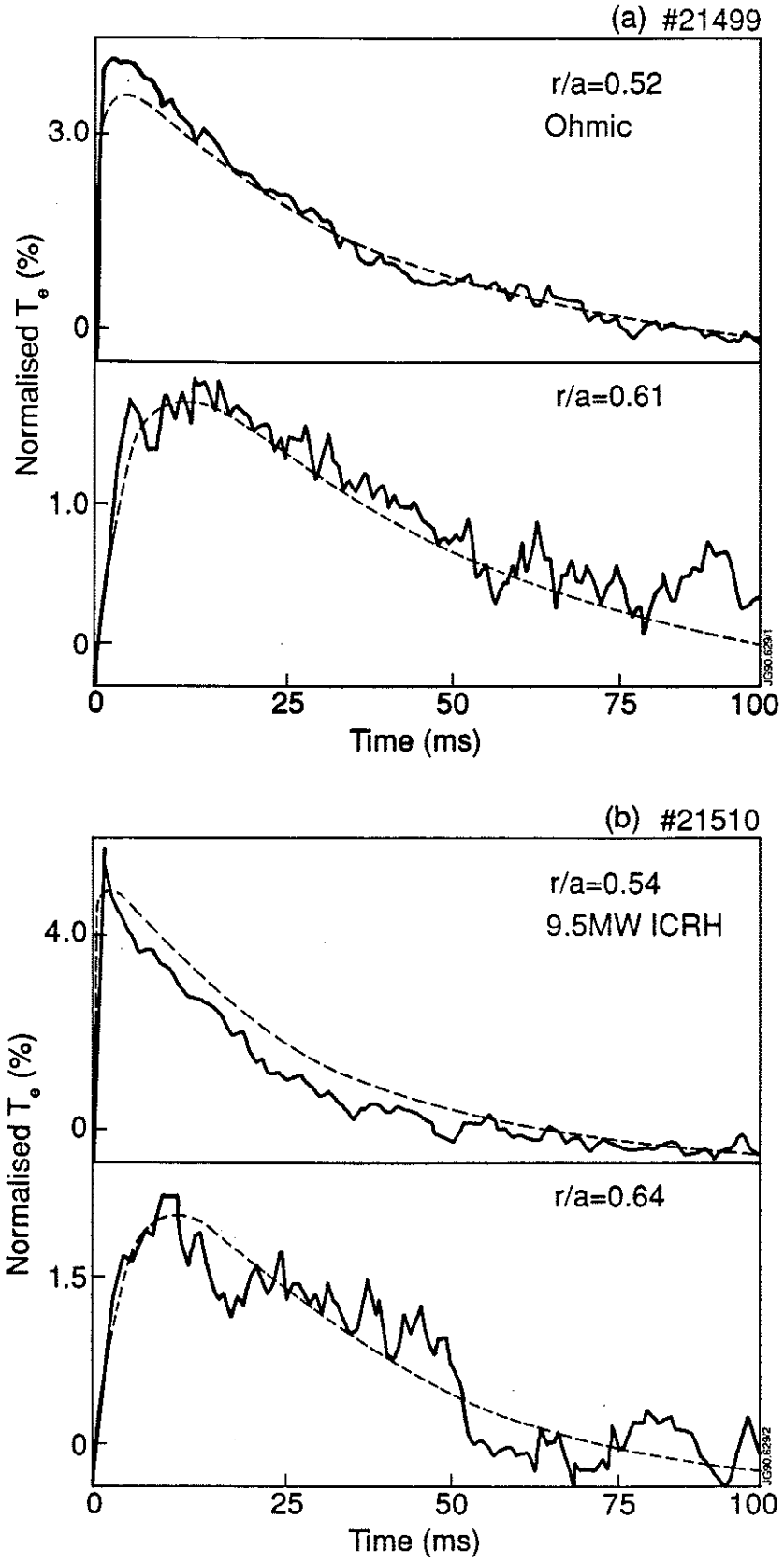

Fig. 9 Temporal evolution of electron temperature perturbations (normalised to the central electron temperature prior to the collapse of a sawtooth) at different radii for 3MA/2.8T discharges with (a) ohmic heating only and (b) 9.5MW ICRH. Dashed lines are from model calculations using $\chi_{HP}=3.2m^2s^{-1}$.

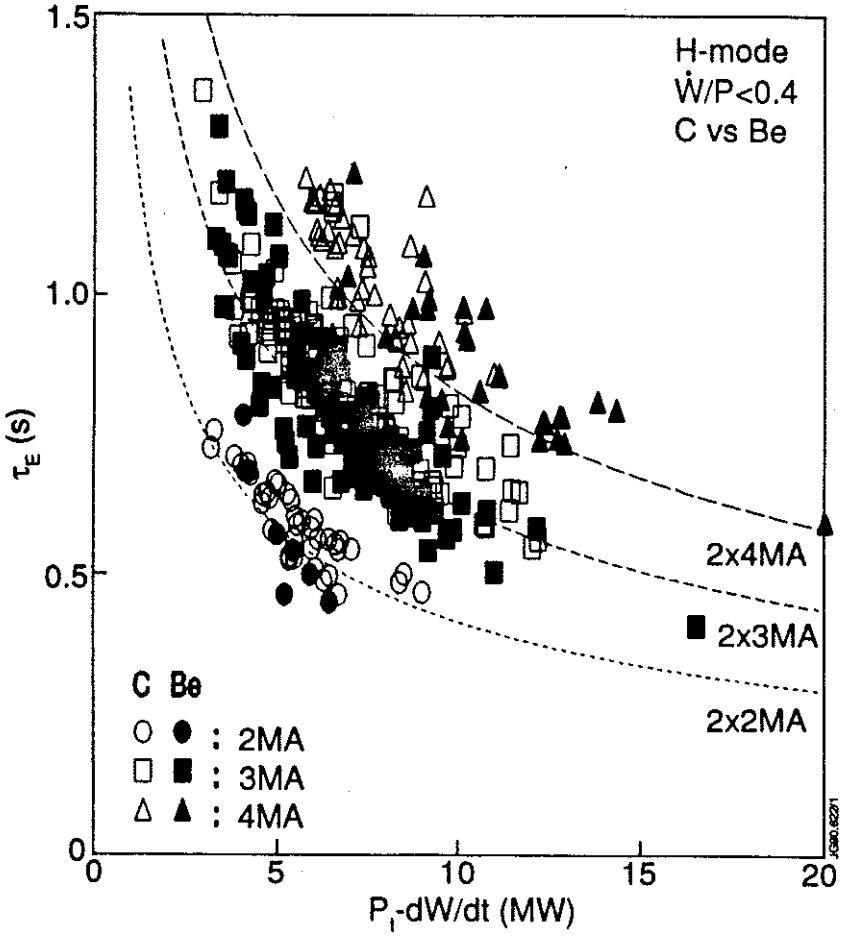

Fig. 10 Global energy confinement time (τ_E) during the H-mode as a function of net input power for different currents and first wall materials.

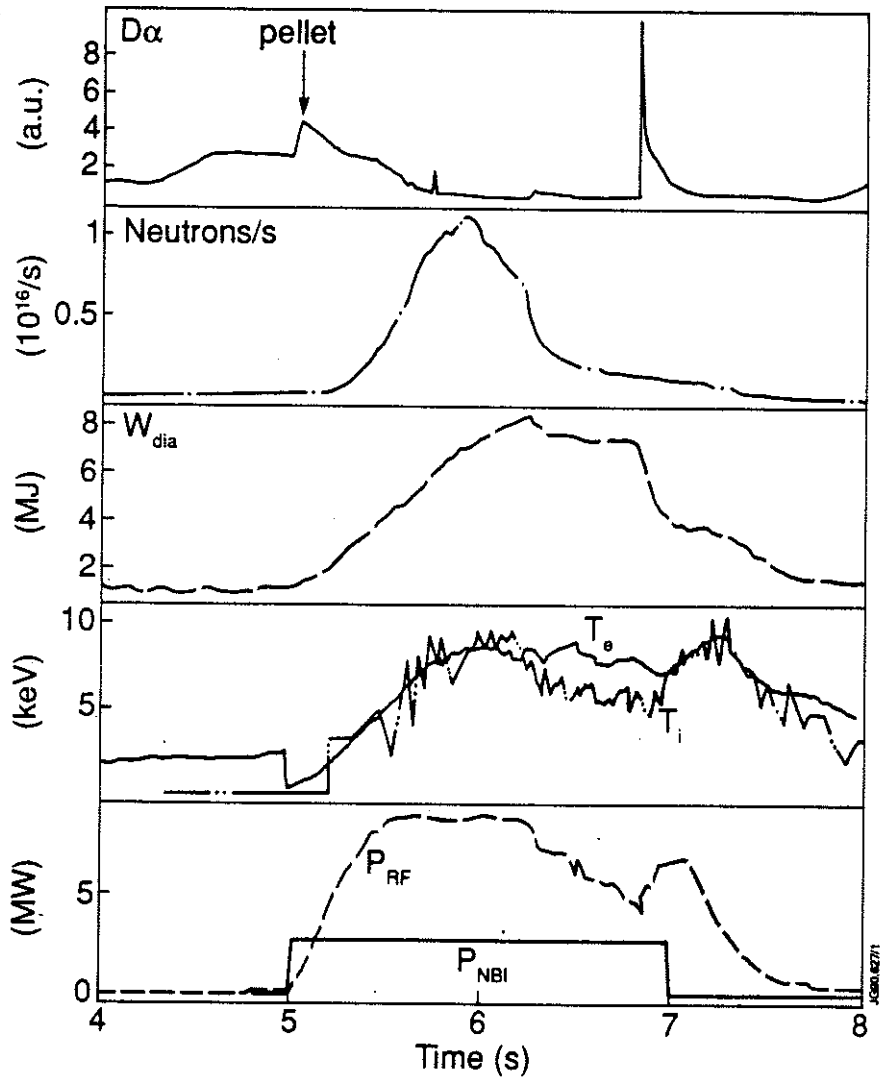

Fig. 11 Characteristics of JET Pulse 22490 in which the good confinement properties of the H-mode and central pellet injection are combined.

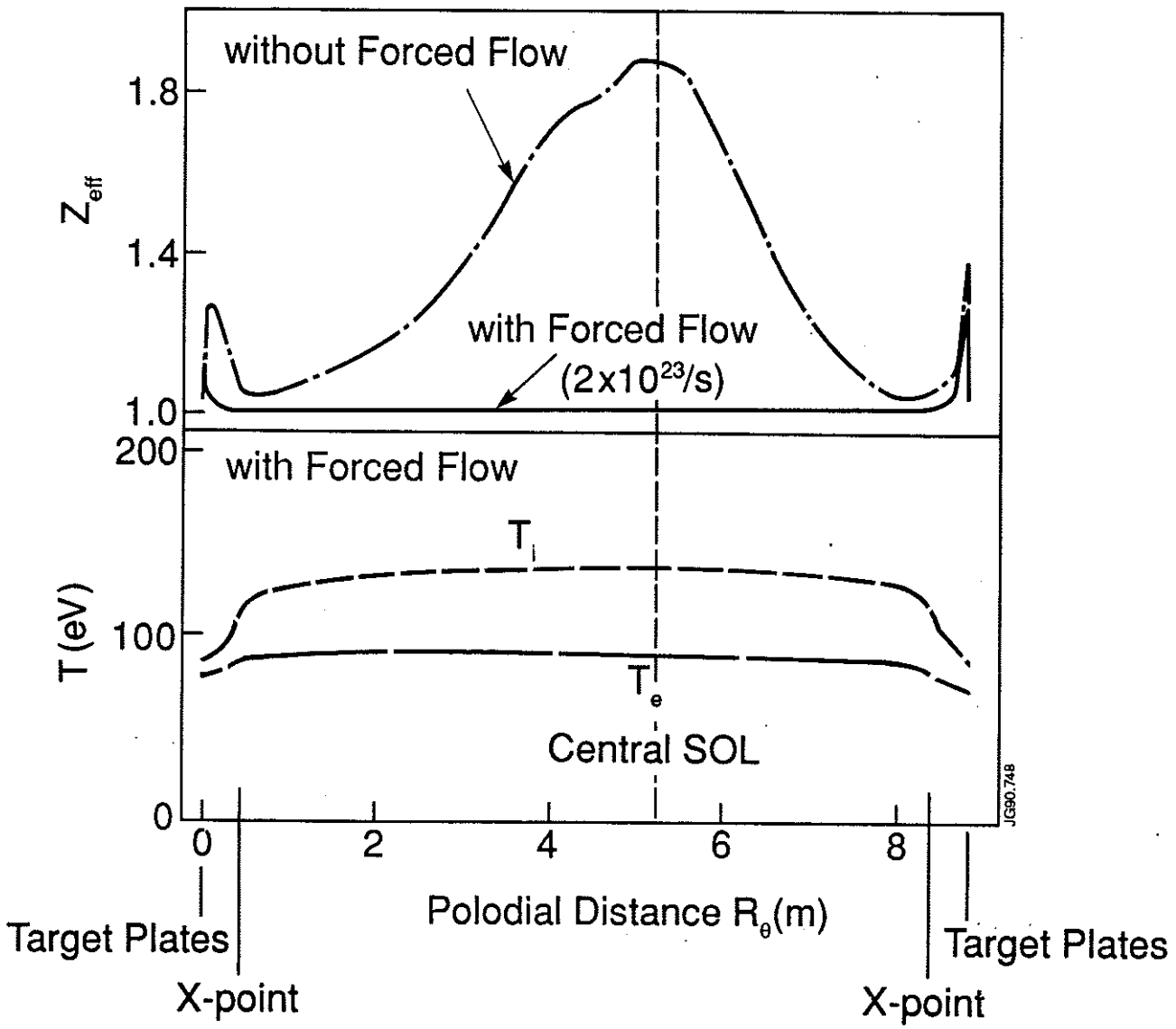

Fig. 12 Poloidal distribution in the SOL and DCP between target plates of (a) the effective ionic charge, Z_{eff}, for cases with and without flow and (b) the electron and ion temperatures for the case with flow.

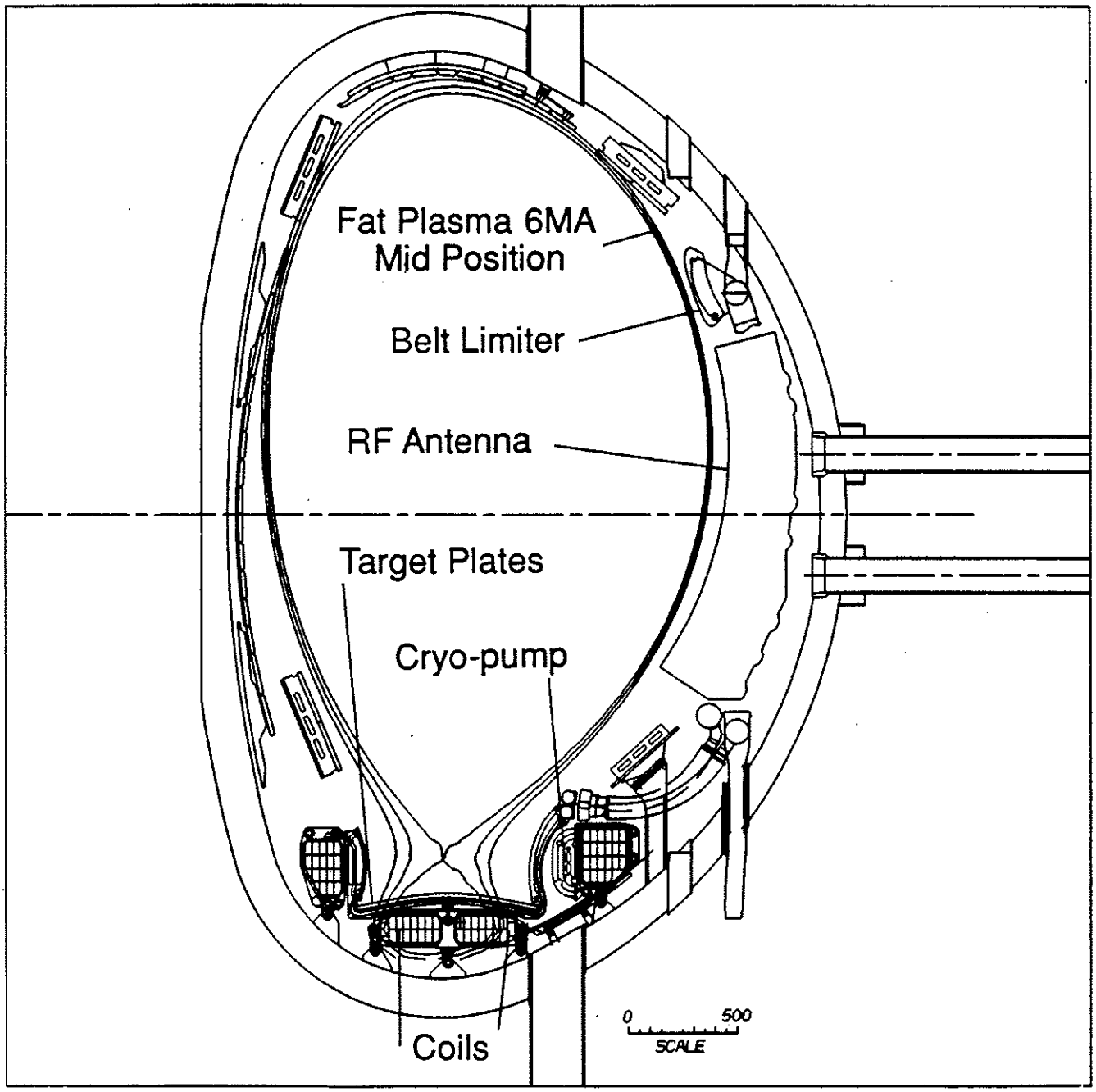

Fig. 13 Cross-section of JET showing the plasma and main elements of the pumped divertor planned for the New Phase of JET.

IAEA-CN-53/A-6-2

Optimisation of Performance in JET Limiter Plasmas

by

The JET Team*
(presented by PJ Lomas)

JET Joint Undertaking, Abingdon,
Oxon, OX14 3EA, UK

* See P-H Rebut and the JET Team, 13th Int. Conf. on Plasma Physics and Contr. Fusion Research, Washinton, USA. (1990) to be published in Nuclear Fusion Supplement

OPTIMISATION OF PERFORMANCE IN JET LIMITER PLASMAS

Abstract

Improvements to the performance of JET limiter plasmas have been made by increasing the plasma current, by suppressing sawteeth, by peaking the density profile and by using Beryllium evaporation and employing Beryllium limiters. Central electron temperatures $T_e \sim 12keV$, ion temperatures $T_i \sim 18keV$, central electron densities $n_{e0} \sim 2.3 \times 10^{20} m^{-3}$ have been demonstrated in limiter plasmas with currents 3-5MA. A 7MA discharge with $q_\psi \sim 3.2$ has been demonstrated and heating experiments have just begun.

1. Introduction

It has already been shown [1] that the confinement of high current low q limiter plasmas in JET is in line with the expectations of Goldston or Rebut-Lallia scalings [2,3], but that the profiles of density and temperature are rather flat. Projections of the D-T fusion performance of such L mode plasmas in JET [4] suggest that $Q_{DT} \sim 0.5 - 0.8$ might be obtained at 7MA (including the beam driven yield). A more direct extrapolation to DT operation of 4.5MA H mode plasmas already run in Deuterium suggests [5] that higher fusion performance will be obtained using such divertor configurations rather than a limiter configuration despite the higher plasma current. In order to enhance the fusion performance of limiter plasmas without employing a regime of enhanced confinement, it is necessary to make the profiles of density and temperature more peaked as has already been demonstrated at low current in the pellet enhanced plasma [6]. In order to obtain peaked profiles it is necessary to suppress sawteeth as for example in the monster sawtooth regime [7]. Furthermore, in sawtoothing discharges with centrally deposited power, it appears that the incremental confinement time no longer scales favourably with plasma current for $q_{CYL} \lesssim 3$ [8]. With the broad density profiles characteristic of high current sawtoothing discharges neutral beam penetration is poor. This reduces the central ion temperature, reduces beam refuelling of the core and reduces the beam driven fusion yield.

Thus to optimise the fusion yield in JET limiter plasmas requires more than a simple increase of plasma current. It is clearly necessary to suppress sawteeth, produce a high central density, maintain a low edge

density and keep the influx of impurities to a minimum. The following sections describe experiments addressing these issues for plasma currents of 3-5MA. The progess of experiments at 7MA currently underway is briefly described.

2. Sawtooth suppression at 5MA

Sawtooth stabilisation during the current rise phase has already been demonstrated [9]. By using a faster current ramp at constant $q_\psi \sim 3.5$ and employing Beryllium evaporation to control the density it has been possible to extend the sawtooth free periods well into the flat top at 5MA [10] as shown in fig 1. An axial electron temperature $T_{e0} \sim 12kev$ has been obtained with a strongly peaked profile as shown in fig 2. The ion temperature is only $T_{i0} \sim 5keV$ so the fusion performance is modest. Note that there are a few sawtooth crashes during the ICRH and during this time the soft X ray inversion radius grows from a small value to $r/a \sim 0.3$. Faraday rotation measurements indicate $q_0 = 0.95 \pm 0.15$ and constant in time during the sawtooth free periods. Since the inversion radius is large we infer that the q profile is rather flat. The fast ion slowing down time is long because the density is low and the electron temperature is high and therefore the fast ion energy content is large (35-50% of total). Normal sawteeth resume shortly after the ICRH is switched off. It is probable that the sawtooth is being transiently stabilised by the fast ions in manner similar to that of the normal monster. However since monster sawteeth do not normally occur during flat top heating at 5MA the detailed q profile shape must be important or it must be necessary to build up a high fast ion pressure to stabilise the sawtooth at high current. It is expected that a continuation of the current ramp will permit sawtooth stabilisation at higher current. The confinement time is plotted against power input for these plasmas and 5MA sawtoothing plasmas in fig 3. It can be seen that the confinement is very close to the Goldston prediction when allowance is made for the fast ion energy content.

3. Peaked density profiles at 5MA

The injection of a string of pellets during the current rise, as shown in fig 4, leads to high central densities $n_{e0} \sim 2.3 \times 10^{20} m^{-3}$ at 5MA. In order to obtain the strongly peaked density profile shown in fig 5 it is necessary that the pellets penetrate deeply and this is achieved by careful choice of pellet timing. The small inversion radius sawteeth present before the first sawteeth are suppressed by the pellets and indeed polarimetric measurements show that q_0 is raised above unity. It is important to keep q_ψ roughly constant during the current ramp and pellet injection since disruptions invariably occur at $q_\psi \sim 4$ if q_ψ is allowed to fall. 6MW of

ICRF heating were applied at 5MA after the last pellet and, as shown in fig 4, a transiently enhanced D-D rate is observed. 1.5 sec after the start of ICRH, and after the peak D-D rate, the central density has decayed to $n_{e0} \sim 6 \times 10^{19} m^{-3}$. T_{e0} is much lower than in the experiment of section 2, but $T_{i0} \sim T_{e0} \sim 5keV$ and $Q_{DD} \sim 5 \times 10^{-4}$. The global confinement time is enhanced transiently by $\sim 30\%$ compared with gas fuelled discharges as shown in fig 3.

4. Density profile control in plasmas with strong ion heating

The use of Beryllium limiters has permitted operation with low $Z_{eff} \lesssim 1.5$ at moderate density [11]. However at low density, $P_{TOT}/\langle n_e \rangle \gtrsim 5 \times 10^{-19} MWm^{-3}$, the deuterium concentration n_D/n_e is typically ~ 0.6 similar to Carbon limiters conditioned by Beryllium evaporation or by extensive pulsing in Helium. The main effect of Beryllium (either limiters or evaporation) is improved density control which extends the range of P_{NB}/n_{e0} and, as shown in fig 6, this has resulted in higher ion temperatures in 3MA belt limiter plasmas.

For the case of Carbon limiters and Beryllium evaporation a density profile peaking factor $n_{e0}/\langle n_e \rangle \sim 3$ was obtained as a result of central beam fuelling and low edge recylcling compared to $n_{e0}/\langle n_e \rangle \sim 1.5$ for bare carbon belt limiter plasmas [12]. Unexpectedly, for low density plasmas with Beryllium limiters the density profiles were flat even with central beam fuelling. In order to produce peaked density profiles in this case it was necessary to fuel the target plasma with deeply penetrating pellets. Fig 7 shows the time history of the density profile reconstructed from a series of similar shots. It can be seen that the initial central density is $n_{e0} \sim 7 \times 10^{19} m^{-3}$ with a peaking factor $n_{e0}/\langle n_e \rangle \sim 4$, but that the central density decays during the heating though the profile shape remains peaked. The ion temperature reaches $T_{i0} \sim 18kev$ with a strongly peaked profile $T_{i0}/\langle T_i \rangle \sim 7$. This profile peaking enhances the thermonuclear performance by a factor 3 compared with 'normal' flat profiles in L mode, even though the global confinement is unchanged. In these discharges the ICRH suppresses sawteeth which otherwise would flatten the profiles. In addition ICRF acceleration of injected deuterons increases the driven D-D reactivity by 30-40% in such discharges [13]. The broadening of the neutron spectum due to the ICRF is clearly visible in fig 8. In this case the D-D fusion gain was $Q_{DD} \sim 9 \times 10^{-4}$ which was slightly improved over previous inner wall plasmas at 3MA. Recently yet higher gains, $Q_{DD} \sim 1 \times 10^{-3}$, were obtained in inner wall plasmas at 4.7MA.

5. 7MA plasmas

Plasma currents of 7MA were demonstrated in 1988 [1]. These plasmas were obtained using a simultaneous ramp of toroidal field and plasma current with $q_\psi \sim 2.5$. The flat top was only 2 seconds limited by volts seconds. In order to pass $q_\psi = 3$ early in the current rise without disruption it was necessary to establish early sawteeth by strong gas puffing. This discharge is not suitable for current rise heating because of the variation in toroidal field. Recently, the fast current rise developed for the experiments described in sections 2 and 3 has been extended to 7MA. The flat top was 3 seconds long but 8 Volt-sec remain to extend this further. By making the plasma more D shaped q_ψ was held at ~ 3.2 at 7MA. Sawtooth have been suppressed well into the flat top of a 6MA discharge and suppressed during the rise to 7MA by applying ICRF in the current rise. An electon temperature $T_{e0} \sim 9keV$ was obtained in both cases. Ion heating experiments, using NBI, have begun in these high current discharges.

6. Conclusions

It has been shown that sawtooth can be suppressed and peaked density profiles formed at high current low q belt limiter plasmas. The former produces very high electron temperatures $T_{e0} \sim 12kev$, the latter high densities $n_{e0} \sim 2.3 \times 10^{20} m^{-3}$. The use of Beryllium to control recycling together with central fuelling by pellets has allowed peaked density profiles in 3MA beam heated plasmas with ion temperatures up to 18keV enhancing the thermonuclear reactivity over normal flat profiles. Here ICRF suppresses sawteeth and enhances the beam plasma reactivity by the acceleration of injected deuterons. The highest values of D-D fusion gain yet obtained in a limiter plasma on JET is $Q_{DD} \sim 1 \times 10^{-3}$.

Thus the foundations have been laid for performance optimisation at the highest plasma currents in JET (up to 7MA). These promising results suggest that the performance projections for 7MA D-T operation in JET [4] might indeed be pessimistic.

Acknowledgements

It is a pleasure to acknowledge the other members of the Task Forces who carried out this work- D.Bartlett, M.Brusati, J.P.Christiansen, H.D'Esch, R.Giannella, A.Gondhalekar, G.Cottrell, T.T.C.Jones, P.Kupschus, G.Magyar, F.Marcus, P.Nielsen, D.Pasini, R.Prentice, G.Sadler, M.Stamp, A.Tanga, A.Taroni, and H.Weisen.

References

[1] Bickerton R.J and the JET Team, Plasma Physics and Controlled Nuclear Fusion Research, Proceedings 12th IAEA Conference, Nice, Vol **1** (1988) p41

[2] Goldston R.J. Plasma Physics and Controlled Nuclear Fusion, **26** p87 1984

[3] Rebut P-H, Lallia P, Watkins ML, Plasma Physics and Controlled Nuclear Fusion Research, Proceedings 12th IAEA Conference, Nice, Vol **2** (1988) p191.

[4] Gibson A and the JET Team Plasma Physics and Controlled Nuclear Fusion, **30** p1390 1988.

[5] Tanga A and the JET Team, This conference

[6] G.L.Schmidt and the JET Team, Plasma Physics and Controlled Nuclear Fusion Research, Proceedings 12th IAEA Conference, Nice, Vol **1** (1988) p215.

[7] Campbell D.J et al, Phys. Rev. Lett. **60** p2148 1988

[8] Bhatnagar V.P et al, Plasma Physics and Controlled Fusion **31** (1989) p333 and JET-P(88)51.

[9] Bures M et al, Plasma Physics and Controlled Fusion **31** (1989) p1843 and JET-P(89)03 p77.

[10] Lomas P.J et al, Proc 17 European Conference on Controlled Fusion and Plasma Heating **1** p5 (Amsterdam) 1990.

[11] Keilhacker M and the JET Team, Phys. Fluids B **2** p1291 1990.

[12] Jones T.T.C et al, Proc 17 European Conference on Controlled Fusion and Plasma Heating **1** p9 (Amsterdam) 1990.

[13] Sadler G et al, Proc 17 European Conference on Controlled Fusion and Plasma Heating **1** p1 (Amsterdam) 1990.

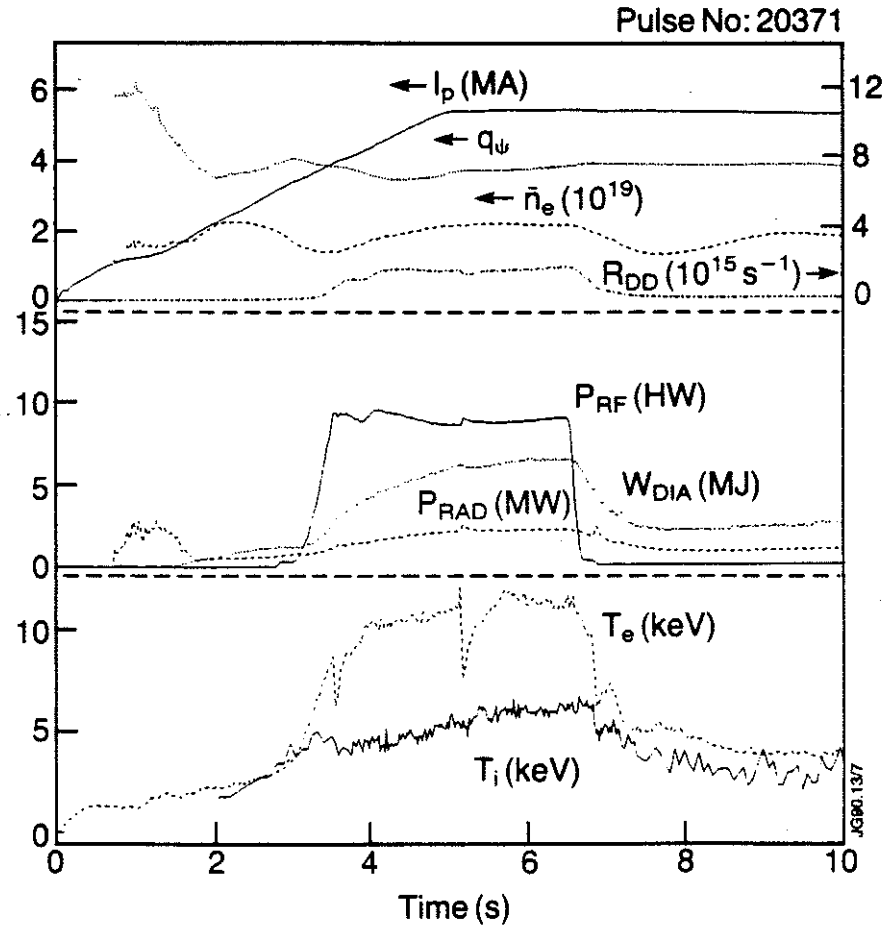

Fig 1. Various time traces for a 5MA plasma where ICRF is applied during the current rise and showing sawtooth stabilisation.

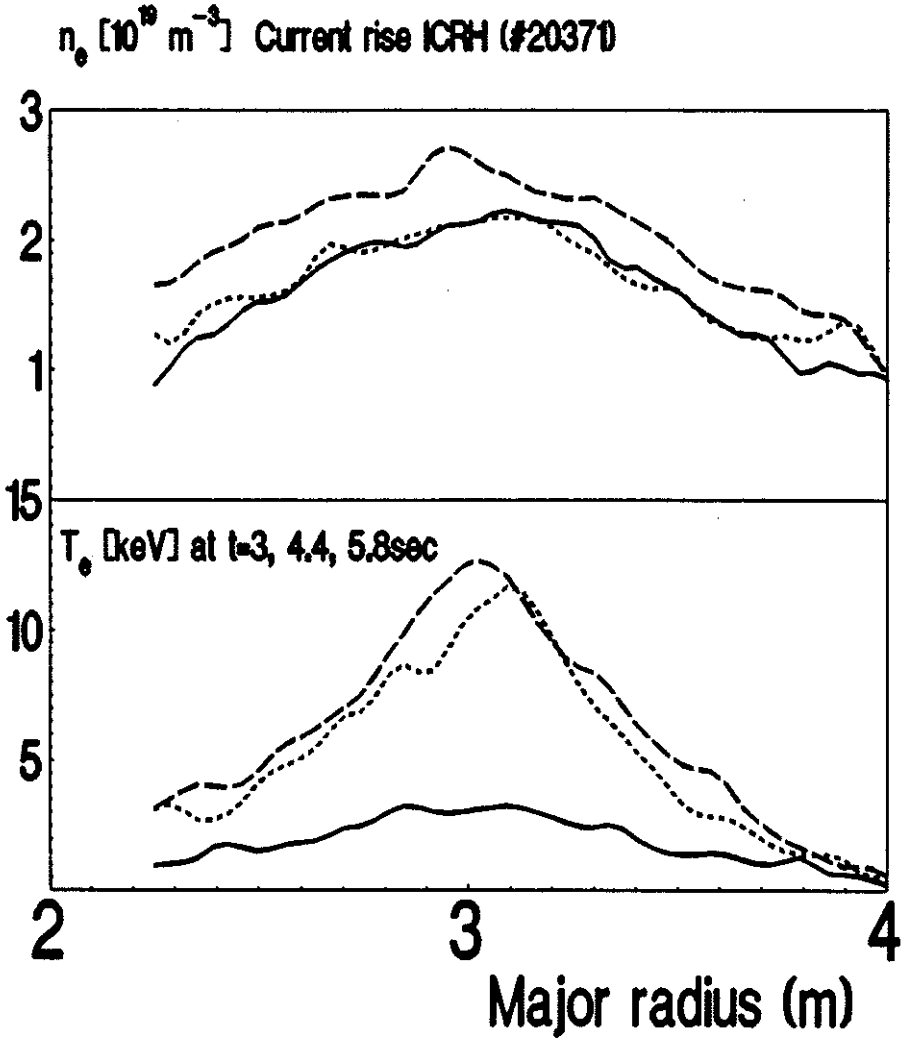

Fig 2. Density and temperature profiles for the pulse illustrated in fig 1.

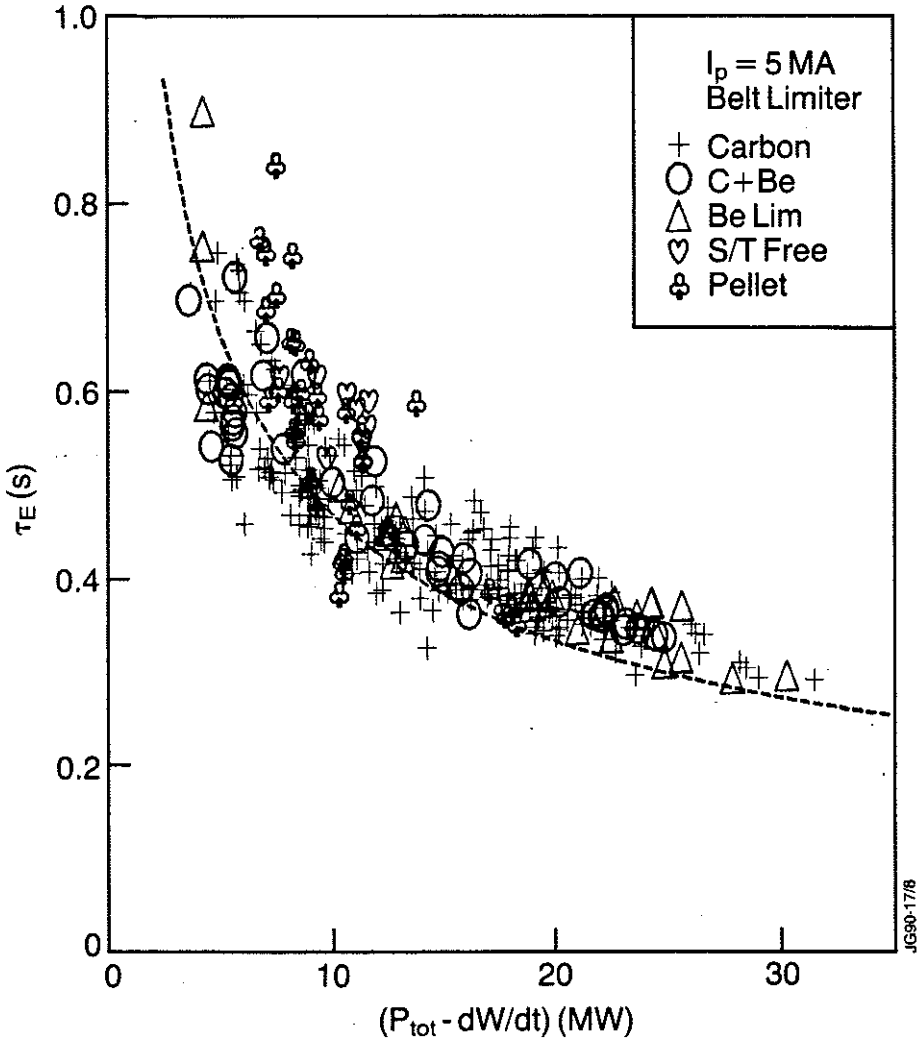

Fig 3. Confinement time plotted against loss power for 5MA belt limiter plasmas. The various symbols indicate the limiter material and distinguish the sawtooth free cases described in section 2 and the pellet cases of section 3.

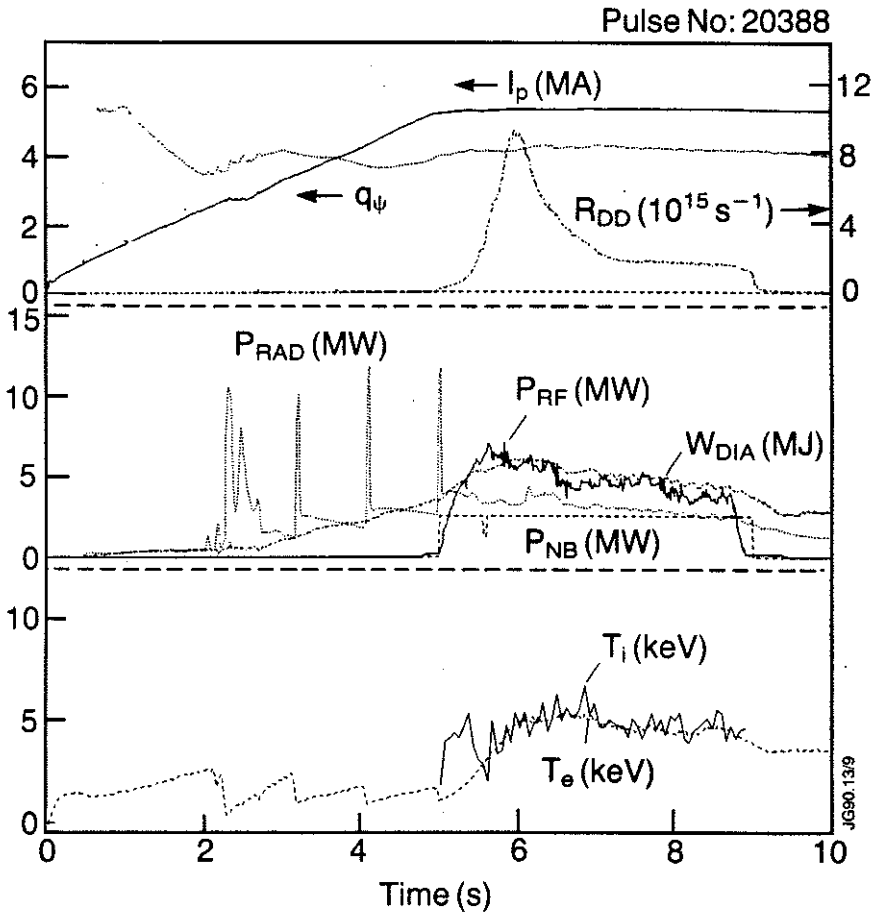

Fig 4. Various time traces for a 5MA plasma with pellet injection during the current rise followed by ICRF heating in the flat top.

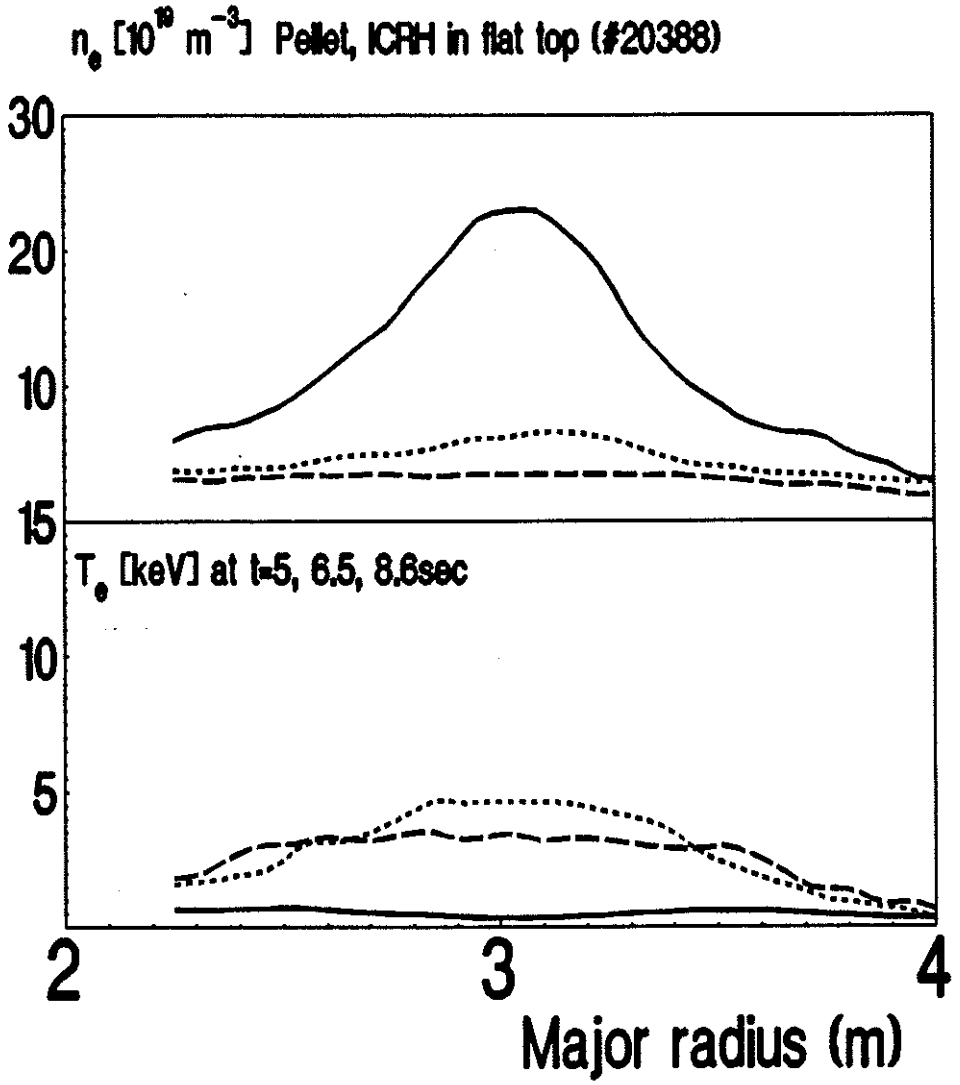

Fig 5. Density and temperature profiles for the pulse illustrated in fig 4.

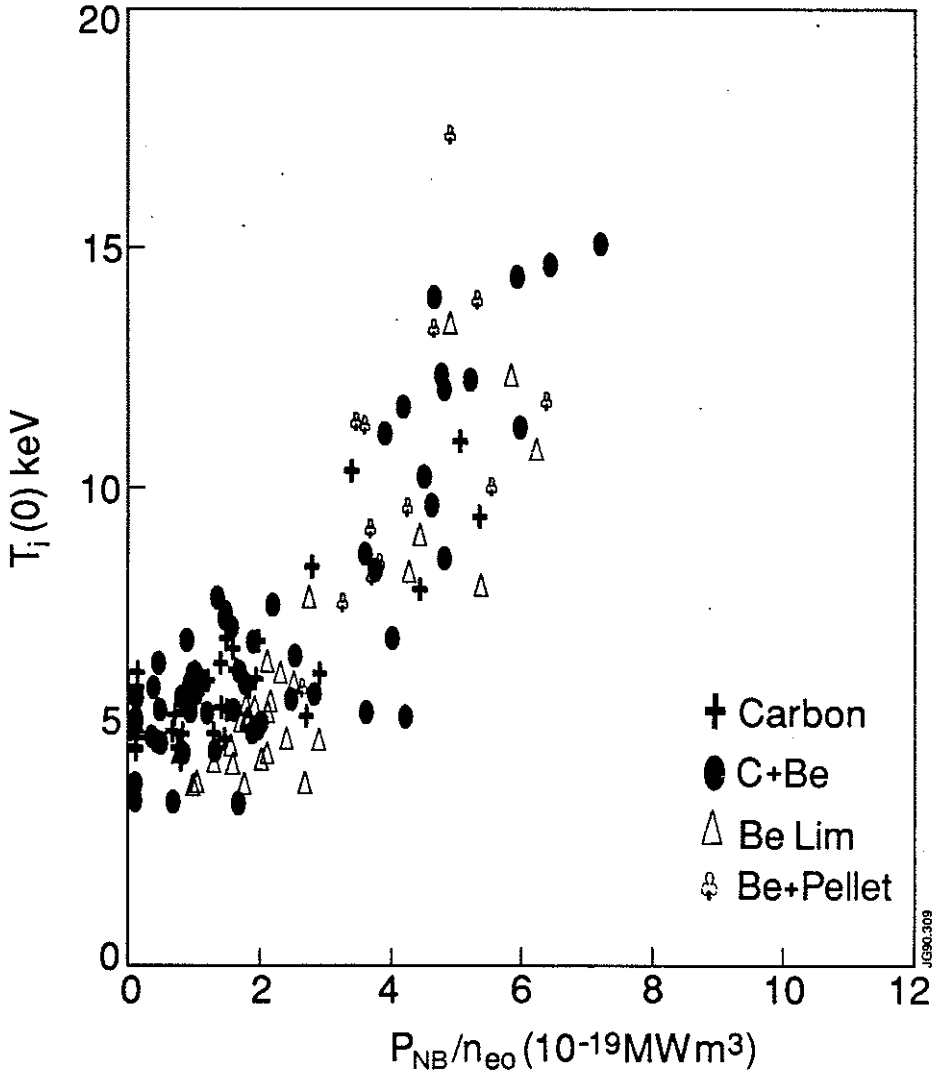

Fig 6 Axial ion temperature plotted against Neutral Beam power normalised to the axial density for 3MA belt limiter plasmas. The symbols indicate the limiter material and distinguish pellet fuelled target plasmas.

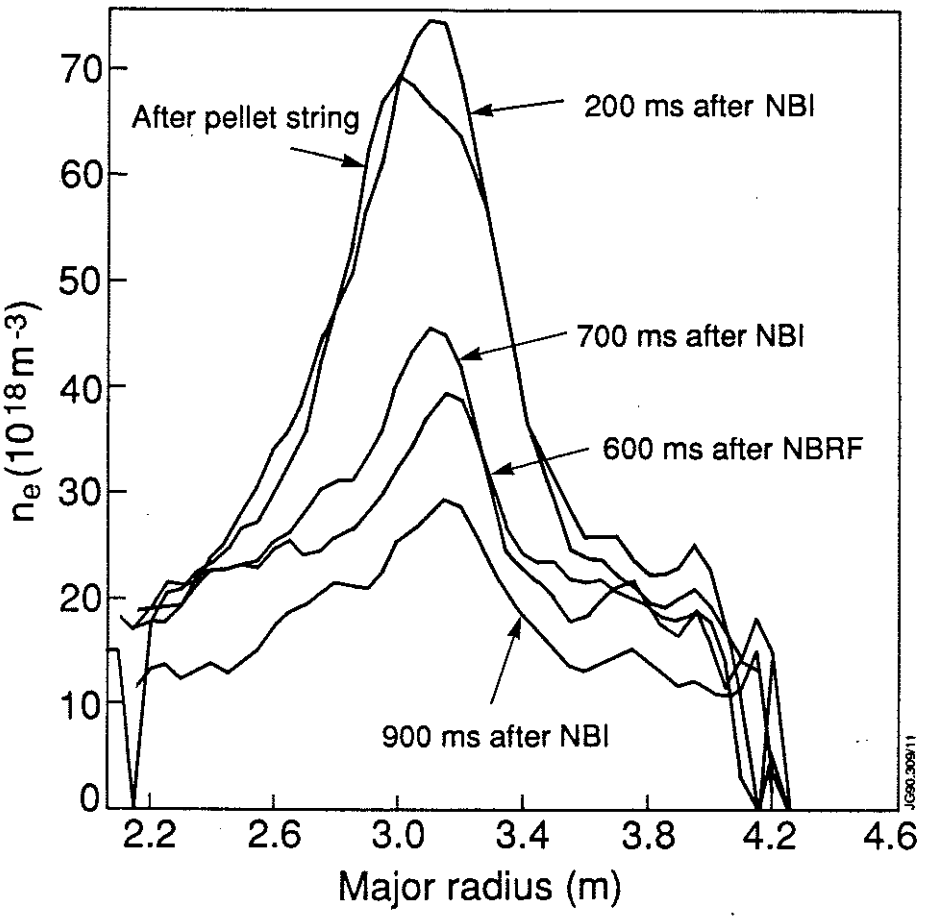

Fig 7. Density profile evolution reconstructed using LIDAR data for several similar discharges where heating was applied to pellet fuelled target plasmas.

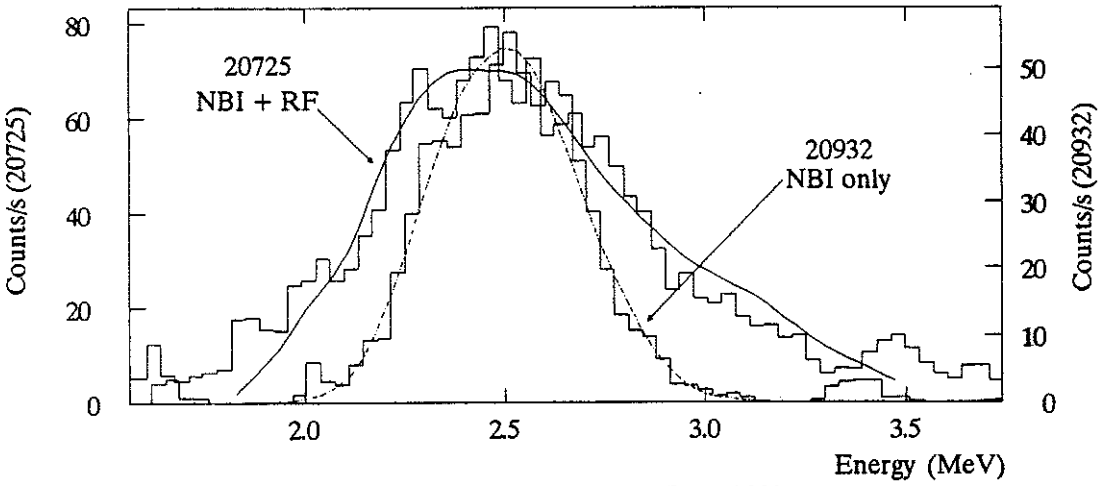

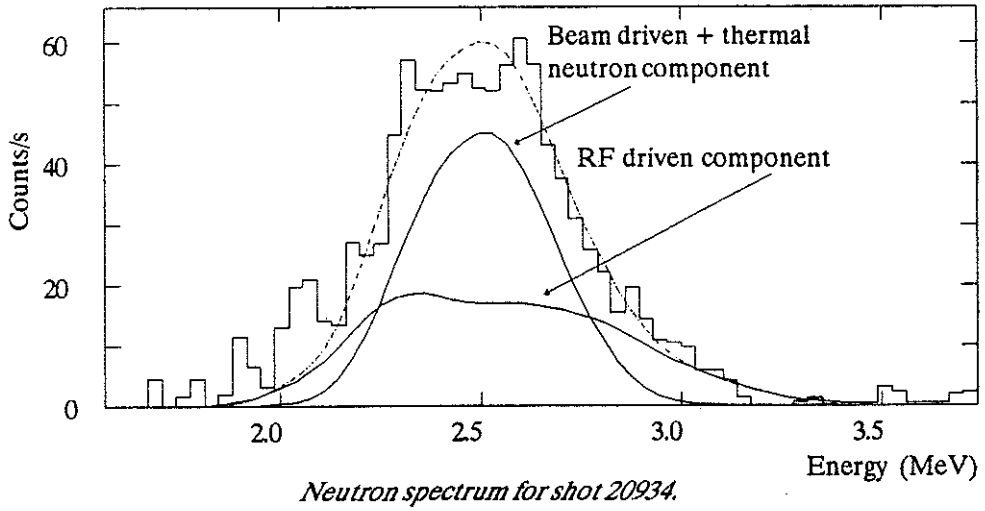

Fig 8 Neutron energy spectra illustrating ICRF enhanced reactivity. Top compares two discharges with similar neutral beam power with and without ICRF and shows the broadening of the spectrum. The bottom shows an unfolding of the spectrum to illustrate the ICRF driven component.

IAEA-CN-53/A-4-1

High Performance H-modes in JET

by

The JET Team*
(presented by A Tanga)

JET Joint Undertaking, Abingdon,
Oxon, OX14 3EA, UK

* See P-H Rebut and the JET Team, 13th Int. Conf. on Plasma Physics and Contr. Fusion Research, Washinton, USA. (1990)
to be published in Nuclear Fusion Supplement

High performance H modes in JET

The JET Team

(presented by A.Tanga)

JET Joint Undertaking, Abingdon, Oxon OX14 3EA, UK.

Abstract

In JET the scientific properties and technical basis of good confinement regimes have been evaluated in the light of the potential extrapolation of such regimes to reactor requirements. In this paper the main experimental H-mode results are discussed highlighting global confinement scaling, low q regimes, the role of the target plate material, the density limit, and finally sawtooth suppression and hot-ion mode.

1. Introduction

The H-mode in JET has been demonstrated with single and double null x-point configurations, which in general are marginally limiting at the x-point target tiles. H-modes have been achieved with NB heating, ICRF heating and with combined NB and ICRF heating. The power threshold for the H-mode and the global energy confinement time does not depend on the heating method. In the ELM free H-mode there is an improvement of about a factor of two in the global confinement time compared to JET limiter L-modes, up to the total additional power of 25MW.

The development of the JET H-mode, towards steady state conditions, depends on wall conditioning and on the material of the divertor target plates, which determines the amount and type of impurity released, and affect the time evolution of plasma density. The substantial reduction of Z_{eff} ($\simeq$ 2.) and improvement of n_D/n_e to 0.8-0.9, produced by routine Beryllium gettering of the graphite tiles was probably mainly due to the nearly complete removal of Oxygen and Oxygen generated Carbon sputtering. The reduction of Nickel was mainly due to the Beryllium gettering of the ICRF antennae screens. As a consequence of lower radiation losses and improved density control longer ELM free H-mode phases have been achieved ($\lesssim$ 5.4s) .

The transport of impurities in the JET H-mode is characterized by a balance between neoclassical effects and anomalous transport leading to a build up of impurities in the plasma ($\tau_{imp}/\tau_E > 1$) [1]. Further local analysis of energy transport in high power H modes confirms the reduction in thermal conductivity (energy flux/gradT) across the whole plasma cross section reported earlier [2] .

In the JET H-mode the density limit corresponds to the radiative collapse which ends the H phase.

With additional power well above the threshold, the H-mode can occur simultaneously with other plasma regimes such as the monster sawtooth or the hot-ion mode.

In the hot-ion H-mode, with NB(D)injection, at moderate plasma densities ($< n > 1 \div 4.10^{19}$ m^{-3}) T_i is 2 or 3 times larger than T_e ($T_i \gtrsim 22$keV, $Q_{dd} \simeq 2.5 \times 10^{-3}$). The values of Q_{DT} for D-T simulated versions of the same discharges are above 0.5 for times of the order of one energy confinement time.

2. Operational regimes

The H-mode in JET has been demonstrated in single null ($I_p < 5$MA) and double null ($I_p < 4.5$MA) configurations , generally with the plasma limiting on the x-point target tiles , but also with the plasma in contact with the inner wall. In single null configuration the H-mode has been achieved with NB at 80keV and at 140keV both in deuterium and hydrogen target plasmas. In double null configuration, where it has been possible to obtain good RF coupling, the H-mode has been achieved with ICRF alone in dipole with Hydrogen minority, and in combination with NB(D) in Deuterium plasmas. The JET H-mode is characterized by a transition to an ELM free period lasting several seconds. The duration of the H-mode is considerably shorter for power in excess of 10MW due to a strong carbon influx from overheated graphite dump tiles [3] .

The threshold power for the H-mode was similar for double and single null configurations, with ICRF and NB heating. The H-mode power threshold was lower with a well conditioned vessel. The power threshold, while scaling approximately linearly with the applied toroidal field as reported earlier [4], does not show a clear dependence on plasma current or plasma density. Scans of the plasma radial position show a minimum power threshold if the gap between the plasma and limiter, or between the plasma and the inner wall is above 5-8cm. For shorter distances the threshold power increases. H-mode was achieved even with the plasma in contact with the inner wall protection tiles, which required a threshold power of 10 MW at $B_T = 2.2$T. Plasma recycling and power load were distributed on the inner wall. We think that this regime is similar to the inner wall H-mode achieved in DIII-D [5] . Fig 1. shows the plot of additional heating power versus the gap between the plasma and the inner wall. L marks the discharges which had not undergone an H transition, while H marks the H modes. The H-mode power threshold is a function also of the position of the x-point as determined from magnetic diagnostics [6] . The threshold for H-mode has only a weak dependece on the location of the x-point within 10 cm outside the surface of the dump plate, with the plasma in a marginal limiter configuration or 10 cm inside, with plasma in x-point configuration.

3. Global confinement

The main properties of global confinement time of the JET H-mode have been extended to higher additional power. The general trend of the global energy confinement time, as a function of the total loss power, is shown in fig 2. The two main trends of increase with plasma current and degradation with heating power continue at high powers the trend reported earlier [4] . The scaling of the global confinement time is similar in single null and double null configuration. From the analysis the data it appears that the global confinement time has only a weak dependence on the toroidal field (as $B_T^{0.3+0.07}$). In operation at low values $q_{0.95}$ it appeared that there was not an abroupt deterioration of confinement in the approach to $q_{0.95}$ of 2, as shown in fig 3. [7]. The scaling of the global confinement time observed in the JET H-mode is similar to that observed in other tokamaks. A size scaling has been derived by combining data from JET and DIII-D [8]. A large database with data from JET, DIII-D, ASDEX, JFT2-M, PDX and PBX has been created, the scaling obtained by the analysis of the data of all these tokamak is $\tau_E = 0.07 A^{.5} I^{.94} P^{-.48} R^{1.72} k^{0.48} (R/a)^{-0.13}$, when the toroidal field and density dependence are suppressed [9]. As an example a plot of the JET data versus the combined H-mode scaling, is shown in fig. 4. A detailed analysis of the local transport of JET H-mode will also be presented at this conferece [10].

4 Approach to steady state conditions

The ELM free H-mode is a transient effect which is terminated either by radiative collapse, for additional input power below 10MW, [11]; or by carbon influx, for power in excess of 10MW.

4.1 Carbon Influx

A strong carbon influx, which terminates the H-mode, enter the plasma when the surface temperature of the dump plates exceeds the temperature of 2500 C. The onset of the carbon influx can be delayed by radial sweeping of the x-point position or/and by a strong gas puff. With strong puff long ELM free H-modes phases have been obtained, exceeding 5 seconds as shown in fig 5(a,b) The main effect of strong gas puff is a reduction of the surface temperature of the x-point tiles (fig 5 c,d) in the heated zone where the power is deposited by fast ions on drift orbits. [3,6] . The reduction in temperature is probably caused by reduced ion temperature and/or increased ion collisionality. The reduction in temperature leads to a significant drop in carbon sublimation and radiation enhanced sputtering. The gas puff causes increased divertor radiation losses with general reduction in conduction losses.

4.2 Radiative collapse.

The impurity confinement time, as determined by laser blow off measurements and impurities transport computer simulation [12] is much longer than the energy confinement time, with typical values up to 4s. [1,12] As an example the time evolution of the concentration of NickelXXV and NickelXXVI, obtained by laser blow-off of a Nickel coated target, are shown in fig 6. the result of transport analysis show that there is an outward flow of impurities, [1,12] . The plasma behaves as a " leaky " integrator. For intrinsic impurities, in the H-mode, the outward flow is an order of magnitude smaller than the inward flow, which is generated by the plasma interaction with the dump plates. Consequently, during the ELM free H-mode the concentration of the intrinsic

impurities increases continously as a function of time, until the total radiated power becomes excessive [11] . However if the inflow of intrinsic impurities could be reduced by at least a facor of 5, by for example the use of a pump divertor, the simulations show that a balance could be reached after a few impurity confinement times at levels of radiation compatible with the input power.

5. Effects of dump plate material on the H-mode.

The comparative properties of graphite and Beryllium gettered graphite have been studied.

With graphite tiles Oxygen and Carbon were the dominant impurities , radiative losses by Oxygen were dominant at high densities. Among other impurities Nickel, mainly generated by the ICFR antennae screens, accounted for a 10% fraction of the radiated power. With Beryllium gettered graphite tiles the concentration of Oxygen was reduced to a negligible amount. The reducion of Carbon concentration can be explained as due to the absence of Oxygen sputtering generated Carbon impurities as in the case of Beryllium gettered graphite limiter [13] .

In fig 7 the trend of Z_{eff} , as measured by visible bremsstrahlung, versus the total loss power (total input power minus the time derivative of the plasma energy) is shown. Fig 7 shows an average reduction of 1-2 units, at all levels of power. Consequently charge exchange spectroscopy measurements show that with Beryllium gettred graphite dump plates the ratio of electron to deuteron density was 0.8-0.9, whilst without Beryllium gettering it was 0.5-0.6.

6 Density limits

During the H-mode generally the plasma density increases continuosly until a radiative collapse of the H-mode occurs, [11] , precipitating an H to L transition and sometimes a full plasma disruption. For the H-mode the density limit coincides with the high density prior to the H to L transition. The limit on the plasma density is caused by the fact that the power which is radiated by the bulk of the plasma approaches the input power. It is therefore natural to expect the density limit to scale with the square root of the total input power with a scaling similar to that observed in in recent JET limiter discharges [14] . The values of the maximum volume average electron density prior to the H to L mode transition have been plotted versus the total input power in fig 8, for a series of 3MA H-mode discharges. the experimental points with Z_{eff} smaller than 3 (crosses) have a higer density than those with Z_{eff} larger than 3. For reference a Hugill plot of the non disrupting H-mode pulses is shown in fig 9 for discharges with Beryllium gettering.The line $qnR/B_t = 20x10^{19} m^{-2} T^{-1}$ encompasses the values for the dicharges with moderate additional heating (< 10MW) and fuelled by gas puffing. The lower limit $qnR/B_t = 12x10^{19} m^{-2} T^{-1}$ refers to Ohmic x-point

discharges. Preliminary results have been achieved with central pellet fuelling which have produced more peaked density profiles. The values of the pellet fuelled discharges are not shown in fig 9.

7. Sawtooth stabilization

Sawtooth suppression has been observed in H-mode discharges with NB and ICRF heating. The time evolution of a series of discharges showing sawtooth suppression during H-mode is presented in fig.10.

With NB heating in excess of 8MW, at least twice the power threshold for H-mode transition, injected into a relatively low density ohmic deuterium target, the H-mode is accompained by a period of sawtooth stabilization of the duration of.6 -.8 s. In this phase a modest enhancement (10-15%) of central ion and electron temperatures is observed.

With ICRF heating during the H-mode [15] sawtooth suppression occurs routinely with ICRF input powers in excess of 7MW. The maximum duration of the monster sowtooth has been 2.5s. The start and end time of sawtooth suppression was not correlated with the H-mode phase, but sometimes the monster crash caused an H to L transition. The temperature peaking factor obtained in sawtooth suppressed H-modes is enhanced by approximately 50% . A series of electron temperature profile shapes with sawtooth suppressed H-modes is shown in fig 11. Here the peaking factor ranges between 3 and 4 (with electron pressure peaking factors between 4 and 5) with values of cylindrical $q = 3.2$ and averages densities in in the range $2 - 4 \times 10^{19} m^{-3}$. It should be noted that in this case the shape of the electron temperature profiles are similar to those obtained in the case of limiter monsters [16] and that the value of the edge plasma temperature is not very high.

With combined ICRF/NB heating sawtooth suppresion in H-mode has also been achieved, as shown by one of the traces in fig 12. In this pulse, ($P_{RF} = 2$MW and $P_{NB} = 6$MW, $< n > = 2.5$E19m-3). Polarimetric analysis of the safety factor radial profile indicate that the central value of q is driven below unity in a way similar to other monster sawtooth, while estimates of the content of fast particles confirm the agreement with the theoretical expectations of sawtooth stabilization.

8. Hot-ion H-mode

In x-point configuration with NB injection in a low density ohmic target it has been possible to produce simultaneously a hot-ion plasma and an H-mode transition. This regime is characterzed by very high ion temperatures in excess of 20keV, while the electron temperature vas 8-10keV. For large values of NB power and low densities the ion temperature profile is very peaked : The ratio of central to volume average ion temperature reaches values of 4-5 .

The D-T performances of these pulses ara examined by considering the standard $n_D \tau_E T_i$ diagram, shown in fig 13. Here the Q curves are for parabolic profiles of density and temperature raised to the power 1/2 and 3/2 respectively. The Q curves are rather insensitive to the form of the profiles. The time evolution of plasma parameters for pulse 20981 are shown in fig 14.

The time behaviour of the pulse was simulated by the 1 1/2-d TRANSP code for the actual conditions of NB injection and background plasma. A good check on the consistency of this data is that of the predicted and measured neutron yeld. The D-T simulations are completed by rerunning the code with the same measured profiles and replacing the background deuterium plasma with a tritium or with a 50-50 D-T mixture. The results are shown in fig 15. Here the time evolution of the fusion power is shown in its components for the case of deuterium injection in a Tritium plasma. The NB power was 17MW, the time derivative of plasma stored energy was 8MW. With Q defined as follow $Q = P_{th-th}/(P - dW/dt) + (P_{b-th} + P_{bb})/P$, the peak value corresponds to $Q = 0.77$ [17].

9. Conclusions

a) The experiments at JET have shown that the ELM free H-mode is a transient plasma regime. The analysis of the results of impurities injection experiment and of the spectroscopical data suggests that if one could control the plasma density and drastically reduce the influx of impurities the H-mode could reach a steady state transport equilibrium.

b) The H-mode is achieved in a configuration with a magnetic separatrix, which can be marginally limiting on the x-point dump plates or on the inner wall protection plates. A parameter related to the shear at the plasma edge, for this marginally limiting configurations, could be the ratio between q_ψ and q_{cyl}. H-mode has been achieved with q_ψ larger or equal to 7-8 while q_{cyl} was 2-3.

c) In the H-mode the global energy confinement time shows an improvement of approximately a factor of two over the limiter L-mode independently of the heating method and in the range of additional power up to 25MW.

d)The radiation collapse, which terminates the H-mode, determines the values of the density limit, which scales with square root of the input power.

e) An improvement in plasma purity and reduction of fuel dilution has been achieved with Beryllium gettering of graphite tiles.

f) In low density ohmic target, and largely with ICRF heating it as been possible to achieve transient stabilization of sawteeth during the H-mode

g) With NB injection in low density deuterium plasmas a hot-ion plasma has been created during the H-mode. In these discharges the highest plasma thermonuclear reactivities have been obtained.

References :

1) Giannella R. et al. in Proc. of 16th European Conference on Contr. Fusion and Plasma Phys., Venice, 1989 Vol. I p.209.

2) Watkins M.L. et al. Plasma Phys. and Contr. Fusion Vol 31, p. 1713, (1989).

3) Stork D., et al. Proceedings of 9th International Conference on Plasma Surface Interactions, 21-25 May 1990, Bournemouth,UK paper P 25.

4) Keilhaker M. for the JET Team, Proc. 12th Conference on Plasma Physics and Controlled Nuclear Fusion, 12-19 October 1988, Nice, France, Vol I p. 159.

5) Jackson G.L., et al., Bull. Am. Soc. Vol 33 p. 1963 (1988)

6) O'Brien D.P., et al., Proc. 17th EPS Conference on Controlled Fusion and Plasma Physics, 25-29 June 1990, Amsterdam, The Netherlands, Vol I p.251.

7) Lazzaro E., et al., "H-mode confinement at low q and high beta in JET " to be published in Nuclear Fusion.

8) Shissel D.P., De Boo J.C., et al., Tubbing B.J.D., et al. "H-mode Energy Confinement scaling from DII-D and JET Tokamaks" to be published in Nuclear Fusion

9) Cordey J.G., et al., at this conference paper IAEA-CN-53/F/3-19

10) Taroni A., Tibone F., et al., at this conference paper IAEA-CN-53/A/2-1

11) Tanga A., et al., Nucl. Fus. Vol 27, p. 1877 (1987).

12) Lauro-Taroni L., et al., in Proc. 17th EPS Conference on Controlled Fusion and Plasma Physics, 25-29 June 1990, Amsterdam, The Netherlands, Vol I p.247.

13) Thomas P.R. for the JET Team, "Results of JET operation with Beryllium", Proceedings of 9th International Conference on Plasma Surface Interactions, 21-25 May 1990, Bournemouth,UK paper I:01.

14) Gibson A. for the JET Team " Fusion relevant performances in JET ", invited paper 17th EPS Conference on Controlled Fusion and Plasma Physics, 25-29 June 1990, Amsterdam, The Netherlands, to be published on Plasma Physics and Controlled Fusion
and Smeulders P. for the JET Team, at this conference, paper IAEA-CN53/A-3-4.

15) Tubbing B.J.D., et al., Nucl. Fus. vol 29, p. 1953 (1989)

16) Campbell D.J., et al., Proc. 11th Conference on Plasma Physics and Controlled Nuclear Fusion, 13-20 November 1986, Kyoto, Japan, Vol I p. 441.

17) Stubberfield P.M., Balet B. and Cordey J.G., "Extrapolation of the high performances JET plasmas to D-T operation " to be publlished on Plasma Physics and Controlled Fusion.

Figure captions

1) Plot of power threshold for H-mode transition as a function of the gap between the plasma and the inner wall protection tiles, for a series of NB heated disharges. Plasma current was 3MA, Toroidal field 2.2T. The symbol H represents the discharges which made the transition, the symbol L represents those discharges which stayed in L-mode. In the H area there are some discharges which did not make the transition.

2) Global energy confinement time versus total loss power for all the 3MA and 4MA discharges with $(dW/dt)/P < 0.3$. The solid points refer to pellet fuelled discharges.

3) Global enegrgy confinement time as a function of the safety factor at 95% of the flux surfaces. The data refer to a set of 3MA discharges in deuterium with NB heating in a narrow power range around 9MW. The range of toroidal field is betwwen 1.2 and 2.4T.

4) Global energy confinement time as measured, versus H-mode scaling derived by combining data from JET, DIII-D, PDX, PBX, JFT2-M.

5) Comparison of long pulse H-mode (pulse 21022) with (a) added gas, and (b) a discharge with same plasma and similar NB power with no added gas. The early carbon influx in the no gas shot can be clearly seen.in (c) and (d) the measured surface maximum temperature of the dump plate carbon tiles for the discharges in (a) and (b) respectively.

7) Comparison of the values of Z_{eff} from horizontal bremsstrahlung betwwen Carbon and Beryllium gettering for 3MA H-modes.

8) Volume average electron density at the end of 3MA H-mode pulses versus total input pover. The crosses refer to pulses with Z_{eff} less than 3.0 , while the squares refer to pulses with Z larger than 3.0. The line is $n_e(10^{19}m^{-3}) = 2.12 \times P^{0.5}(MW)$

9) Hugill plot for ohmic and additionally heated x-point discharges. Symbols: diamonds represent ohmically heated plasmas, crosses represent Neutral Beam heated plasmas, asterisks represent combined ICRF and NB heated plasmas.

10) Time evolution of central electron temperature in H-modes with suppressed sawtooth: pulse no.14834 NB heating, pulse no. 19797 NB/ICRF, pulses no.19995 and no.20231 ICRF heating.

11) LIDAR electron temperature profiles of H-mode with suppressed sawtooth, 1. pulse no. 20231, 3. pulse no. 19995, 4. pulse no. 19796, 2. limiter comparison case pulse no. 12924

12) Time evolution of ion and electron temperature for a sawtooth suppressed H-mode with combined ICRF and NB heating

13) $n_D \tau_E T_i$ versus T_i (0)

14) Time evolution of high fusion yeld pulse no 20981. from top to bottom are depicted the central ion temperature T_i , the total neutron yeld Y_n the plasma diamagnetic energy W_{dia} , the volume average electron density n_e , and D_α intensity near the x-point, the neutral beam power and the radiated power loss

as a function of time. The carbon influx at 11.5 s is followed by the loss of the H-mode.

15) TRANSP code simulation of a D-T version of pulse no. 20981 obtained by using the same set of the experimental measurements which are a good representation of the D-D case . The only changes are the species mix and the injection energy. This figure shows total fusion power, thermal and beam-thermal contributions, assuming 15MW of D (at 140keV) injection on a target Tritium plasma. Only D-T reactions have been considered.

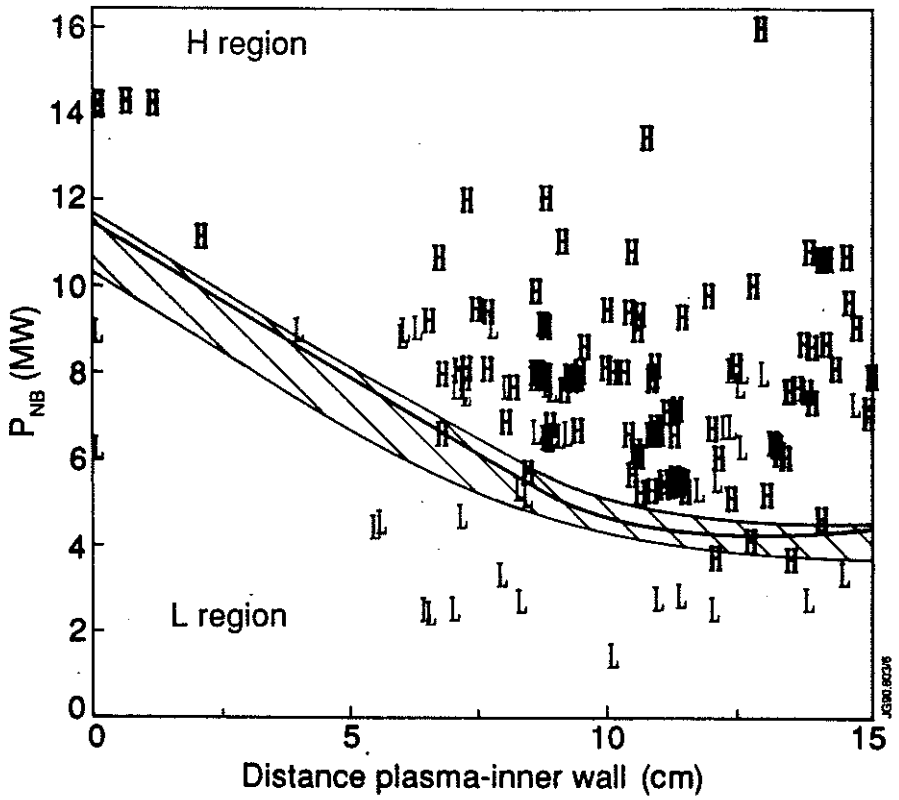

1) Plot of power threshold for H-mode transition as a function of the gap between the plasma and the inner wall protection tiles, for a series of NB heated disharges. Plasma current was 3MA, Toroidal field 2.2T. The symbol H represents the discharges which made the transition, the symbol L represents those discharges which stayed in L-mode. In the H area there are some discharges which did not make the transition.

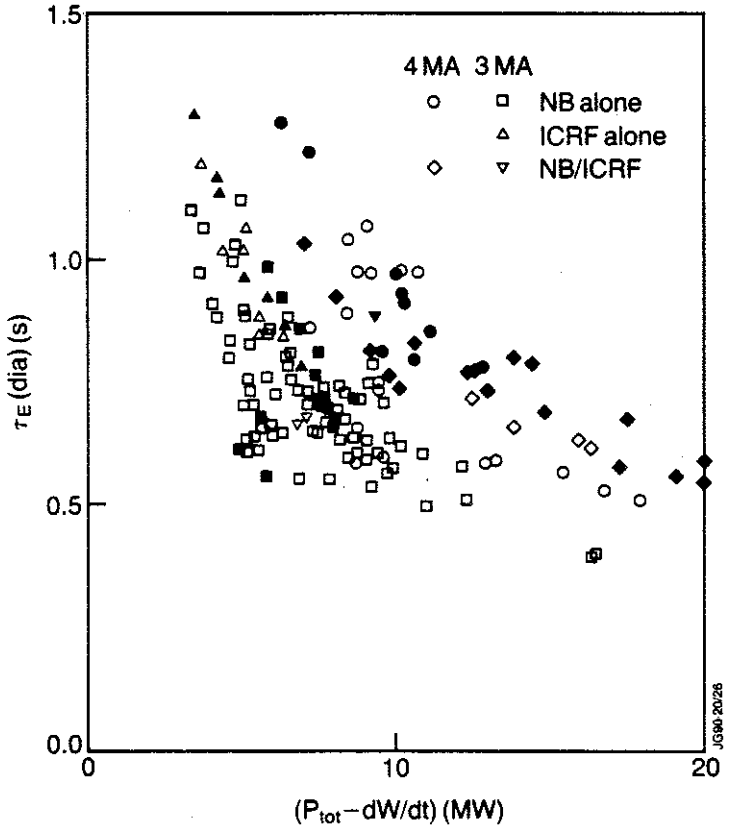

2) Global energy confinement time versus total loss power for all the 3MA and 4MA discharges with $(dW/dt)/P < 0.3$. The solid points refer to pellet fuelled discharges.

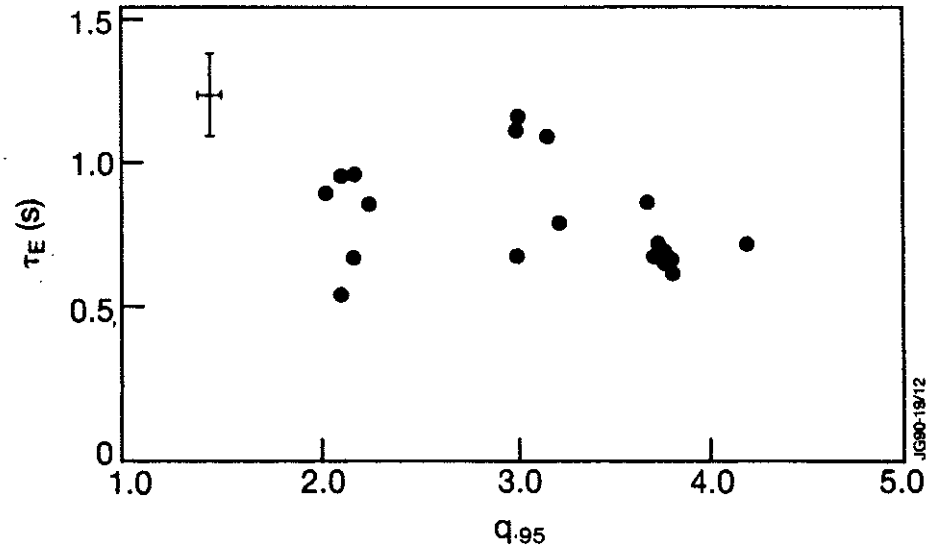

3) Global energy confinement time as a function of the safety factor at 95% of the flux surfaces. The data refer to a set of 3MA discharges in deuterium with NB heating in a narrow power range around 9MW. The range of toroidal field is betwwen 1.2 and 2.4T.

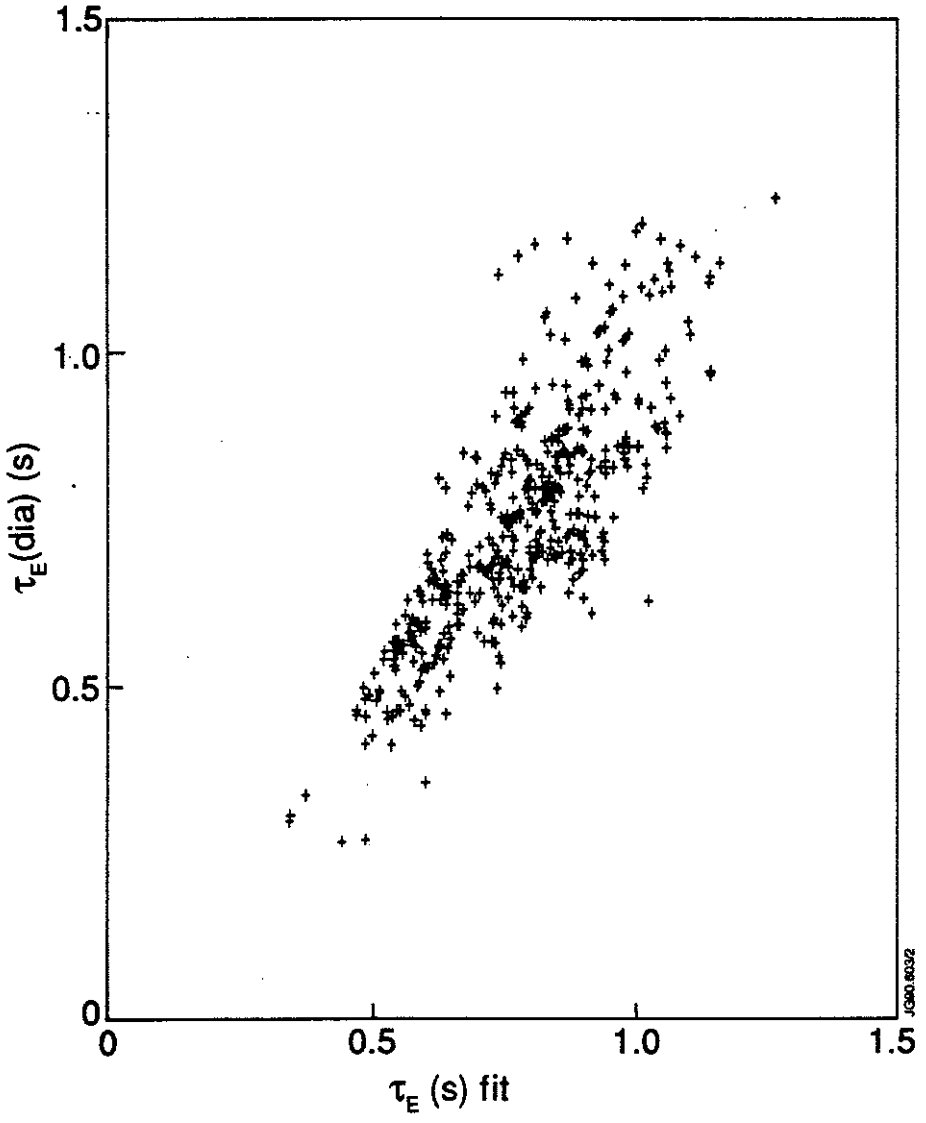

4) Global energy confinement time as measured, versus H-mode scaling derived by combining data from JET, DIII-D, PDX, PBX, JFT2-M.

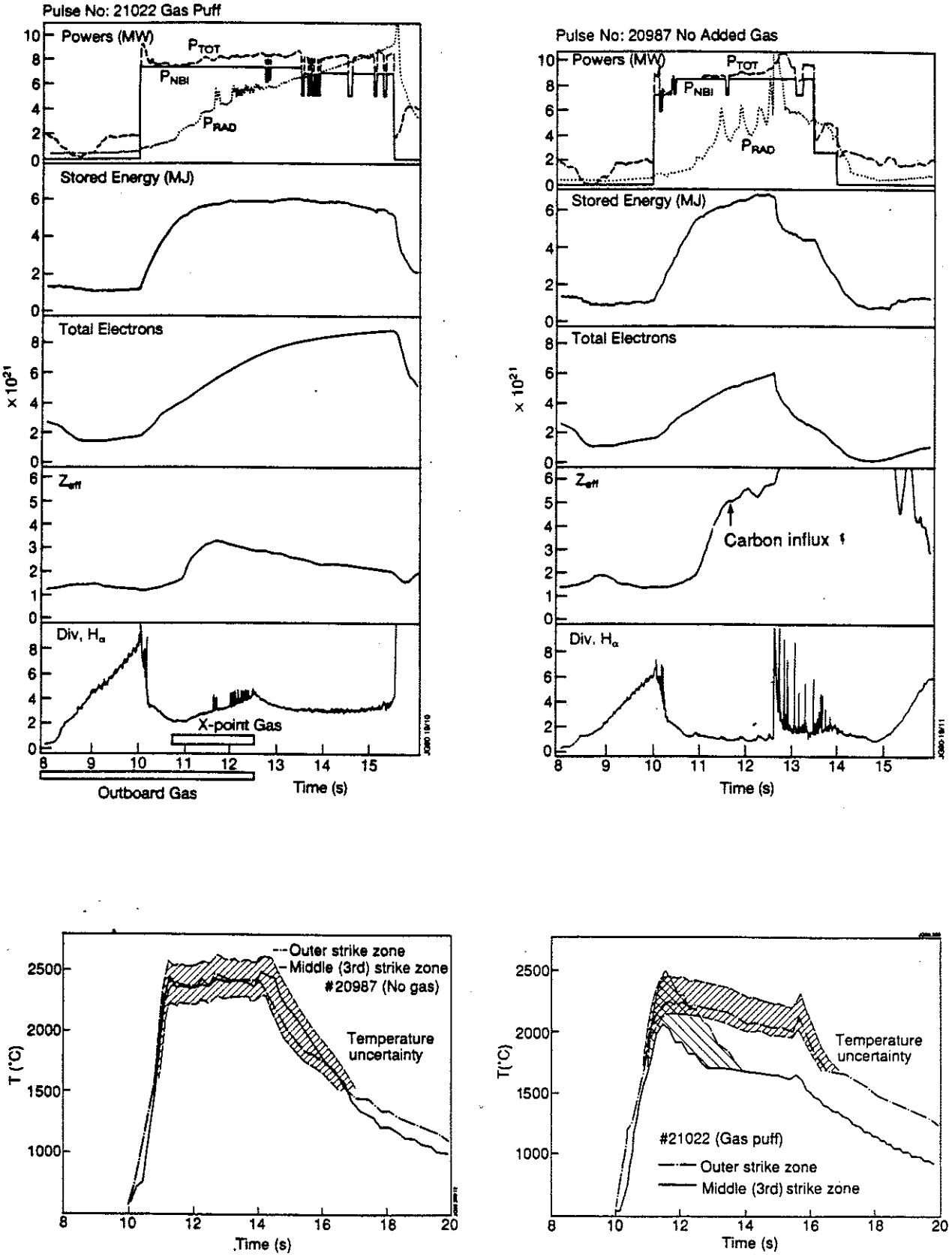

5) Comparison of long pulse H-mode (pulse 21022) with (a) added gas, and (b) a discharge with same plasma and similar NB power with no added gas. The early carbon influx in the no gas shot can be clearly seen.in (c) and (d) the measured surface maximum temperature of the dump plate carbon tiles for the discharges in (a) and (b) respectively.

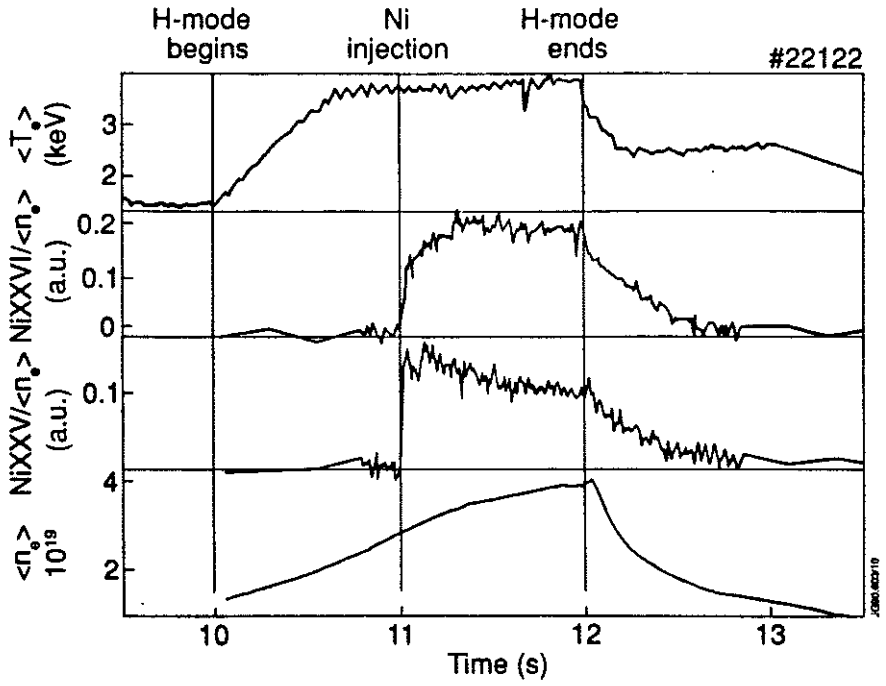

6) Time evolution of the ratio of the Nickel intensities during an H-mode. the Nickel is injected with laser blow-off tecnique at t = 11 s. Form top to bottom Volume average electron temperature, traces of density normalised NickelXXVI and NickelXXV, volume average plasma density.

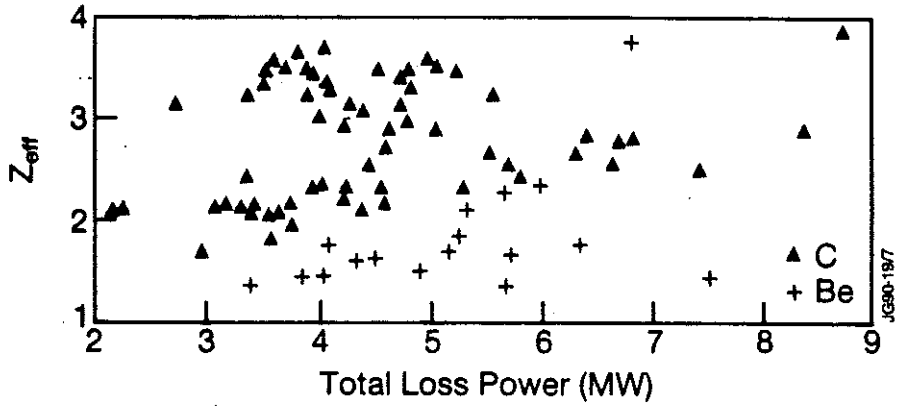

7) Comparison of the values of Z_{eff} from horizontal bremsstrahlung between Carbon and Beryllium gettering for 3MA H-modes.

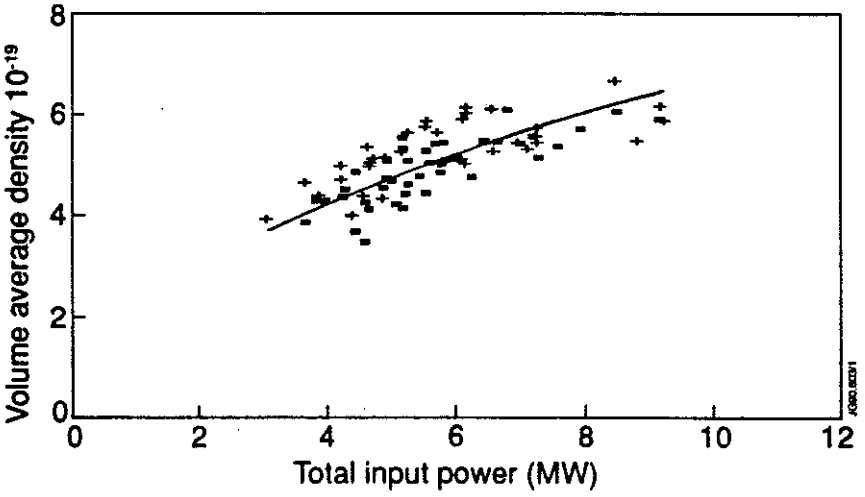

8) Volume average electron density at the end of 3MA H-mode pulses versus total input pover. The crosses refer to pulses with Z_{eff} less than 3.0 , while the squares refer to pulses with Z larger than 3.0. The line is $n_e(10^{19}m^{-3}) = 2.12 \times P^{0.5}(MW)$

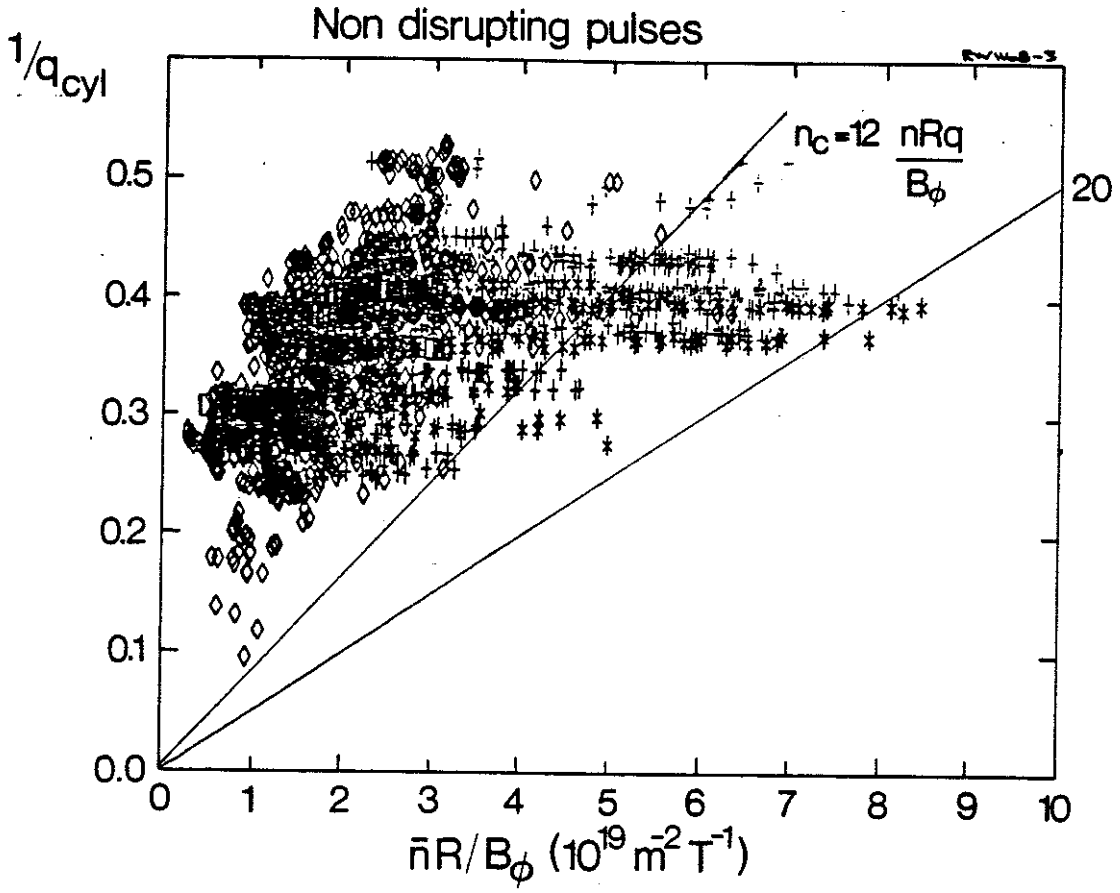

9) Hugill plot for ohmic and additionally heated x-point discharges. Symbols: diamonds represent ohmically heated plasmas, crosses represent Neutral Beam heated plasmas, asterisks represent combined ICRF and NB heated plasmas.

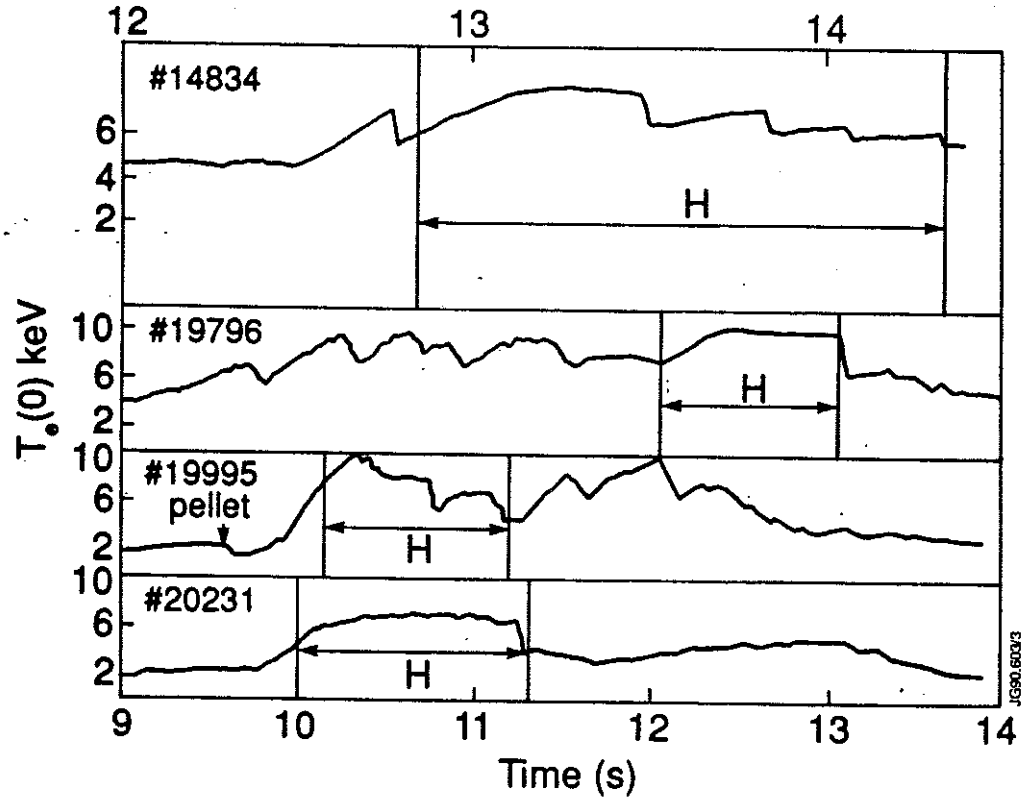

10) Time evolution of central electron temperature in H-modes with suppressed sawtooth: pulse no.14834 NB heating, pulse no. 19796 NB/ICRF, pulses no.19995 and no.20231 ICRF heating.

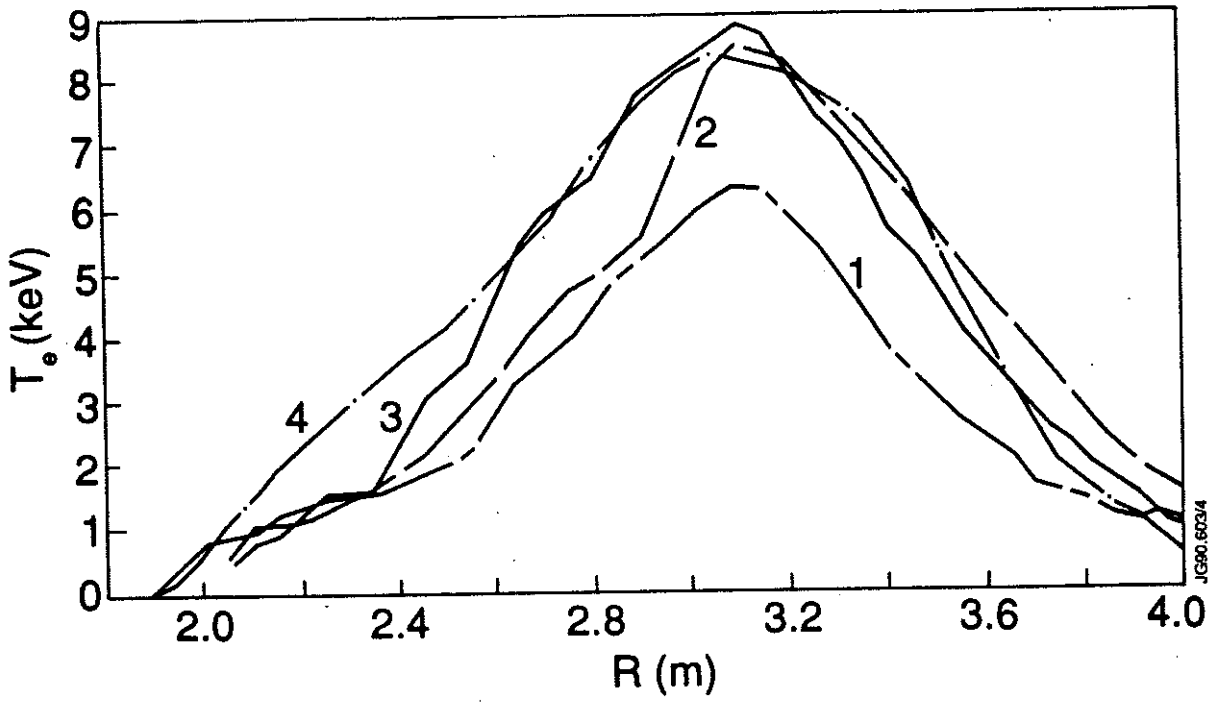

11) LIDAR electron temperature profiles of H-mode with suppressed sawtooth, 1. pulse no. 20231, 3. pulse no. 19995, 4. pulse no. 19796, 2. limiter comparison case pulse no. 12924

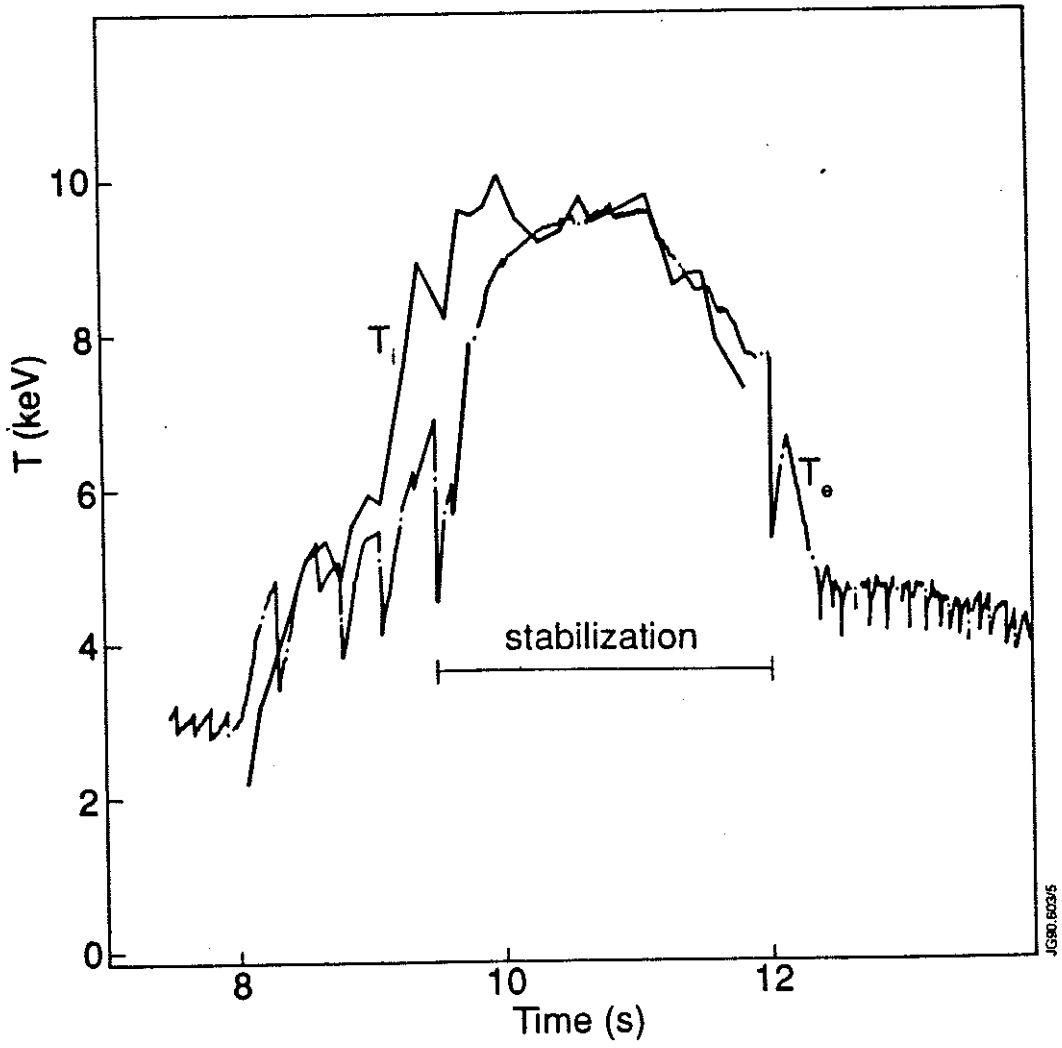

12) Time evolution of ion and electron temperature for a sawtooth suppressed H-mode with combined ICRF and NB heating

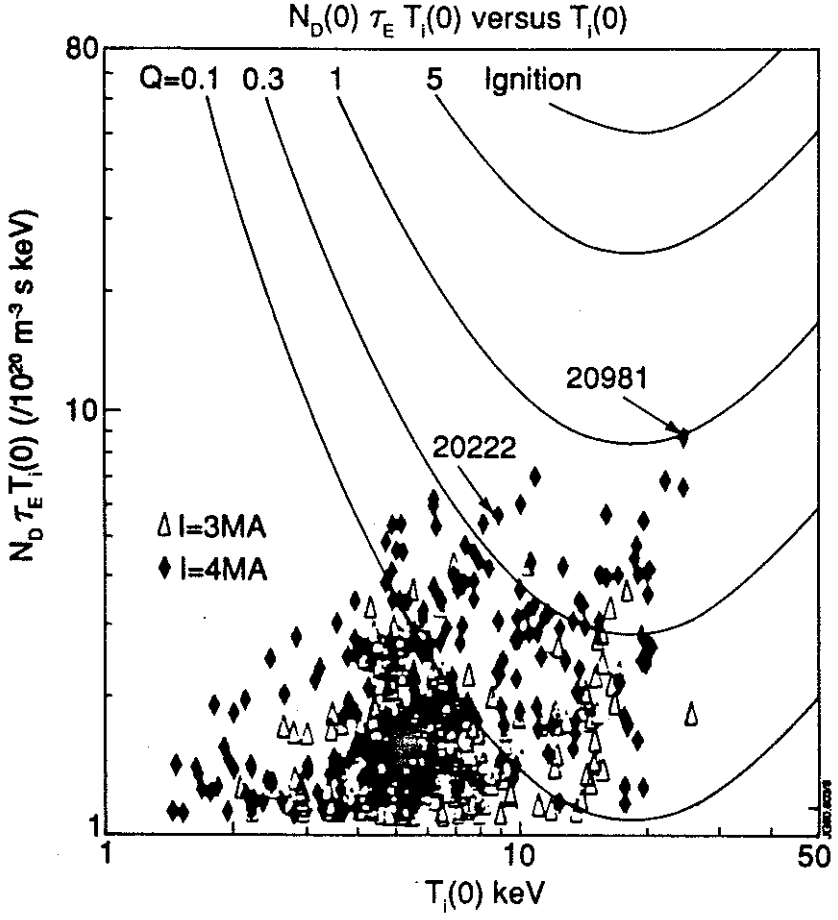

13) $n_D \tau_E T_i$ versus T_i (0)

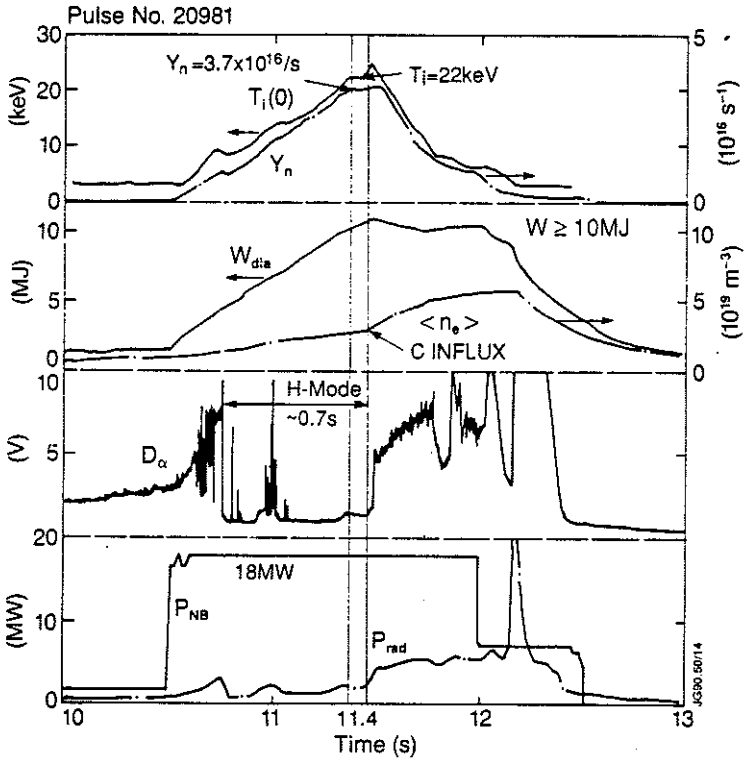

14) Time evolution of high fusion yeld pulse no 20981. from top to bottom are depicted the central ion temperature T_i , the total neutron yeld Y_n the plasma diamagnetic energy W_{dia} , the volume average electron density n_e , and D_α intensity near the x-point, the neutral beam power and the radiated power loss as a function of time. The carbon influx at 11.5 s is followed by the loss of the H-mode.

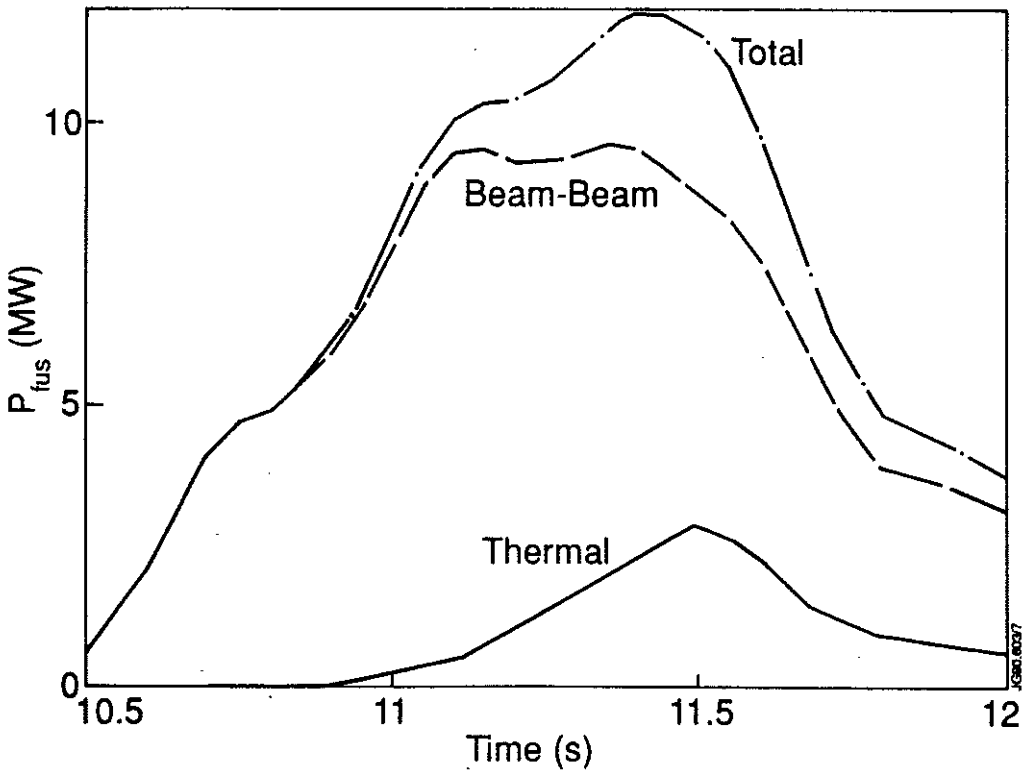

15) TRANSP code simulation of a D-T version of pulse no. 20981 obtained by using the same set of the experimental measurements which are a good representation of the D-D case . The only changes are the species mix and the injection energy. This figure shows total fusion power, thermal and beam-thermal contributions, assuming 15MW of D (at 140keV) injection on a target Tritium plasma. Only D-T reactions have been considered.

IAEA-CN-53/A-2-1

INTERPRETATION AND MODELLING OF ENERGY AND PARTICLE TRANSPORT IN JET

by

A. Taroni, F. Tibone, B. Balet, D. Boucher, J.P. Christiansen, J.G. Cordey, G.C. Corrigan, D.F. Düchs, R. Giannella, A. Gondhalekar, N. Gottardi, G.M.D. Hogeweij, L. Lauro-Taroni, K. Lawson, M. Mattioli*, D. Muir, J. O'Rourke, D. Pasini, P.H. Rebut, C. Sack, G. Sips, E. Springmann, T.E. Stringer, P. Stubberfield, K. Thomsen, M.L. Watkins, H. Weisen

JET Joint Undertaking, Abingdon, Oxon., OX14 3EA, UK.
*EURATOM-CEA Association, Cadarache, France

INTERPRETATION AND MODELLING OF ENERGY AND PARTICLE TRANSPORT IN JET

Abstract

The study of energy and particle confinement in JET plasmas has been performed by means of various interpretive and predictive techniques. This paper deals with the most recent and relevant results obtained, concentrating on local rather than on global analysis. Electron and ion energy transport and particle transport are studied and their relationship is examined. Comparisons with the predictions of theoretical models are presented, with special attention to transport coefficients derived from the theory of ion temperature gradient driven turbulence and to the critical electron temperature transport model of Rebut et al. [1].

1. Introduction

In this paper we report on the results of studies carried out to assess the local energy and particle transport properties on the basis of JET experimental data. The important issue of global confinement and its relationship to local transport models is discussed extensively in another contribution to this conference [2] where JET data are analysed together with data from other tokamaks collected in the so-called ITER data base. The global confinement of JET plasmas can also be found in other contributions to this conference [3-5].

A proper understanding of plasma transport requires the derivation of a complete transport model applicable in all relevant regimes. It must be capable of predicting the evolution of plasma profiles in the present and next step generation of tokamak devices. We have not reached this goal, but we have made much progress in:

— identifying the most important phenomena to be explained, pointing out correlations between the transport of electron and ion energy and the transport of particles;

— assessing various models proposed to explain and predict the plasma performance in tokamak devices.

In Section 2 we address the problem of electron and ion energy transport. We quantify the absolute and relative magnitudes of the electron and ion heat transport coefficients. A comparison with the predictions of models based on the theory of the ion temperature gradient driven turbulence is presented. We summarise the results obtained and assess the validity of the critical electron temperature gradient model of Rebut et al. (R-L-W in the following) [1].

The evolution of electron density profiles is analysed in Section 3, and it refers mainly to full transport code simulations based on an extension of the R-L-W model to include particle transport.

Section 4 presents the results of an integrated analysis of the propagation of the electron temperature and density perturbation following a sawtooth crash and their implications for transport models. An impurity transport analysis which implies a departure from simple conventional modelling assumptions

and the relevance of neoclassical transport theory, is discussed in Section 5. Some concluding remarks are given in Section 6.

2. Electron and Ion Heat Transport

There are regimes in JET where the electron and ion contributions to heat transport can be separated with the aid of interpretive codes. Among these regimes are the hot ion L and H-modes, sawtooth free discharges with strong RF heating (a "diagnostic" low power NBI is used to determine T_i by charge exchange recombination spectroscopy) and pellet fuelled discharges with combined heating [6,7]. Figure 1 illustrates results for two typical cases. The first is a hot ion H-mode discharge with plasma current I_p = 4MA, toroidal field B_T = 2.8T, neutral beam injected power P_{NBI} = 17.9MW, peak electron density $n_e(o)$ = $4.8 \times 10^{19} m^{-3}$ and peak electron and ion temperatures $T_e(o)$ = 8.8keV and $T_i(o)$ = 22.3keV. The second is a monster sawtooth discharge with I_p = 3MA, B_T = 3T, P_{NBI} = 2.6MW, ICRH power 8.9MW, $n_e(o) = 4.5 \times 10^{19} m^{-3}$, $T_e(o)$ = 8.8keV and $T_i(o)$ = 6.1keV. The figure illustrates the spatial dependence of the electron and ion heat diffusivities χ_e and χ_i, evaluated using the interpretive code TRANSP under the assumption of a diagonal transport matrix with no heat pinch term. The ion transport is clearly anomalous, except perhaps in the central region of the hot ion H-mode. (See also [6-9] for pellet fuelled cases). We also find as a general trend that $\chi_i \gtrsim \chi_e$ in the outer region of the plasma while χ_e becomes comparable or more important in the central region. Plots of the temperature increase in the central region as a function of the power input per particle to electrons and ions (fig. 2) illustrate in a crude, but rather general way, that as T_{eo} increases, χ_e must become larger in the central plasma region; this is not so for T_{io} and χ_i.

Several attempts to relate the observed heat transport to predictions of models derived from the theory of electrostatic microinstabilities have failed to reproduce JET results [7-10]. The most recent study [8] has considered models of the anomalous ion energy transport derived from the theory of ∇T_i-driven turbulence [11-13]. The analysis shows that, while there is some qualitative agreement (e.g. in pellet fuelled auxiliary heated discharges [14]) between theoretical predictions and experimental findings, there is a serious quantitative disagreement, namely:

— all models predict too low ion energy transport in the region $\rho \gtrsim 0.7$ ($\rho \leq 1$ is a normalised radius) even when fully developed turbulence is taken into account.

— all models predict a large χ_i in the central and intermediate plasma region. Hence one expects T_i to be determined by $\eta_i = n_i \nabla T_i / T_i \nabla n_i$ close to the instability threshold η_i^{cr}. Thus to reconcile theory with JET results a substantial increase of η_i^{cr} is required (Fig. 3).

An extensive campaign of simulations using predictive transport codes has allowed the assessment of heat transport models [15]. Ohmic and L-mode discharges have been considered, covering the following range of parameters: I ≈ 3-5MA, average electron density $\bar{n}_e \approx 1.5\text{-}7.10^{19} m^{-3}$, $B_T \approx$ 2.2-3.4T, auxiliary power (ICRH, NBI or combined) up to 25MW. These computations show that among the theory-based models adapted empirically to simulate experimental results, the R-L-W model emerges as rather good and complete; it covers electron and

ion heat and particle transport (see also Section 3). These results confirm previous findings, carried out on a more restricted set of discharges which also included the H-mode regime [9], [16].

We recall that the R-L-W model predicts the existence of a critical electron temperature gradient ∇T_e^{cr} such that the electron heat flow is given by:

$$q_e = -n_e \chi_e^{RLW} \nabla T_e \left(1 - \left| \frac{\nabla T_e^{cr}}{\nabla T_e} \right| \right) \tag{1}$$

when $|\nabla T_e| > |\nabla T_e^{cr}|$. The expressions for ∇T_e^{cr} and χ_e^{RLW} can be found in ref. [1]. Transport is assumed to be neoclassical when $|\nabla T_e| < |\nabla T_e^{cr}|$ or $\nabla q < 0$, q being the safety factor. Moreover:

$$\chi_i \propto \frac{Z_i}{\sqrt{1+Z_{eff}}} \sqrt{\frac{T_e}{T_i}} \chi_e^b, \qquad D_e \propto \chi_e^b, \qquad \chi_e^b = \chi_e^{RL} \left(1 - \left| \frac{\nabla T_e^{cr}}{\nabla T_e} \right| \right). \tag{2}$$

D_e is the electron diffusion coefficient, Z_i and Z_{eff} the ion charge and the plasma effective charge.

If, in an interpretive analysis, the ∇T_e^{cr} term in Eq. (1) is not taken into account explicitly, the resulting χ_e must be compared to χ_e^b. On the other hand χ_e^{RLW} applies to the analysis of heat pulse propagation (see Section 4). It should be noted that no critical ion temperature gradient is predicted for ion energy transport, consistent with the results shown in Figs 1 and 2. Similarly no inward particle pinch is predicted for a pure plasma.

The main deficiencies with the R-L-W model have been found in the outer region of the plasma, especially at low density, where $|\nabla T_e^{cr}|$ tends to exceed the observed $|\nabla T_e|$. It is expected that the model, based on a single phenomenon [1], has to be modified here. Atomic physics processes may affect the model [17] and phenomena related to MHD instabilities might be important. An empirical solution to this problem, adopted in the predictive $1^1/_2$-D code JETTO, is to reduce the anomalous transport gradually when $|\nabla T_e|$ approaches and becomes smaller than $|\nabla T_e^{cr}|$. We also remark that a quantitative validation of the R-L-W model in the central region of the plasma is subject to large uncertainties owing to the dependence of χ_e^{RLW} on the local shear and the practical difficulty of measuring ∇q in this region. A similar remark applies to other models and in particular to η_i related transport coefficients which depend sensitively on the local shear length.

3. Simulation of the Plasma Density Evolution

JETTO code simulations have been used to study simultaneously the evolution of density and temperature profiles in the ohmic and L-mode plasmas described in Section 2. The following expression (based on the R-L-W model) have been used for the flux of the hydrogenic species:

$$\Gamma_i = -D\nabla n_i + n_i(v_{an} + v_w)$$

$$D = \alpha\chi_e^b, \quad v_{an} = -\alpha_{in} \frac{2Dr}{a^2}. \tag{3}$$

v_w and v_{an} are the neoclassical (Ware) [18] and anomalous inward pinch velocities; α and α_{in} are constants to be determined; a is the minor radius.

The impurity ion density profiles needed to compute the electron density n_e are not modelled but evaluated from Z_{eff} (from visible bremsstrahlung or charge exchange recombination spectroscopy) and the concentrations of the most relevant impurities (from UV spectroscopy). It is assumed that the impurity ions are fully ionised and this is valid for most of the plasma, when dominated by relatively low Z impurities ($Z \lesssim 8$).

We find that the time scale of the evolution of n_e requires $\alpha \approx 0.3$-0.5. There are cases, in particular with RF heating alone and $Z_{eff} \gtrsim 2.5$, where an anomalous inward term seems to be required in the region $\rho \gtrsim 0.3$-0.4, and $v_{an}/v_{ware} \gtrsim 10$. Figure 4a illustrates such a case. Various regimes however, do not need an anomalous inward velocity, as first pointed out in [19] for discharges with pellet injection. Other cases are found in ohmic low Z_{eff} discharges and with NBI heated discharges where a high density is reached, developing a flat or even hollow density profile. An example, corresponding to a relatively clean plasma ($Z_{eff} \lesssim 1.5$) is illustrated in fig. 4b, where for comparison we also show the peaked profile of n_e that would be obtained with the same inward pinch as in the previous case.

4. Analysis of Heat and Density Pulse Propagation Measurements

The analysis of fast transients provides a method for determining a linearised matrix of transport coefficients from measured data and complements interpretive and predictive studies. Recent work at JET has been based on an analysis of the heat and density pulses following sawtooth crashes which takes into account the coupling between heat and particle transport [20]. The main result of the analysis is the determination of the 2 x 2 diffusion matrix in a system of linearised diffusion/convection equations simulating the propagation of the perturbations. Figure 5 shows the measured and simulated temperature and density perturbations evolving at various radii in a typical case. Values of the linearised particle and thermal diffusion coefficients D^P and χ_e^P with $D^P/\chi_e^P \lesssim 0.1$ are derived in the outer plasma region $\rho \gtrsim 0.65$ from this kind of analysis. These values are consistent with the values of D and χ_e^{RLW} found in the simulation of the same pulse (fig. 6). In fact a linearisation of such a model shows that D and χ_e^{RLW} are dominant diagonal terms and can be compared to D^P and χ_e^P.

The pulse propagation analysis shows that there is a linear coupling between particle inward pinch and negative temperature gradient. The sign and magnitude of the coupling are correlated to the initial density decrease (see fig. 5b at r/a = 0.69) coinciding with the location of the maximum temperature perturbation. Such a term is not found linearising the R-L-W model for a pure plasma. It is possible that it is due to an anomalous inward flux of impurities

proportional to ∇T_e, related to a thermoelectric force in the direction parallel to the magnetic field. This has not been considered in the model so far.

5. Transport of Impurities

The study of impurity transport has largely been based on the calculated evolution of impurity density profiles in prescribed experimental plasma profiles. Computed and experimental emissivities from individual lines [21,22] and soft X-ray profiles [23] and radiation profiles are compared. The conventional approach assumes the impurity flux Γ_I to be given by:

$$\Gamma_I = -D_I \nabla n_I + n_I v_I$$
$$v_I = -\alpha_I D_I r / a^2. \qquad (4)$$

where n_I is the impurity density. The diffusion coefficient D_I and the convective velocity v_I are to be determined from the simulations and are assumed to be the same for all ionisation states.

In many cases the simple approach with D_I and α_I radially constant, fails. For example impurity transport appears to be reduced to a level close to neoclassical in the central region of "good confinement" in pellet fuelled discharges [21] and also in the central region of ohmic and RF heated discharges [23].

The simple approach (4) with constant coefficients also fails for the analysis of H-mode discharges: a rather low diffusion coefficient $D_I \approx 0.1 m^2/s$, and a spatial variation of v_I which depends on the plasma temperature and density profiles [22] is needed. Figure 7 shows the empirically determined spatial profile of v_I during the H-phase of a high density pulse ($\bar{n}_e \gtrsim 7 \times 10^{19} m^{-3}$, developing a hollow profile, $Z_{eff} \approx 2$, decreasing with time, I_p = 3.1MA, B_T = 2.2T, P_{NBI} = 8MW). Before density steady state, in a phase lasting 3.5 seconds, the velocity v_I has to be outward in the region $\rho \lesssim .8$ in order to explain the nickel emissivity lines and radiated power; the empirical convective velocity v_I is consistent, within the large uncertainties of the analysis, with neoclassical theory [24]. This situation is reminiscent of the absence of an anomalous inward pinch term in the modelling of the electron density evolution in L-mode plasmas as shown in fig. 4b.

6. Conclusions

The analysis carried out at JET shows that no pure theoretical model is sufficiently correct or complete enough to explain all features exhibited by the wide variety of plasma regimes found in JET. We underline the problems associated with a quantitative assessment of such models using the theory of instabilities driven by ∇T_i as an example. Time dependent simulations of a variety of phenomena evolving on different time scales indicate a correlation between energy and particle transport. In particular, we find that D/χ_e as normally defined in interpretive codes is larger than D^P/χ_e^P from pulse propagation analysis. We also find that neoclassical theory may be relevant for impurity transport under various circumstances. These results are generally

impurity transport under various circumstances. These results are generally consistent with the picture of the energy and particle transport assumed by the critical electron temperature model of Rebut et al. [1]. This model, which has been successfully tested in a variety of JET plasma conditions, is a good candidate for predicting tokamak plasma performance.

Acknowledgements

We are indebted to the entire JET team and in particular to the diagnostics and data management groups for providing the basic data for this study.

References

[1] REBUT, P.H. et al., Plasma Physics and Controlled Nuclear Fusion Research, 1988, (Proc. 12th Int. Conf., Nice 1988) 2, 191.
[2] CORDEY, J.G. et al. IAEA - CN-53/F-3-19, these Proceedings.
[3] REBUT, P.H. and the JET Team, IAEA - CN-53/A-1-2, these Proceedings.
[4] LOMAS, P.J. et al., IAEA - CN-53/A-6-2, these Proceedings.
[5] TANGA, A. and the JET Team, IAEA - CN-53/A-4-1, these Proceedings.
[6] WATKINS, M.L. et al., Plasma Physics and Controlled Fusion 31, 1713 (1989).
[7] BALET, B. et al., Proc. of 17th EPS Conference on Controlled Fusion and Plasma Heating, Amsterdam 1990, 1, 162.
[8] TIBONE, F. et al., as Ref. [7], 2, 805.
[9] TARONI, A. et al., as Ref. [5], 1, 367.
[10] DÜCHS, D.F. et al., Plasma Physics and Controlled Nuclear Fusion Research, 1986 (Proc. 11th Int. Conf., Kyoto 1986) 1, 325.
[11] LEE, G.S. and DIAMOND, P.H., Physics of Fluids 29, 3291 (1986).
[12] ROMANELLI, F., Physics of Fluids B 1, 1018 (1989).
[13] MATTOR, N., Culham Laboratory Report CLM-P872(1990).
[14] SCHMIDT, G.L. et al., as Ref. [5], 1, 215.
[15] SACK, C.. et.al., as Ref. [7], 2, 801.
[16] WATKINS, M.L. et al., Proc. of 15th EPS Conference on Controlled Fusion and Plasma Heating, Dubrovnik, 1988, 1, 247.
[17] REBUT, P.H. and HUGON, M., Plasma Physics and Controlled Nuclear Fusion Research 1984 (Proc. 10th Int. Conf., London 1984) 2, 197.
[18] HIRSHMAN, S.P. and SIGMAR, D.J., Physics of Fluids, 20, 418 (1977).
[19] BAYLOR, L.R. et al. Bull. Am. Phys. Soc. 34 (9), 2057 (1989) and JET Report JET-P(90)01.
[20] HOGEWEIJ, G.M.D., as Ref. [6], 1, 158.
[21] BEHRINGER, K. et al., IAEA-TEC DOC-534, 167, IAEA, Vienna (1989).
[22] LAURO-TARONI, L. et al., as Ref. [6], 1, 247.
[23] PASINI, D. et al., JET Report JET-P(90)01, acccepted for publication in Nuclear Fusion.
[24] FUSSMANN, G. et al., Journal of Nuclear Materials 162-164, 14 (1989).

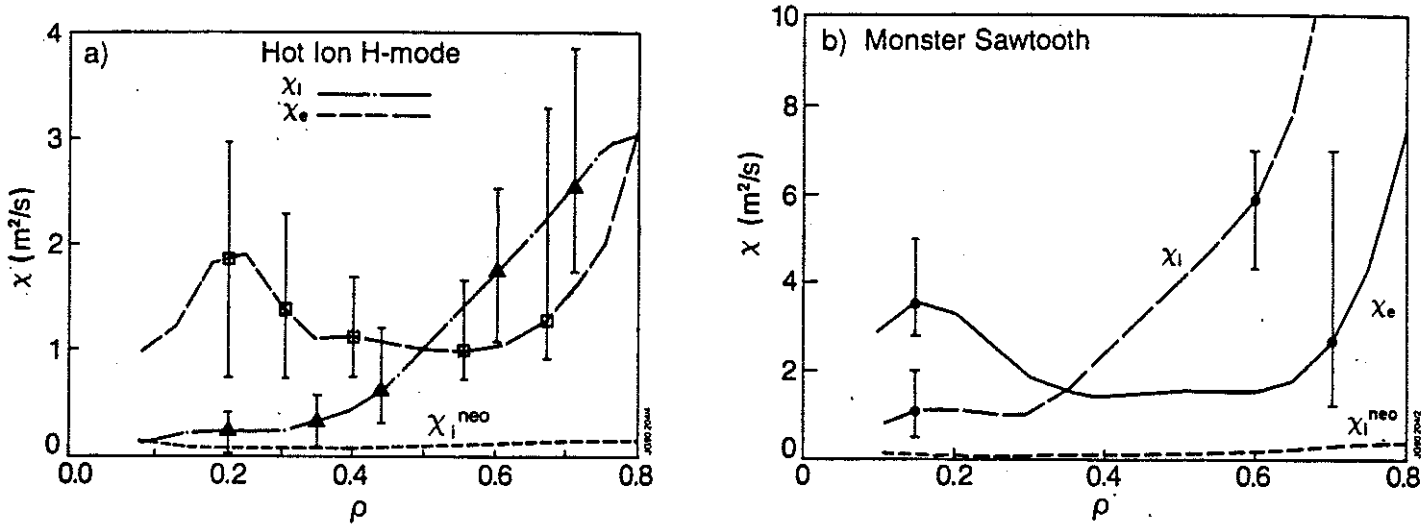

Fig. 1 Radial dependence of χ_e and χ_i for a hot ion H-mode (case a, pulse 20981) and a RF heated non-sawtoothing discharge (case b, pulse 19739).

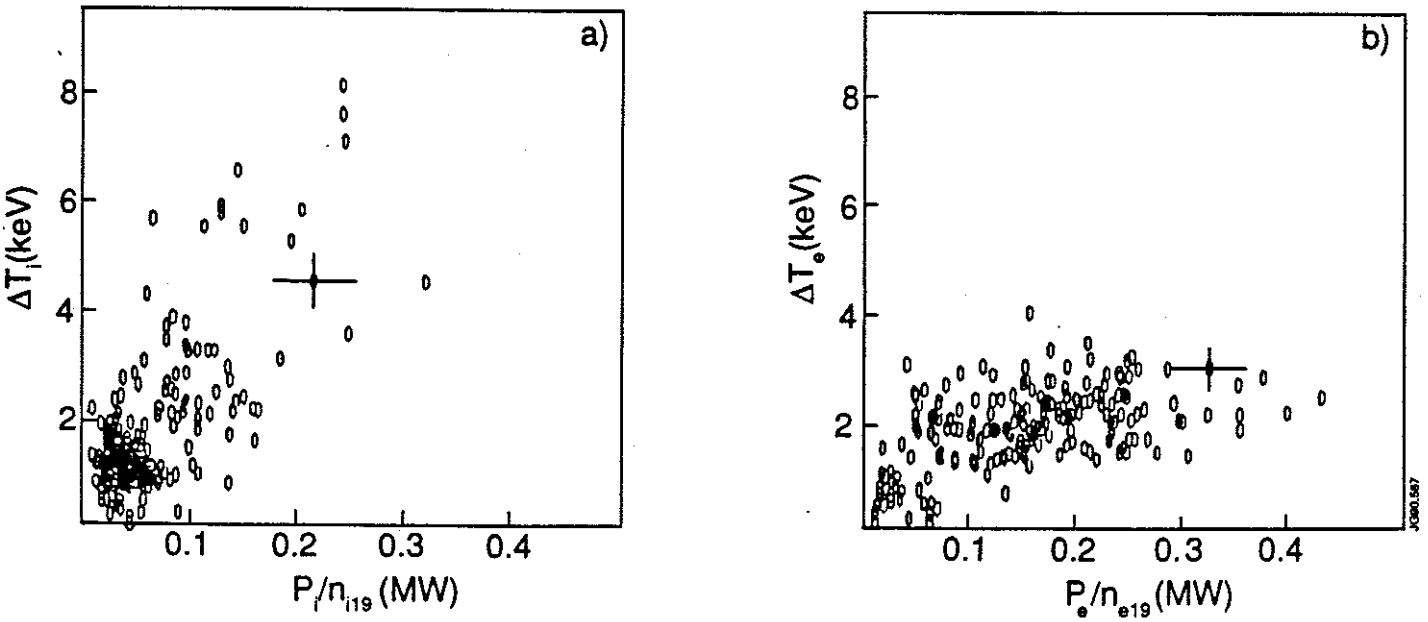

Fig. 2 Increase of the ion (case a) and electron temperature (case b) as a function of P/n; ΔT, P and n refer to $\rho < 1/3$. Sawtooth-free L and H-mode plasmas with $2 \lesssim P_{tot} \lesssim 25$MW, $1 \leq n_e \leq 5\times10^{19}$m^{-3} and various combinations of ICRF and NBI are considered.

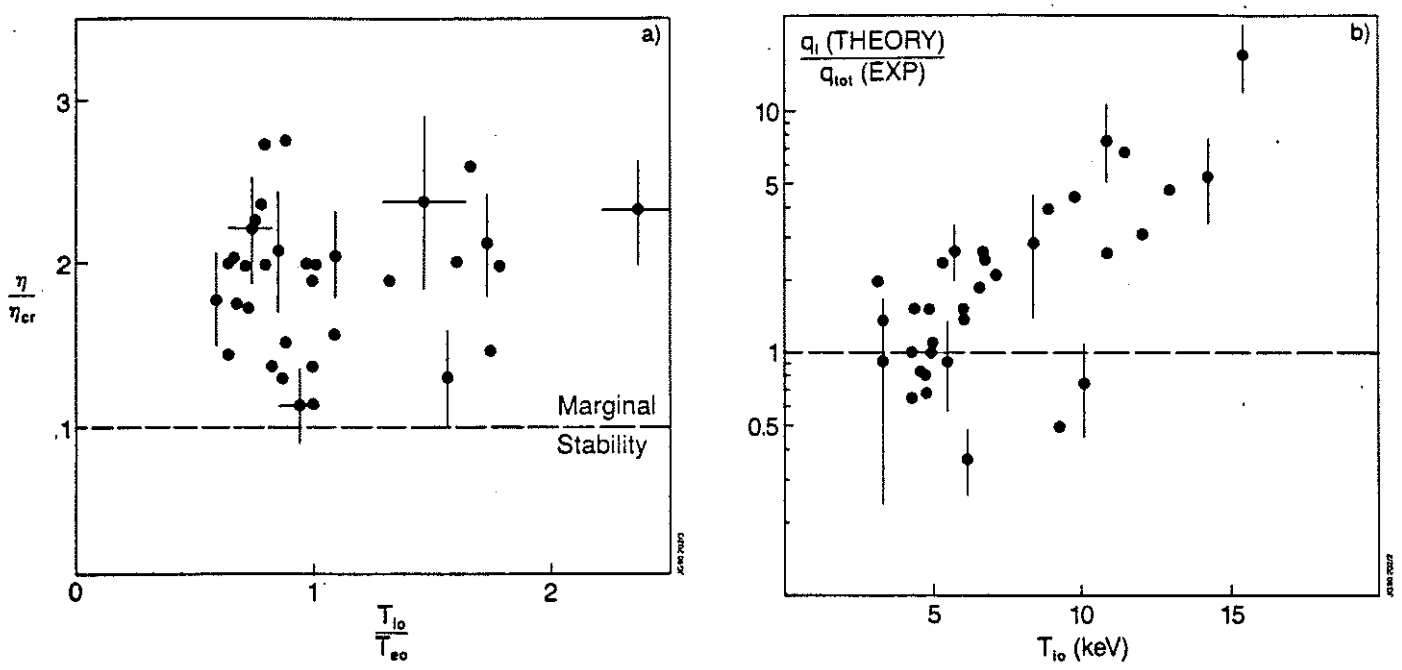

Fig. 3 JET data (referring to sawtooth-free, L-mode, 3MA pulses) compared with the predictions of one of the published versions of η_i-mode theory [13]: a) ratio of the measured $\eta \equiv L_{n_e}/L_{T_i}$ to the theoryetical threshold value as a function of T_{io}/T_{eo}; b) ratio of the predicted ion heat flux to the total measured heat flux at ρ = 0.4, as a function of peak ion temperature.

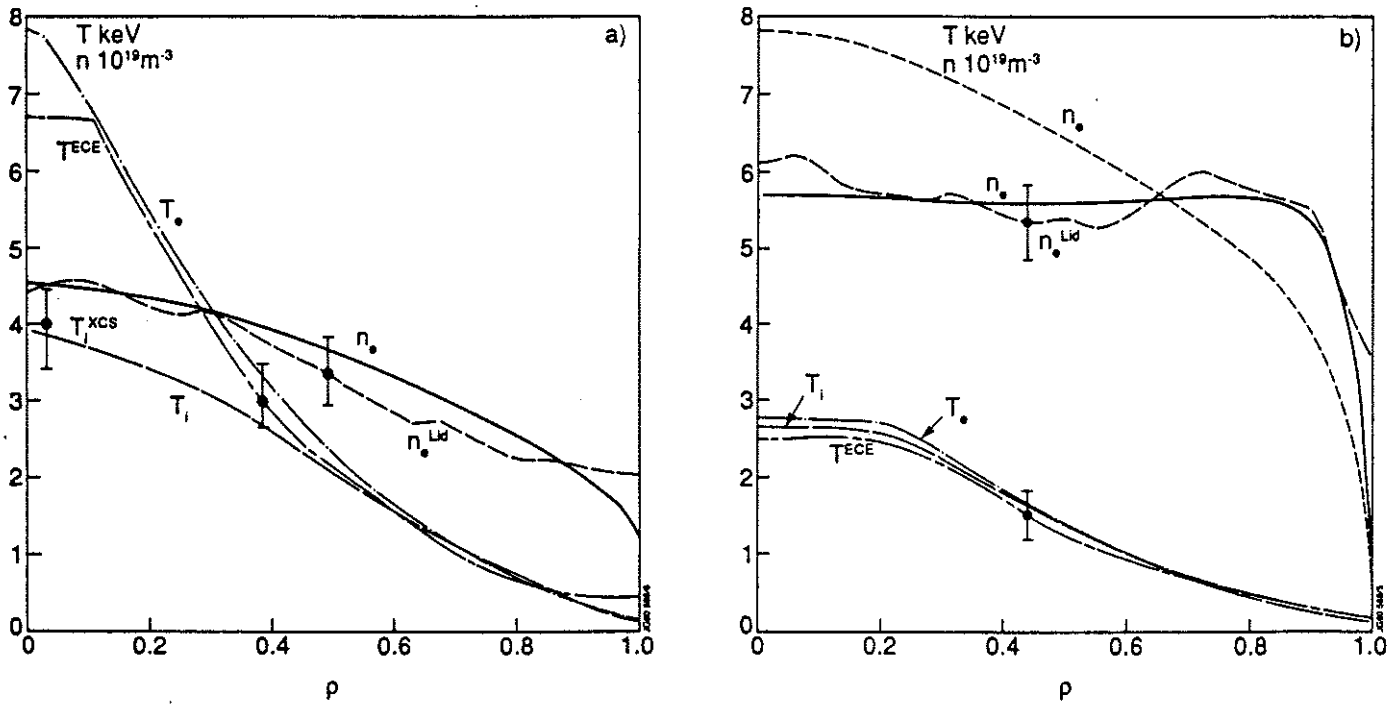

Fig. 4 Comparison of computed and experimental T_e and n_e profiles for a sawtoothing RF discharge (case a, pulse 19617, B_T = 3.1T, I = 3MA, P_{RF} = 8MW) and a sawtoothing NBI discharge (case b, pulse 20334, B_T = 3.1T, I = 3MA, P_{NBI} = 8MW). In case b, the peaked density profile was computed with the same v_{an} as in case a, the flat one was computed with v_{an} = 0.

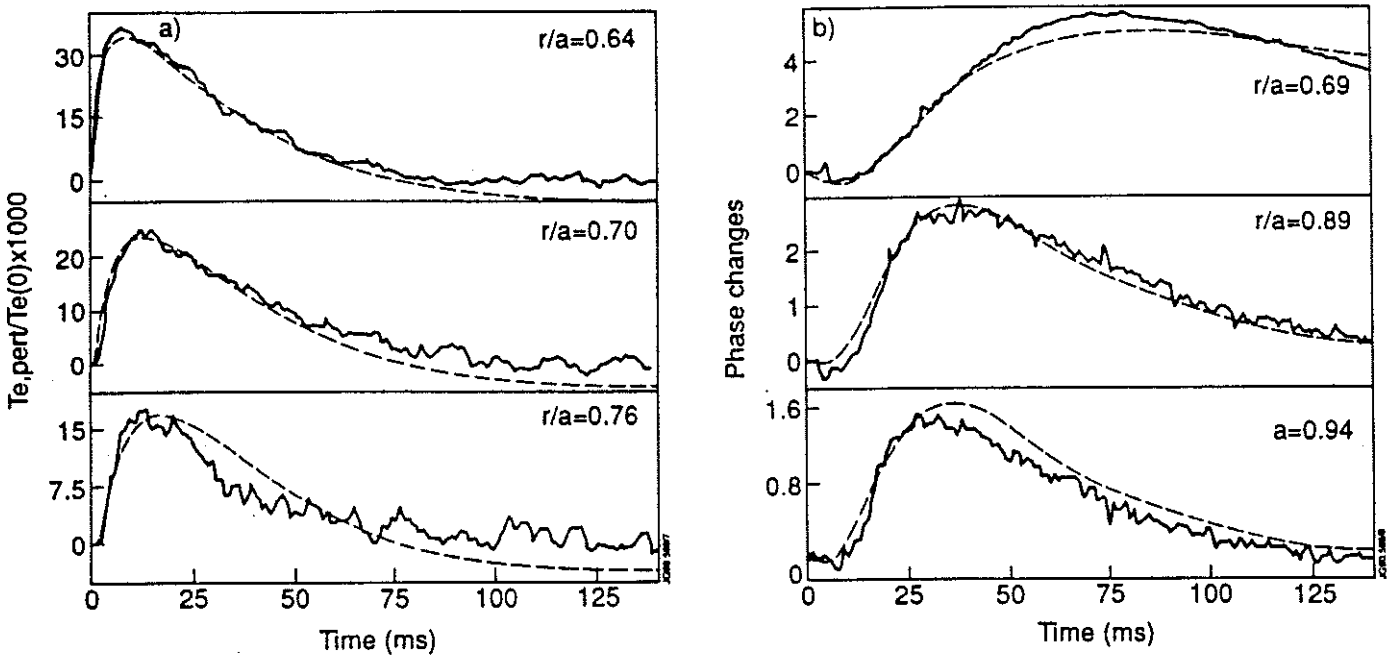

Fig. 5 Measurements and simulations of the propagating perturbation of T_e (case a) and n_e (case b); ΔT_e is normalised to the central temperature before the sawtooth crash, Δn_e is given by the phase changes of the reflectometer. Pulse 19617 is considered, as in fig. 4a.

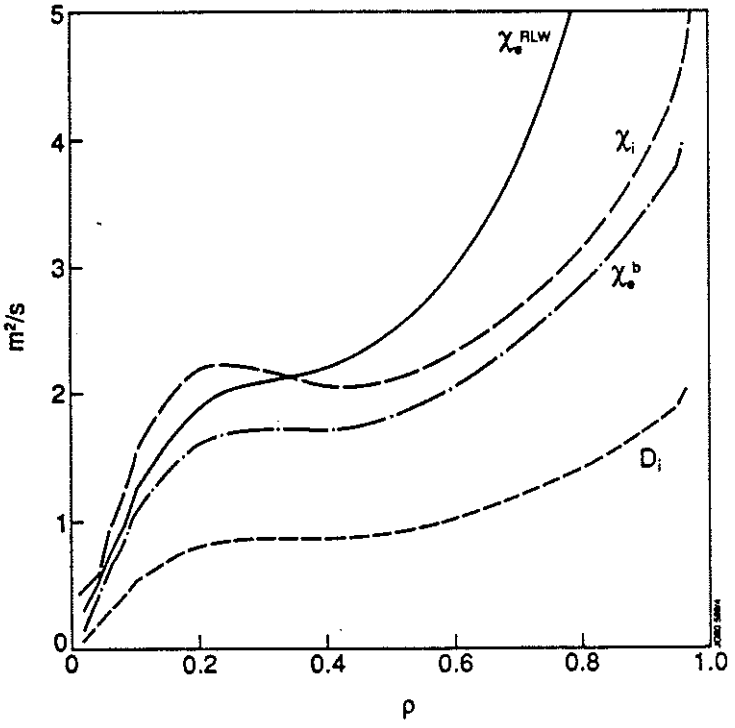

Fig. 6 Radial variation of χ_e^{RL}, χ_e^b, χ_i and D_i obtained from the simulation of pulse 19617 (see figs. 4a and 5).

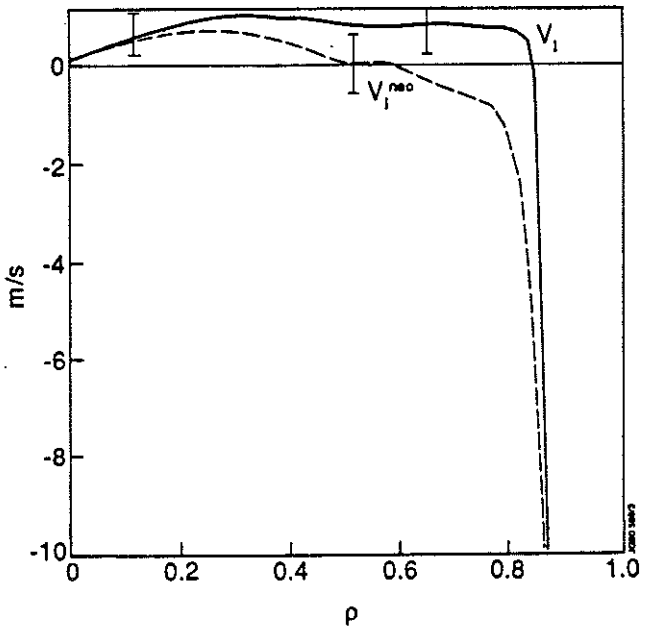

Fig. 7 Radial dependence of the empirical and neoclassical v_I found by simulating the impurity behaviour in an H-mode with a hollow density profile (pulse 21022).

High Density Regimes and Beta Limits in JET

by

The JET Team*
(presented by P Smeulders)

JET Joint Undertaking, Abingdon,
Oxon, OX14 3EA,UK.

* See : P-H.Rebut et al, 13th Int.Conf. on Plasma Physics and Contr. Nucl. Fusion Research, Washington (1990), to be published in Nuclear Fusion Supplement. Including the following: J.P.Goedbloed and G.Huysmans: FOM-Instituut voor Plasma Fysica, Nieuwegein, NL; and T.C Hender and O.J.Kwon,: UKAEA/ EURATOM Fusion Association, Culham Laboratory, UK.

High Density Regimes and Beta Limits in JET

Abstract

Results are first presented on the density limit in JET discharges with graphite (C), Be gettered graphite and Be limiters. There is a clear improvement in the case of Be limiters. The Be gettered phase showed no increase in the gas fuelled density limit, except with Ion Cyclotron Resonance Heating (ICRH), but, the limit changed character. During MARFE-formation, any further increase in density was prevented, leading to a soft density limit. The soft density limit was a function of input power and impurity content with a weak dependence on q. Helium and pellet fuelled discharges exceeded the gas-fuelled global density limits, but essentially had the same edge limit. In the second part, results are presented of high β operation in low-B Double-Null (DN) X-point configurations with Be-gettered carbon target plates. The Troyon limit was reached during H-mode discharges and toroidal β values of 5.5% were obtained. At high beta, the sawteeth were modified and characterised by very rapid heat-waves and fishbone-like pre- and post-cursors with strongly ballooning character.

1. OPERATION NEAR THE DENSITY LIMIT

Operation near the density limit has been systematically studied in JET for limiter discharges, with C limiters, with evaporated Be layers and with Be limiters [1]. The operating density in tokamaks is usually presented in the form given in Fig.1. Each point represents the maximum obtained normalised density during a discharge with either Ohmic (OH), Neutral Beam (NBI), ICRH or combined heating. The broken lines marked by OH (C) and NBI(C) are the highest limits obtained in the previous campaigns with C walls and limiters [2] ($nRq_c/B_t = 12$ for OH and $20\times10^{19}m^{-2}T^{-1}$ with NBI). There are clear improvements due to the Be limiters and Be coated walls. After conditioning of the Be limiter, which led to a strong reduction of Cl, the limit was substantially extended beyond that with Be gettering, so that $nRq_c/B_t \approx 33$ was reached with combined heating, ICRH and NBI heating. Furthermore the limiting density increases with the applied power as we shall see shortly. Pellet fuelled and He discharges have exceeded the deuterium gas fuelled limits. There is strong evidence that the edge density determines the limit. The limit at low q (q~2), however, is unchanged and is still set by major current disruptions.

There has not yet been such a systematic study for X-point discharges, but the behaviour is similar, with somewhat lower density limits. The highest densities so far in X-point discharges are obtained in H-modes with $nRq_c/B_t \approx 20\times10^{19}m^{-2}T^{-1}$. At higher densities, typically when $P_{rad}/P_t \approx 60\%$, an H to L- mode transition occurs and the density falls without causing a disruption. In limiter discharges the nature of the limit is different for C and Be limiters. With C, the limit is marked by an asymmetrical edge radiation (MARFE) that leads to a symmetric radiative collapse and ends in a hard disruption. With Be limiters the limit is generally marked by the appearance of a MARFE which, in gas fuelled discharges, is accompanied by a fall in recycling and reduction in density. This typically leads to a soft density limit with a relaxation oscillation of density, radiation and MARFE near the limit. The internal inductance of the plasma during the MARFE generally did not increase, indicating that the plasma was not contracting significantly, as in the pure C limiter during the radiation collapse. This is consistent with the absence of strong MHD fluctuations and disruptions in the Be-gettered and limiter plasmas.

The line-averaged density could be substantially increased with pellet fuelling, providing the pellets penetrated deeply. The limit for both pellet and gas fuelled discharges can be unified by considering the edge density and the input power (Fig. 2). The dependence of the density limit on the total power P_t and in particular on the radiation power balance in the edge region of the discharge has been suggested in a number of papers [2-5]. These models suggest that the limit should increase approximately as $P_t^{1/2}$. The MARFE limit for pellet and gas fuelled discharges does lie at the boundary of the existence region.

2. CONCLUSIONS: DENSITY LIMIT

Operation near the density limit in JET can be summarised as follows :

- The density limit for additionally heated discharges in JET is now independent of the heating method and exceeds $nRq_c/B_t = 33 \times 10^{19} m^{-2} T^{-1}$ for Be limiters and $20 \times 10^{19} m^{-2} T^{-1}$ for the H-mode;
- The density limit has a different MARFE behaviour for Be limiters compared with C limiters and leads to a density pump-out returning the discharge to a stable operation region;
- The density limit in gas and pellet fuelled discharges increases with input power approximately as $P_t^{1/2}$ and is determined by edge parameters, particularly the edge density;
- The high limit obtained in JET means that acceptable densities should be reached in next step devices provided that sufficient degree of impurity exclusion can be obtained.

3. BETA LIMITS

High β operation has been achieved at low toroidal fields ($B < 1.2$ T) where the Troyon limit [6] is reached with additional heating at power levels ~10MW below that at which carbon self-sputtering becomes important [7]. It has not yet been possible to surpass the Troyon limit as has been done in DIII-D [8].

Fig.3 shows the maximum toroidal β_φ as a function of q_c^{-1} obtained for all discharges between 1986 and 1989. A steady state β_φ of 5.5% has been reached for DN H-modes in a hydrogen plasma. In these discharges with Be coated walls, β saturation is generally observed without disruptions. The saturation is related to MHD-modes, ELM's and n=1 activity. Sawtooth and fishbone events occur and sometimes continuous n=1, 2, or 3 modes appear, which can lead to a β decline. A peaked and roughly triangular p(r) profile develops from an initially broad profile. The internal inductance decreases from ~ 1 to 0.7, which indicates a broadening of j(r) towards those profiles used in the β-optimisation by Troyon [6]. The decrease of the inductance is calculated to be due to the bootstrap current, which is approximately 25% of the total current.

4. BETA SATURATION

The evolution of β for the discharge with the highest β obtained so far is shown in Fig.4. Also shown is the MHD activity, central ion temperature and volume-averaged density as a function of time. The main β-limiting mechanism in this discharge is the high-β sawtooth. Increased MHD (n=1 and n=3) activity (around t=15 s) leads to a diminished rate of rise in β after the crash and to a decline in the central ion temperature and so contributes to the β saturation.

The high-β sawteeth differ from those at low β in two ways :

1. The associated heat pulse is very rapid with τ_{HP}~100μs instead of ~10 ms.
2. Dominant (1,1), (2,1) and higher m pre- and postcursors are seen, similar to high-

β fishbones but of twice the amplitude. The modes have a ballooning character near the outer edge with a ratio in amplitude from the low to high B-side of ~10 as seen by the X-rays. Similar to a normal sawtooth, a high-β sawtooth causes a flattening of the pressure profile within the q=1 radius.

5. HEAT LOSSES

Like other H-mode discharges in JET the high-β discharge has a confinement time twice that of the Goldston L-mode [9]. The observed plasma energy W_{DIA} lies close to the energy W_G calculated from the effective power input and $\tau_E = 2 \times \tau_G$ [10]. The fraction of the losses due to high β sawteeth is 10 to 15% and that due to the intermittently appearing MHD-modes 20 to 30% of the total energy losses. This is sufficient to prevent further β increase since the heating power P is close to the critical power required to reach the Troyon limit. The fishbones and especially the sawtooth events strongly affect the fast particle distribution as measured by the neutron emission with consequences for future α-particle heating.

The central neutron emission drops by 70 % (Fig.5) and its total rate by 30 % during a sawtooth [11]. Fishbones are observed which individually cause up to 10% drop in the global neutron emission. However they occur about 10 times more frequently than sawteeth and may contribute appreciably to the central loss of fast particles and energy. Relatively large heat losses (150 kW) have also been measured by the neutral particle analyser with losses that are proportional to the MHD mode amplitude. Measurements with a multi-channel O-mode reflectometer indicate that high frequency density fluctuations grow exponentially with β_N. The measurements are carried out between 3.9 and 4.1 m with frequencies ~130 kHz well above the n=1 MHD modes present; perhaps, indicating high-n ballooning-mode activity.

6. BETA COLLAPSE

In a few JET cases, high β collapses occur triggered or preceded by large n=2 (or sometimes n=1 or 3) MHD activity with δB~15 G at the edge, and differ from β-saturation in various ways [7]:

- a dominant (3,2) and other coupled n=2 modes are responsible as seen from SXR analysis,
- there is a drop in the electron density in contrast to the saturation due to the high β-sawteeth,
- the central ion temperature and the fast ions are not affected at first.

7. PLASMA STABILITY

The stability of the high-β discharges has been examined with various stability codes : ERATO [12], HBT [13], BALLOON [14] and FAR code [15]. These stability studies are discussed more fully in [16]. It is found that before a high-β sawtooth the central plasma over more than half its radius is close to or even above the marginal ideal ballooning stability threshold. The ideal n=1 internal kink is also found to be strongly unstable for $\beta_N \approx 1$ when $q_0 \leq 1$. This instability may be linked to the observed (1,1) instabilities which seem to cause the β-saturation. We have calculated the fast particle effects on the internal kink. It is found that at the β values reached, the fast particles can no longer stabilise the internal kink. The operation is outside the Porcelli-Pegoraro stable region in the $(\gamma_{MHD}, \omega_{*i}, \beta_{ph})$ space with experimental values of (1.0, 0.5, 1.5) [17]. In addition, severe fishbone activity is expected in this regime, resulting from the coupling with high energetic beam ions above 40 keV. It is further found that in the cases where the β-collapse occurs internal modes of either n=2 or n=1 structure, appear to be responsible for the enhanced plasma losses. These modes have been simulated

by the FAR code where the q-profile has been tuned to match the measured X-ray fluctuations over the plasma cross-section [16]. In the case where n=1 modes are dominant, the q-profile had to be relatively flat in the centre with $q(0) \approx 1.1$, supported by Faraday-rotation measurements.

8. CONCLUSIONS: BETA LIMIT

In low q discharges at high β, saturation of the plasma energy is observed without disruptions. Global n=1 modes in the form of high-β sawteeth and fishbones are generally responsible for this saturation. Occasionally, β-collapses occur which seem to be related to large n=2 (some- times n=1 or 3) MHD modes. Triangular temperature profiles exist at the limit, which together with the rather flat density profiles lead to constant ∇p across the plasma. Such peaked pressure profiles are favourable for a fusion reactor. Both the fishbones and sawteeth strongly affect the fast particle distribution. This has important consequences for future α-particle heating, burn control and wall loading. The role of the ballooning limit in the inner part of the plasma is not yet clear. Generally good agreement between theoretically predicted internal modes and observations at the beta limit, has been obtained. The role of the fast particles on the beta limit needs further study both theoretically and experimentally. Further experiments in JET are required to see if the beta limit remains a soft limit even at much higher input powers.

9. REFERENCES

[1] C.Lowry et al, Proc.17th Eur.Conf.on Contr.Fusion & Plasma Phys., Amsterdam (1990)

[2] J.Wesson et al. Nuclear Fusion **29**, 641 (1989)

[3] D.Campbell et al, Proc. 11th Int.Conf. on Plasma Physics and Contr. Nucl. Fusion Research, Kyoto, Nuclear Fusion Supp. (1987)

[4] A.Gibson, Nuclear Fusion,**16** (1976) 546.

[5] P-H.Rebut amd B.Green, Proc. 6th Int.Conf. on Plasma Physics and Contr.Nucl. Fusion Research, Berchtesgaden, Nuclear Fusion Supp. 1977

[6] F.Troyon, R.Gruber et al, Plasma Phys.& Contr. Fusion **26**(1984)209

[7] P.Smeulders et al, Proc.17th Eur.Conf.on Contr.Fusion & Plasma Phys., Amsterdam (1990)

[8] J.Ferron et al, Proc.17th Eur.Conf.on Contr.Fusion & Plasma Phys., Amsterdam (1990)

[9] R.Goldston, Proc.11th Eur.Conf.on Contr.Fusion & Plasma Phys., Aachen (1984)

[10] A.Gibson et al, Proc. 17th Eur.Conf.on Contr.Fusion & Plasma Phys., Amsterdam (1990), to be published in Plasma Phys. & Contr.Nucl.Fusion.

[11] F.Marcus et al, Proc.17th Eur.Conf.on Contr.Fusion & Plasma Phys., Amsterdam (1990)

[12] R.Gruber et al, Computer Phys. Commun. **21** (1981) 323

[13] J.P.Goedbloed,G.M.D.Hogewey et al, Proc.10th Int.Conf. on Plasma Phys.and Contr. Fusion, London 1984, IAEA (1985)165

[14] D.P.O'Brien, C.M.Bishop et al, Proc. 16th Eur. Conf. on Contr.Fusion and Plasma Phys., Venice (1989)

[15] L.A.Charlton et al, Journal Comp. Phys. **86**, 270 (1990)

[16] T.C.Hender et al, Proc.17th Eur. Conf. on Contr. Fusion & Plasma Phys., Amsterdam (1990)

[17] F.Porcelli et al, Proc.17th Eur.Conf.on Contr.Fusion & Plasma Phys., Amsterdam (1990)

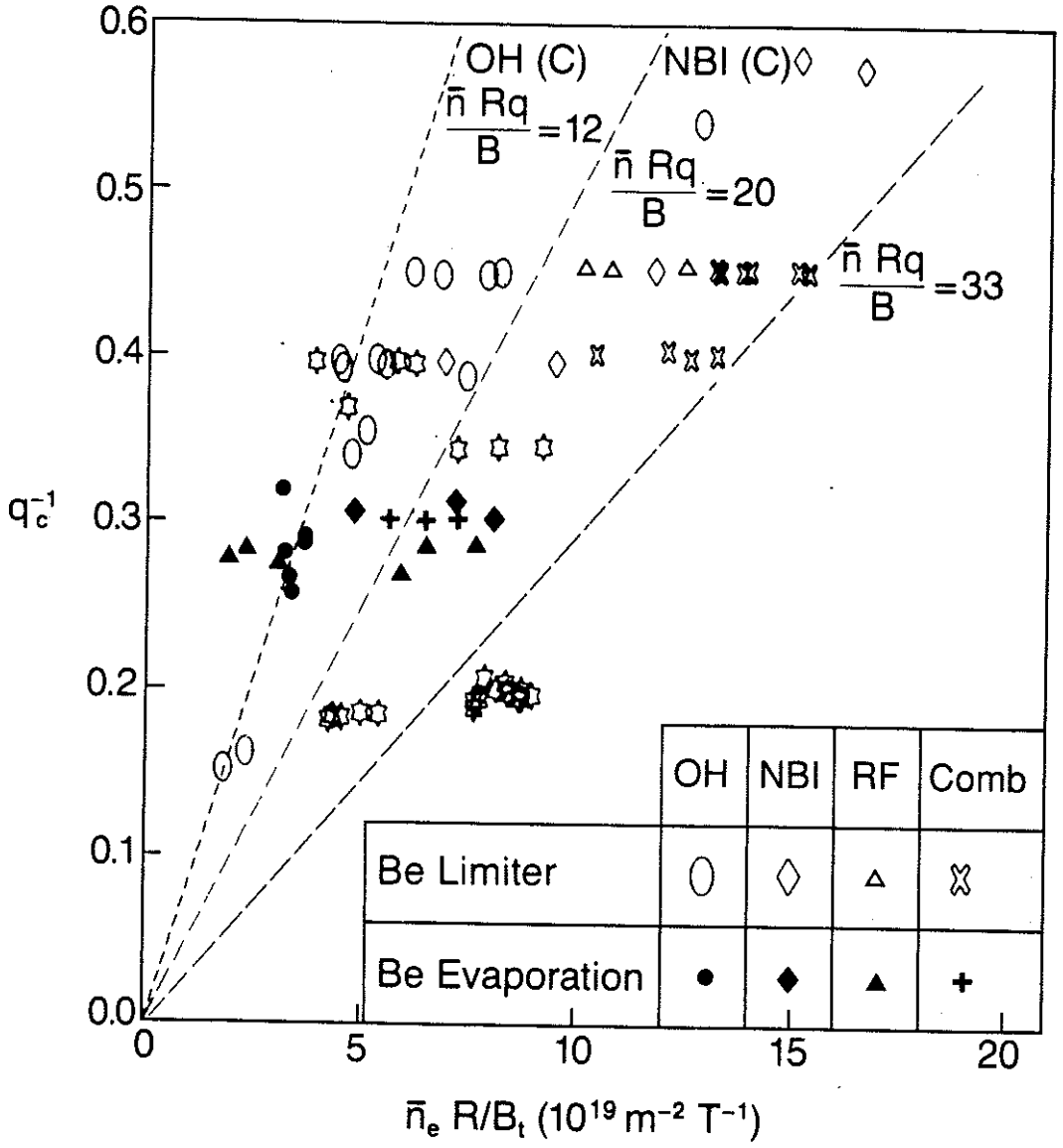

Fig.1 The operating density range for JET shown as normalised current $q_c^{-1} = \pi RI_p/5AB_\varphi$ [m,MA,m^2,T] versus normalised density n_eR/B [10^{19}m^{-3},m,T]. Comparison is made between carbon disruptions (two broken lines at left) and MARFES with Be evaporation (solid symbols) and Be limiter (open symbols)

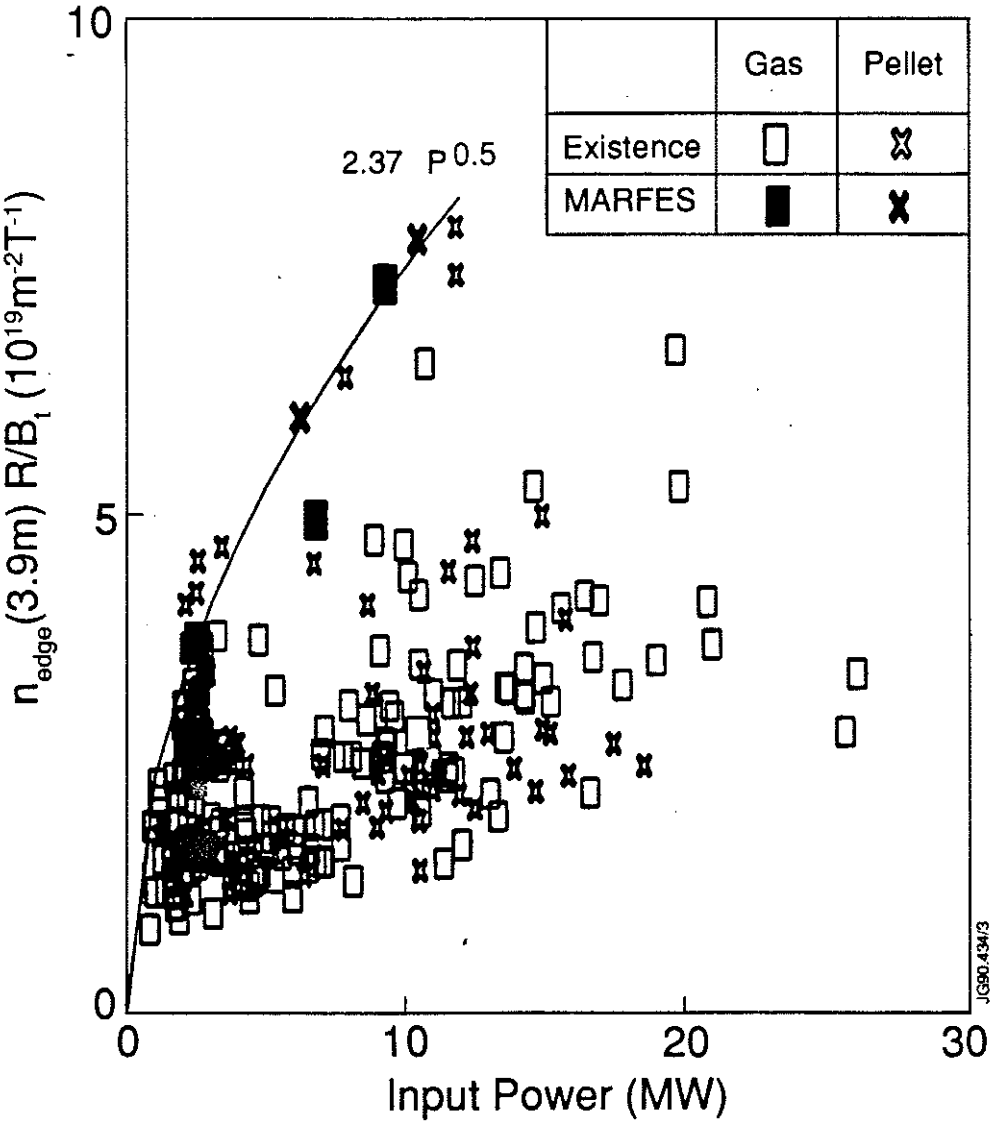

Fig.2. The normalised edge density versus input power showing that the MARFE density limit occurs at the boundary of the existence region close to the curve $n_{edge}R/B_\varphi = 2.37\ P_t^{1/2}$ [$10^{19}m^{-3}$, m, T, MW]. B_φ varies in the range 1.4 to 2.6 T.

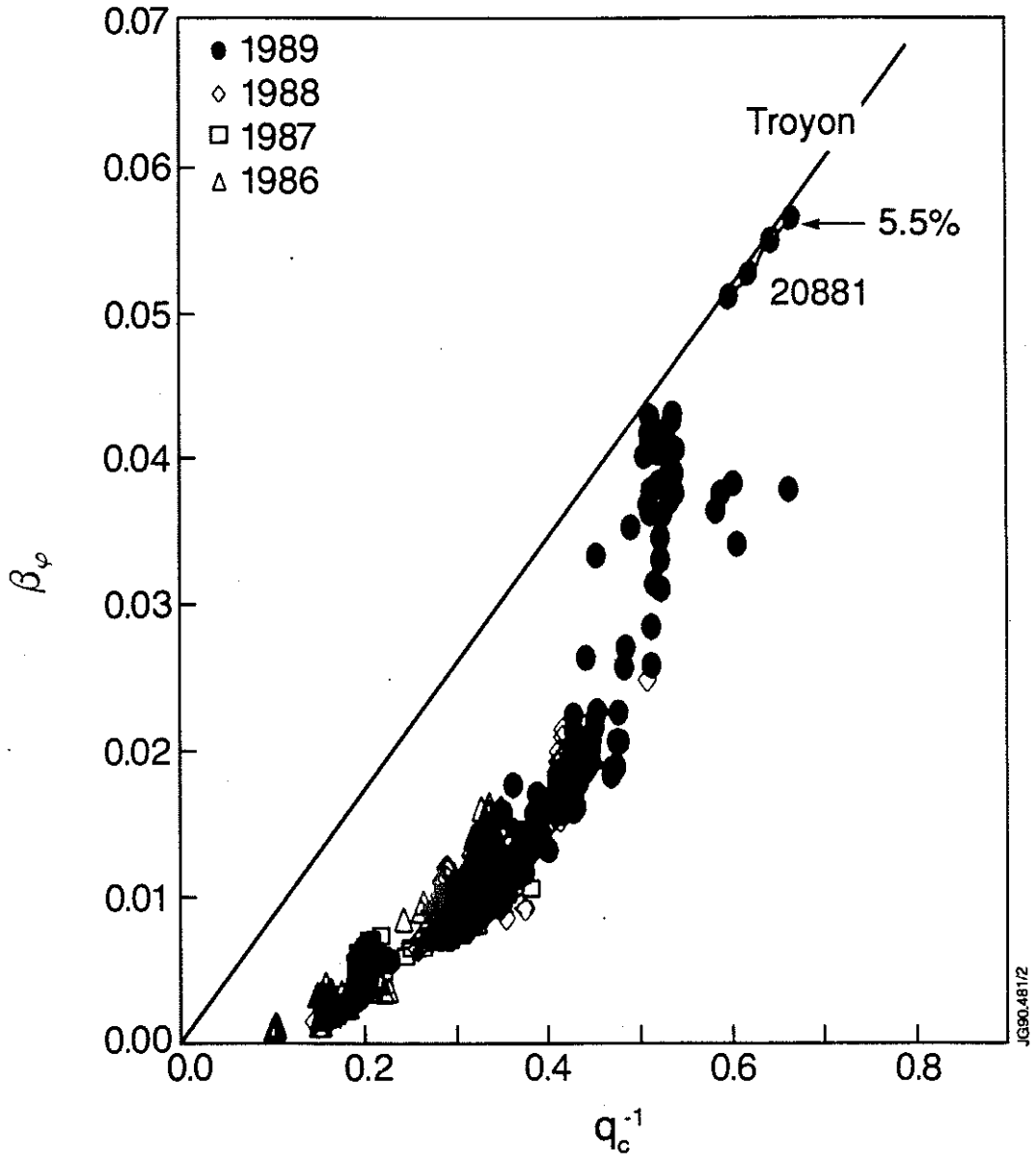

Fig.3. The maximum toroidal beta ($\beta_\varphi = 2\mu_0 \langle p \rangle / B_\varphi^2$) as a function of q_c^{-1} (proportional to normalised current $I_p/B_\varphi a$[MA,T,m]), for all JET discharges with the poloidal beta $\beta_\theta > 0.4$. The line is the Troyon limit $\beta_{Troyon} = 0.028\ I_p/B_\varphi a$ [MA,T,m]. The highest β is 5.5%.

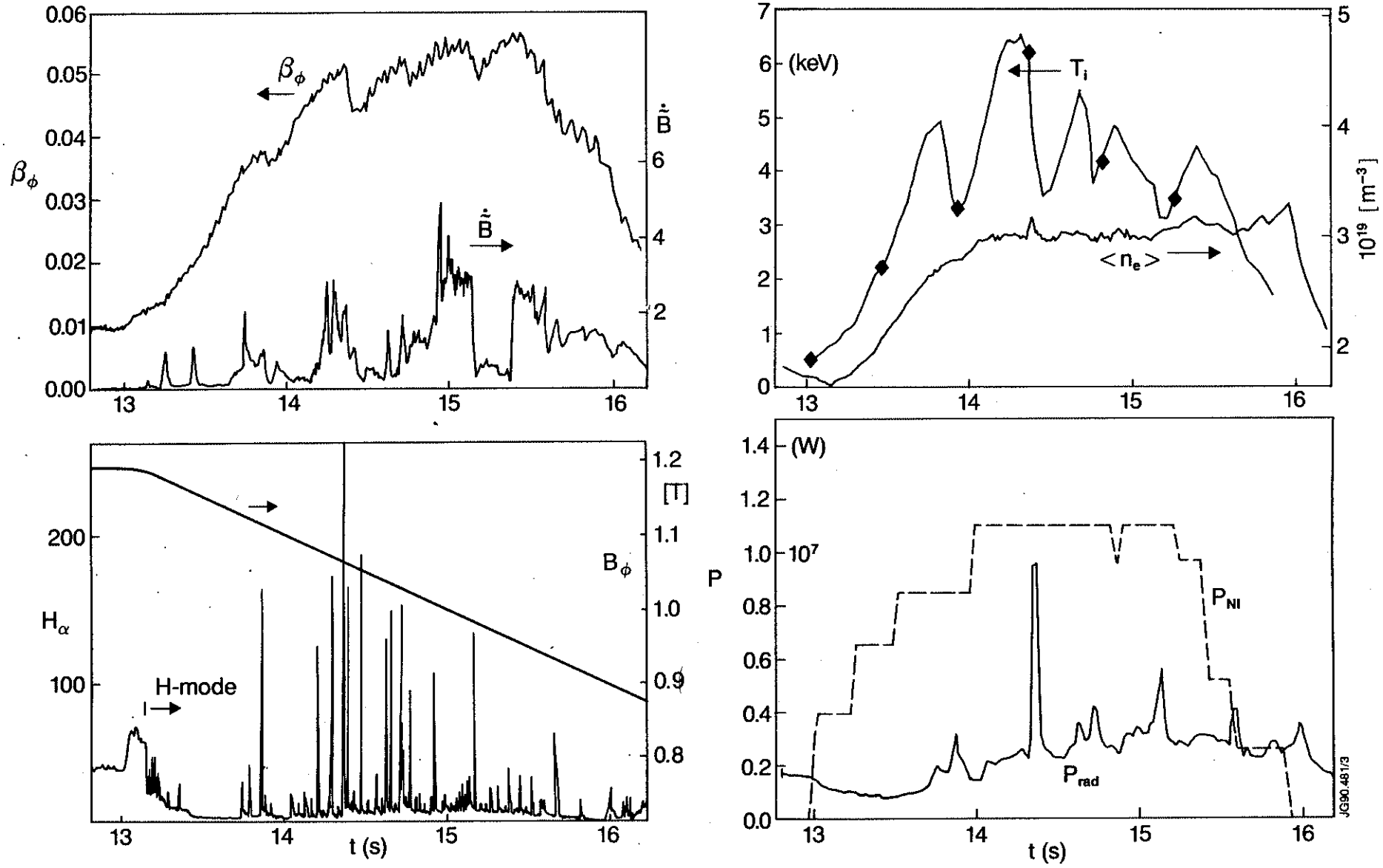

Fig.4. Evolution of β_φ, MHD-mode amplitude $\tilde{B}_\varphi$ (top-left); H_α and magnetic field B_φ (bottom-left); ion temperature T_i, volume average density $<n>$ (top-right); and injected power P_{NI}, radiated power P_{rad} for the 5.5 % β discharge, a 2MA Double-Null H-mode at 0.9T with 11MW 80 kV D-injection into a H plasma. $T_e(0)$ and $T_i(0)$ of 3.5 and 6 keV were obtained in these low q discharges ($q_{95} \approx 2.2$ or $q_c \approx 1.6$) and κ of 1.8. Z_{eff} slowly increases in time from 1.3 and levels off at ~2.5. The confinement time $\tau_E = 0.35$ s.

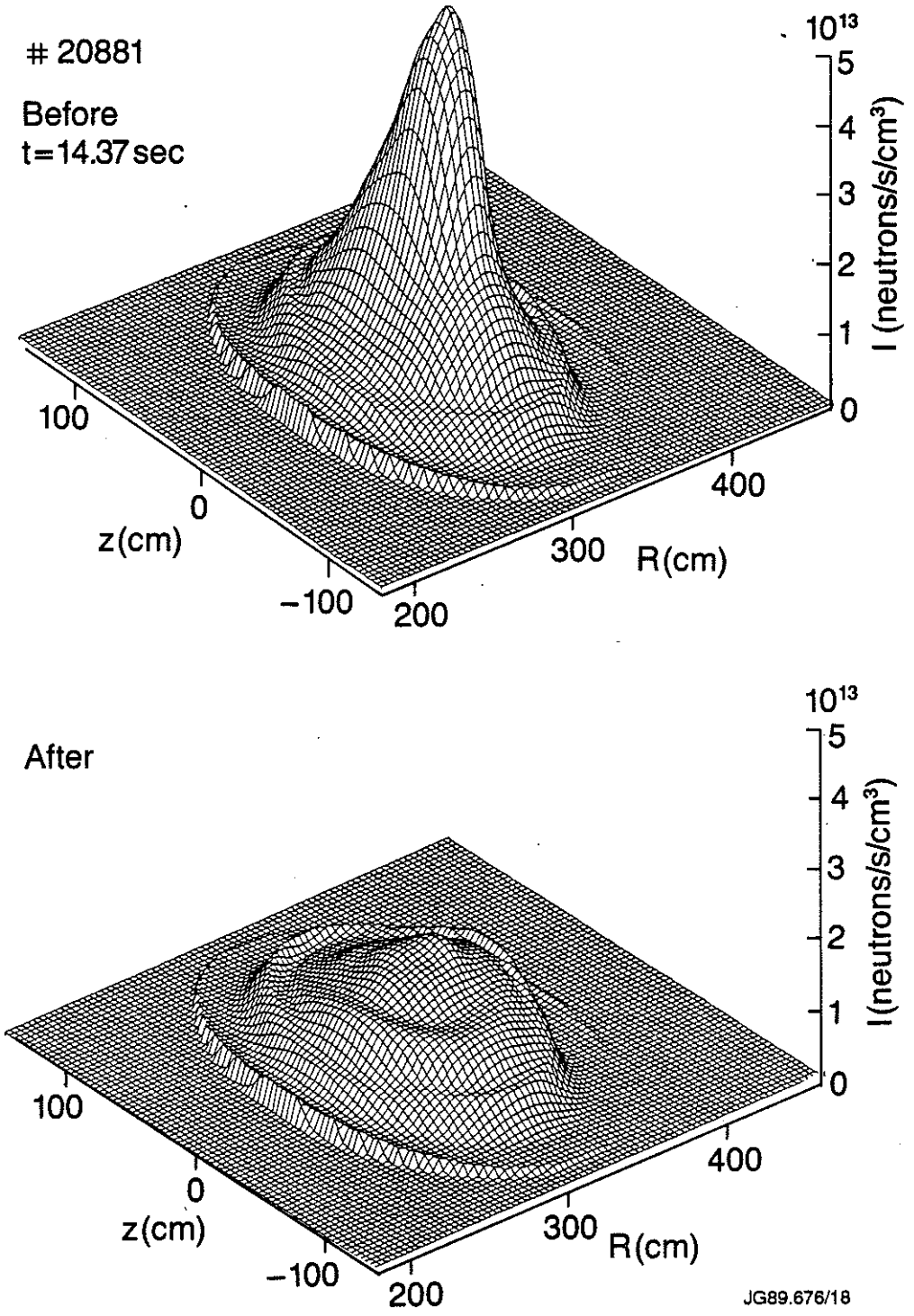

Fig.5. Cross-sections of the plasma neutron emissivity before and after a beta crash. The central emission drops by 70%. The integration time is 100ms.

IAEA-CN-53/A-5-1

Modelling Impurity Control by Plasma Flows in the JET Pumped Divertor

by

M Keilhacker, E Deksnis, P Harbour, PH Rebut, R Simonini
A Taroni, GC Vlases and ML Watkins

JET Joint Undertaking, Abingdon,
Oxon, OX14 3EA, UK

Modelling Impurity Control by Plasma Flows in the JET Pumped Divertor

M. Keilhacker, E. Deksnis, P. Harbour, P. H. Rebut, R. Simonini, A. Taroni, G.C. Vlases, M.L. Watkins

Abstract

A pumped divertor is planned for the extension phase of JET (1993 - 96) in order to control impurities during long pulse, high power operation. Target-produced impurities tend to migrate along the field lines, out of the divertor, due to temperature gradient forces. This is opposed by the friction forces arising from the streaming of hydrogen into the divertor. This problem is studied using both analytic and numerical methods. For the highest power anticipated, impurities will be trapped by "natural divertor recycling" only at high scrape-off layer (SOL) densities approaching $10^{20}m^{-3}$. At lower densities, a forced flow or "external recirculation" must be induced, e.g. by shallow pellet injection or gas puffing, to insure impurity retention. Steady state then requires removal of an equal amount of neutral flow from the divertor, which imposes fairly severe pumping requirements. Less flow is needed, for a given SOL density, as the ion power flow is reduced.

I. Introduction

The aim of the planned extension of JET (1993 - 1996) is to demonstrate effective methods of impurity control in operating conditions relevant to a Next Step Tokamak. The central task of this phase will be to investigate impurity control in a new divertor configuration, the primary functions of which are to remove the principal source of impurities as far from the main plasma as possible, and to retain the impurities produced at the divertor target plates. The production of impurities will be minimized by reducing the divertor plasma temperature as far as possible, and by proper selection of target plate materials. Retention of the impurities in the divertor region will be enhanced by inducing a strong flow of deuterium towards the target plates.

The general features of the proposed divertor are illustrated in Fig. 1. It is of the "open" type, with Beryllium-clad, water-cooled (Hypervapotron) copper target plates. The in-vessel four-coil system allows both for horizontal sweeping of the plasma along the target to spread the heat load, and for vertical motion of the X-point to vary the connection length and plasma volume. The possible divertor configurations span the range from a "slim" 6 MA plasma (total divertor coil current of 1.8 MA) with a connection length in the divertor region, corresponding to a field line 1 cm away from the separatrix in the equatorial plane, of about 6.7 m, to a "fat" 6 MA plasma (divertor current of 0.74 MA) with a connection length 3.5 m.

Impurities produced at the target plates are subject to several forces, the most important of which, in steady state, are the ion thermal force, directed away from the target plates, the deuterium-impurity friction force towards the target, and the impurity pressure gradient force which arises to establish a force balance. The ion thermal force is determined principally by the ion heat flow in the scrape-off layer (SOL), while the counter-acting friction force depends on the magnitude and spatial distribution along the field (coordinate s) of the deuterium particle flux, $\Gamma(s)$, and is inversely proportional to the ion temperature to the 3/2 power. Thus the friction force can in principle be set at a level sufficient to overcome the thermal force. From global balance considerations of the SOL and the divertor channel plasma (DCP), the magnitude of the flux at the divertor target plate, Γ_t, is determined by the mid-plane SOL plasma density and the power flow in the SOL. The form of $\Gamma(s)$, denoted $\hat{\Gamma}(s) \equiv \Gamma(s)/\Gamma_t$, is controlled by the hydrogen particle source distribution in the SOL and the DCP as sketched in Fig. 2. In the "local recycling" zone, which extends approximately one effective ionization length normal to the target, $\hat{\Gamma}(s)$ increases rapidly going towards the plate, due to ionization of neutrals emanating from the target plates. Some of the neutrals, however, are not locally recycled, but escape and then may re-enter the DCP further up the flux tube via reflection from the side walls, or transmission across the private flux region. We refer to this as "distant recycling". It extends the region of significant hydrogen flux further from the target plates, thus enhancing the effectiveness of the friction force term. Case a of Fig. 2 corresponds to purely local recycling at the target plates, while Case b corresponds to roughly half of the target plate flux being

uniformly "distantly recycled" between the local recycling zone and the X-point. The relative amount and distribution of the distantly recycled particles depend both on divertor plasma conditions and on divertor geometry.

It is also possible, in principle, to extract some of the incident neutralized ion flux from the targets and directly "recirculate" it, e.g. by baffles, into the X-point region, as was suggested in Ref. [1]. This would produce a $\hat{\Gamma}(s)$ distribution as shown in Case c, Fig. 2. Finally it may be necessary in some cases, for impurity retention, to induce a moderate $\hat{\Gamma}(s)$ in the SOL, in excess of the natural flow from the main plasma, by strong gas puffing or shallow pellet injection. This imposed flow, which we term "external recirculation", would require pumping of an equivalent neutral flux from the divertor chamber to maintain a steady state. The resulting flux distribution is shown as Case d.

The purpose of this paper is to determine the conditions under which the recycling (local plus distant) is sufficient to retain target-produced impurities in the divertor, and to calculate the amount of additional "recirculation" flow required when the "natural" flow is insufficient. We begin (Section 2) with a simple analytic model which elucidates the most important physical processes. This is followed by a discussion of the full 1-1/2 code and its results (Sect. 3). Conclusions are drawn in Section 4.

II. Impurity Retention Overview

Impurity retention in the divertor may be estimated by examining the magnitude of the different forces on the impurity ions as given by the steady state momentum equation

$$m_z n_z v_z \frac{dv_z}{ds} = -\frac{dp_z}{ds} + n_z ZeE + \frac{m_z n_z (v_i - v_z)}{\tau_{zi}} + n_z \alpha_z \frac{dT_e}{ds} + n_z \beta_z \frac{dT_i}{ds}. \quad (1)$$

Here we have considered a single impurity species of charge state Z, mass m_z, density n_z, temperature T_z, pressure p_z, and flow speed v_z. The simplification to a single charge state is well justified, because the most important forces acting on the impurity all scale approximately as Z^2, and thus their ratio is independent of Z. The subscripts e and i refer to the electrons and the hydrogenic ions, and

τ_{zi} is the hydrogenic ion-impurity collision time. The forces on the right hand side of Eq. (1) are due to the impurity pressure gradient, where $p_z = n_z T_z$, the electric field E, the frictional force, and the thermal forces with coefficients α_z for electrons and β_z for ions.

This equation, along with the other appropriate conservation equations, are solved in detail using a 1-1/2 code, as discussed in Section 3. To gain insight into those results, however, we begin with a simplified analytic description of the impurity distribution, as deduced from Eq. (1) in the trace approximation, where the hydrogenic flow is specified *a priori*, and is not affected by the impurities.

The electric field may be eliminated from Eq. (1) by using the electron momentum equation and taking the electron pressure to be nearly constant along s. In addition, we take $\frac{dv_z}{ds} = 0$ and $T_z \cong T_i$, so that Eq. (1) becomes.

$$\frac{T_i}{n_z}\frac{dn_z}{ds} = \frac{m_z(v_i - v_z)}{\tau_{zi}} + (\alpha_z - 0.71\,Z)\frac{dT_e}{ds} + (\beta_z - 1)\frac{dT_i}{ds} \qquad (2)$$

with $\alpha_z = 0.71Z^2$, and $\beta_z = 1.76Z^2$ for the case of Beryllium with Z = 3 [2].

For most cases of interest $\nabla T_e \ll \nabla T_i$, since they are both determined by classical heat conduction and $\kappa_{\|e} \gg \kappa_{\|i}$, so that we can neglect the ∇T_e term in Eq (2). In addition, we take $v_z = f_v v_i$ as a further simplification, where $f_v = 0$ everywhere except in a thin impurity ionization zone near the target. Integrating the resulting equation gives

$$\frac{n_z(s)}{n_z(o)} = \exp\left\{-\int_o^s F_{fi}\,ds + \int_o^s F_{Ti}\,ds\right\} \qquad (3)$$

with $$F_{fi}(s) = C_f \cdot Z^2 \frac{\Gamma(s)}{T_i(s)^{5/2}} \quad m^{-1}, \qquad (4)$$

and $$F_{Ti}(s) = (\beta_z - 1)\frac{1}{T_i}\frac{dT_i}{ds} \quad m^{-1}. \qquad (5)$$

Note that F_{fi} and F_{Ti} are inverse local scale lengths associated with the friction and thermal forces, respectively. Here and in the

following, the units are MKS, except for T_i, which is expressed in eV. The value of C_f is then 1.2×10^{-20}.

For a large enough deuterium flux, Γ, the impurity density decreases going towards the X-point until the point where $\Gamma(s)$, determined by the distribution of recirculated neutrals, becomes small enough that $F_{fi} < F_{Ti}$. Beyond that point, $n_z(s)$ begins to increase. Fig. 2b shows qualitatively the behaviour of the solution for the four source distributions of Fig. 2a. If we adopt the criterion that $n_z(L)/n_z(0)$ be less than a certain value, say e^{-3}, the criterion for retention of impurities becomes

$$\int_o^L F_{fi}(s)ds \geq \int_o^L F_{Ti}(s)ds + 3. \tag{6}$$

In order to carry out the integrals, the hydrogenic ion temperature and particle flux distributions along s must be specified. The latter is postulated, and then checked by a Monte-Carlo calculation, as described in section 3. The temperature is governed by both conduction and convection, and is given, to close approximation, by

$$T_i(s)^{7/2} = \frac{7}{2}\left(\frac{q_{eff}}{K_{o,i}}\right)s + T_{di}^{7/2} \tag{7}$$

where $q_{eff} \cong .6\ q_i$, the ion heat flow per unit area, for values of recirculated Γ near the minimum required to entrench the impurities [3], T_{di} is the divertor ion temperature, and $K_{o,i}$ is a constant.

Combining equations (4), (5), and (7), shows that the ratio of the ion friction and thermo-electric terms scales approximately as

$$\frac{F_{fi}(s)}{F_{Ti}(s)} \sim \Gamma(s)\cdot(s+s_o)^{2/7}, \tag{8}$$

$$\text{where } s_o = \frac{2}{7}\left(\frac{K_{o,i}}{q_{eff}}\right)T_{di}^{7/2}.$$

Consider the case $\Gamma(s)$ ~ constant over some interval,for example Case c of Fig. 2. Because of the relatively weak variation of F_{fi}/F_{Ti} with s, it can be shifted from less than one to greater than one over most of the interval by a small change in Γ. Thus, one can go from a case of very poor impurity retention to good retention with

small changes in Γ which extend over long distances, e.g. by distant recycling and/or external recirculation.

Incorporating equations (4), (5) and (7) into (6) yields, as the criterion for retention of impurities,

$$\frac{C_f(1-f_v)Z^2\Gamma_t}{\left(\frac{7}{2}\frac{q_{eff}}{K_{o,i}}\right)^{5/7}}\int_o^L \frac{\hat{\Gamma}(s)ds}{(s+s_o)^{5/7}} \geq \left(\frac{2}{7}\right)(\beta_z-1)\ln\left(\frac{L}{s_o}+1\right)+3. \qquad (9)$$

The target flux, Γ_t, is determined by specifying the mid-plane or, more generally, the stagnation point separatrix plasma density n_b, and the parallel heat fluxes, $q_{\|e}$ and $q_{\|i}$, using a model similar to that of Ref. [4]. For given power into the divertor and very high values of n_b, Γ_t is sufficiently high that local plus distant recycling alone is sufficient to satisfy relation (9) for the proposed divertor geometry. As n_b is decreased for a given power, Γ_t decreases and T_{di} increases, which tends to reduce the left hand side of relation (9). In order to retain impurities, $\hat{\Gamma}(s)$ must be "extended" further up the field line, either by (single point) recirculation, e.g. at the X-point (Case c), or by injection of particles uniformly into the SOL (Case d).

For X-point injection, the flux required for impurity retention is

$$\Gamma_x \geq \frac{\frac{2}{7}\left(\frac{7q_{eff}}{2K_{o,i}}\right)^{5/7}}{C_f Z^2} \frac{\left[\frac{2}{7}(\beta_z-1)\ln\left(1+\frac{L}{s_o}\right)+3\right]}{\left[(s_x+s_o)^{2/7}-s_o^{2/7}\right]}. \qquad (10)$$

The relation (10) assumes Γ_x is constant along s, and thus does not include the contribution of the local high recycling region, which is small for Γ_x non-negligible compared with Γ_t.

Relation (10) implies that the minimum required flux can be written

$$\Gamma_x \sim q_{eff}^{5/7} f(q_{eff}, T_{di}, s_x, L) \qquad (11)$$

where the variation of f with its arguments is small. For example, a change of q_{eff} by a factor of 10 changes f by only 5 %. Furthermore, a factor of 4 variation in T_{di} changes f by 20%, while doubling the distance to the injection point, s_x, from 4m to 8m reduces f by ~25%.

Thus, as the main result, this simple analysis predicts that for the case of single point recirculation at the X-point, the required Γ_x depends primarily on the ion heat flow and somewhat less strongly on the connection length. Γ_x scales as $P_i^{5/7} \cdot s_x^{-2/7}$ for $s_x^{2/7} >> s_o^{2/7}$.

We note that the electron temperature does not enter this analysis directly, since the dominant forces are associated with the ions. However, the electron temperature and density in the divertor are important in that they determine the fraction of neutrals that is distantly recycled, rather than locally, and thus they control the amount of "recirculation", which must be added to retain impurities.

The integrals in Eq. (3) can be evaluated for simple $\hat{\Gamma}(s)$ other than the step function form corresponding to relation (10), without changing the basic scaling appreciably. For example, for uniform injection into the DCP between s=0 and s_x, corresponding approximately to the expected distant recycling pattern at low SOL densities, the required flow is increased by 35% relative to X-point injection, while uniform injection into the SOL between s_x and L (external recirculation) reduces Γ_x by about 23%.

III. Code Calculations of Impurity Retention

a) The Model

To study the requirements for effective impurity control in more detail a 1-1/2D model (EDGE1D) of the plasma boundary in the proposed pumped divertor configuration has been developed. (For a detailed description of the model see Ref. [5].). The model is based on the plasma model of the JET 2D boundary code EDGE2D [6] and the impurity model of Ref. [7]. The latter is valid for arbitrarily high impurity concentrations.

Fluid equations for the conservation of particles, momentum and energy along the magnetic field are solved for electrons, hydrogenic ions and impurity ions. Transport coefficients, friction, thermal forces and electric fields (not necessarily ambipolar) are classical [8] and allow for arbitrarily high impurity concentrations [7]. In general, the full non-coronal distribution of impurity charge states and the corresponding radiated energy losses are determined. A single impurity temperature, set equal to the hydrogen

temperature, is assumed. The electron density is evaluated from quasi-neutrality.

For the boundary conditions at the target plates the Bohm condition is adopted, i.e. it is assumed that hydrogenic and impurity ions reach their sound speed at the plates. The heat fluxes at the plates are prescribed with the appropriate energy transmission coefficients for a two component plasma.

Transport transverse to the magnetic field is replaced by specified temperature and density profiles assumed to decay exponentially outwards from the separatrix with decay lengths, λ_T = 1.5 cm and λ_n = 1 cm, respectively. The width, $\delta = 3\,\lambda_T$, of the SOL plasma is chosen such that the residual fluxes are negligible.

A full 2-D Monte Carlo code (NIMBUS) [9] is retained for the sources of neutral particles. Deuterium particles are recycled at the target plates as neutrals. The Monte Carlo code defines the spatial distribution of the ionisation sources in the vicinity of the target plates. To enhance the plasma flow in the divertor region, some of the recycled neutrals are removed and recirculated into the scrape-off layer as plasma ions, with prescribed spatial distribution along the separatrix.

The Monte Carlo code defines also the spatial distribution of the impurity sources due to erosion at the target plates. Impurity atoms are generated by sputtering due to plasma ions and neutrals of any species. An effective sputtering coefficient is taken into account following Ref. [10]. However, it is also possible to normalise the source of impurities to their outgoing flux onto the target plates, thus implying a prescribed impurity content.

Work is currently in progress to implement a full 2-D version of the plasma flow, including impurities at arbitrary concentrations.

b) Numerical Results

As an example, we now discuss results of calculations based on the "slim" divertor configuration. Figure 3 shows the corresponding computational mesh and the most important input parameters. As a "reference" case we choose a total input power of 40 MW, corresponding to the maximum available power in JET. This power is shared equally between the ions and electrons ($P_e = P_i$) and is input uniformly along the separatrix into the SOL. The calculations are for beryllium impurities which are produced self-consistently by

sputtering from the target plates. The magnitude of the externally recirculated flux is varied parametrically and, in most cases, is injected uniformly along the separatrix from the main plasma into the SOL. For given n_b, P_i, P_e and external recirculation fraction f_R of the target flux, all other SOL and DCP parameters are determined.

Figure 4 shows calculated profiles of the deuterium and total impurity densities, the ion and electron temperatures, and the principal forces acting on the impurity ions as functions of the distance along the field line from the outside target for runs typical of poor (run 724) and good (run 712) impurity retention. It can be seen that for run 724, a large fraction of the impurities accumulate in the SOL adjacent to the main plasma. To quantify the degree of impurity retention we use the ratio of the number of beryllium ions retained in the two divertor regions to the total number in the SOL and DCP; we call this ratio $\eta(\%)$. The two cases displayed in Fig. 4 differ mainly in the level of external recirculation, and only slightly in the separatrix stagnation point density (n_b = 8.3 and 9.1 x $10^{19}m^{-3}$, respectively). For run 724 there was no external recirculation while for run 712 10% of the target flux was extracted and reinjected uniformly into the SOL. It can be seen that this relatively small external recirculation makes a major change in the retention, increasing η from 16% to 92%.

The second set of frames for Fig. 4 shows the electron and ion temperatures. In all our simulations the ion temperature in the SOL is higher than that of the electrons, mainly due to the lower ion thermal conductivity along field lines. The increased ion temperature near the stagnation point in run 724 arises from the high impurity density there, and the dependence of thermal conductivity on the effective charge state. The prediction that the ion temperature in the SOL should exceed the electron temperature is in agreement with experimental observations in JET [11]. Also the temperatures near the target plates are in the 10 - 20 eV range at higher edge densities and correspondingly larger hydrogen fluxes to the targets.

The third frame of Fig. 4 shows the force balance. For $f_R = 0$, the distribution of Γ, which arises from recycling alone, does not provide a large enough integrated friction force to retain the impurities, and they accumulate near the point of maximum temperature, with the impurity pressure gradient force balancing the

ion thermal force. For $f_R = 0.1$, the external recirculation extends the range of the friction force sufficiently to enable it to overcome the thermal force all the way to the SOL, and the impurities are effectively retained in the DCP. The fourth frame shows the distribution of fluxes, on an enlarged scale, for the two cases. It can be seen that the change in the level of the flux is small compared to the target fluxes (which are off scale, and correspond to 7.0 and 6.0 x $10^{24}m^{-2}s^{-1}$, respectively), but nevertheless the impurity distribution is completely altered.

Relation (9), which gives the criterion for impurity retention, can be satisfied in either of two ways. One can increase the target flux Γ_t to a large value, which occurs automatically at very high SOL densities. Alternatively, when operating at moderate SOL densities, and hence moderate target fluxes, the integral can be increased by extending the range of $\hat{\Gamma}$ by the combined effects of distant recycling and, when necessary, external recirculation. Figure 5 shows the distribution of flux for four different code runs, corresponding to different target fluxes and distributions. Each of these runs produced retention greater than 90%, achieved by different combinations of target flux and external recirculation, as indicated on the figure. Figure 5b displays the normalized flux, $\hat{\Gamma} = \Gamma(s)/\Gamma_t$, which shows its "extension", and hence the extension of the friction force, to larger values of s by the use of uniform external recirculation in the SOL. Figure 5a shows the non-normalized flux, $\Gamma(s)$, and indicates that the values of the actual local $\Gamma(s)$ over much of the divertor plasma (0 to 8m) are roughly similar, in agreement with the predictions of the analytic model.

Figure 6 summarizes the results of an extensive set of runs. Fig. 6a shows the fraction, f_R, of the target flux Γ_t which must be externally recirculated in order to retain 90% of the impurities in the DCP versus SOL density , n_b, for three values of the total (to both targets) ion heat flow, 20 MW, 10 MW and 5 MW. A simple SOL model (e.g. that of Ref. [4]) shows that $\Gamma_t \sim n_b^2$ for $T_d > 15$ ev. Thus, at high values of n_b, Γ_t is very large and the friction force integral arising from the natural recycling which occurs is sufficient to retain impurities. As the edge density is decreased, Γ_t decreases and an increasingly large flow fraction f_R must be externally recirculated. The required recirculated flow itself, however, becomes relatively independent of density for low and medium n_b (Fig. 6b), consistent

with Equs. (10) and (11). Under these conditions the required externally recirculated flow is fairly large and is probably not compatible with achievable steady state pumping rates.

The solid curves of Fig. 6 are results obtained by using a self-consistent beryllium sputtering model. In those simulations, the ratio of the total number of beryllium ions to deuterium ions in the edge plasma decreases from 1,5% at the lower densities to 0.1% at $n_b \cong 1 \times 10^{20} m^{-3}$. Since these values are somewhat lower than those which have been observed in JET experiments with beryllium to date, we have repeated the simulations with a fixed relative impurity content of 1.5% and the results are shown as dashed lines in Fig. 6a. In this case, the required fractions f_R are increased slightly.

The situation is somewhat improved for reduced power flows, as can be seen from the graphs in Fig. 6. Lower values of f_R are required for a given SOL density, n_b. This arises in part because the divertor density falls substantially. This increases the distant recycling in the divertor and reduces the flow which must be provided by external recirculation. This effect is illustrated in Fig. 7, which shows the fraction of neutrals, which emanate from the plate and are reionized in the DCP, as a function of computational mesh point (as shown in Fig. 3). For high power, most of the ionization occurs very near the target, whereas at lower power, the effective range of ionization extends much further along the DCP. The increased effective ionization range also increases the fraction of neutrals which are pumped by the cryopump.

Preliminary results from the code indicate that the flow requirements for the "fat" magnetic configuration are relatively unchanged from those of the "slim" magnetic configuration described above.

IV. Conclusions

The entrenchment of impurities in a forced flow of plasma towards the target plates is a candidate concept for impurity control in Next Step Tokamaks, and is the focus of the Pumped Divertor planned for JET. Analysis shows that the effectiveness of the friction force in overcoming the ion thermal force is strongly reduced at high ion temperature in the SOL, which occurs at high ion power flows (P_i). The hydrogenic flow required for effective impurity retention

increases approximately as $P_i^{5/7}$. At high SOL densities, recycling at the target plates is very high, and this "natural" recycling flux is sufficient to retain the impurities effectively. At moderate and low SOL densities, however, the "natural" recycling flux must be augmented by "external recirculation" to retain impurities. The fraction of the target flux needed for impurity retention increases as density decreases, but decreases with decreasing ion power flow. Pumping the required external recirculation flows is likely to be possible only at rather high edge densities, approaching $n_b \sim 10^{20} m^{-3}$. The situation improves at lower P_i. Operation with clean plasmas is likely, therefore, only at high densities. This may have severe consequences, e.g. for current drive.

First steps towards validating these complex SOL models have been taken by establishing consistency with observed edge data in JET X-point operation [11]. In particular, the predicted conditions $T_i > T_e$ in the SOL, and divertor temperatures T_{ed} in the range 10 - 20 eV at high n_b, have been observed.

Acknowledgements:

The authors wish to thank G. Radford, D. Reiter (KFA, Jülich) and J. Spence for their help with the numerical analysis.

References

[1] Workshop on the New Phase of JET, Report No: JET-R(89)16.

[2] NEUHAUSER, J., SCHNEIDER, W., WUNDERLICH, R., LACKNER, K., Nucl. Fus. 24 (1984) 39.

[3] VLASES, G.C., JET Report (to be published, 1990).

[4] LACKNER, K., Plasma Phys. and Contr. Fus. 26 (1984) 105.

[5] KEILHACKER, M., SIMONINI, R., TARONI, A. and WATKINS, M.L., Nucl. Fus. (to be published)

[6] SIMONINI, R., KEILHACKER, M., TARONI, A. and WATKINS, M.L., 17th EPS Conf. on Contr. Fusion and Plasma Heating, Amsterdam, 1990, Vol. III, p. 1369.

[7] IGITKHANOV, Y.u.L., Contributions to Plasma Physics 28 (1988) 477.

[8] BRAGINSKII, S.I., Review of Plasma Physics 1, Consultants Bureau, New York (1965), p. 205.

[9] CUPINI, E., DeMATTEIS, A., SIMONINI, R. NET Report EUR XII-324/9 (1984).

[10] HUGON, M., LALLIA, P.P. and REBUT, P.H., Report No: JET-R(89)14.

[11] HARBOUR, P.J., SIMONINI, R., TAGLE, J.A., GOTTARDI, N., VON HELLERMANN, M., et al., 9th Int. Conf. on Plasma Surface Interactions in Contr. Fusion Devices, Bournemouth, 21-25 May 1990 (to be published in J. Nucl. Mat.).

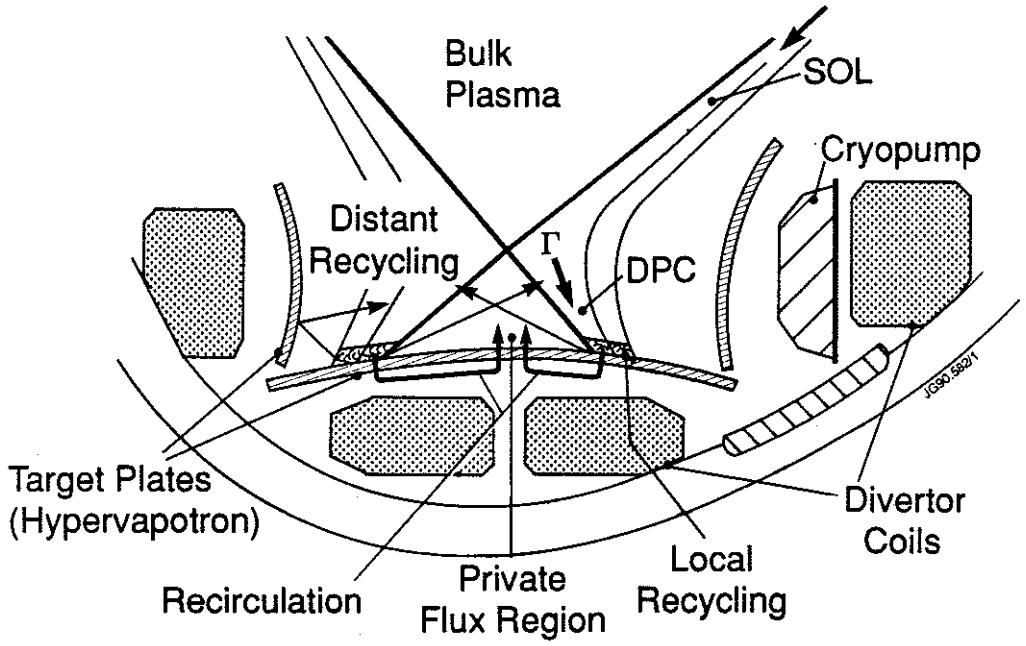

FIG. 1. *Schematic Diagram of the JET Pumped Divertor*

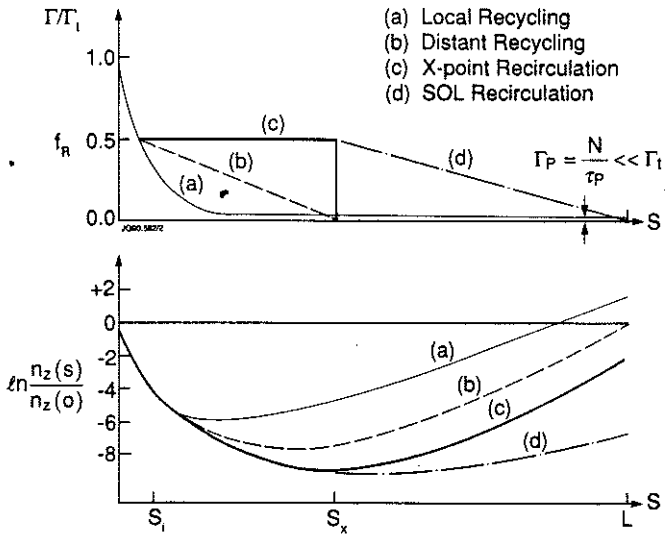

FIG. 2. *Sketch of the Behaviour of the Hydrogenic Flux to the Target (above) and the Resulting Impurity Distribution (below) for Various Recirculation Patterns. s is the distance along a field line from the target, while s_i, s_x, and L refer to the effective ionization length, connection length, and stagnation point locations.*

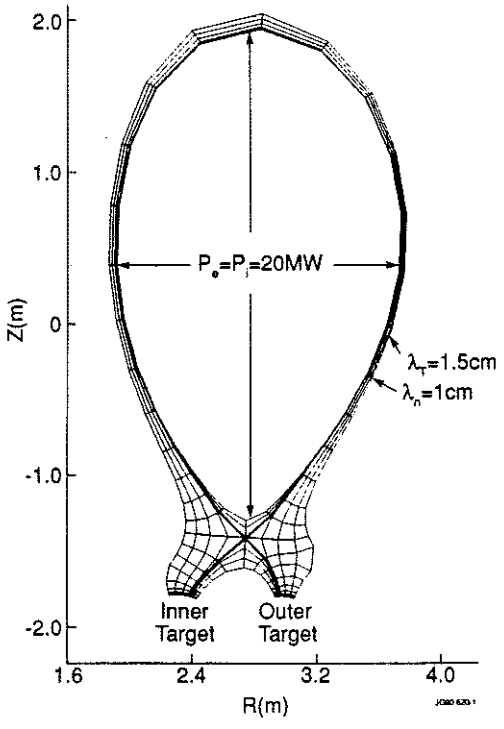

FIG. 3. *The Computational Mesh and some Input Parameters used for the EDGE1D Code Calculations.*

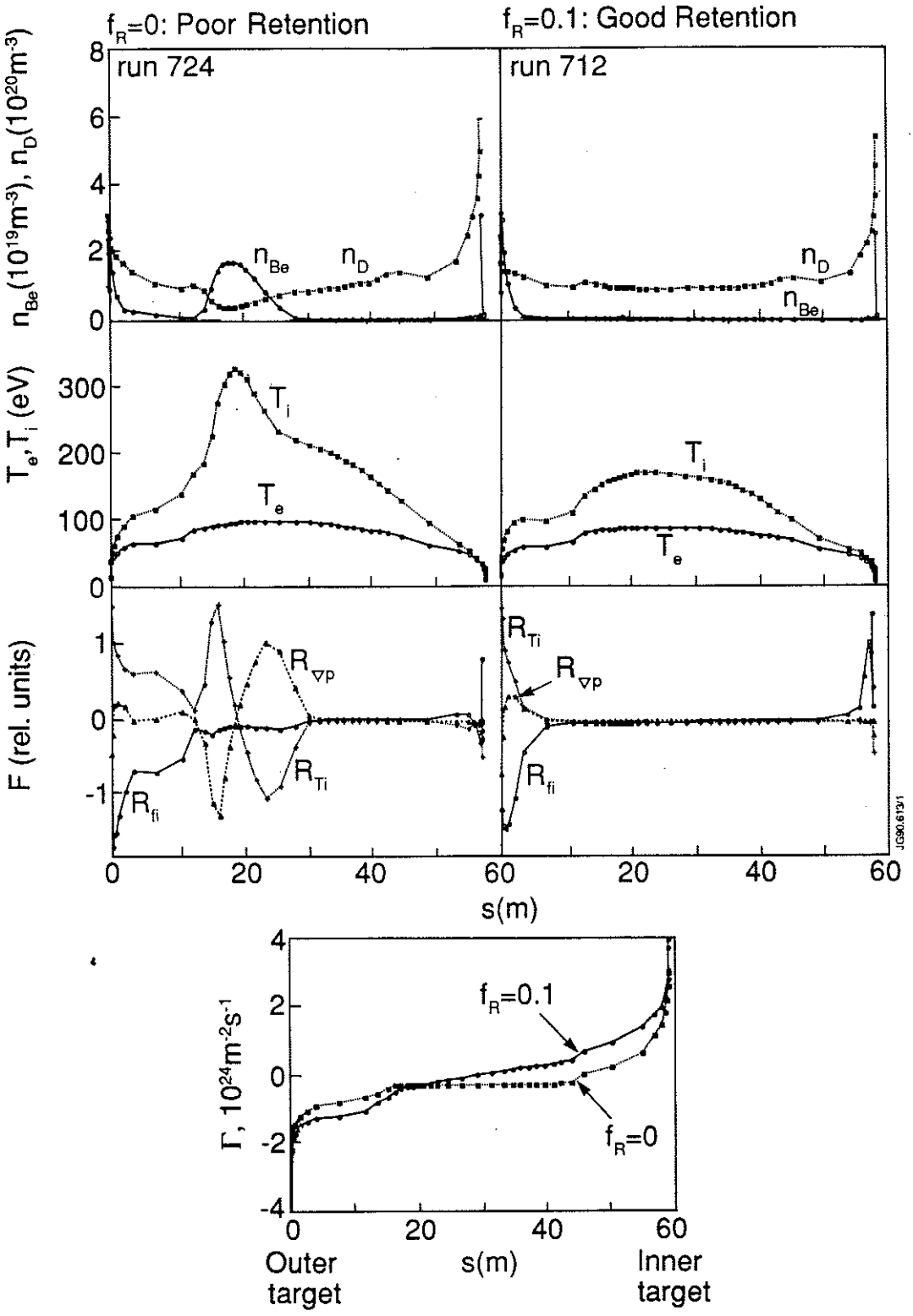

FIG. 4. *Behaviour of Various Plasma Parameters versus s, for a Case of Poor Impurity Retention (left) and Good Impurity Retention (right). f_R is the Fraction of Target Flux which is Externally Recirculated.*

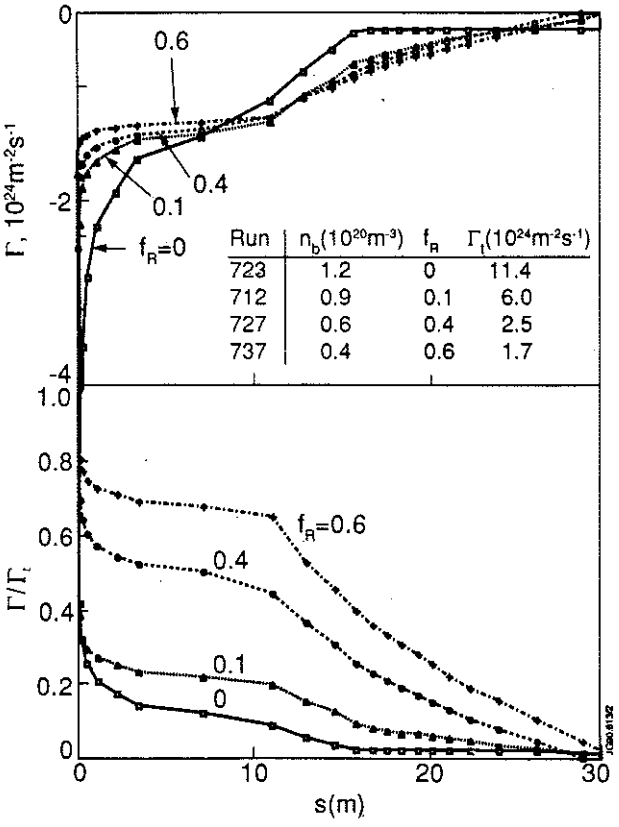

FIG. 5. *Distribution of Hydrogenic Flux (above), and Normalized Hydrogenic Flux* $\hat{\Gamma}(s) \equiv \Gamma(s)/\Gamma_t$ *(below) for four High Retention Runs with Varying Recirculation Fractions.*

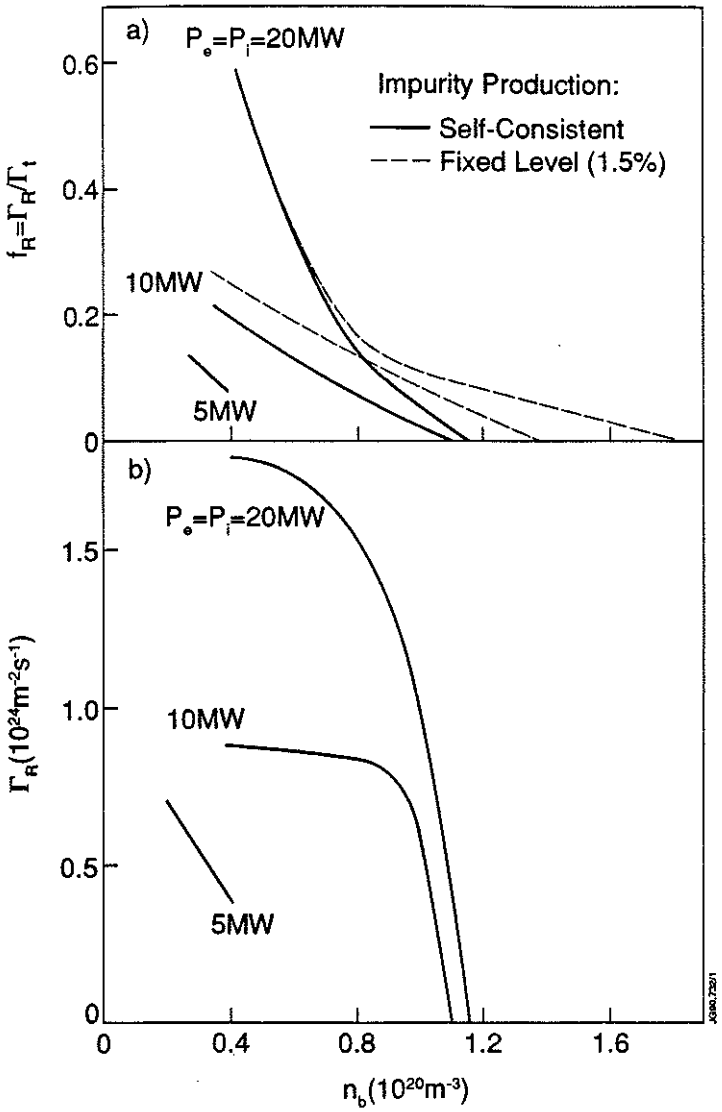

FIG. 6. (a) External Recirculation Particle Flux Fraction f_R*, and (b) Particle Flux* Γ_R *required for 90% Impurity Retention versus SOL Density, for Three Values of Ion Power Flow in the SOL.*

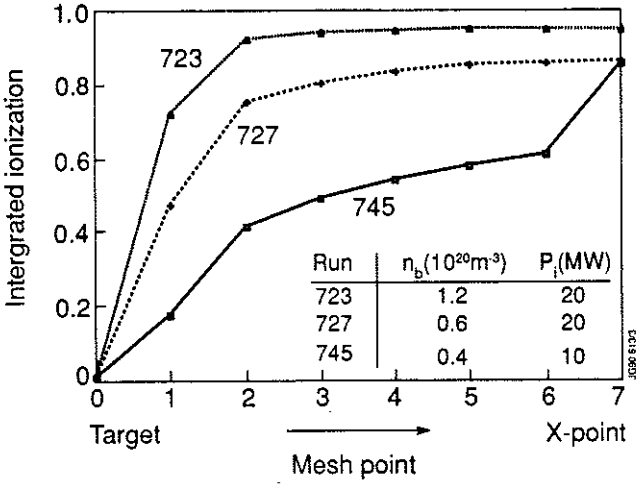

FIG. 7. *Integral of Ionization versus Computational Mesh Point. The distant recycling fraction increases as SOL power decreases.*

IAEA-CN-53/A-5-3

Comparison of Beryllium and Graphite First-Walls in JET

by

The JET Team*
(presented by PR Thomas)

JET Joint Undertaking, Abingdon,
Oxon, OX14 3EA, UK

* See P-H Rebut and the JET Team, 13th Int. Conf. on Plasma Physics and Contr. Fusion Research, Washinton, USA. (1990) to be published in Nuclear Fusion Supplement

COMPARISON OF BERYLLIUM AND GRAPHITE FIRST-WALLS IN JET

Abstract

JET has operated with beryllium as a first-wall material in 1989 and 1990. An initial period with beryllium evaporation onto the original graphite surfaces was followed by operation with beryllium belt-limiter tiles. Beryllium Faraday shields for the ICRH antennae and lower X-point target tiles were installed for experiments in 1990. The use of beryllium has increased the density limit, significantly reduced deconditioning following disruptions, allowed heavy gas fuelling for impurity control, reduced the impurity influx from the ICRH antennae so that ICRH-only H modes were possible for the first time and permitted hot-ion plasmas on the outer limiters. This paper describes the primary effects of beryllium which led to these improvements in performance.

1. INTRODUCTION

JET has used graphite limiters, X-point target plates and vessel protection tiles since the start of operation. Although high performance plasmas have been obtained, it has become apparent that the lack of density control, the fuel dilution, radiative density limit and the "carbon bloom" all present serious obstacles to the development of the JET programme. Beryllium was proposed [1] for JET as an alternative to graphite in order to circumvent some of the these difficulties. It has the obvious advantage that its nuclear charge (and so radiative cooling rate) is lower than carbon whilst having physical sputtering yields which are similar to graphite. Although beryllium melts at a very much lower temperature than graphite sublimes, this disadvantage is offset by its higher thermal conductivity and the phenomenon of "radiation enhanced sublimation" in graphite. Pilot experiments with beryllium limiters were conducted on the UNITOR [2] and ISX-B [3] tokamaks. The results of these experiments were sufficiently encouraging that the decision was made early in 1989 to conduct the beryllium experiment on JET.

There have been four experimental phases of the beryllium experiment:

(i) **A graphite only** phase which was used to bring the machine back into operation following the 1988/89 shut-down. Since the machine was poorly conditioned in this phase, data representative of graphite operation is taken from 1988 experiments.

(ii) The **beryllium evaporation** phase was intended to separate the gettering effect of beryllium from its use as a material limiter. Four evaporators, equispaced in the mid-plane of the machine, were used to deposit a layer about 150 Å thick on the inside wall and about ten times that on surfaces near to the evaporators. The evaporations were performed overnight in order not to interrupt tokamak operation.

(iii) The **beryllium limiter** phase saw the replacement of the graphite tiles in the two outer belt-limiters by beryllium components. Evaporation continued to be used to coat the ICRH antennae, the X-point target tiles and the inner-wall.

iv) In **1990** the nickel Faraday shields of the ICRH antennae were replaced by beryllium components and a trial set of lower x-point targets were constructed out of tiles originally intended for the protective frame around the ICRH antennae.

This paper describes the primary effects of the use of beryllium and compares them with observations from the graphite only phase. The resulting high performance plasmas are described in greater detail in the other JET papers which are presented at this conference [4,5,6,7,8].

2. IMPURITY SOURCES

2.1 Graphite Only Phase

Although there was some variability, according to the kind of operation and its timing relative to vessel vents, the sources of carbon and nickel during operation with graphite surfaces were consistent with expectations based on laboratory sputtering data. The effective yield of carbon (which is defined as the ratio of the carbon to deuterium source rates) falls from about 8% at low density to 4% near the high density limit, as shown in Fig. 1. As the input power is increased, the effective yield curve moves to higher density. Calculations of the effective yield, which take account of self sputtering and use Langmuir probe data for the boundary plasma conditions, give a satisfactory account of the experimental data [9]. Measurements of the amount of erosion found at the wettest part of the limiters are in general agreement with this picture. For the main part, the nickel source emanated from the ICRH Faraday shields. Again, when use was made of a model for the plasma in front of the antenna and the circuit formed between it and the Faraday shields, the data could be described by sputtering [10]. Sputtering of nickel by carbon is an important component of the ICRH induced nickel source.

Oxygen and chlorine behave quite differently from carbon and nickel. Both depend on the conditioning history of the machine. The sources are strongest close to the density limit. An interesting result, which became apparent after the beryllium gettering, is that a significant proportion of the carbon source is due to sputtering by oxygen, (which has a yield close to unity). Thus, periods close to major vents, such as that early in 1989, are characterised by larger effective sputtering yields for *carbon* than when the surfaces are well conditioned.

2.2 Beryllium Evaporation

The most obvious effect of the beryllium evaporation was the almost total disappearance of the oxygen source due to gettering. For otherwise similar plasma conditions, the OII signal fell by a factor of more than 20, the carbon source was also reduced; a factor of two being typical. Whilst this could be due to the coverage of graphite surfaces with beryllium, modelling of this and the variability in the graphite phase suggests that it is the elimination of

oxygen sputtering which is responsible. Once beryllium had been introduced in the vacuum vessel, chlorine became the next most important impurity instead of oxygen.

Following an evaporation, the beryllium film would be removed from the region of the limiters in contact with the plasma in a few pulses. In the course of these pulses, the carbon source increased with the exposed graphite surface area. Subsequently there would be very little development in any of the impurity sources over periods of at least 40 pulses. The coating of the ICRH Faraday shields by beryllium reduced the nickel source and would gradually deteriorate over 10-20 pulses.

2.3 Beryllium Limiter Phase

The installation of the beryllium limiters had the obvious effect, for limiter plasmas at least, of replacing the carbon source by beryllium. This further reduction in the carbon source and its consequent effect on the ICRH antennae brought about the virtual elimination of the nickel influx from the Faraday shields. As will be described later, the improvement in the operating range with ICRH was dramatic.

The beryllium effective yield behaves in a similar fashion with density and power to that of carbon, as shown in Fig. 2. However, the yield is as much as 2-3 times greater at the low density end of the curve than that anticipated from normal incidence physical sputtering. The boundary ion temperature is inferred from measurements to be much greater than that of the electrons in these plasmas. A possible result of this is that the ions arrive at the limiter surface at grazing incidence so that the effective yield is enhanced, particularly by self-sputtering.

Both carbon and beryllium limiters had hot spots at which sublimation or evaporation took place. The effective yields described above pertain to power levels and regions of the limiters which are not significantly affected by hot spots. The impurity source from the hot spots causes the "carbon (or beryllium) bloom" which has a severe effect on high performance plasmas [11].

The beryllium X-point targets have been used for plasma experiments but, at the time of writing, the results have not yet been evaluated.

3. IMPURITY CONCENTRATIONS AND PLASMA RADIATION

The impurity concentrations observed in the different phases of operation can be broadly summarised by remarking that the effective yield for all the impurity species is nearly identical with the ratio of the core density of that species to the deuteron density. This is a somewhat surprising result because the ionization lengths for each of the species involved are quite different. Nevertheless, the relationship holds for the spectroscopically derived particle sources and the density ratios n_C/n_D and n_{Be}/n_D as shown in the lower halves of Figs. 1 and 2.

The deuterium pumping conferred by the beryllium limiter allows heavy gas fuelling to be used to reduce impurity concentrations during high power heating. This gas fuelling has little effect on the density of the core plasma but does raise the density at the boundary. The discharges used in

Fig. 2 had just enough fuelling to sustain the line density by feedback. However it should be noted that the effective yield and the Z_{eff} value can by multi-valued at a given density. Interestingly, the relationship between the effective yield and n_{Be}/n_D is maintained during the heavy fuelling. This shows that its effect must be to reduce the overall particle confinement time. The mechanism behind this is not understood and is being investigated.

The radiated power is measured with bolometers and VUV/XUV survey spectrometers. The sum of radiation components from each species, calculated from selected line strengths, give good agreement with the bolometric total radiated power.

With graphite limiters the radiated power accounted for 30-100% of the input power even with beryllium evaporation. Carbon and oxygen contributed the bulk of the radiation prior to the introduction of beryllium. In the evaporation phase, chlorine became an important radiator, particularly near the density limit, and carbon provided the rest.

Plasmas on the beryllium limiters radiate 15-60% of the input power with the lower end of the range being typical. Only chlorine and beryllium contribute significantly. During operation, the chlorine was gradually eliminated and thus led to a considerable improvement in the density limit, which is described in the next section. Thus the lower charge of beryllium, compared with that of carbon, has conferred a definite advantage by reducing the radiated power and increasing the operating range.

4. THE DENSITY LIMIT

The density limit is determined by the loss of thermal stability when the radiated power becomes a substantial fraction of the input power. A MARFE forms, whereupoon the plasma column either contracts radially until it becomes MHD unstable and disrupts or the MARFE ejects which ejects a sufficient number of particles that thermal stability and poloidal symmetry are restored without a plasma disruption. In JET the former behaviour is associated with graphite limiters and the radial contraction occurs when the radiated power is 100% of the input. The softer limit is observed with beryllium limiters and is triggered when 50-60% of the power is radiated. During the MARFEing phase the radiation can exceed 100% of the input.

The Ohmic heating density limit on the beryllium limiters at $q_\psi \approx 3.8$ and $I_p = 3MA$, was improved by 50% over the best value achieved with the graphite limiters. Reducing the field to (1.55) T, so that $q_\psi \approx 2.6$ was obtained, increased the density limit by a further 20%. The line average density was $0.6 \times 10^{20} m^{-3}$.

In the graphite phase, NBH could be used to increase the density limit. As expected from simple power balance arguments, the density increases as the square root of the total input power. On the other hand, with ICRH the limit remained close to the Ohmic value because of the impurity influx from the antennae. However, the beryllium evaporation coated the Faraday shields sufficiently that the performance with ICRH became identical to that with NBH. When the beryllium limiter was introduced the impurity influx was so reduced that ICRH only H-modes became possible for the first time.

5. PLASMA PUMPING

Density control with graphite surfaces had always been a problem in JET because the recycling coefficient was close to unity. As shown in Fig. 3, the characteristic decay time for the deuteron density, when the gas feed was switched off, was typically 30 seconds. The density control could be improved for a few pulses by conditioning the limiter with helium plasmas.

Beryllium evaporation caused a long term change in this behaviour and the density decay time dropped to about 5-12 seconds. It can be seen in Fig. 3 that the pumping was still effective after one days operation, although the decay time would approximately double. The beryllium limiters brought about a further improvement and the pumping time fell to 1-2 seconds. Some temporary deconditioning would occur after very high power (>30MW) heating. Helium plasmas are also pumped by the beryllium limiters but not at all by the graphite (even with beryllium evaporation). The density decay rates are fairly similar to those of deuterium.

In respect of the deuterium pumping, JET with beryllium is very similar to other all metal tokamaks. This pumping brings about the following improvements in plasma operation:

(i) Effective density control is possible,
(ii) as noted earlier, large influxes of deuterium can be used to control impurities during additional heating without a consequent density rise and
(iii) the deconditioning effect of MARFE's or disruptions has been significantly reduced.

With graphite limiters, gas desorption in pulses subsequent to a major disruption would often be sufficient to prevent plasma start-up. It often proved necessary to recondition the chamber by GDC in helium for a few hours. This loss of experimental time has largely been eliminated by the used of beryllium, either because the gas load following a disruption is reduced or because of the pumping of the following start-up. Many more high performance pulses can be obtained in a session as a result.

The pressure in the torus falls off as $\sim t^{-0.75\pm0.1}$ following a plasma shot with beryllium surfaces. At least 80% of the deuterium used is recovered in the pumps. From the time dependence of the D_2 and DH fractions, it is concluded that the gas release is recombination dominated.

6. CONCLUSIONS

JET has been successfully operated with beryllium evaporation onto graphite surfaces and with beryllium limiters, ICRH Faraday shields and X-point target tiles. Although hot spots and surface melting have been observed on the beryllium components, the plasmas can be optimised so that improved performance over the graphite phase is obtained.

Beryllium has shown itself to be a viable replacement for graphite as a plasma facing material. Applications can be seen for both in the first wall of a next step tokamak. However neither material can satisfactorily match the

requirements for divertor target tiles, because of the problem of blooms, unless most of the power is radiated from the target plasma. The demonstration of a divertor configuration consistent with the requirements of next step tokamaks is the goal of the proposed pumped divertor phase of JET.

7. REFERENCES

[1] REBUT, P.H., et al., JET Report (85) 03.
[2] HACKMAN, J., UHLENBUSCH, J.,J. Nucl. Mater., **128-129** (1984) 418.
[3] ISLER, R.C., et. al., Nuclear Fusion **25** (1985) 1635.
[4] REBUT, P.H., et al., IAEA-CN-53/A-1-2, these Proceedings.
[5] LOMAS, P.J., et al., IAEA-CN-53/A-6-2, these Proceedings.
[6] TANGA, A., et al., IAEA-CN-53/A-4-1, these Proceedings
[7] START, D., et. al., IAEA-CN-53/E-2-1, these Proceedings.
[8] SMEULDERS, P., et al., IAEA-CN-53/A-3-4, these Proceedings.
[9] KEILHACKER M., et. al., Phys. Fluids B2 (1990) 1291.
[10] BURES, M., et. al., Fusion Engineering and Design **12** (1990) 209.
[11] ULRICKSON, M., et. al., to be published in J. Nucl. Mater., (1990)

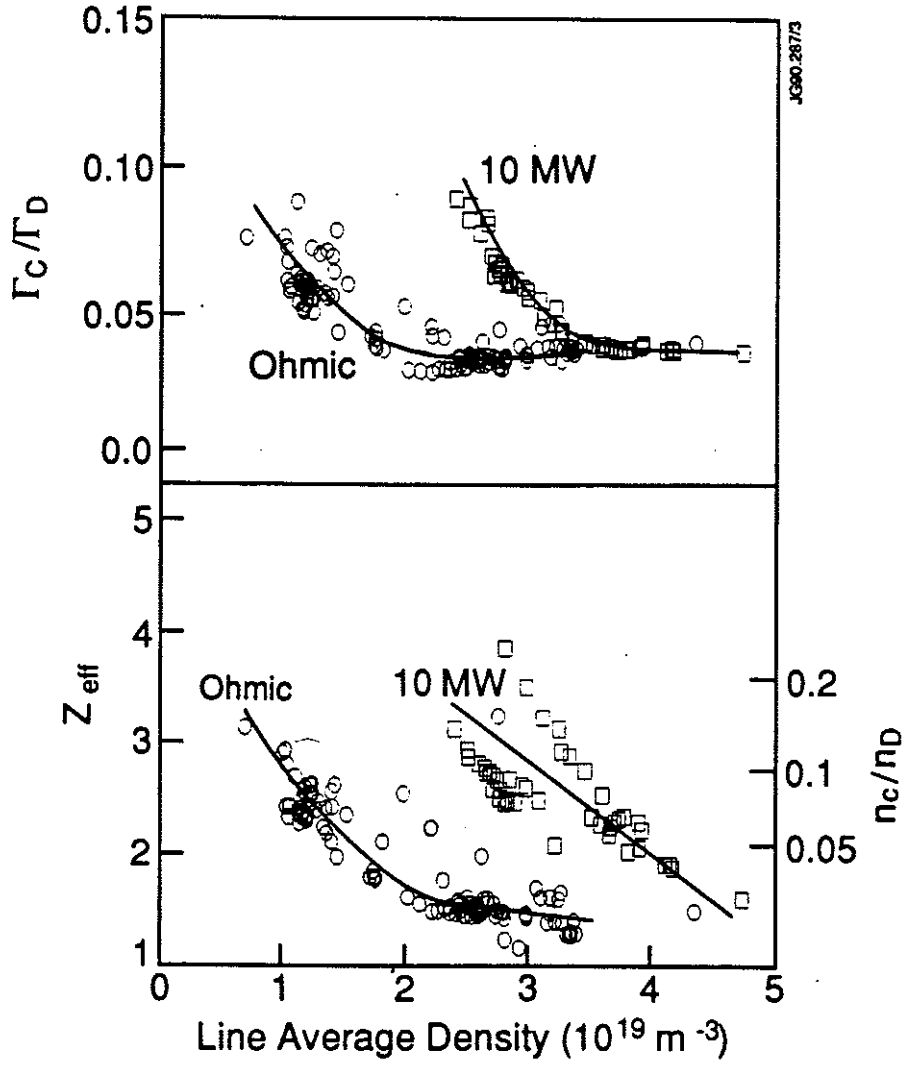

Fig 1: The effective yield (Γ_c/Γ_D), Z_{eff} from visible Bremsstrahlung and central ionic concentration ratio (n_C/n_D) against line average density for Ohmic and additionally heated (10MW) discharges during the graphite phase of operation.

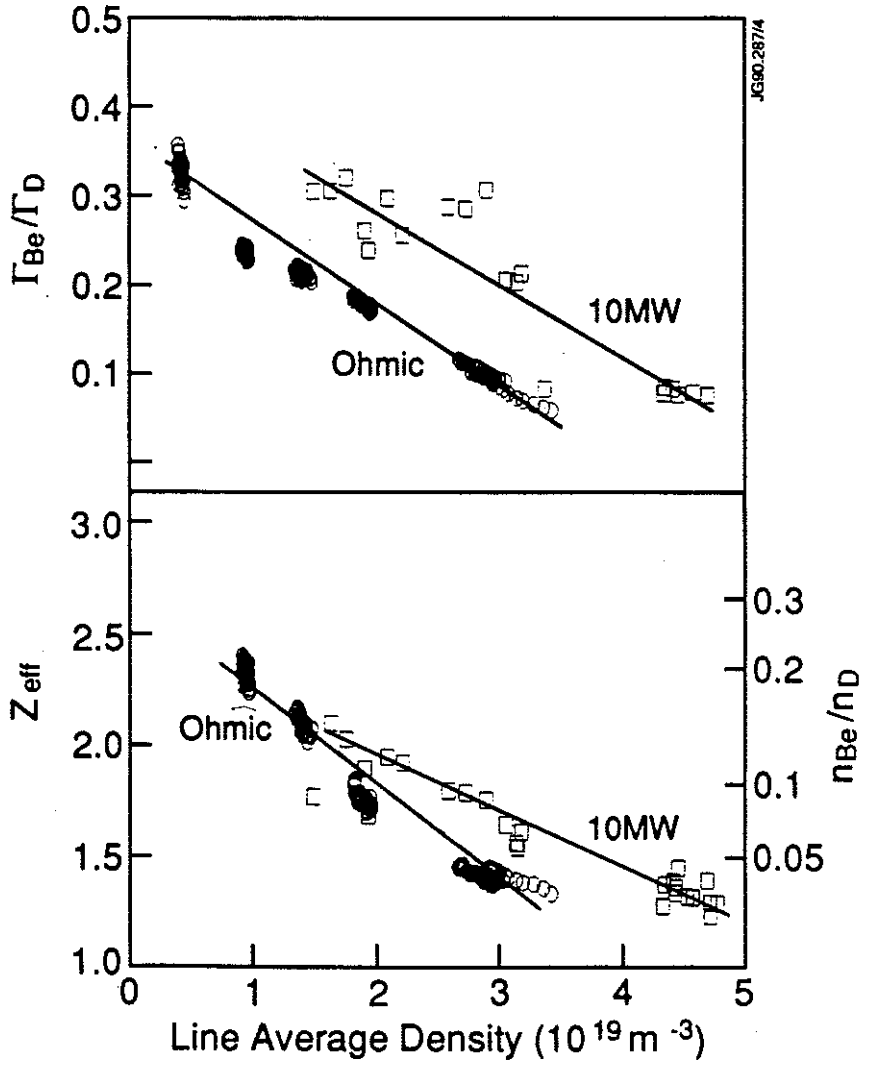

Fig 2: The effective yield (Γ_{Be}/Γ_D), Z_{eff} from visible Bremsstrahlung and central ionic concentration ratio ($n_{Be}n_D$) against line average density for Ohmic and additionally heated (10MW) discharges during the beryllium limiter phase of operation.

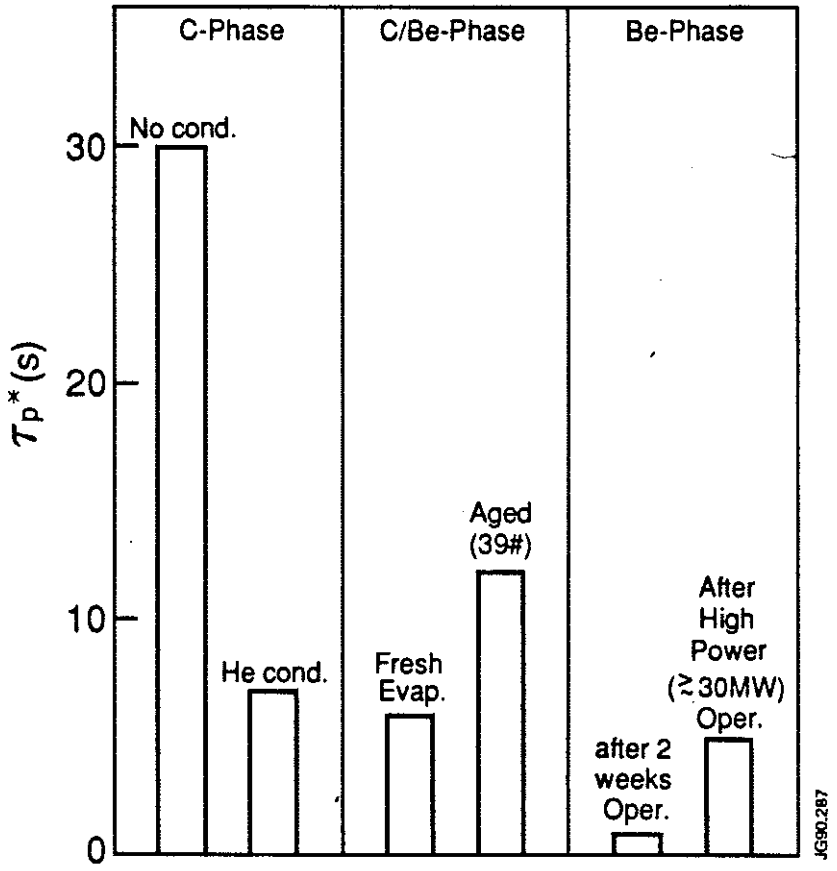

Fig 3: The characteristic decay time for the electron density after switching the gas feed off for different phases of recent JET operation.

IAEA-CN-53/E-2-1-1

ICRF Heating in Reactor Grade Plasmas

by

The JET Team*
(presented by DFH Start)

JET Joint Undertaking, Abingdon,
Oxon, OX14 3EA, UK

* See P-H Rebut and the JET Team, 13th Int. Conf. on Plasma Physics and Contr. Fusion Research, Washinton, USA. (1990) to be published in Nuclear Fusion Supplement

ICRF HEATING IN REACTOR GRADE PLASMAS.

Performance of ICRH in JET Plasmas – The JET Team.

A Fast Wave Heating and Current Drive System for NET/ITER

J Jacquinot, V P Bhatnagar, M Bures, G A Cottrell, L–G Eriksson,
T Hellsten[1], R Koch[2], D Moreau[3], C H Sack, D F H Start, and A Taroni.

Presented by D F H Start

JET Joint Undertaking, Abingdon, Oxon, OX14 3EA, UK

[1]Royal Institute of Technology S–10044, Stockholm, Sweden.
[2]LPP–ERM/KMS EUR–EB Association, 1040 Brussels, Belgium.
[3]CEA Centre d'Etudes Nucleaires de Cadarache, France.

ICRF HEATING IN REACTOR GRADE PLASMAS.

Abstract

Impurity influxes in JET discharges due to ICRH have been reduced to insignificant levels. This has allowed high quality H–modes to be produced with ICRH alone and has enhanced the density limit which is now the same as the NBI limit. Improvement in the deuterium fuel fraction has led to the generation of 100kW of non thermal ^{3}He–D fusion power. Alpha–particle simulations using MeV ions created by ICRH show classical energy loss and suggest that α–heating in a reactor will be highly efficient. A clear demonstration of TTMP damping of the fast wave in high beta plasmas has been achieved. A broadband ICRH system is proposed for NET/ITER which will allow fast wave current drive and central ion heating for burn control and ignition.

1. Introduction

During JET operation in late 1989 and 1990 the impurity problems associated directly with ICRF heating have been eliminated for all practical purposes. This has been due mainly to beryllium gettering of the nickel RF antenna screens and their subsequent replacement by screens with Be elements. Other important measures to reduce sputtering from the screens have been dipole antenna phasing and alignment of the screen elements with the magnetic field. These improvements have enabled ICRH on JET to make substantial advances in several important areas of plasma performance and these are described in the present paper. For the first time, long 'elm'–free H–modes have been created by minority ICRH alone and have identical characteristics with those produced by neutral beam injection. Similarly, the density limit no longer depends on the type of additional heating. Fast ions created by ICRH have been used to produce 100kW of fusion power from non–thermal ^{3}He–D fusion reactions and to simulate the behaviour of α–particles in a reactor. Section 5 shows the results of Be influx measurements and section 6 describes a demonstration of TTMP absorbtion of 48MHz fast magnetosonic waves in high beta plasmas. The final section describes a proposal for NET/ITER of a broadband ICRH system operating between 17MHz to 40MHz to give fast wave current drive, central bulk ion heating and non–thermal D–T fusion.

2. H–modes produced by ICRH alone

An example of an H–mode created by RF alone in a double–null X–point plasma with I_p=3MA, B_t=2.8T is shown in fig.1. The RF power was 7MW and dipole phasing was used. The Dα signal shows the H–mode to extend for 1.3s during which time the energy content given by the diamagnetic loop reaches 6MJ. Comparison with the energy obtained from magnetic analysis suggests that 1.3MJ of this is due to fast ions. The confinement time of the thermal component alone is 0.7s which is twice the Goldstone L–mode value and is similar to values obtained with neutral beam injection (NBI) for the same power level. In fig 1 the central

electron temperature reached 9.5keV at the end of the H–mode when the central density had risen to $3.7 \times 10^{19} m^{-3}$. Monopole phasing ($P_{rf} \approx 10MW$) also produces H–modes and, in some of these, Monster sawteeth occur.

These experiments were assisted by a new feedback system which keeps the coupling restance (R_c) constant by controlling the separation (X_a in fig. 1) of the last closed flux surface from the antenna. In pulse 21906 the requested 3.5 ohm coupling was maintained across the L–H transition and throughout the H–mode phase by plasma movements of the order of 0.01m. Without feedback control R_c is reduced by a factor of three during the H–mode causing generator trips and RF power loss[1].

3. ^{3}He–D non–thermal fusion experiments

The fusion reaction $^3He + D \rightarrow {}^4He(3.6MeV) + p(14.7MeV)$ has been studied in JET using ^{3}He minority ICRH. The first experiments with carbon coating of the vessel achieved 60kW of fusion power [2]. Recently, experiments with Be coating have reached 100kW as shown in fig 2a. The maximum value of Q ($=P_{fus}/P_{rf}$) was 1% (fig 2b). The later results were obtained with $I_p = 3MA$, $B_t = (3.0–3.4)T$, $ne(0) \approx 4 \times 10^{19} m^{-3}$ and $P_{rf} \leq 14MW$. As previously, the reaction rate was measured by detecting the 16.6MeV γ–rays from the weak branch $^3He + D \rightarrow {}^5Li + \gamma$. In most discharges the ICRF resonance was on axis. Some data were taken with off–axis heating to reduce the power density and test for heating of the ^{3}He ions beyond the energy for maximum fusion rate ($\simeq$0.5MeV). The yields were similar with on and off–axis heating implying that the ^{3}He energy was about optimum. A Stix code [2] agrees well with the yields in the carbon vessel for a fuelling ratio $n_d/n_e \simeq 0.4$. To fit the data with Be gettering this model requires $n_d/n_e \simeq 0.7$ which is consistent with $Z_{eff} \simeq 2.5$ compared with $Z_{eff} \simeq 3.5$ previously.

4. Alpha–particle simulation studies

Minority ions created by ICRH in JET can reach MeV energies. The anisotropic distribution allows their energy content to be deduced from diamagnetic loop and Shafranov shift measurements. The energy content can then be compared with theory to test for non–classical loss processes which might reduce the α–particle heating in a reactor. Such comparisons have been made for near steady state Monster sawtooth data which avoids fast ion redistribution by sawteeth. Results are shown in figs 3a and 3b for H–minority ions. Values of W_{fast} are plotted against model calculations which assume a) an RF power density of Gaussian form with a width of 0.3m, b) that 65% of P_{rf} is absorbed by the minority (as deduced from modulation experiments) and c) that the fast ions form a Stix[3] distribution on each flux surface. This basic model is supplemented by corrections for the effect of the fast ion orbits on the slowing down time. The slowing down time is averaged over both the orbit and the energy distribution. Fig 3a shows W_{fast} compared with the results of the basic model only which generally overestimates W_{fast}. However, including orbit effects gives excellent agreement (fig. 3b). A lower limit of 2s is placed on any anomalous loss time which implies that α–particles in a reactor will yield all their energy to the plasma, at least in the absence of mhd.

5. Beryllium influx from the antenna screens

It is well known that impurity fluxes are released from the screens of powered ICRF antennae on JET. The flux depends on antenna voltage, the plasma density near the screen, the angle of the screen bars to the magnetic field, the phasing and the screen material. The sensitivity to voltage and phasing are illustrated in fig 4 for Be coated screens. Note the threefold reduction with dipole phasing. Beryllium coating of the screens and its use as a first wall material, together with dipole phasing and alignment of the screen bars with the field, have reduced the influxes to insignificant levels. The behaviour can largely be understood in terms of sputtering due to RF field rectification in the sheaths formed where the magnetic field intercepts the screen bars[4]. With the present antenna the field can connect a) adjacent bars and b) different points on the front face of the same bar by virtue of its V–shape. The latter effect is sensitive to phasing and disappears for dipole operation. Beryllium gettering is beneficial partly because of the low sputtering coefficient (especially for self sputtering) and partly because it strongly pumps oxygen and other impurities. The influx contribution to Z_{eff} is $\Delta Z_{eff} \simeq 0.05 - 0.1$

6. TTMP damping of the fast wave

Directed fast waves are a strong candidate for non–inductive current drive in reactor plasmas where TTMP is the predominant direct electron damping process. So far, fast wave current drive experiments have been made in low β plasmas and with high RF frequency[5] such that the absorption was mainly by electron Landau damping (ELD). The present experiments were carried out in I_p=2MA, B_t=1.3T, double–null X–point hydrogen plasmas with the ICRF (48MHz) tuned to $2\omega_{ch}$ on the high field side of the magnetic axis. No mode conversion layers existed in the plasma centre where direct electron heating could only occur through damping of the fast wave by combined TTMP and ELD. The electron β was 1.5% so that TTMP was expected to contribute significantly. The electron heating power density was obtained from the T_e (ECE) response to RF power modulation. The profile is peaked on axis as shown in fig 5a and accounts for 22±5% of the input power, the rest being absorbed at $2\omega_{ch}$. Full wave and ray tracing calculations predict more peaked profiles (fig. 5a) but agree with the fraction of the total power absorbed. Data were also obtained from soft X–ray cameras which viewed more of the minor radius than the ECE measurements. Note that the damping is almost zero near the q=1 surface (see fig 5b). A recent Hamiltonian treatment of the wave–particle interaction [6] predicts that quasilinear theory is most likely to break down at q = 1 resulting in just such a reduced absorption.

7. A broadband ICRH system for NET/ITER

An ICRH system operating between frequencies of 17MHz and 40MHz has been proposed for the NET and ITER tokamaks. At 40MHz deuterium minority heating takes place in the centre of the machine. The 'minority' fraction, $n_d/(n_d + n_t)$, is about 30% for which more than 50% of P_{rf} is damped on the deuterium ions. This high minority density also

restricts the fast ion tail temperature ($T_t \simeq 150$keV for $P_{rf} \simeq 50$MW) with the essential effect of providing an intense ion heating source near the magnetic axis. This ion heating is the most important aspect in achieving ignition or burn control according to simulations using the transport code JETTO[7,8]. For Kaye–Goldston scaling[9] the fusion reaction rate is typically 40% higher than that achieved using electron heating methods (ECRH or NBI at MeV energies)[see ref 8]. The advantage of ion heating depends on the confinement scaling assumed and is greatest for Rebut–Lallia[9] and smallest for H–modes ($\tau_h \simeq 2\tau_{kg}$) which are predicted to readily achieve ignition. The Kaye–Goldston case almost ignites so that the ICRH could be used for burn control [9] in this situation.

17MHz is chosen for fast wave current drive by TTMP + ELD since there is no competing cyclotron damping at this frequency. Current drive calculations have been made using 3–D ray tracing and analytic fits to current drive efficiencies[10]. The current achieved is found to depend on the antenna position (on or above the midplane) and on the poloidal field; different geometries give different shifts in the parallel wave vector as each ray propagates. The maximum value of γ ($= \langle n_e \rangle I_p R/P_{rf}$) is 0.3×10^{20}A/W/m^2 for antennae in the midplane as shown in fig 6. The largest value of γ for antennae above the midplane is 0.2×10^{20}A/W/m^2.

8. Summary

Substantially reduced impurity influx has allowed ICRH on JET to produce high quality H–modes, an enhanced density limit and 100kW of non–thermal ^{3}He–D fusion power. Alpha particle simulations using ICRF accelerated minority ions imply efficient α–heating in reactors. TTMP damping of the fast wave has been demonstrated in high β plasmas. The dual purpose ICRH system proposed for NET/ITER allows both central bulk ion heating at 40 MHz for burn control, and fast wave current drive at 17MHz with $\gamma \simeq 0.3 \times 10^{20}$A/W/m^2.

9. References

1) Tubbing B J D et al. Nuclear Fusion 29(1989)1953.
2) Boyd D A et al., Nuclear Fusion 29(1989)593.
3) Stix T H, Nuclear Fusion 15(1975)737.
4) D'Ippolito D and Myra J, Proc. IAEA Tech. Comm. Meeting on Fusion Engineering and Design, Garching, FRG(1989).
5) Moreau D, O'Brien M R, Cox M, and Start D F H, in Controlled Fusion and Plasma Physics (Proc. 14th Eur. Conf., Madrid, 1987) Vol III, European Physical Society (1987) 1007.
6) Becoulet A et al., paper IAEA–CN–53 E–3–10, this Conference.
7) Cenacchi G and Taroni A, JET Report JET–IR88/03 (1988).
8) Koch R et al paper IAEA–CN–53 G–2–9 this conference.
9) Corrigan G et al, Proc 17th European Conf. on Controlled Fusion and Plasma Heating, Amsterdam,1990, Vol II p 801.
10) Bhatnagar V P et al., Proc. Joint Varenna–Lausanne Int. Workshop on Theory of Fusion Plasmas, 1990, to be published.

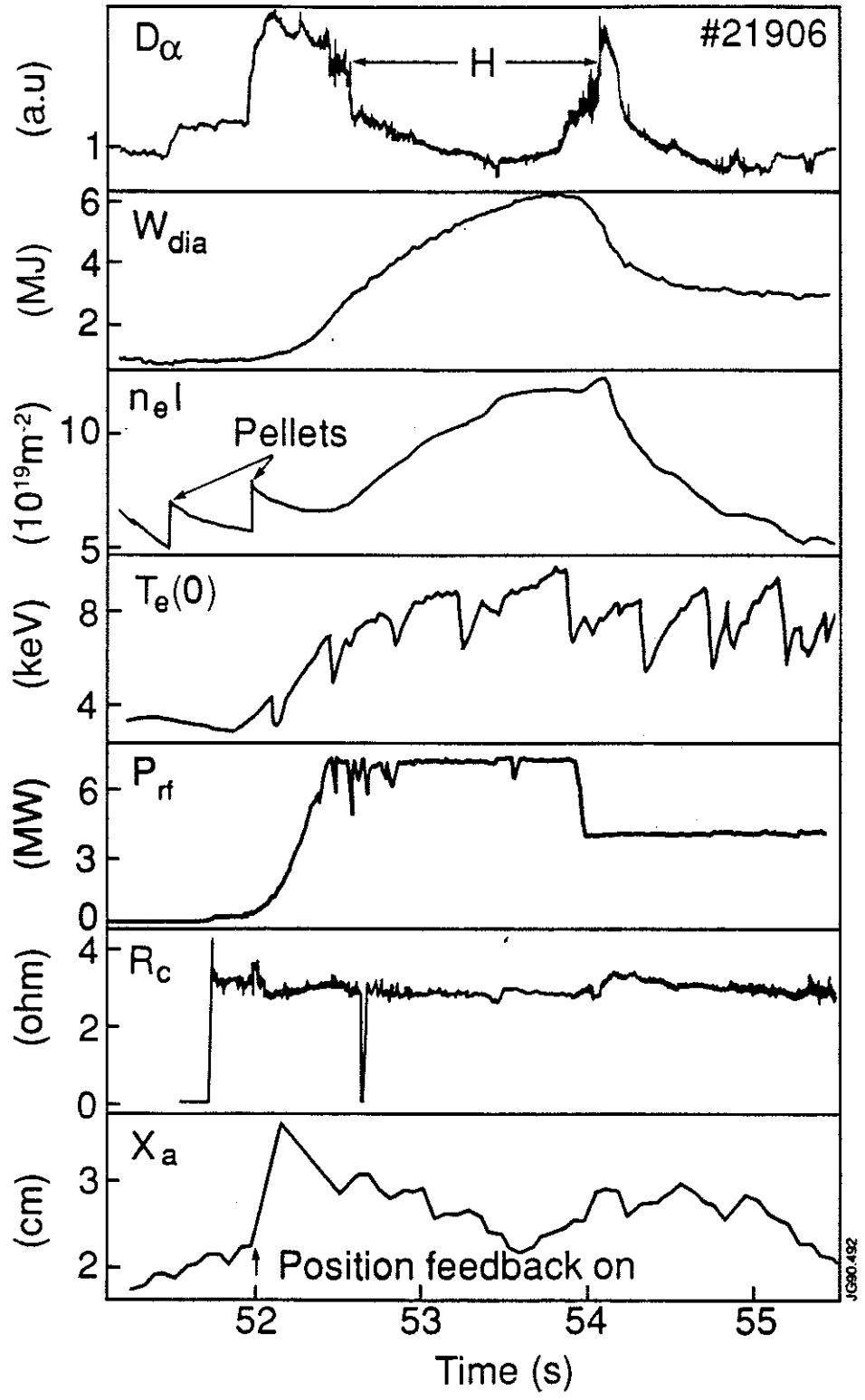

Fig. 1 Plasma parameters during ICRF only H–mode. Note the plasma position control to keep the coupling resistance constant.

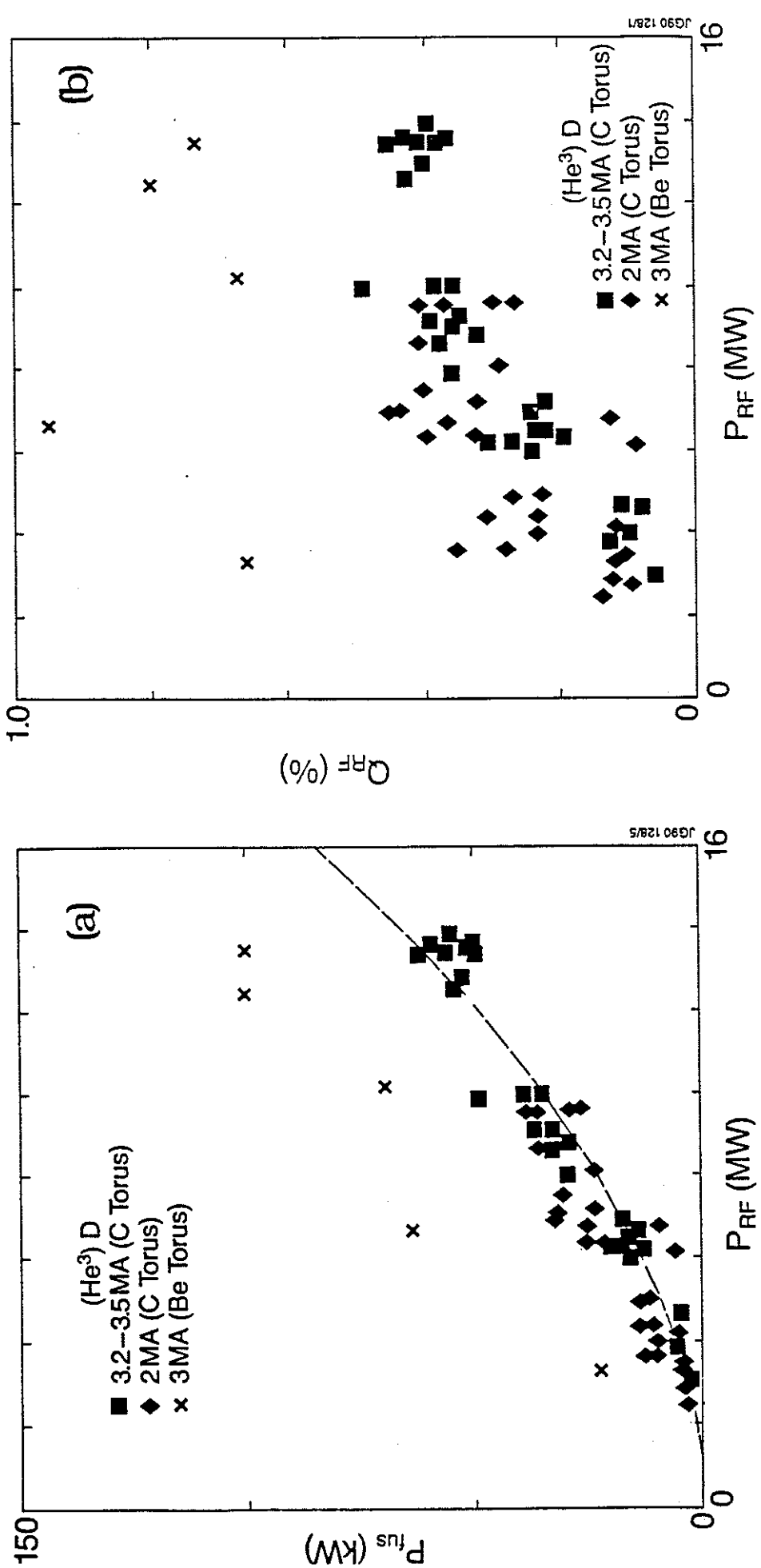

Fig. 2 a) ^{3}He–D fusion yield versus P_{rf} and b) Q–value versus P_{rf}.

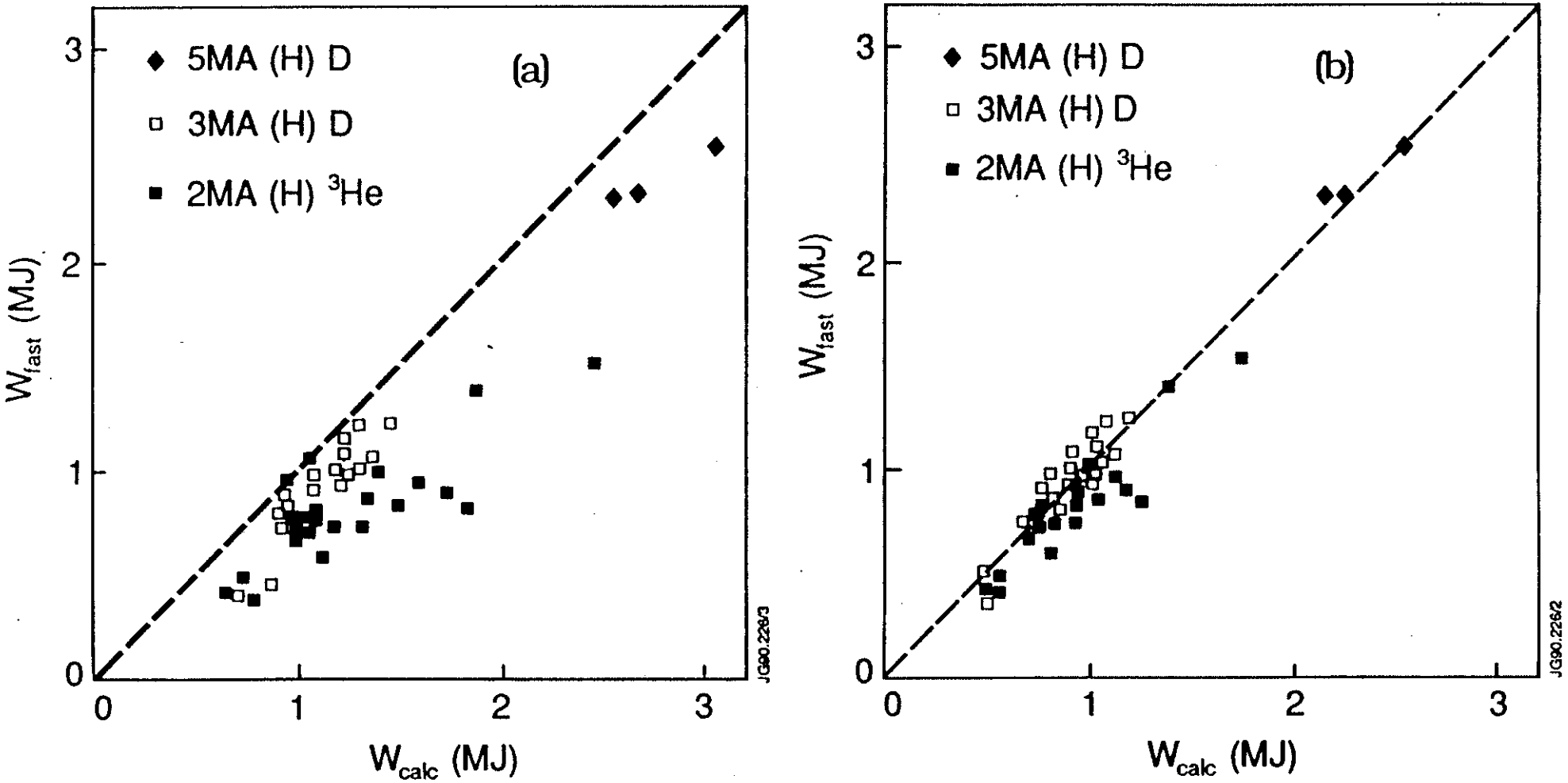

Fig. 3 W_{fast} versus theoretical values for a) no orbit corrections and b) with orbit corrections.

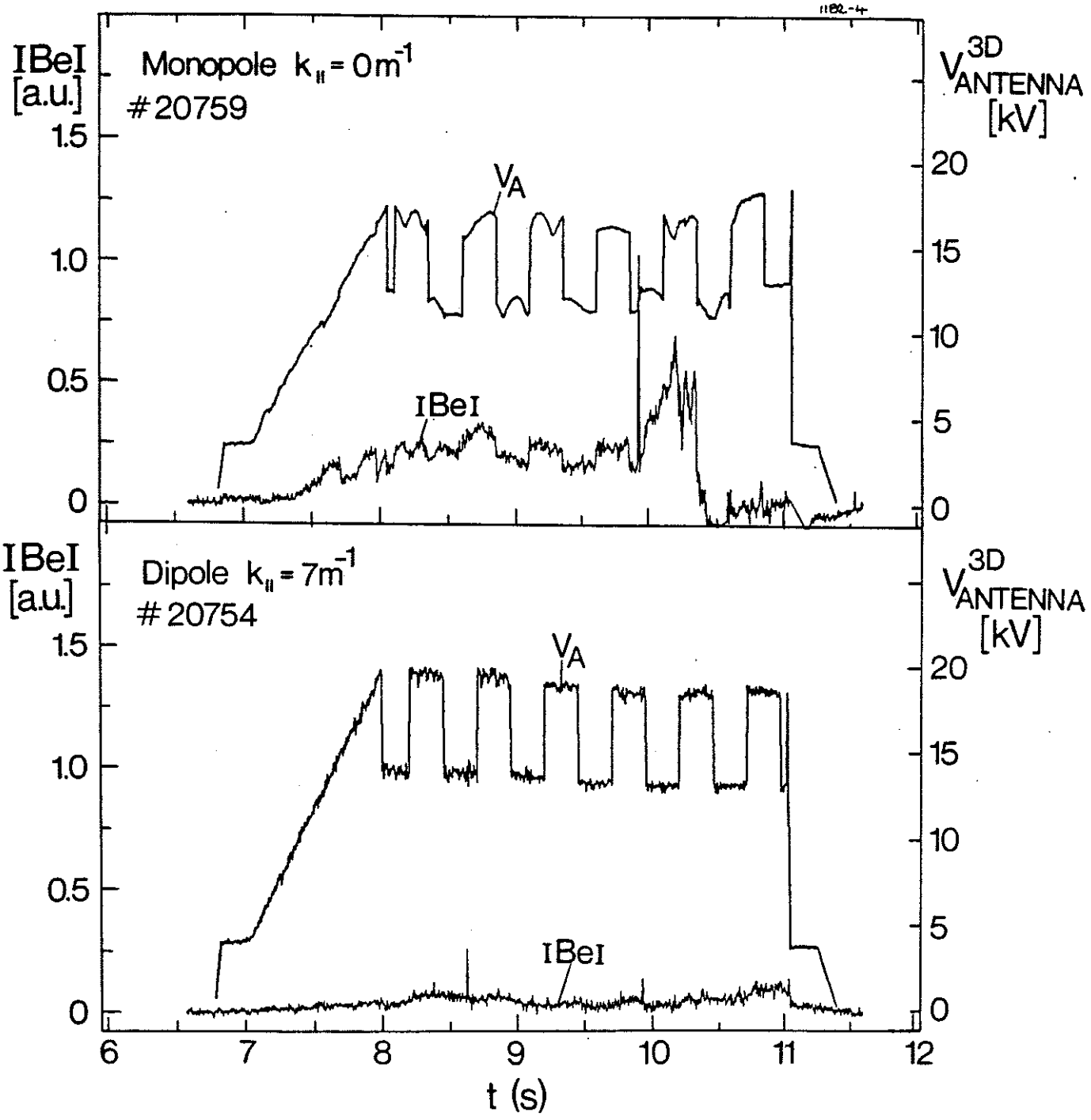

Fig. 4 Be influx sensitivity to antenna voltage and phasing.

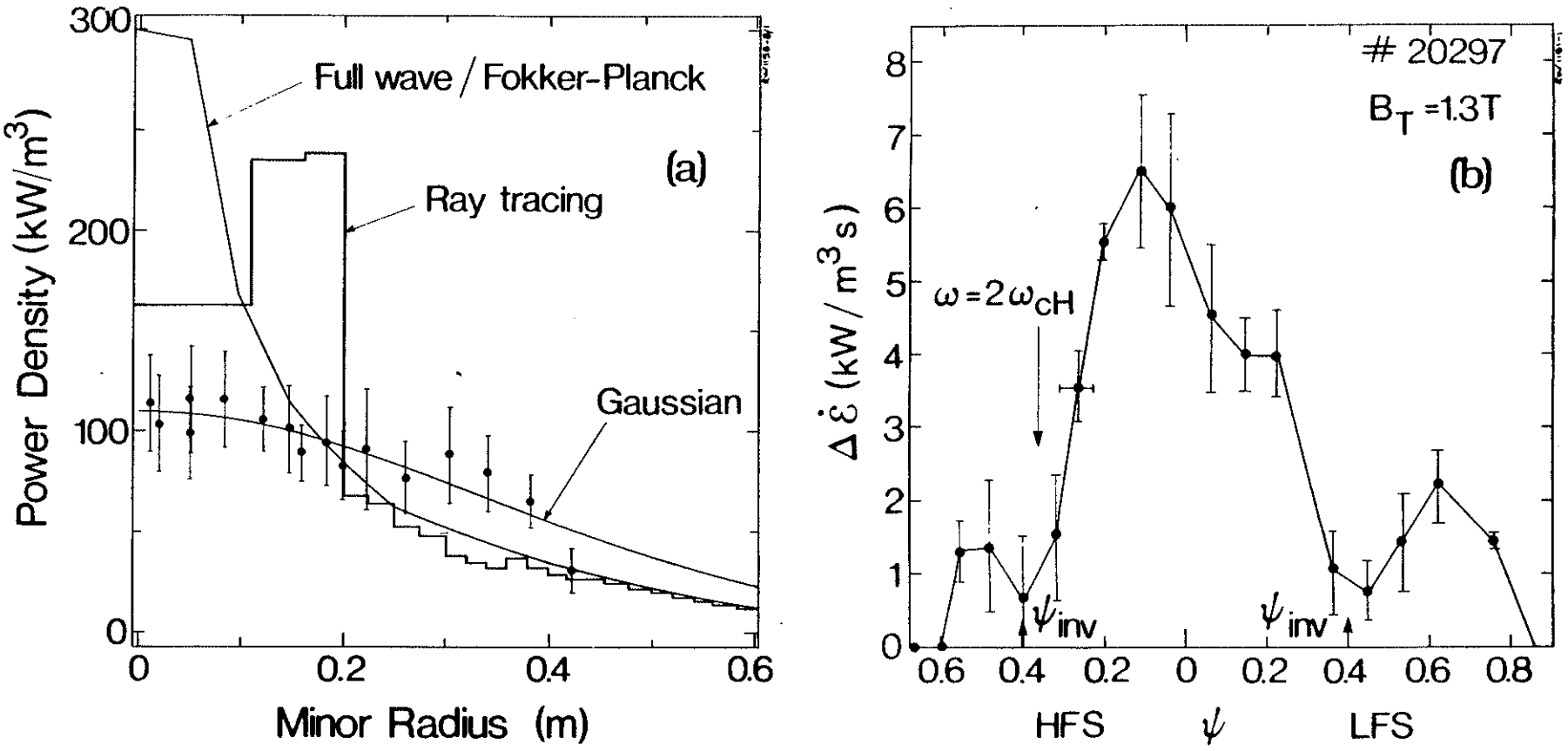

Fig. 5 TTMP + ELD power density profiles from a) theory and ECE measurements and b) soft X–ray emission. ψ is the magnetic flux normalised to unity at the boundary.

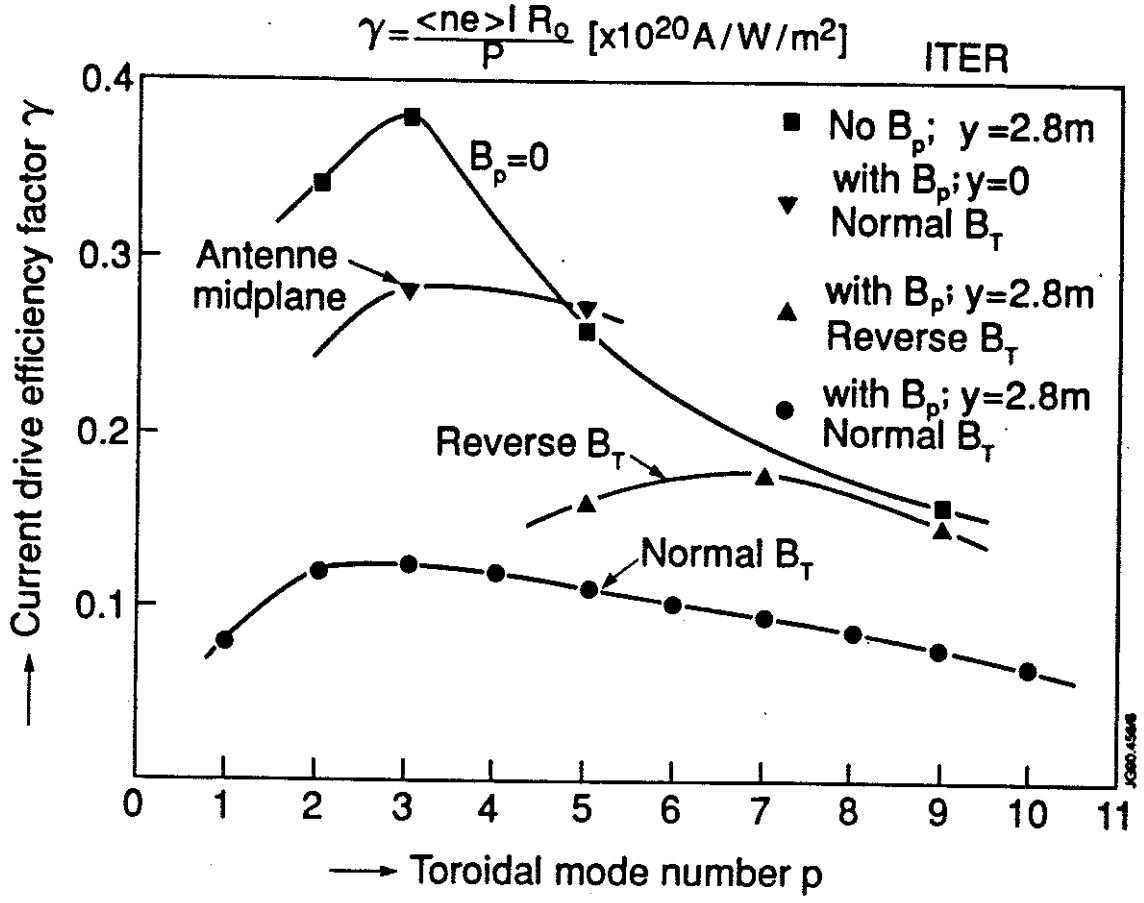

Fig. 6 FWCD current drive efficiency for various antennae and magnetic field configurations. The distance y is the height of the antenna centre above the midplane.

IAEA-CN-53/A-6-3

Sawteeth and their Stabilization in JET

by

The JET Team*
(presented by DJ Campbell)

JET Joint Undertaking, Abingdon,
Oxon, OX14 3EA, UK

* See P-H Rebut and the JET Team, 13th Int. Conf. on Plasma Physics and Contr. Fusion Research, Washinton, USA. (1990)
to be published in Nuclear Fusion Supplement

SAWTEETH AND THEIR STABILIZATION IN JET

Abstract

Sawtooth relaxations control the central plasma parameters in most JET discharges and, as a result, have a significant influence on fusion performance. Several techniques have, therefore, been developed for the stabilization of sawteeth in various JET operating regimes. Under some circumstances, sawtooth suppression appears to be associated with the central safety factor, q_0, rising above unity. However, in other cases, q_0 remains significantly below unity and it is thought that stabilization is due to the influence of a population of energetic particles. Detailed measurements of the evolution of the current profile in JET during sawteeth have confirmed that q_0 remains below unity throughout the sawtooth cycle and thus the trigger for the sawtooth collapse remains problematic. Further diagnostic investigations of the sawtooth collapse have shown that the collapse takes the form of a convective plasma flow, but the cause of the resultant energy transport is not understood.

1. Introduction

Sawteeth are one of the fundamental mhd instabilities of tokamak plasmas. They play a key role in limiting central plasma parameters, and thereby fusion reactivity, in the near–ignition regime. Nevertheless, in spite of considerable experimental and theoretical investigations, both at JET (see e.g. [1]) and elsewhere, no consistent picture of the instability has emerged. Furthermore, while several techniques for sawtooth stabilization exist [2–4], their extension to reactor relevant plasmas is not assured in view of the limited understanding of the mechanisms involved.

Recent experiments at JET have focussed on a number of aspects of the sawtooth problem: the development of a detailed description of the sawtooth instability and its relationship to the the q–profile; the attainment of sawtooth stabilization at the highest plasma parameters; and, finally, the investigation of the interaction between the sawtooth instability and energetic particles, both in relation to fusion performance and to the stability of the m=1 mode.

2. The Sawtooth Instability

In JET, sawteeth are accompanied by a variety of mhd activity [1] which may give rise to island–like structures with poloidal and toroidal mode numbers m=n=1. However, these do not appear to play a role in the sawtooth instability, which occurs as a rapidly growing helical deformation of the plasma core, also with m=n=1, followed by a flattening of temperature and density profiles across the central plasma, the entire event having a timescale of ~100μs. The topology of the sawtooth collapse in JET, as first elucidated by tomographic analysis of soft X–ray (SXR)

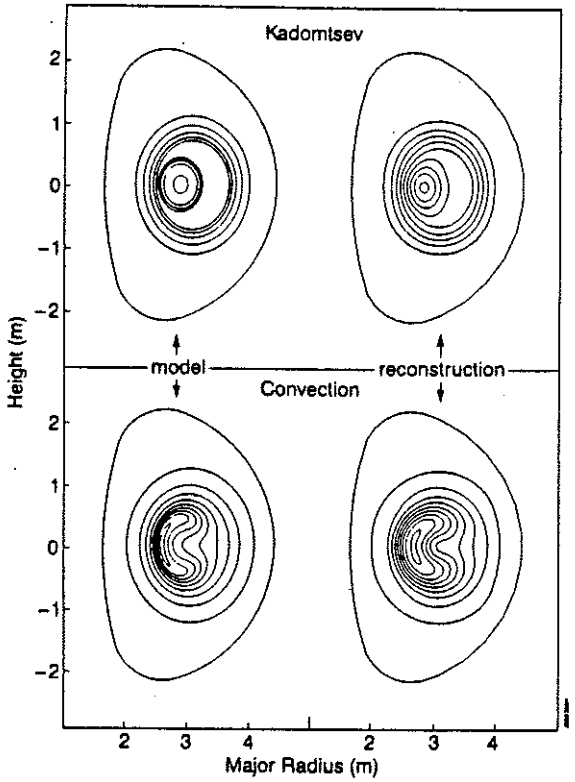

FIG 1: *Comparison of simulated soft X–ray analyses of the two most common models for the sawtooth collapse: full–reconnection (Kadomtsev) and 'quasi–interchange' (convection).*

emission measurements made with orthogonal cameras [5], resembles the convective flow of plasma suggested by the 'quasi–interchange' model [6] rather than the behaviour proposed by full–reconnection models (e.g. [7]).

Recently, possible limitations of the SXR analysis, particularly in relation to its poloidal resolution, have been explored by simulation of the behaviour expected from different models of the collapse [8]. In these investigations, flow patterns predicted by the 'quasi–interchange' and full reconnection models were used to generate SXR emission profiles and the line–integrated measurements which would be obtained from the X–ray cameras. The 'observations' were analyzed to produce tomographically inverted profiles such as those derived experimentally. The results are illustrated in figure 1, which shows the input and output flow patterns. There are clear differences between the reconstructions which enable the topologies associated with the two models to be unambiguously distinguished. More generally, it was found that, for the case commonly studied in JET (in which the plasma core is displaced along the major radius), the analysis technique accurately reproduced the emission profiles.

Further confirmation of the topology of the sawtooth collapse was obtained from two–dimensional reconstructions of local temperatures derived from electron cyclotron emission (ECE) measurements obtained with a 12–channel grating polychromator [9]. The method exploits the rotation of mhd structures using assumptions about their helical symmetry (for sawteeth, it is assumed that reconstructed modes have m=n) [10]. Application of the technique is, therefore, restricted to cases where the structure changes on a timescale somewhat greater than its rotational

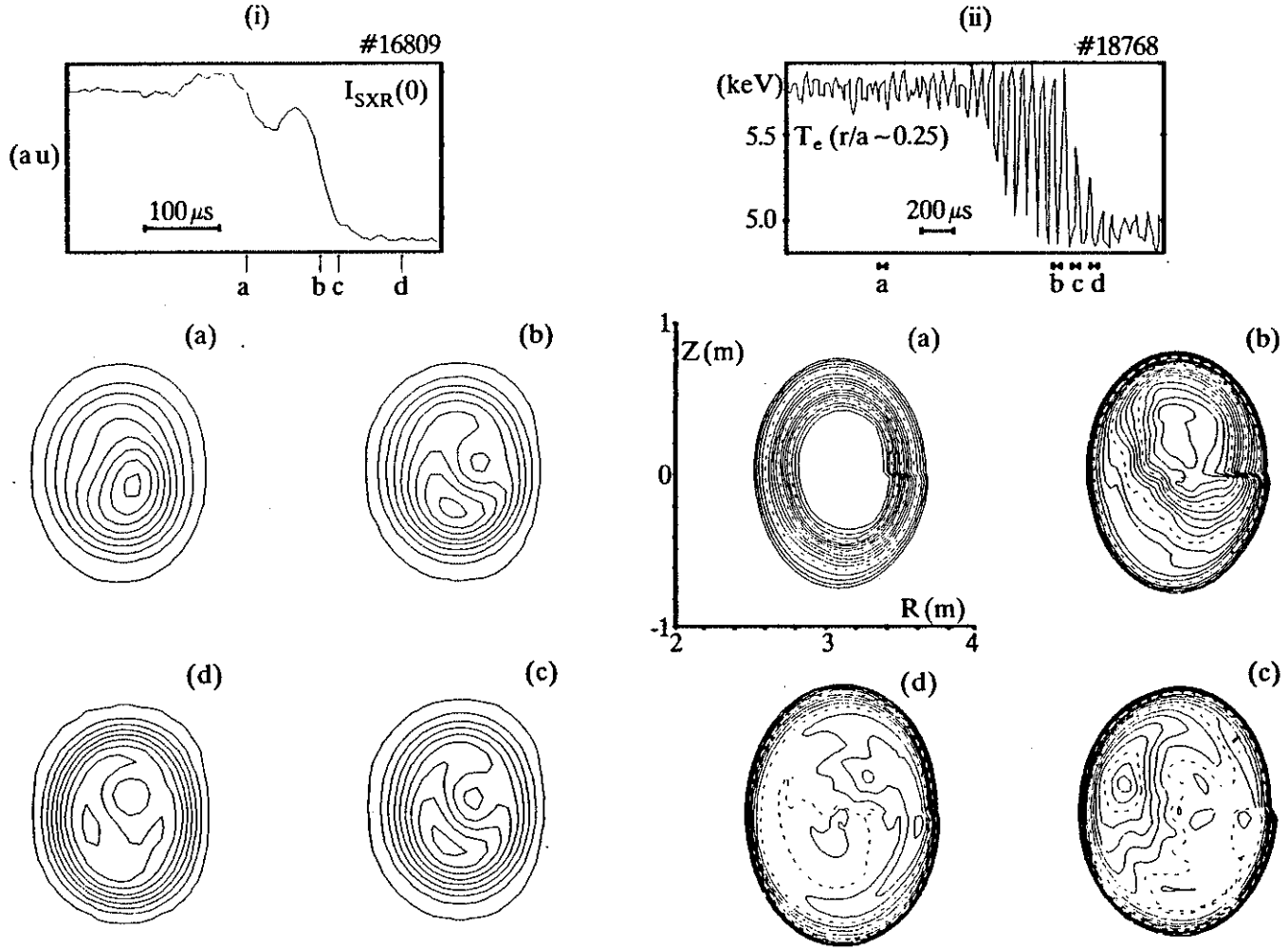

FIG 2: *Comparison of two–dimensional reconstructions of the rapid sawtooth collapse in JET as obtained by:*

(i) soft X–ray tomography

and

(ii) ECE reconstructions

The reconstructions, which were derived from data obtained on similar discharges, show a convective rather than a reconnection behaviour.

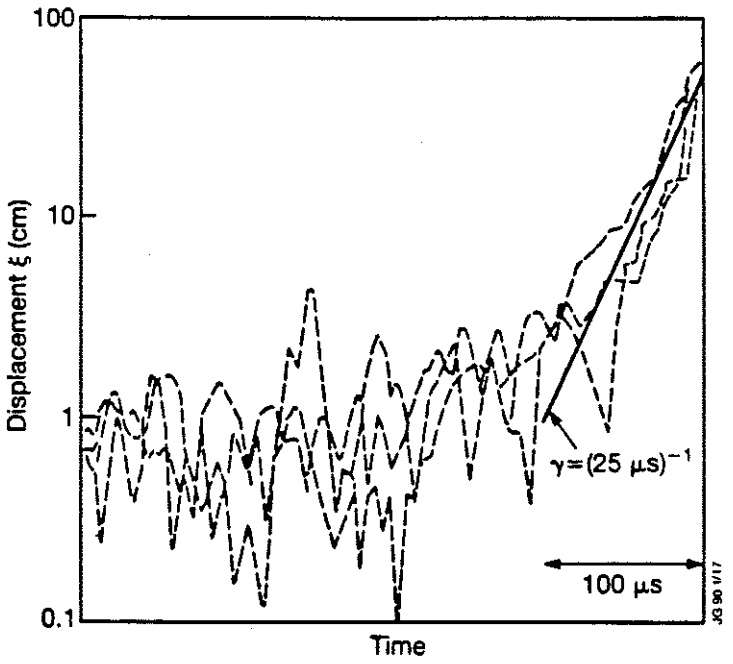

FIG 3: *The displacement of the peak of the soft X–ray emission, derived from two–dimensional tomographic reconstructions, during the fast sawtooth collapse. Experimental results for three cases are illustrated. The data shows that a growth rate of $(25\mu s)^{-1}$ is achieved even before the displacement is large enough to be detected above the experimental noise.*

period. For example, analysis of the sawtooth collapse requires rotational frequencies of ~10–20kHz and is limited to discharges with high power NBI. Figure 2 compares an ECE reconstruction of a sawtooth collapse with a SXR tomographic reconstruction from a similar discharge. Both show the formation of a crescent–shaped, or 'convective', structure.

It has been recognized for some time (e.g. [6]) that the rapid timescale of the sawtooth collapse presents a significant challenge to theoretical models. More fundamentally, it is found that the rapid growth of the m=1 arises spontaneously and cannot be explained by the increase of a linear growth rate arising from the evolution of the plasma equilibrium [11]. Figure 3 shows the growth of the instability, as deduced from the displacement of the peak of tomographically inverted SXR profiles, for three sawtooth collapses in different discharges. The initial noise level is ~1cm and the displacement rises out of this noise with a growth rate $\sim(25\mu s)^{-1}$. Extrapolation of this growth backwards in time yields a displacement equal to the Debye length, perhaps the smallest realistic scale for the instability, on a timescale of order $\sim 100\mu s$. In contrast, existing models of the instability involve changes in quantities such as q or β which would require timescales ~100ms to generate such large growth rates.

3. Current and Safety Factor Profiles

The determination of the q–profile or, perhaps more precisely, the way in which the q–profile is modulated by sawtooth activity, is one of the central problems in understanding sawteeth. On JET, the principal diagnostic of

the q–profile is a multichannel far–infrared interferometer/ polarimeter. A new analysis of the polarimetric signals [12], which combines the constraints imposed by polarimetric measurements of the internal poloidal fields with external magnetic measurements in a self–consistent equilibrium calculation, has confirmed earlier conclusions that q_0 remains well below unity (0.75 ± 0.15) during normal sawteeth.

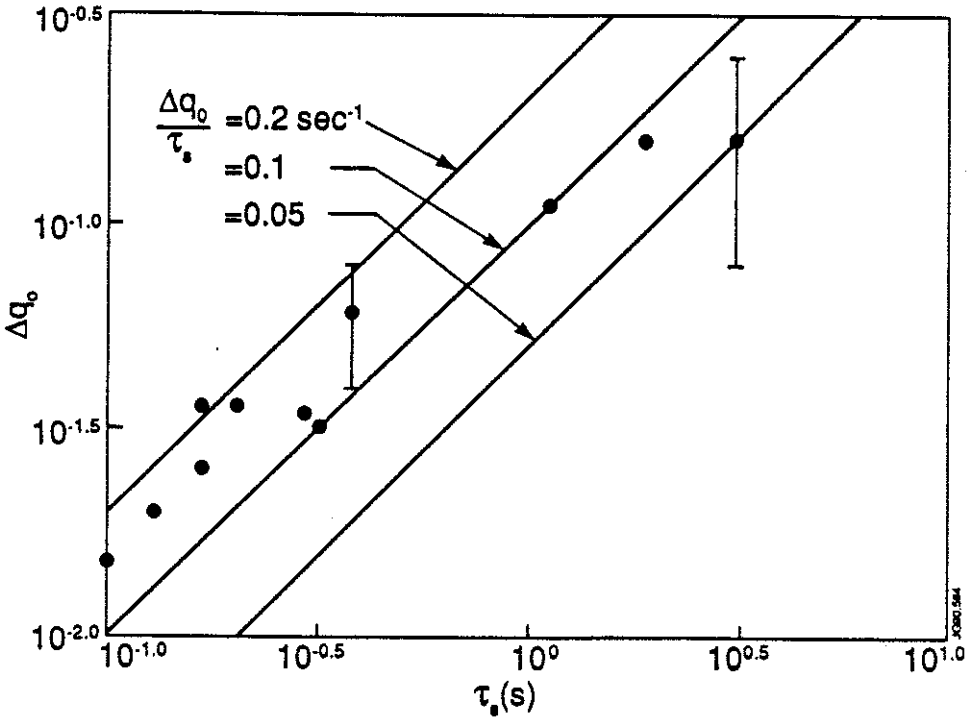

FIG 4: *Plot of the change in the central safety factor, Δq_0, vs the time between sawtooth collapses, τ_s, derived from polarimetric measurements.*

By Abel–inverting the difference in polarimetric signals before and after a sawtooth collapse, it has been possible to study the variation of q_0 during both sawteeth and sawtooth–free periods. As the sawtooth period is significantly longer than the integration time of the diagnostic electronics, sawteeth are visible in the raw data, so that coherent averaging over many sawteeth is unnecessary. Results of this analysis for a series of discharges with ohmic and ICRF heating are shown in Figure 4. It is found that Δq_0 increases with τ_s, the time between sawtooth collapses, at a rate of $0.05 - 0.2 s^{-1}$. Further confirmation of such modulation of the central q–profile has been obtained by analysis of the expansion of the sawtooth inversion radius with increasing sawtooth duration. The difference in the inversion radii, Δr_i, of successive sawtooth collapses was deduced from tomographically inverted SXR emission profiles and a relationship $\Delta r_i / \Delta \tau_s = 0.06 ms^{-1}$ obtained.

A major inconsistency remains, however, in our understanding of the behaviour of the q–profile during sawtooth activity. The most direct determination shows that q_0 remains well below unity during sawteeth, and does not return to unity at sawtooth collapses, a result which is supported by the observation of m=1 magnetic structures immediately following the sawtooth collapse. In contrast, measurements of shear at the

q=1 surface, as inferred from observations of the 'snake' [13] and of pellet ablation [14], indicate that very low values of shear ($dq/dr \sim 5\times10^{-2}$) persist throughout the sawtooth cycle. Simple considerations of resistive diffusion suggest that such persistence implies the existence of a low shear region across the plasma centre, with q_0 within 1–2% of unity. Such a conclusion would also be consistent with the convective flow observed during the sawtooth collapse in JET.

4. Sawtooth Stabilization

Several techniques for sawtooth stabilization have been investigated in JET, and another, lower hybrid current drive, is currently being commissioned. Sawteeth have been suppressed for up to 5s following the injection of pellets, both in the current rise phase and during the flat–top. As is illustrated in figure 5, polarimetric measurements of q_0 indicate that sawtooth suppression is due to a broadening of the current profile, leading to $q_0 > 1$, which results from the substantial changes in electron temperature produced by pellet ablation. This is supported by observations of mhd activity with mode numbers (m,n) = (3,2) and (2,1) deep in the plasma core.

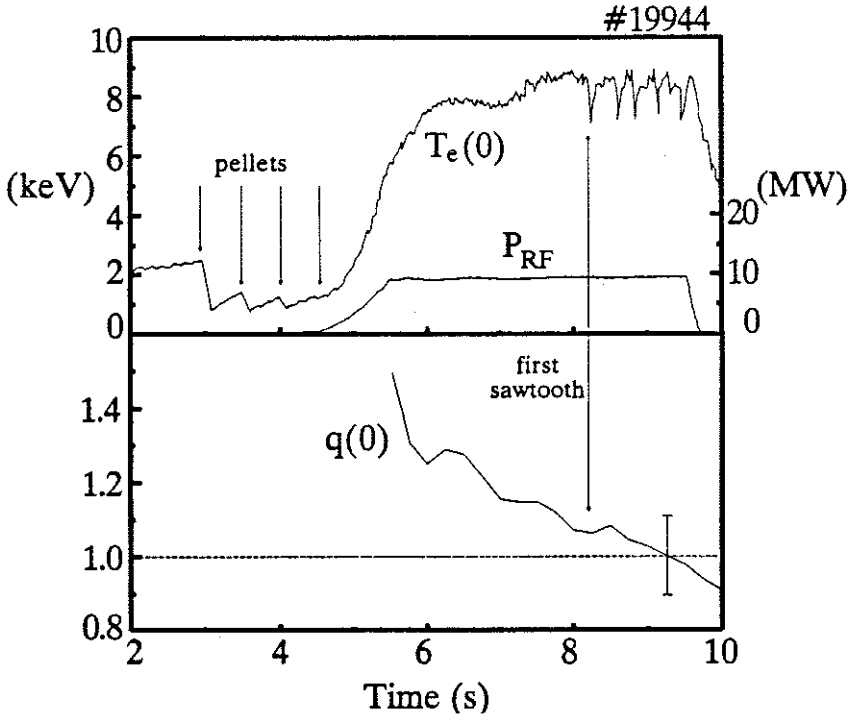

FIG 5: *Suppression of sawtooth activity following pellet injection in JET. Polarimetric measurements indicate that the suppression is due to q_0 remaining above unity.*

The 'monster' sawtooth regime [3], in which sawteeth are stabilized as a result of central heating, has been the subject of detailed investigations. By scanning the position of the ICRH resonance across the plasma centre, it has been found that stabilization is produced most efficiently (i.e. the longest stable periods are obtained for a given power) when the heating

resonance is located at the magnetic axis. In addition, stabilization is achieved only for heating inside the sawtooth inversion radius. The results of this experiment are shown in figure 6, where the longest stable period observed is plotted against the major radius of the heating resonance. In each case, the corresponding sawtooth inversion radius is indicated. It has also been observed that stabilization is most probable at low ICRH minority concentrations, when the stored energy in the fast particle population is maximized.

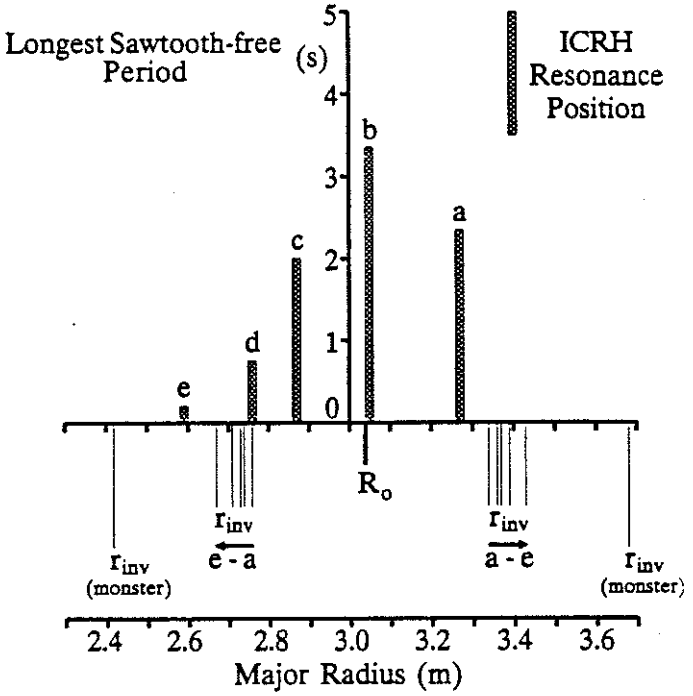

FIG 6: *Results of a scan of the ICRH resonance position. The longest sawtooth–free period at each resonance position is plotted against the resonance major radius. The sawtooth inversion radius (r_{inv}) is indicated for each case, as is the inversion radius of the longest 'monster' sawtooth.*

In 3MA discharges with $q_\psi \sim 4$, stable periods of up to 5s have been obtained and previously reported observations [1] that q_0 is significantly below unity ($q_0 \sim 0.6$–0.8 ± 0.15) have been confirmed. In addition, long sawtooth–free H–modes are now produced routinely during ICRF and ICRF/ NBI combined heating of X–point plasmas. However, stabilization by this technique becomes more difficult as the edge safety factor decreases ($q_\psi < 4$). To extend the regime to higher current, therefore, auxiliary heating has been applied during the current rise phase, either just before or just after sawteeth start. The high electron temperature attained is expected to slow the inward diffusion of current, but the smaller radius of the q=1 surface at such times may also be a significant factor. This approach has succeeded in extending stabilization to plasma currents of 5–6MA (see e.g. [15]).

5. Interaction of Sawteeth and Energetic Particles

Interactions between the sawtooth instability and energetic particle populations, produced either by auxiliary heating or by fusion reactions,

are of growing importance as fusion plasmas approach breakeven conditions. For example, considerable attention has been given to the suggestion [16] that energetic ions, accelerated by RF fields, might be responsible for sawtooth stabilization in the 'monster' sawtooth regime. This process can occur when the average fast ion energy, E_h, is such that the bounce–averaged magnetic drift frequency of deeply trapped fast ions, $\omega_{Dh} = E_h/Z_h eB_\varphi R_o r_1$, exceeds the mode frequency in the plasma rest frame (Z_h is the hot ion charge, B_φ the toroidal magnetic field, R_o the plasma major radius and r_1 the radius of the q=1 surface).

A growing body of experimental evidence is now consistent with this interpretation. Not only is it known that ICRF minority heating in JET can accelerate minority ions to energies of order 1MeV, well above the relevant energy threshold (<100keV), but several experimental observations are as expected from theory. The result that stabilization is produced most efficiently with on–axis heating is consistent with the requirement that the hot ion pressure profile be peaked. As noted previously, low minority concentrations, corresponding to high stored energy in the fast ions, are also optimal for attaining stabilization. The difficulty experienced in producing stabilization as q_ψ falls below values ~4 can be associated with the prediction that the maximum stable values of β_p and β_{ph} scale as $(r_1/a)^{-\alpha}$, where $\alpha = 1.5$ for β_p and $2.0 < \alpha < 2.5$ for β_{ph}. Moreover, this observation stimulated the development of the current–rise heating scenario, which takes advantage of the smaller q=1 radius in the initial phase of plasma development to extend the stabilization to higher currents and lower values of q_ψ. Perhaps the most direct evidence for the role played by fast ions is the observation that, following switch–off of RF heating, a sawtooth collapse terminates the stable period within 200ms (often far less), i.e. on a timescale which is of the order of the average fast ion slowing down time within the q=1 radius.

Quantitative investigation of the theory is limited by difficulties associated with the determination of the fast ion distribution in space and energy, with uncertainties in the q–profile and with the general uncertainty surrounding the nature of the sawtooth instability. Nevertheless, by making several simplifying assumptions, essentially that certain local quantities can be approximated by global parameters, such a quantitative comparison between theory and experiment has been performed [17]. The analysis is performed in the (Γ, H) plane, where,

$$\Gamma = \frac{\gamma_{mhd}}{\omega_{Dh}^{max}} \qquad H = \frac{r_1}{s_o R_o} \frac{\omega_A}{\omega_{Dh}^{max}} <\beta_{ph}>_a. \qquad (1)$$

γ_{mhd} is the ideal mhd growth rate, ω_{Dh}^{max} the maximum fast ion precession frequency as defined previously, ω_A the Alfvén frequency, s_o the shear at the q=1 radius and $<\beta_{ph}>_a$ the poloidal beta associated with the perpendicular fast ion energy (which, for central ICRH, is a reasonable measure of the fast ion energy within the q=1 radius).

Results of this analysis are shown in figure 7, where the area enclosed by the curve represents the stable region and the dashed lines indicate the trajectories followed by discharges as the q=1 radius expands during a

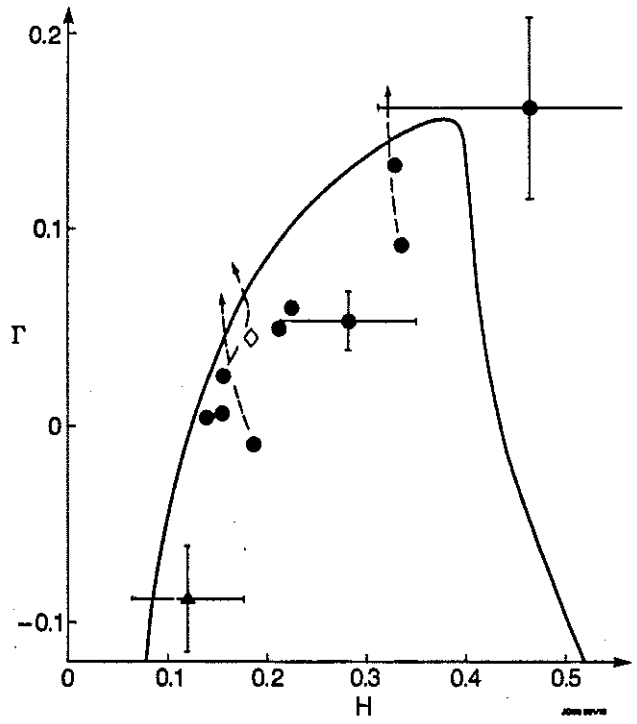

FIG 7: *Analysis of a series of sawtooth–free discharges in terms of the fast–particle stabilization theory [16,17]. Γ and H are defined in the text. The solid curve encloses the region predicted to be stable. The dashed lines indicate the trajectories of the discharges in the stability diagram as the q=1 radius expands during the sawtooth–free period.*

sawtooth–free period. Closed circles represent discharges in a variety of conditions ($4 \leq q_\psi \leq 9$, $7 \leq P_{RF} \leq 10$MW, $<n_e> = 2–3\times10^{19}m^{-3}$) where stabilization is readily obtained. The closed triangle corresponds to a pulse in which stabilization was obtained at the lowest power to date (P_{RF} ~ 1.2MW) and the open symbol to one of the longest sawtooth free periods (5s). Both pulses had q_ψ ~ 4.5. As is indicated, the experimental uncertainties in the calculations are large, and significant approximations have been applied to the theory to facilitate the analysis. Nevertheless, in the light of the more detailed experimental observations outlined above, the theory provides a working hypothesis for the development of an understanding of the stabilization mechanism.

In JET plasmas with ohmic and ICRF heating, neutron emission is modulated in accordance with expectations based on the redistribution of ion thermal energy at the sawtooth collapse. However, the major contribution to the fusion yield of high performance discharges is non–thermal in nature and is due to beam–plasma and beam–beam reactions. The modulation of the reactivity due to m=1 activity and, in particular, the way in which m=1 instabilities affect energetic ions is, therefore, central to the optimization of fusion reactivity. While 'fishbone'–like bursts are observed in both NBI– and ICRF–heated plasmas [18], only at the highest β_t values is there evidence of detectable (<10%) modulation of neutron production. However, recent studies of neutron emission profiles derived by tomographic analysis of measurements obtained from orthogonal arrays of neutron detectors has revealed a strong modulation of central neutron production due to sawteeth [19].

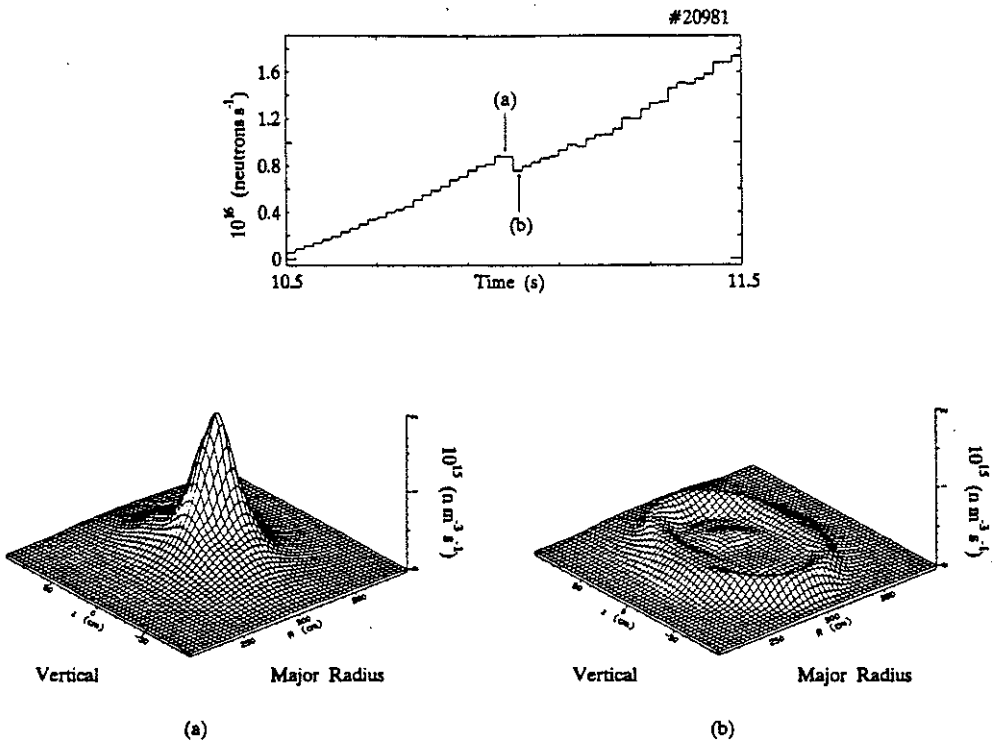

FIG 8: *Comparison of local neutron emission profiles measured before and after a sawtooth collapse. Although the global neutron emission falls by only 18%, the axial emission falls by a factor of 6.*

Figure 8 shows neutron emission profiles calculated at timeslices just before and just after a sawtooth collapse in a JET hot–ion H–mode plasma heated with 18MW of NBI. While the modulation of the global neutron yield is small, ~18%, it is found that the emission profile is changed dramatically, the FWHM broadening from 0.36m before to 1.2m after the collapse. In addition, the axial neutron emission falls by a factor of 6, from $1.9\times10^{15}m^{-3}s^{-1}$ to $2–3\times10^{14}m^{-3}s^{-1}$. Calculations show that, in this case, the emission is almost entirely non–thermal and that the ratio of beam–plasma to beam–beam reactions is 2:1. The fall in central emission can be explained, therefore, by a substantial redistribution of the fast, beam–injected ions to large minor radii, the redistribution occurring on a timescale of < 1ms.

6. Discussion

A complete understanding of the sawtooth instability remains elusive, but several key diagnostic observations of the sawtooth collapse phase have been confirmed. Thus, the initial phase of the collapse, which resembles the convective behaviour predicted by the 'quasi–interchange' model, has now been observed in SXR and ECE reconstructions. However, the rapid timescale of the collapse and, more fundamentally, the rapid switch–on of the instability, are not understood.

Measurements of the q–profile show that q_0 remains well below unity throughout the sawtooth cycle. The persistence of a q=1 surface is further confirmed by observations of the 'snake' and of other long–lived m=1

structures. However, the topology of the sawtooth collapse implies that $q_0 \simeq 1$, as does the observation, derived from pellet ablation measurements, that a region of very low shear exists close to the q=1 surface at all phases of the sawtooth. More precise measurements of the evolution of the q–profile during sawteeth are required to resolve this basic inconsistency.

Sawtooth stabilization, lasting for up to 5s, is now routinely obtained in L– and H–mode plasmas and at currents of up to 6MA. Its importance has been emphasized by recent demonstrations of local modulation of fusion reactivity and the redistribution of high energy ions due to sawteeth. In cases where stabilization follows pellet injection, the dominant effect is the modification of the current profile, due to pellet ablation, which causes q_0 to rise above unity. On the other hand, in the 'monster' sawtooth regime q_0 is below unity and there is growing evidence that the stabilization is due to an energetic particle population.

7. Acknowledgements

It is a pleasure to acknowledge contributions to this work and many helpful discussions with our colleagues in the JET Project.

8. References

[1] Campbell, D.J., et al, *"Sawtooth activity and current density profiles in JET"*, Plasma Physics and Controlled Nuclear Fusion Research 1988 (Proc. 12th Int. Conf. Nice, 1988) Vol. 1, IAEA, Vienna (1989) 377.

[2] Söldner, F.X., et al, *Suppression of sawtooth oscillations by lower hybrid current drive in the ASDEX tokamak*, Phys. Rev. Lett. **57** 1137 (1986).

[3] Campbell, D.J., et al, *Stabilization of sawteeth with additional heating in the JET tokamak*, Phys. Rev. Lett. **60** (1988) 2148.

[4] Schmidt, G.L., et al,*"Heating of peaked density profiles produced by pellet injection in JET"*, ibid. [1] Vol. 1, 215.

[5] Edwards, A.W., et al, *Rapid collapse of a plasma sawtooth oscillation in the JET tokamak*, Phys. Rev. Lett. **57** (1986) 210.

[6] Wesson, J.A., et al, *"Sawtooth oscillations"*, Plasma Physics and Controlled Nuclear Fusion Research 1986 (Proc. 11th Int. Conf., Kyoto, 1986) Vol. 2, IAEA, Vienna (1987) 3.

[7] Kadomtsev, B.B., *Disruptive instability in tokamaks*, Fiz. Plazmy **1** (1975) 710.

[8] Wolfe, S.W., et al, *"The detailed topology of the m=1 instability in the JET sawtooth collapse"*, Controlled Fusion and Plasma Heating (Proc. 17th Euro. Conf., Amsterdam, 1990) Vol. 14B(I), Euro. Conf. Abstracts (1990) 335.

[9] Campbell, D.J., et al, *"Sawteeth and the m=1 mode in JET"*, Controlled Fusion and Plasma Heating (Proc. 16th Euro. Conf., Venice, 1989) Vol. 13B(II), Euro. Conf. Abstracts (1989) 509.

[10] Westerhof, E., et al, *Observations of sawtooth postcursor oscillations in JET and their bearing on the nature of the sawtooth collapse*, Nucl. Fus. **29** (1989) 1056.

[11] Wesson, J.A., et al, *Spontaneous m=1 instability in JET sawtooth collapse*, JET Preprint JET–P(90)03, 1990 (to be published).
[12] O'Rourke, J. and Lazzaro, E., *"Faraday rotation measurements on JET, and the change in the safety factor profile during a sawtooth collapse"*, ibid [8] Vol. 14B(I), 343.
[13] Weller, A., et al, *Persistent density perturbations at rational–q surfaces following pellet injection in the Joint European Torus*, Phys. Rev. Lett. **59** (1987) 2303.
[14] Gill, R.D., et al, *Determination of the shear on the q=1 surface of the JET tokamak*, Nucl. Fus. **29** (1989) 821.
[15] Lomas, P.J., et al, *"Optimisation of performance in JET Limiter Plasmas"*, Paper IAEA–CN–53/A–6–2, this Conference.
[16] Pegoraro. F., et al, *"Theory of sawtooth stabilisation in the presence of energetic ions"*, ibid. [1] Vol. 2, 243.
[17] Porcelli, F., et al, *"Sawtooth stabilisation by fast ions: comparison between theory and experiments"*, ibid [8] Vol. 14B(I), 327.
[18] Nave, M.F.F., et al, *Fishbone activity in JET*, JET Preprint JET–P(90)32, 1990 (to be published).
[19] Marcus, F.B., et al, *"JET neutron emission profiles and fast ion redistribution from sawteeth"*, ibid [8] Vol. 14B(I), 331.

IAEA-CN-53/D-1-4

Self-Consistent Magnetic Chaos induced by Electron Temperature Gradient

by

M Hugon and P-H Rebut

JET Joint Undertaking, Abingdon,
Oxon, OX14 3EA, UK

Self-Consistent Magnetic Chaos induced by Electron Temperature Gradient

Abstract

Two mechanisms for the self-sustainment of magnetic islands are studied in cylindrical geometry. The first one is based on the different behaviour of electrons and ions in the presence of the islands as a result of their different Larmor radii. This mechanism could maintain magnetic turbulence resulting from a mixture between islands of the size of the ion Larmor radius and chaotic regions. The second mechanism is a pseudo-gravity, used here as a simple analogue for pressure gradient/field curvature modes. It could sustain islands much larger than the ion Larmor radius.

1. INTRODUCTION

There is no agreed explanation of the observed particle and energy losses in tokamaks. One possible cause for these losses is magnetic turbulence, which allows transport along chaotic field lines linking different regions of the plasma [1,2]. The magnetic turbulence could result from a mixture of small islands and chaotic regions [3].

This paper investigates two mechanisms for the self-sustainment of magnetic islands in a collisionless plasma in the cylindrical case. The first one results from the different response of electrons and ions to the islands due to their different Larmor radii. This effect requires a minimum threshold, since it is dependent on the presence of magnetic chaos [4]. The second one is a

pseudo-gravity, which is here used as a simple analogue for pressure gradient/field curvature modes. The electron and ion drift velocities, associated with the pseudo-gravity, combine to produce the current sustaining the island. As this mechanism does not depend on the existence of magnetic chaos, it has no threshold. These effects have been also studied for non linear microtearing modes with a transverse particle diffusion [5].

The magnetic topology is first defined: it consists of islands separated by nested magnetic surfaces or by a chaotic region. Quasi-neutrality is imposed both inside and outside an island to determine the perturbed potential. This potential produces a net diamagnetic current and the divergence of this current drives an electron current along the field lines thus maintaining the island. Finally, Ampère's law for the island leads to the self-sustainment condition.

2. MAGNETIC TOPOLOGY

The calculation is made in a slab geometry with the coordinates $x = r - r_s$ and $y = r_s(\theta - z/q_s R) = \Theta/k_y$, where r, θ and z are the cylindrical coordinates. r_s is the radius of the resonant surface, R is the major radius of the plasma and q_s is the safety factor at $r = r_s$. The poloidal wave number is $k_y = m/r_s$, where m is the poloidal mode number.

The overlapping parameter γ is the ratio of the virtual island width 2ε to the distance between two island chains $\Delta = 1.5q^2/q' m\delta m$, where q' is the shear and δm is the range of poloidal mode numbers around m . For $\gamma < 0.75$ the topology consists in islands separated by nested magnetic surfaces, for $0.75 < \gamma < 1.50$ the islands are embedded in a chaotic zone and for $\gamma \gtrsim 1.50$ the system

is fully chaotic [6]. Fig.1-a shows part of a Poincaré map computed by integrating the field line equations with $\gamma = 1.05$. The island is defined by its poloidal extension $2\Theta_0/k_y \leq 2\pi/k_y$ and its radial width $2b_0 \leq 2\varepsilon$. It is assumed to be thin, that is $k_y\, b_0 \ll 1$.

A first integral does not exist in the chaotic zone shown in Fig.1-a. However, the vector potential needs to be defined in this region to calculate the effect of both mechanisms investigated here. This is done by modelling the region outside the island by nested surfaces as represented in Fig.1-b. This defines an approximate magnetic flux $\mathcal{A}^*_z$, which is only used to calculate the perturbed electric potential imposed by the presence of the island:

$$\begin{cases} \mathcal{A}^*_z(x,y) = \dfrac{B'_0}{2}\, x^2 + \dfrac{\tilde{\tilde{B}}}{k_y}\, A(x,y) = \left(- \dfrac{\tilde{\tilde{B}}}{k_y} \right) \mathbb{A}(x,y) \\ \\ \mathbb{A}(x,y) = 2\, \dfrac{x^2}{b_0^{\,2}} - A(x,y) \end{cases} \qquad (1)$$

where $B'_0 = (r_s q'(r_s)/R q_s^{\,2}) B_z$ is the shear factor, B_z being the toroidal field, and $\tilde{\tilde{B}}$ is the amplitude of the perturbing radial field. From symmetry, A(x,y) is an even function of y with a period $2\pi/k_y$. It is independent of x and equal to $a(y)$ inside the island. The last closed surface of the island is defined by $\mathcal{A}^*_z(x,y) = 0$ and its radial coordinates are given by:

$$b(y) = b_0 \sqrt{a(y)/2} \qquad (2)$$

3. QUASI-NEUTRALITY CONDITION

The particles have a charge q_j (j = e,i) and are assumed to experience a fictitious gravitational potential ϕ_{Gj}, which is given by:

$$\phi_{Gj} = - G_j x \qquad \text{with:} \quad q_j G_j > 0 \qquad (3)$$

For $\gamma \gtrsim 0.75$, quasi-neutrality is ensured in the chaotic region by equating the electron to the ion flow. This leads to the radial electric field E_0 in the reference frame rotating with the islands:

$$E_0 = \frac{KT_e}{q_e}\left(\frac{n'_e}{n_e} + \frac{1}{2}\frac{T'_e}{T_e}\right) - G_e \qquad (4)$$

K is the Boltzmann constant. n'_e and T'_e are the average gradients of electron density n_e and temperature T_e.

When the ion Larmor radius $\rho_i = \sqrt{m_i KT} \;/\; q_i B_z$ is of the order of the island half-width b_0, the potential ϕ_i experienced by the ions can be expressed as:

$$\phi_i = - E_0 x + b_0 (E_0 + G_i) \int_{-\infty}^{+\infty} G(x-x') \, \tilde{\varphi}(x',y) \, dx' \qquad (5)$$

The perturbed potential $\tilde{\varphi}(x,y)$ is dimensionless and the integral containing G(x-x') is the finite ion Larmor radius operator. This operator is derived by averaging the Fourier components of the perturbed electric field over a gyroperiod and the phase of the motion of a single ion and over a maxwellian distribution of velocities.

As the electron Larmor radius is much smaller than b_0, the electric potential ϕ_e felt by the electrons is given by:

$$\phi_e = - E_0 x + b_0 (E_0 + G_i) \, \tilde{\varphi}(x,y) \qquad (6)$$

The ion density n_i is a function of the potential $\phi_i + \phi_{Gi}$ and the electron density n_e depends on $\phi_e + \phi_{Ge}$ and on the approximate magnetic flux $\mathcal{A}^*_z$. $\mathcal{A}^*_z$ is an even function of x (see Eq.(1)) and only the part of $\tilde{\varphi}(x,y)$, which is odd with respect to x, contributes to the current sustaining the island (see Section 4). A function of $\mathcal{A}^*_z$, odd with respect to x, is formed by taking the square

root of $\mathbb{A}(x,y)$ defined by Eq.(1). As $\mathbb{A}(x,y)$ is negative inside the island and positive outside, n_e is assumed to be independent of $\mathcal{A}_z^*$ inside the island, but to depend on the odd function $\pm\sqrt{\mathbb{A}}$ outside, where the upper symbol refers to $x \geq b(y)$ and the lower symbol to $x \leq -b(y)$.

The perturbed potential $\tilde{\varphi}(x,y)$ is determined by imposing quasi-neutrality $n_e = n_i$ inside and outside the island. n_e and n_i are expanded at first order as a function of $\phi_e + \phi_{Ge}$ and $\pm\sqrt{\mathbb{A}}$ and of $\phi_i + \phi_{Gi}$ respectively in the vicinity of 0. Replacing these quantities by their definitions given by Eqs.(1), (3), (5) and (6) leads to two integral equations satisfied by $\tilde{\varphi}(x,y)$. A good approximation for the solution of these equations writes:

$$\tilde{\varphi}(x,y) = \frac{\frac{1}{2}\frac{T'_e}{T_e}}{\frac{n'_e}{n_e}\left(1 - \overline{J_0^2}\right) + \frac{1}{2}\frac{T'_e}{T_e} - \left(\frac{q_e G_e + q_i G_i}{KT_e}\right)} \frac{x}{b_0}\left(1 - \mathcal{P}\sqrt{1 - \frac{b_0^2 a(y)}{2x^2}}\right) \qquad (7)$$

with: $\mathcal{P} = \begin{cases} 0 \text{ for } -b(y) \leq x \leq b(y) \\ 1 \text{ for } x \leq -b(y) \text{ and } x \geq b(y) \end{cases}$

$\overline{J_0^2}$ is an approximation for the finite ion Larmor radius operator, which is defined by:

$$\overline{J_0^2} = e^{-(\rho_i/b_0)^2} I_0\left[(\rho_i/b_0)^2\right] \qquad (8)$$

where $I_0(z)$ is one of the modified Bessel functions of zeroth order. $\overline{J_0^2}$ is equal to 1 for very small Larmor radii ($\rho_i \ll b_0$) and tends toward zero for very large ρ_i ($\rho_i \gg b_0$).

Eq.(7) shows that the perturbed potential $\tilde{\varphi}(x,y)$ is a function, which is odd with respect to x and which is independent of y inside the island.

The system of integral equations has been solved by

numerical iteration. The result for $\tilde{\varphi}(x,y)$ is plotted versus x/b_0 in Fig.2 in the case of $y = 0$, $\rho_i/b_0 = 1$, $n'_e/n_e = 1\ m^{-1}$, $T'_e/T_e = 2\ m^{-1}$ and $G_e = G_i = 0$.

4. CURRENT DENSITY SUSTAINING THE ISLAND

The perturbed current density sustaining the island $\delta J_{\parallel}(x,y)$ is obtained from current conservation in steady state:

$$\nabla\cdot(J_{\parallel}\mathbf{e}_{\parallel} + n_i q_i \mathbf{v}_{\mathbf{Di}} + n_e q_e \mathbf{v}_{\mathbf{De}}) = 0 \qquad (9)$$

$J_{\parallel}$ is the electron current density along the field lines, being the sum of the constant plasma current density and $\delta J_{\parallel}(x,y)$. $\mathbf{e}_{\parallel}$ is equal to $\mathbf{B}/B$. $\mathbf{v}_{\mathbf{Di}} = [-\nabla(\phi_i + \phi_{Gi})\times \mathbf{B}] / B^2$ is the ion drift velocity and $\mathbf{v}_{\mathbf{De}}$, the electron drift velocity, is given by a similar expression.

The leading term of $\nabla\cdot(J_{\parallel}\mathbf{e}_{\parallel})$ is $(-B'_0 x/B)\nabla_y \delta J_{\parallel}(x,y)$. In the limit of low β, $\nabla\cdot(n_i q_i \mathbf{v}_{\mathbf{Di}})$ is zero, because n_i is a function of $\phi_i + \phi_{Gi}$. Taking account of quasi-neutrality $n_e = n_i$, it follows that:

$$\nabla\cdot(n_e q_e \mathbf{v}_{\mathbf{De}}) = -\frac{q_e}{B^2}\,\mathbf{B}\cdot\left(\nabla n_i \times \nabla(\phi_e + \phi_{Ge})\right) \qquad (10)$$

where, since $n_i = n_i(\phi_i + \phi_{Gi})$, ∇n_i is equal to $dn_i/d(\phi_i + \phi_{Gi})\ \nabla(\phi_i + \phi_{Gi})$ with $dn_i/d(\phi_i + \phi_{Gi}) = -n'_i/(E_0+G_i)$. From the expressions for the potentials given by Eqs.(3), (5) and (6), it can be shown that the right-hand side of Eq.(10) depends on $\nabla_y\tilde{\varphi}(x,y)$. Eq.(9) is integrated with respect to y. The perturbed current density sustaining the island $\delta J_{\parallel}(x,y)$ is then given by:

$$\delta J_{\parallel}(x,y) = \frac{n'_e}{B'_0}\left(-KT_e\left(\frac{n'_e}{n_e} + \frac{1}{2}\frac{T'_e}{T_e}\right)\left(1-\overline{J_0^2}\right) + (q_e G_e + q_i G_i)\right)\frac{b_0}{x}\,\tilde{\varphi}(x,y) \qquad (11)$$

where an additive function of $\mathcal{A}^*_z$ due to integration is omitted. This function is determined by taking into account other effects such as

collisions: the resistivity is assumed to be the same inside and outside the island. Finally, $\delta J_{\parallel}$ has been computed using the data of $\tilde{\varphi}(x,0)$ shown in Fig.2 and normalised values are plotted as a function of x/b_0 in Fig.2. $\delta J_{\parallel}(x,y)$ is an even function of x.

5. MAGNETIC ISLAND SELF-SUSTAINMENT

Ampère's law for thin islands ($k_y\, b_0 \ll 1$) can be written as:

$$\frac{\tilde{\tilde{B}}}{k_y}\, \nabla_x^2 A(x,y) = -\, \mu_0\, \delta J_{\parallel}(x,y) \qquad (12)$$

The jump in the derivative of the vector potential across the region associated with the island is equal to the integral of $\delta J_{\parallel}(x,y)$ with respect to x. This leads to an equation in y and Θ_0, which is solved by computing the Fourier components of the vector potential with respect to y for different values of Θ_0 [4]. Eq.(12) then becomes:

$$\mu_0\, \frac{n_e K T_e}{B_0'^2}\, \frac{1}{2}\, \frac{T_e'}{T_e}\, \frac{n_e'}{n_e}\, \frac{\left(\frac{n_e'}{n_e} + \frac{1}{2}\,\frac{T_e'}{T_e}\right)\left(1-\overline{J_0^2}\right) - \left(\frac{q_e G_e + q_i G_i}{K T_e}\right)}{\frac{n_e'}{n_e}\left(1-\overline{J_0^2}\right) + \frac{1}{2}\,\frac{T_e'}{T_e} - \left(\frac{q_e G_e + q_i G_i}{K T_e}\right)}\, \frac{1}{k_y \Delta} = F(\Theta_0) \qquad (13)$$

The left-hand side of Eq.(13) is proportional to the poloidal β and is independent of the sign of the shear q'. The numerator of the large fraction contains two terms. The first one is due to the finite ion Larmor radius effect and is maximum, when $\overline{J_0^2}$ is zero for island widths much smaller than ρ_i. Note that $\overline{J_0^2}$ is close to 1/2 for an island width equal to $2\rho_i$. This effect has a threshold, because it is switched off, when $n_e'/n_e + (1/2)\, T_e'/T_e$ is zero, that is when islands are separated by nested magnetic surfaces for $\gamma \lesssim 0.75$ (see Eq.(4)). The second term results from the pseudo-gravity effect. It is generally smaller in modulus than the absolute values of T_e'/T_e

and n_e'/n_e. This effect is therefore dominant, when $\overline{J_0^2}$ is close to 1, that is when the island is much larger than ρ_i. It can sustain islands even when they are separated by nested surfaces for $\gamma \lesssim 0.75$, since it has no threshold. An example of pseudo-gravity is given by the interchange instabilities in the cylindrical approximation: $(q_e G_e + q_i G_i) n_e'$ is identified with $2rP_s'/(q_s R)^2$, where $r/(q_s R)^2$ is the inverse of the radius of curvature of an helix on the resonant surface at $r = r_s$ in the limit $r \ll q_s R$ and P_s' is the gradient of plasma pressure at $r = r_s$. In this case, Eq.(11) with $\overline{J_0^2} = 1$ gives the same perturbed current outside the island as the MHD equations [7].

$F(\Theta_0)$ is determined from Poincaré map computation using the Fourier components of the vector potential calculated above. Table I shows that $F(\Theta_0)$ increases, as Θ_0 decreases, that is as the island is destroyed. The minimum threshold for turbulence self-sustainment by the finite ion Larmor radius effect is $F(\Theta_0) = 0.20$, which corresponds to an overlapping parameter $\gamma \simeq 0.75$.

6. CONCLUSION

Two mechanisms have been proposed for the self-sustainment of magnetic islands. Both produce a net diamagnetic current in the region associated with the island.

The first effect is due to the difference between the electron and ion drift velocities as a result of their different Larmor radii. It could maintain a magnetic turbulence in which islands with a width of the order of the ion Larmor radius are embedded in a chaotic region. The turbulence is self-sustained, when the left-hand side of Eq.(13) is larger than 0.20.

In the second mechanism, the current results from the

addition of electron and ion drift velocities associated with the pseudo-gravity. This effect has no threshold and could sustain islands much larger than the ion Larmor radius. This result can be also directly demonstrated from the MHD equations in cylindrical geometry [7] and could be extended to ballooning modes in toroidal geometry.

7.REFERENCES

[1] Rechester A.B. and Rosenbluth M.N., Phys. Rev. Lett. 40 (1978) 38-41.

[2] Kadomtsev B.B. and Pogutse O.P., Proc. 7th Int. Conf. on Plasma Physics and Controlled Nuclear Fusion Research, Innsbruck, 1978, Vol.1, IAEA, Vienna (1979) 649-663.

[3] Rebut P.H., Brusati M., Hugon M. and Lallia P.P., Proc. 11th Int. Conf. on Plasma Physics and Controlled Nuclear Fusion Research, Kyoto, 1986, Vol.2, IAEA, Vienna (1987) 187-196.

[4] Rebut P.H. and Hugon M., submitted to Plasma Phys. Contr. Fusion.

[5] Garbet X., Mourgues F. and Samain A., Plasma Phys. Contr. Fusion 30 (1988) 343-363.

[6] Rebut P.H. and Brusati M., Plasma Phys. Contr. Fusion 28 (1986) 113-124.

[7] Rebut P.H. and Hugon M., to be published.

8.ACKNOWLEDGEMENTS

The authors are very indebted to Dr. J.Wesson for valuable comments. They also acknowledge with thanks fruitful discussions with Dr. D.Baldwin.

Table I

Numerical results for $F(\Theta_0)$ obtained from the Poincaré map computation as a function of Θ_0 and of the overlapping parameter γ.

γ	0.4	0.7	1.0	1.2	1.4
Θ_0	0.91π	0.70π	0.44π	0.32π	0.13π
$F(\Theta_0)$	0.16	0.20	0.30	0.46	2.04

Figure Captions

Fig.1: (a) Poincaré map computed for an overlapping parameter $\gamma = 1.05$ showing magnetic islands in equilibrium in a chaotic region; the island is defined by its poloidal extension $2\Theta_0/k_y \leq 2\pi/k_y$ and its radial width $2b_0$; Δ is the distance between two island chains. (b) The chaotic zone is modelled by nested magnetic surfaces to define the vector potential outside the island.

Fig.2: Result of computation of the perturbed potential $\tilde{\varphi}(x,0)$ and the current density, $\delta J_{\parallel}(x,0)$, sustaining the island versus x/b_0. The island lies between $x = -b_0$ and $x = b_0$. For this case, the ion Larmor radius ρ_i is equal to the island half-width b_0, $n'_e/n_e = 1\ m^{-1}$, $T'_e/T_e = 2\ m^{-1}$ and $G_e = G_i = 0$. $\delta J_{\parallel}(x,0)$ is normalised to $-q_e E_0 n'_e/B'_0$.

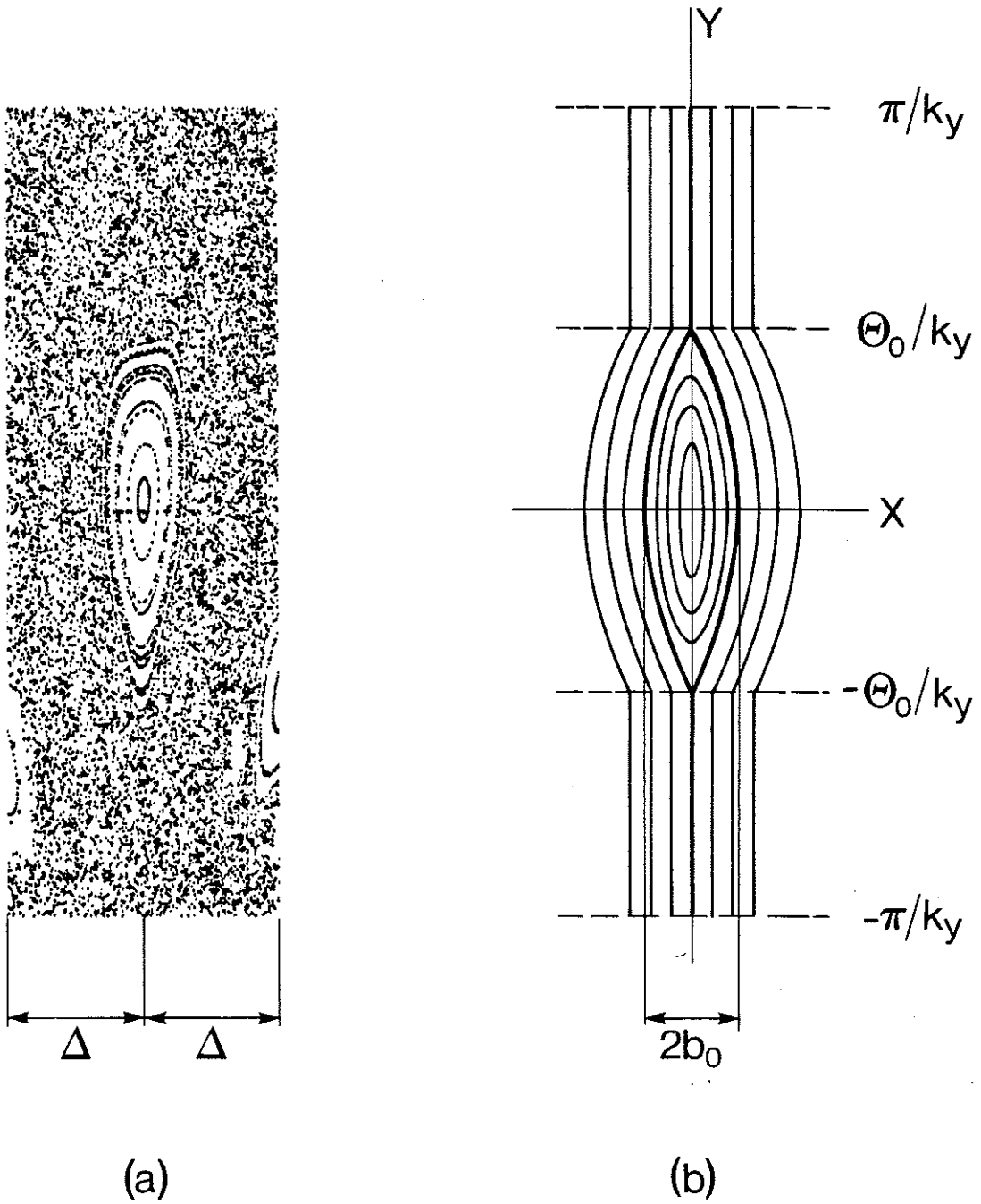

Fig.1: (a) Poincaré map computed for an overlapping parameter $\gamma = 1.05$ showing magnetic islands in equilibrium in a chaotic region; the island is defined by its poloidal extension $2\Theta_0/k_y \leq 2\pi k_y$ and its radial width $2b_0$; Δ is the distance between two island chains ; (b) The chaotic zone is modelled by nested magnetic surfaces to define the vector potential outside the island.

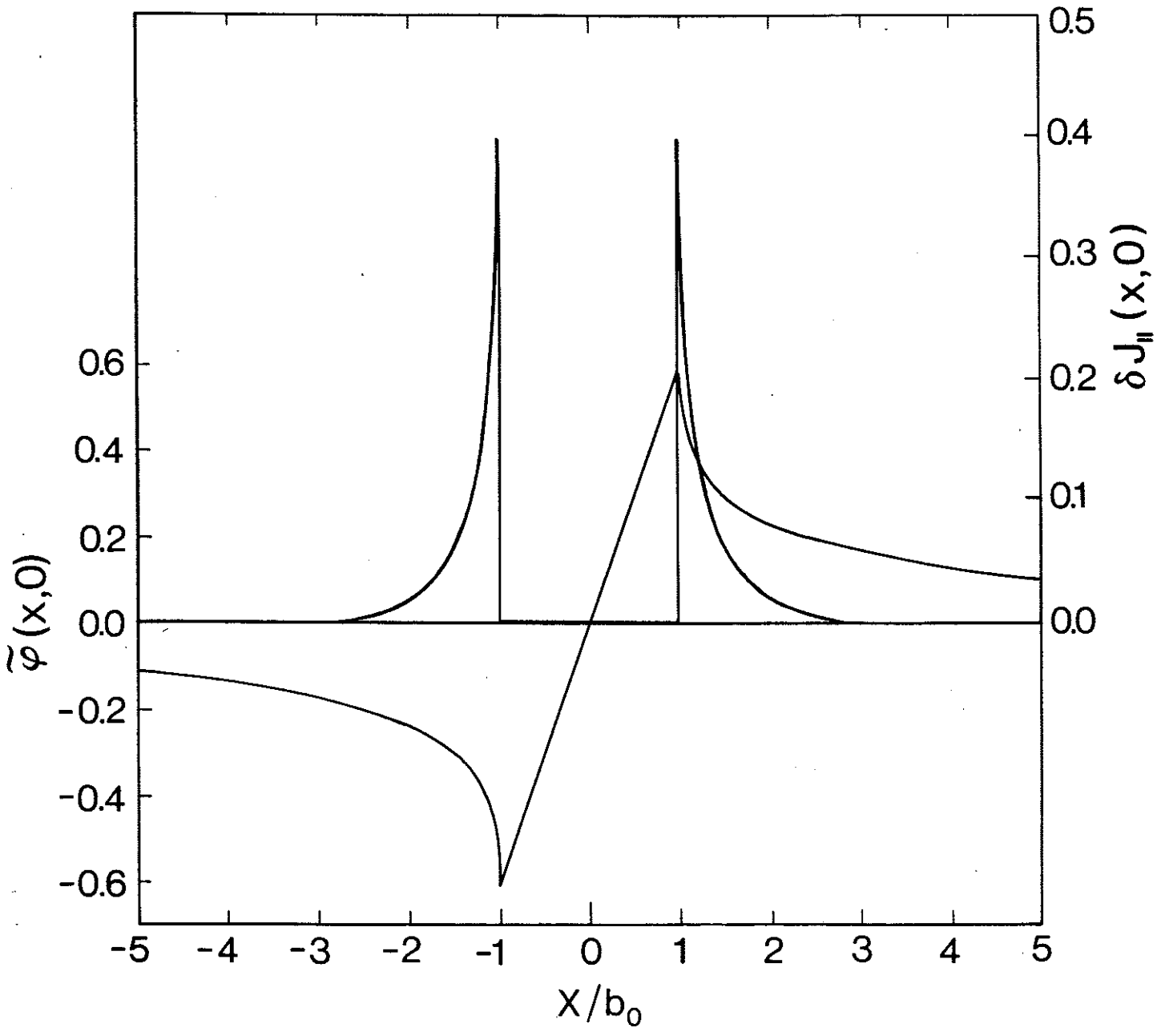

Fig.2: Result of computation of the peturbed potential $\tilde{\varphi}(x,0)$ and normalized current density, $\delta J_{\parallel}(x,0)$, sustaining the island versus x/b_0. The island lies between $x = -b_0$ and $x = b_0$. The ratio of ion Larmor radius ρ_i to island half-width b_0 is unity.

Post-Deadline Paper

Sawtooth Reconnection

by

JA Wesson

JET Joint Undertaking, Abingdon,
Oxon, OX14 3EA, UK

Sawtooth Reconnection

J.A. Wesson

JET Joint Undertaking, Abingdon, Oxon., U.K.

Abstract

Resistive mhd is inappropriate to describe tokamak sawtooth reconnection. It is found that under usual conditions the electric field resulting from flux reconnection is very large. The resulting acceleration of the electrons is such that reconnection is determined by electron inertia rather than electron collisions.

Introduction

It is well known that sawtooth oscillations are not understood. There are several features which are not in agreement with theoretical predictions based on resistive mhd. One of the discrepancies is that, in large experiments, the sawtooth collapse is an order of magnitude faster than predicted by Kadomtsev's model which is based on Sweet-Parker reconnection.

The natural response to this situation has been to examine the assumptions underlying both the theory and the experimental procedures. This has led to the realisation that use of the resistive form of Ohm's law is incorrect.

In the m=1 instability the core of the plasma is expected to behave as perfectly conducting fluid. The core moves toward the q=1 surface and drives a narrow current layer at this surface. In the layer the perfect conductivity equation is invalid and reconnection takes place. It is the behaviour in this reconnection layer which we shall examine.

Reconnection Layer

Figure 1 shows the basic geometry. The core moves toward the reconnection layer with a velocity v. The plasma enters the narrow layer, of thickness δ, and then flows out into the island region with a much higher velocity u. The pressure driving the flow comes from the perturbed helical field B^* and the strong gradient in this field implies the layer current mentioned above.

The electric field which drives this current is determined by the rate of change of the helical flux.

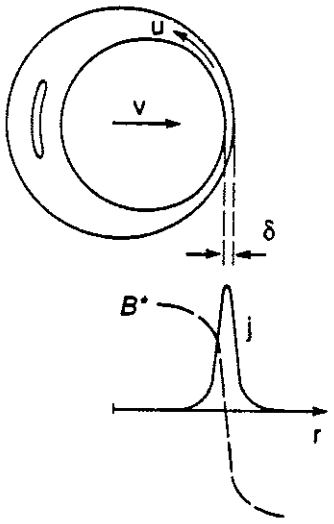

Figure 1. Diagram of reconnection model and the associated current layer.

Helical Flux

The helical flux which is reconnected is given by the magnetic field which crosses an imaginary sheet for which $d\theta/d\phi = 1$, where θ and ϕ are the poloidal and toroidal angles. Such a sheet is shown in Figure 2.

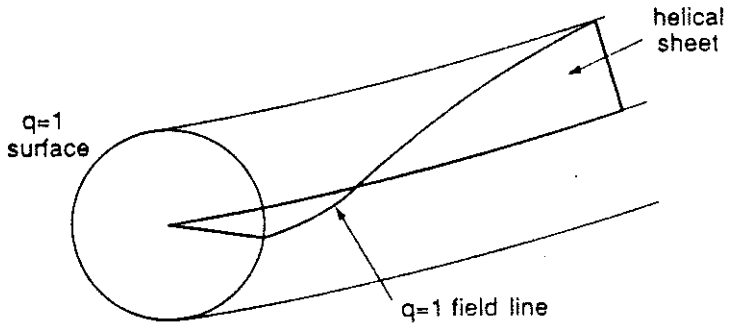

Figure 2. Helical sheet having $d\theta/d\phi = 1$.

Field lines having q = 1 lie in this sheet, and the equilibrium helical flux inside the q = 1 surface, at r = r_1, is given by

$$\Phi = \int_o^{r_1} (1-q)\, B_\theta \, dr \quad .$$

For a parabolic q profile

$$\Phi \equiv \tfrac{1}{4}(1-q_o) B_{\theta 1}\, r_1 \qquad (1)$$

where $B_{\theta 1} = B_\theta\,(r_1)$.

Electric Field

The electric field in the layer resulting from the reconnection of the helical flux can be estimated by noting that, in a full reconnection, this flux is removed in the time, τ_c, of the sawtooth collapse. Then, since there is no electric field in the frame of the core, we have

$$E \sim \frac{\Phi}{\tau_c} \qquad (2)$$

Resistive Model

The current density which would be expected from the resistive model is

$$j = \sigma \frac{\Phi}{\tau_c} \qquad (3)$$

where σ is the electrical conductivity.

Using equations (1) and (3) together with $\sigma = 2\, ne^2\, \tau_e/m$, where τ_e is the electron collsion frequency, the corresponding electron drift velocity is

$$v_d \sim (1-q_o)\frac{r_1}{R}\frac{\tau_e}{\tau_c}\omega_c\, r_1 \quad .$$

For typical JET values (with $(1-q_o) \sim 0.3$) we find

$$v_d \sim 3\times10^8\ ms^{-1} \quad (=c) \quad .$$

It is clear therefore that the resistive model is inappropriate and that under these conditions the electrons would undergo strong runaway.

Electron Behaviour

At first sight it would appear that the runaway electron current would be "superconducting" and would prevent reconnection. However the situation is very different as can be seen from Figure 3.

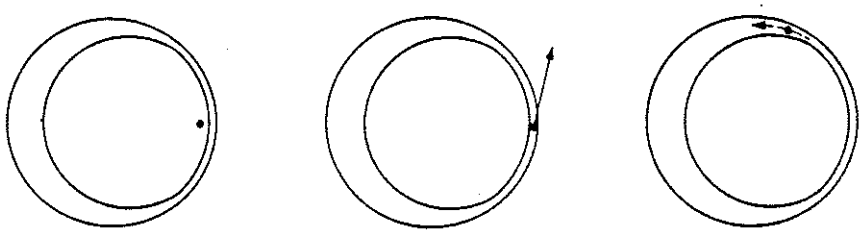

Figure 3. Behaviour of electron during reconnection.

Before entering the layer an electron is effectively stationary. Once in the layer the electron has to move with the required high drift velocity along the direction of the q = 1 field lines. But almost immediately (in ~ μs) the electron is swept out of the layer into the island. Thus the high current density has to be maintained by the continuous acceleration of electrons entering the layer. It is clear therefore that, rather than presenting a low impedance, this form of reconnection gives a high impedance.

Inertial response

When electron inertia dominates, the corresponding term in "Ohm's law" is (m/e) dv/dt. The dominant term is (m/e) v.∇v and neglecting the density gradient the resulting equation is

$$E + \mathrm{v} \times B = \frac{m}{ne^2} \mathrm{v} \cdot \nabla \mathrm{j} \quad . \qquad (4)$$

The electric field in the layer is given by the rate, vB*, at which flux is brought into the layer, where B* is here the helical field at the edge of the layer. Thus, using Ampere's law,

$$\nabla \mathrm{j} \sim \frac{\mathrm{B}^*}{\mu_o \delta^2}$$

and equation (4) gives

$$\delta \sim \frac{c}{\omega_p} \quad ,$$

that is the layer thickness of the order of the collisionless skin depth.

Reconnection Time

We use the same calculation of flow continuity and momentum balance as the conventional model [1]. This gives the core velocity

$$\mathrm{v} \sim \frac{\delta}{\tau_A}$$

where $\tau_A = r_1 / \left(B^* / \sqrt{\mu_o \rho} \right)$. Then, defining the reconnection time

$$\tau = \frac{r_1}{\mathrm{v}} \quad ,$$

we obtain

$$\tau \sim \frac{r_1}{\delta} \tau_A \quad . \qquad (5)$$

In the resistive model $\delta \sim (\tau_A / \tau_R)^{\frac{1}{2}} r_1$, where $\tau_R = \sigma \mu_o r_1^2$, and substitution in to relation (5) gives the Kadomtsev reconnection time

$$\tau_K \sim (\tau_A \tau_R)^{\frac{1}{2}} \quad .$$

In the present model $\delta \sim c/\omega_p$ and the resulting reconnection time is

$$\tau \sim \frac{r_1 \omega_p}{c} \tau_A \quad .$$

Taking JET as an example of a large tokamak, $\tau_A \sim 1\ \mu s$, $\tau_R \sim 10s$, $c/\omega_p \sim 1$ mm and $r_1 \sim 0.3m$. These values give the Kadomtsev reconnection time

$$\tau_K \sim 3ms$$

and the inertial reconnection time

$$\tau \sim 300 \mu s \quad .$$

The observed collapse time on JET is ~ 100 μs and it is clear that the new model is in closer agreement.

Qualifications

The calculation given above indicates that the inertial effect is predominant. The numerical values, however, are clearly imprecise. Furthermore the calculation assumes that reconnection takes place in a particular way, whereas other types of behaviour are in principle possible. Also, we have not included other physical effects such as finite Larmor radius and a possible anomalous electron viscosity [2].

There are two other features which should also be borne in mind. One is that it appears in some experiments [3, 4] that only a fraction of the flux is reconnected, q_o not being restored unity. In this case we might expect a corresponding reduction of the 300 μs reconnection time calculated above. Another effect is the velocity space instability of the runaway electrons. Simulations [5] indicate that this might increase the effective electron mass, again reducing the calculated reconnection time.

Conclusion

The above analysis should be regarded as a clarification of the conventional reconnection model rather than an attempted description of the experimental behaviour. With so many uncertainties regarding the physics of sawtooth oscillations it is not clear that the reconnection is of this type. However it might be that examination of the consequences of the theory presented here could lead to better understanding of the experimental observations.

References

1. Kadomtsev, B.B., Fiz Plasmy 1, 710 (1975) Sov. J. Plasma Physics 1, 389 (1976).
2. Aydemir, A.Y., Phys. Fluids B2, 2135 (1990).
3. Soltwisch, H., et al.l Proc. 10th IAEA Conf., Kyoto 1986, Vol 1 p263.
4. JET Team (presented by D.J. Campbell), this Conference.
5. Wesson, J.A. and Sykes, A., Proc. 5th Eur. Conf. on Controlled Fussion and Plamsa Physics, Grenoble 1972, Vol. 1, p170.

APPENDIX 1.

THE JET TEAM

JET Joint Undertaking, Abingdon, Oxon, OX14 3EA, U.K.

J.M.Adams[1], F.Alladio[4], H.Altmann, R.J.Anderson, G.Appruzzese, W.Bailey, B.Balet, D.V.Bartlett, L.R.Baylor[24], K.Behringer, A.C.Bell, P.Bertoldi, E.Bertolini, V.Bhatnagar, R.J.Bickerton, A.Boileau[3], T.Bonicelli, S.J.Booth, G.Bosia, M.Botman, D.Boyd[31], H.Brelen, H.Brinkschulte, M.Brusati, T.Budd, M.Bures, T.Businaro[4], H.Buttgereit, D.Cacaut, C.Caldwell-Nichols, D.J.Campbell, P.Card, J.Carwardine, G.Celentano, P.Chabert[27], C.D.Challis, A.Cheetham, J.Christiansen, C.Christodoulopoulos, P.Chuilon, R.Claesen, S.Clement[30], J.P.Coad, P.Colestock[6], S.Conroy[13], M.Cooke, S.Cooper, J.G.Cordey, W.Core, S.Corti, A.E.Costley, G.Cottrell, M.Cox[7], P.Cripwell[13], F.Crisanti[4], D.Cross, H.de Blank[16], J.de Haas[16], L.de Kock, E.Deksnis, G.B.Denne, G.Deschamps, G.Devillars, K.J.Dietz, J.Dobbing, S.E.Dorling, P.G.Doyle, D.F.Düchs, H.Duquenoy, A.Edwards, J.Ehrenberg[14], T.Elevant[12], W.Engelhardt, S.K.Erents[7], L.G.Eriksonn[5], M.Evrard[2], H.Falter, D.Flory, M.Forrest[7], C.Froger, K.Fullard, M.Gadeberg[11], A.Galetsas, R.Galvao[8], A.Gibson, R.D.Gill, A.Gondhalekar, C.Gordon, G.Gorini, C.Gormezano, N.A.Gottardi, C.Gowers, B.J.Green, F.S.Griph, M.Gryzinski[26], R.Haange, G.Hammett[6], W.Han[9], C.J.Hancock, P.J.Harbour, N.C.Hawkes[7], P.Haynes[7], T.Hellsten, J.L.Hemmerich, R.Hemsworth, R.F.Herzog, K.Hirsch[14], J.Hoekzema, W.A.Houlberg[24], J.How, M.Huart, A.Hubbard, T.P.Hughes[32], M.Hugon, M.Huguet, J.Jacquinot, O.N.Jarvis, T.C.Jernigan[24], E.Joffrin, E.M.Jones, L.P.D.F.Jones, T.T.C.Jones, J.Källne, A.Kaye, B.E.Keen, M.Keilhacker, G.J.Kelly, A.Khare[15], S.Knowlton, A.Konstantellos, M.Kovanen[21], P.Kupschus, P.Lallia, J.R.Last, L.Lauro-Taroni, M.Laux[33], K.Lawson[7], E.Lazzaro, M.Lennholm, X.Litaudon, P.Lomas, M.Lorentz-Gottardi[2], C.Lowry, G.Magyar, D.Maisonnier, M.Malacarne, V.Marchese, P.Massmann, L.McCarthy[28], G.McCracken[7], P.Mendonca, P.Meriguet, P.Micozzi[4], S.F.Mills, P.Millward, S.L.Milora[24], A.Moissonnier, P.L.Mondino, D.Moreau[17], P.Morgan, H.Morsi[14], G.Murphy, M.F.Nave, M.Newman, L.Nickesson, P.Nielsen, P.Noll, W.Obert, D.O'Brien, J.O'Rourke, M.G.Pacco-Düchs, M.Pain, S.Papastergiou, D.Pasini[20], M.Paume[27], N.Peacock[7], D.Pearson[13], F.Pegoraro, M.Pick, S.Pitcher[7], J.Plancoulaine, J-P.Poffé, F.Porcelli, R.Prentice, T.Raimondi, J.Ramette[17], J.M.Rax[27], C.Raymond, P-H.Rebut, J.Removille, F.Rimini, D.Robinson[7], A.Rolfe, R.T.Ross, L.Rossi, G.Rupprecht[14], R.Rushton, P.Rutter, H.C.Sack, G.Sadler, N.Salmon[13], H.Salzmann[14], A.Santagiustina, D.Schissel[25], P.H.Schild, M.Schmid, G.Schmidt[6], R.L.Shaw, A.Sibley, R.Simonini, J.Sips[16], P.Smeulders, J.Snipes, S.Sommers, L.Sonnerup, K.Sonnenberg, M.Stamp, P.Stangeby[19], D.Start, C.A.Steed, D.Stork, P.E.Stott, T.E.Stringer, D.Stubberfield, T.Sugie[18], D.Summers, H.Summers[20], J.Taboda-Duarte[22], J.Tagle[30], H.Tamnen, A.Tanga, A.Taroni, C.Tebaldi[23], A.Tesini, P.R.Thomas, E.Thompson, K.Thomsen[11], P.Trevalion, M.Tschudin, B.Tubbing, K.Uchino[29], E.Usselmann, H.van der Beken, M.von Hellermann, T.Wade, C.Walker, B.A.Wallander, M.Walravens, K.Walter, D.Ward, M.L.Watkins, J.Wesson, D.H.Wheeler, J.Wilks, U.Willen[12], D.Wilson, T.Winkel, C.Woodward, M.Wykes, I.D.Young, L.Zannelli, M.Zarnstorff[6], D.Zasche[14], J.W.Zwart.

PERMANENT ADDRESS

1. UKAEA, Harwell, Oxon. UK.
2. EUR-EB Association, LPP-ERM/KMS, B-1040 Brussels, Belgium.
3. Institute National des Récherches Scientifique, Quebec, Canada.
4. ENEA-CENTRO Di Frascati, I-00044 Frascati, Roma, Italy.
5. Chalmers University of Technology, Göteborg, Sweden.
6. Princeton Plasma Physics Laboratory, New Jersey, USA.
7. UKAEA Culham Laboratory, Abingdon, Oxon. UK.
8. Plasma Physics Laboratory, Space Research Institute, Sao José dos Campos, Brazil.
9. Institute of Mathematics, University of Oxford, UK.
10. CRPP/EPFL, 21 Avenue des Bains, CH-1007 Lausanne, Switzerland.
11. Risø National Laboratory, DK-4000 Roskilde, Denmark.
12. Swedish Energy Research Commission, S-10072 Stockholm, Sweden.
13. Imperial College of Science and Technology, University of London, UK.
14. Max Planck Institut für Plasmaphysik, D-8046 Garching bei München, FRG.
15. Institute for Plasma Research, Gandhinagar Bhat Gujat, India.
16. FOM Instituut voor Plasmafysica, 3430 Be Nieuwegein, The Netherlands.
17. Commissiariat à L'Energie Atomique, F-92260 Fontenay-aux-Roses, France.
18. JAERI, Tokai Research Establishment, Tokai-Mura, Naka-Gun, Japan.
19. Institute for Aerospace Studies, University of Toronto, Downsview, Ontario, Canada.
20. University of Strathclyde, Glasgow, G4 ONG, U.K.
21. Nuclear Engineering Laboratory, Lapeenranta University, Finland.
22. JNICT, Lisboa, Portugal.
23. Department of Mathematics, Univeristy of Bologna, Italy.
24. Oak Ridge National Laboratory, Oak Ridge, Tenn., USA.
25. G.A. Technologies, San Diego, California, USA.
26. Institute for Nuclear Studies, Swierk, Poland.
27. Commissiariat à l'Energie Atomique, Cadarache, France.
28. School of Physical Sciences, Flinders University of South Australia, South Australia SO42.
29. Kyushi University, Kasagu Fukuoka, Japan.
30. Centro de Investigaciones Energeticas Medioambientales y Techalogicas, Spain.
31. University of Maryland, College Park, Maryland, USA.
32. University of Essex, Colchester, UK.
33. Akademie de Wissenschaften, Berlin, DDR.

CR 88.49.1A